Dynamics of High-Speed Planetary Gears with a Deformable Ring

Chenxin Wang

Dissertation submitted to the Faculty of the
Virginia Polytechnic Institute and State University
in partial fulfillment of the requirements for the degree of

Doctor of Philosophy
in
Mechanical Engineering

Robert G. Parker, Chair
Rakesh K. Kapania
Pablo Tarazaga
Shuming Sun
Corina Sandu

Sep. 03, 2019
Blacksburg, Virginia

Keywords: Dynamics, Planetary Gears, Deformable Ring, High-Speed

Dynamics of High-Speed Planetary Gears with a Deformable Ring

Chenxin Wang

ABSTRACT

This work investigates steady deformations, measured spectra of quasi-static ring deformations, natural frequencies, vibration modes, parametric instabilities, and nonlinear dynamics of high-speed planetary gears with an elastically deformable ring gear and equally-spaced planets.

An analytical dynamic model is developed with rigid sun, carrier, and planets coupled to an elastic continuum ring. Coriolis and centripetal acceleration effects resulting from carrier and ring gear rotation are included. Steady deformations and measured spectra of the ring deflections are examined with a quasi-static model reduced from the dynamic one. The steady deformations calculated from the analytical model agree well with those from a finite element/contact mechanics (FE/CM) model. The spectra of ring deflections measured by sensors fixed to the rotating ring, space-fixed ground, and the rotating carrier are much different. Planet mesh phasing significantly affects the measured spectra. Simple rules are derived to explain the spectra for all three sensor locations for in-phase and out-of-phase systems. A floating central member eliminates spectral content near certain mesh frequency harmonics for out-of-phase systems.

Natural frequencies and vibration modes are calculated from the analytical dynamic model, and they compare well with those from a FE/CM model. Planetary gears have structured modal properties due to cyclic symmetry, but these modal properties are different for spinning systems with gyroscopic effects and stationary systems without gyroscopic effects. Vibration modes for stationary systems are real-valued standing wave modes, while those for spinning systems are complex-valued traveling wave modes. Stationary planetary gears have exactly four types of modes: rotational, translational, planet, and purely ring modes. Each type has distinctive modal properties. Planet modes may not exist or have one or more subtypes depending on the number of planets. Rotational, translational, and planet modes persist with gyroscopic effects included, but purely ring modes evolve into rotational or one subtype of planet modes. Translational and certain subtypes of planet modes are degenerate with multiplicity two for stationary systems. These modes split into two different subtypes of translational or planet modes when gyroscopic effects are included.

Parametric instabilities of planetary gears are examined with the analytical dynamic model subject to time-varying mesh stiffness excitations. With the method of multiple scales, closed-form expressions for the instability boundaries are derived and verified with numerical results from Floquet theory. An instability suppression rule is identified with the modal structure of spinning planetary gears with gyroscopic effects. Each mode is associated with a phase index such that the gear mesh deflections between different planets have unique phase relations. The suppression rule depends on only the modal phase index and planet mesh phasing parameters (gear tooth numbers and the number of planets).

Numerical integration of the analytical model with time-varying mesh stiffnesses and tooth separation nonlinearity gives dynamic responses, and they compare well with those from a FE/CM model. Closed-form solutions for primary, subharmonic, superharmonic, and second harmonic resonances are derived with a perturbation analysis. These analytical results agree well with the results from numerical integration. The analytical solutions show suppression of certain resonances as a result of planet mesh phasing. The tooth separation conditions are analytically determined. The influence of the gyroscopic effects on dynamic response is examined numerically and analytically.

Dynamics of High-Speed Planetary Gears with a Deformable Ring

Chenxin Wang

GENERAL AUDIENCE ABSTRACT

Planetary gears in aerospace applications have thin ring gears for reducing weight. These lightweight ring gears deform elastically when transmitting power. At high speed, Coriolis and centripetal accelerations of planetary gears become significant. This work develops an analytical planetary gear model that takes account of an elastically deformable ring gear and speed-dependent gyroscopic (i.e., Coriolis) and centripetal effects. Steady deformations, measured spectra of quasi-static ring deformations, natural frequencies, vibration modes, parametric instabilities, and dynamic responses of planetary gears with equally-spaced planets are investigated with the analytical model.

Steady deformations refer to quasi-static deflections that result from applied torques and centripetal acceleration effects. These steady deformations vary because of periodically changing mesh interactions. Such variation leads to cyclic stress that reduces system fatigue lives. This work evaluates planetary gear steady deformations with the analytical model and studies the effects of system parameters on the steady deformations.

Ring deflections measured by sensors fixed to the rotating ring gear (e.g., a strain gauge), space-fixed ground (e.g., a displacement probe), and the rotating carrier have much different spectra. The planet mesh phasing, which is determined by gear tooth numbers and the number of planets, significantly influences these spectra. Simple rules are derived that govern the occurrence of spectral content in all the three measurements. Understanding these spectra is of practical significance to planetary gear engineers and researchers.

Planetary gears have highly structured modal properties due to cyclic symmetry. Vibration modes are classified into rotational, translational, and planet modes in terms of the motion of central members (sun and carrier). The central members have only rotation for a rotational mode, only translation for a translational mode, and no motion for a planet mode. Translational modes have two subtypes, rotational modes have only one subtype, and planet modes may not exist or have one or more subtypes depending on the number of planets. For each subtype of modes, all planets have the same motion with a unique phase relation between different planets and the elastic ring gear has unique deformations. Understanding this modal structure is important for modal testing and resonant mode identification in dynamic responses.

Sun-planet and ring-planet mesh interactions change periodically with mesh frequency. These mesh interactions are modeled as time-varying stiffnesses that parametrically excite the planetary gear system. Parametric instabilities, in general, occur when the mesh frequency or one of its harmonics is near twice a natural frequency or combinations of two natural frequencies. Closed-form expressions for parametric instability boundaries that bound the instability region are determined from the analytical model. Certain parametric instabilities are suppressed as a result of planet mesh phasing.

Near resonances, vibration can become large enough that meshing teeth lose contact. The analytical model is extended to include the tooth separation nonlinearity. Closed-form approximations for dynamic responses near resonances are determined from the analytical model, and these analytical results compare well with those from numerical simulations of the analytical model. Tooth separation conditions are analytically determined. The influences of planet mesh phasing and Coriolis acceleration on dynamic responses near resonances are investigated numerically and analytically.

Acknowledgments

I thank Professor Robert G. Parker for his support and guidance during my PhD study. As my advisor, he gives me advices on how to solve research problems, trains me to be an independent researcher, and teaches me how to write scientific papers. I thank Professor Parker for his patience and time in reviewing my manuscripts and giving me feedbacks.

I thank Professor Pablo Tarazaga, Shuming Sun, Rakesh K. Kapania, and Corina Sandu for serving on my doctoral committee. I am deeply impressed by Professor Tarazaga's energetic teaching of mechanical vibrations. Professor Sun's teaching in courses on ordinary differential equations gave me mathematic skills useful for my research. I thank Professor Kapania for his rigorous teaching of elastic stability. I thank Professor Sandu for her encouragement of completing my PhD degree.

I thank Dr. Sandeep Vijayakar for the use and technical support of his Calyx software. I thank GE Avio for financial support of my research.

I thank my lab members: Bin Dong, Xiaoqi Li, Chunguang Liu, Xiang Dai, Kedar Vaidya, Zakia Ahmed, Faris Alsaedi, Yan Song, Li Tan, and Boxi Jiang for their friendship. I thank my family for their support, without which I cannot complete this program.

Contents

List of Figures

List of Tables

Chapter 1

Introduction

1.1 Motivation

Planetary gears in aerospace applications have thin ring gears for the purpose of weight savings. These thin ring gears experience significant elastic deformations under large torque and high speed. Coriolis and centripetal acceleration effects that arise from carrier or ring rotation become significant at the high speed of aerospace applications. These high-speed planetary gears with lightweight ring gears have high risk of noise and vibrations. Planetary gear models that consider both ring gear elastic deformations and high-speed gyroscopic (i.e., Coriolis) and centripetal effects are rare, let alone the study of vibrational behaviors of planetary gears with such features. This work aims to develop an analytical model of planetary gears with an elastic ring and gyroscopic and centripetal effects. We use the model to study steady deformations, measured spectra of quasi-static ring deformations, natural frequencies, vibration modes, parametric instabilities, and dynamic responses of planetary gears.

Planetary gear deformations compose of steady deformations and vibrations about the steady deformed configurations. The steady deformations refer to quasi-static deflections resulting from applied torque excitations and centripetal excitations of carrier-planet or/and ring rotation. These steady deformations vary with periodically changing mesh interactions. Cyclic stress resulting from such variation accelerates damage to the system. Although the vibrations concern engineers and researchers, the steady deformations should get attention as well because they dominate in non-resonant speed regions where the system is designed to operate. Planetary gear steady deformations include elastic ring deformations as well as rigid-body motions of the sun, carrier, and planets.

Some experimental measurements [1–3] of ring deformations demonstrate sidebands near, but not necessarily at, the mesh frequency harmonics. The occurrence of these sidebands varies for different planet mesh phasing and depends on whether the sensor is fixed to the rotating ring, the rotating carrier, or ground. Understanding these sidebands is of practical significance to planetary gear engineers and researchers.

Vibrations become large when the operating speed approaches resonant speeds. Modal analysis is essential to understand the resonant behavior. To be specific, modal analysis can be used to identify which modes are excited for a given resonant peak. Modal analysis also helps identify critical modes having high sun-planet or ring-planet mesh deflections. These critical modes have more potential to damage the planetary gear system when excited. An understanding of planetary gear modal properties is useful for modal test. For example, if an impulse excitation is orthogonal to a vibration mode, that mode is not going to respond. Therefore, the impulse test cannot capture the natural frequency of that mode. Modal analysis is the prerequisite for the study of parametric instabilities and derivation of analytical solutions for the dynamic responses near resonances. The gyroscopic and centripetal effects on the modal properties of planetary gears with an elastic ring are unknown.

The time-varying sun-planet and ring-planet mesh stiffnesses are the source of the vibration. They change periodically with mesh frequency. When the mesh frequency or one of its harmonics is near twice a natural frequency or combinations of two natural frequencies, parametric instabilities in general occur. Large parametric instabilities can severely damage the planetary gear system. Suppression of certain critical parametric instabilities motivates the study of this behavior. Again, the gyroscopic and centripetal effects on the parametric instabilities of planetary gears with an elastic ring are unknown.

Planetary gear dynamics are of primary concern in this work. At large resonances, tooth contact loss can occur. The tooth separation nonlinearity may lead to jump, period doubling, or chaos. These nonlinear behaviors are more dangerous than a resonance without tooth contact loss because of tooth impact. The gyroscopic and centripetal effects on the planetary gear dynamics are rarely touched. Whether these effects are significant or not is unresolved. This work is going to study the dynamics of planetary gears with gyroscopic and centripetal effects, and identify their influences on the dynamic responses. This work also aims to find closed-form solutions for the dynamic responses near resonances. The analytical solutions permit quick estimates of the influences of system parameters on the dynamic responses.

1.2 Literature Review

1.2.1 Planetary Gear Modeling

Various planetary gear models have been used for the study of planetary gear dynamics and vibration. Many papers [4–11] adopted lumped-parameter models where each of the sun, carrier, planets, and ring is treated as a rigid body. The elastic deformation of each member is ignored. Gear contact is modeled as a stiffness connecting two gear bodies. A finite element/contact mechanics (FE/CM) software developed by Vijayakar [12] allows elastic deformation of each member and models gear contact with a specialized algorithm that does not require any external specification of mesh stiffnesses. Many studies have used the FE/CM approach for planetary gear quasi-static analysis [13], dynamic analysis [14–16], and load sharing behaviors[17, 18]. Although the FE/CM approach is multi-functional, it has several limitations. First, it is time-consuming for dynamic simulations of planetary gears. Second, it neglects gyroscopic and centripetal effects that are significant for high-speed systems. Third, it does not provide analytical understanding. A few researches [19–22] have developed lumped-parameter planetary gear models coupled with elastic ring or carrier. Among them, Abousleiman and Velex [19] presented a hybrid planetary gear model that combines rigid-body models of the sun, carrier, and planets with a finite element ring gear. Ref. [20] extended the hybrid model [19] to include a finite element carrier instead of the rigid one. Instead of using finite element modeling, Wu and Parker [21] employed an analytical elastic ring model with partial differential equations coupled to rigid sun, carrier, and planets. This model, however, does not include gyroscopic and centripetal effects. The elastic ring is inextensional without extensional deformation , shear deformation or rotary inertia. Each planet connects the elastic ring through a discrete mesh stiffness directly attached to the ring neutral axis, and a concentrated tooth bending moment resulting from the mesh force on the elastic ring is ignored.

1.2.2 Planetary Gear Steady Deformations

Planetary gear steady deformations refer to quasi-static deflections of the system. One aspect of quasi-static study is the load sharing behaviors of planetary gears subject to manufacturing or assembly errors. Planet load sharing has been studied extensively in

[13, 17, 18, 23–29]. Approaches to improve load sharing include floating a central member, flexible planet pin, and compliant ring gear.

Only a few studies [13, 19, 20] exist on the quasi-static deflections of planetary gears. Kahraman [13] demonstrated that ring gears with thin rims deflect significantly in a quasi-static analysis. Abousleiman and Velex [19] presented quasi-static deflections of a lumped-parameter helical planetary gear model coupled with a finite element ring gear. In an another study, Abousleiman et.al. [20] extended the model in [19] to include a finite element carrier and presented quasi-static deflections of an example planetary gear system. They showed that the carrier elastic deformation is not as significant as the ring elastic deformation.

1.2.3 Planetary Gear Sideband Behavior

A few papers [1–3, 19, 30] have investigated the sidebands near mesh frequency harmonics in measured spectra of ring gear deformations. Abousleiman and Velex [19] demonstrated the sideband behavior of ring displacements at a finite element node in quasi-static and dynamic simulations; no analysis is provided. McFadden and Smith [1] explained that the sideband behavior is an artefact of vibration measurements at a fixed point on the stationary ring gear instead of a feature of planetary gear vibrations. The motion of planets relative to the sensor causes the sideband behavior. They also showed that planet mesh phasing significantly influences the sideband behavior. McNames [2] predicted the locations of the dominant sidebands with a continuous-time Fourier series. Inalpolat and Kahraman [3] investigated sideband behaviors for planetary gears of any planet spacing condition and any planet phasing condition with theoretical analysis and experimental validations. Zghal et.al. [30] developed a lumped parameter model of planetary gears in the stationary ring reference frame to examine the sideband behavior. All of these studies [1–3, 30] focused on the spectra of ring deflection at a fixed point for planetary gears with a stationary ring gear. The spectra of ring deflections for planetary gears where all or any two of the sun gear, carrier, and ring gear can spin measured by sensors fixed to the rotating ring, the rotating carrier, or ground have not been fully examined.

1.2.4 Planetary Gear Modal Properties

Planetary gears have highly structured modal properties due to their cyclic symmetry. Botman [5] identified the modal structure in a study of free vibrations for a three-planet system, where each of the sun, carrier, planets, and ring has two in-plane translational and one rotational degrees of freedom. He categorized the vibration modes into axisymmetric and nonaxisymmetric modes. In the axisymmetric modes, all planets have the same motion and the other components have only rotational motion, while in the nonaxisymmetric modes, the planets do not have the same motion and at least some of the other components have translations. Kahraman[6] classified vibration modes of a four-planet system into in-phase modes, sequentially-phased modes, and counter-phased modes according to whether they are excited under the corresponding mesh phasing conditions. For example, the in-phase modes are excited only under in-phase mesh conditions. Although Botman [5] and Kahraman[6] identified the modal structure for three-planet or four-planet systems, no general conclusions were given.

Lin and Parker[9] identified the modal structure for planetary gears with equally-spaced planets and proved there are exactly three types of modes: rotational, translational, and planet modes. The rotational modes are the same with the axisymmetric modes in [5] and in-phase modes in [6], and the translational modes are the same with the nonaxisymmetric modes in [5] and sequentially-phased modes in [6]. The counter-phased modes in [6] belong to planet modes. Planet modes only exist for systems with four or more planets. Each type of modes has unique properties. For a rotational mode, the central components (the sun, carrier, and ring) have only rotations, and all planets have the same motions that are in-phase. In a translational mode, the central components have only translations. In a planet mode, the central component have no motions, and only the planets vibrate. Ericson and Parker [31] confirmed this modal structure in experiments. Cooley and Parkers [10] showed the modal structure persists for planetary gears with gyroscopic effect, but the real-valued standing wave modes become complex-valued traveling wave modes.

The aforementioned studies [5, 6, 9, 10] focused on lumped-parameter planetary gear models, where the sun, carrier, planets, and ring are treated as rigid bodies. Wu and Parker [21] incorporated an elastic ring into a lumped parameter model from [9]. They grouped vibration modes of the elastic-discrete system into rotational, translational, planet, and purely ring modes. The discrete motions for the rotational, translational, and planet modes are similar to those in [9], and the elastic ring has unique deformations associated with each of the three types of modes. The purely ring modes have only ring deformations, and all the discrete motions vanish.

There exist studies on modal structures of helical planetary gears or compound planetary gears. For helical planetary gears, out-of-plane motions need to be taken into account. Eritenel and Parker [32] derived modal structure for planetary gears with three-dimensional vibrations. Compound planetary gears are used in applications where large reduction ratios are demanded. The modal structure for compound planetary gears was studied in [33–35].

1.2.5 Planetary Gear Parametric Instabilities

The primary source of gear vibration is changing mesh interaction as gear rotates. This change is modeled as time-varying mesh stiffness that parametrically excites the gear system. The study of parametric instability not only identifies regular resonances where the excitation frequency or one of its harmonics coincides with a natural frequency, but also identifies resonances where the excitation frequency or one of its harmonics is near twice a natural frequency or combinations of two natural frequencies.

The parametric instabilities for single or two-stage gear pairs have been investigated in [36–41]. Only a few studies [42–45] have focused on parametric instabilities of planetary gears. Velex and Flamand [42] simulated dynamic response of a three-planet system with time-varying mesh stiffness excitations and found substantial influences of mesh stiffnesses on dynamic tooth loads. Lin and Parker [43] investigated parametric instabilities of planetary gears from mesh stiffness variations with a purely rotational model and derived closed-form expressions for instability boundaries. They concluded that certain parametric instabilities vanish under particular mesh phasing conditions, regardless of any form of mesh stiffness variations. Parker and Wu [44] determined parametric instability boundaries for planetary gears with an elastic ring. An instability existence rule that depends on only planet mesh phasing was derived for any two given modes by using the modal structure defined in [21]. Qiu et.al. [45] investigated planetary gear parametric instabilities with time-varying mesh stiffnesses modulated by speed fluctuations. Sideband instabilities occur due to speed fluctuations.

1.2.6 Planetary Gear Dynamics

Gear may lose contact at large resonances. The tooth separation introduces a softening nonlinearity to the gear system, which has been observed in experiments of spur gear pairs [46, 47] and planetary gears [48].

Planetary gear dynamics with tooth separation nonlinearity were studied numerically with numerical simulations or harmonic balance method or analytically with the method of multiple scales. Ambarisha and Parker [16] simulated nonlinear dynamics of planetary gears with a lumped-parameter model and a finite element/contact mechanics model. Successful correlations between the dynamic responses from these two models were achieved. Rich nonlinear behaviors including jumps, period-doubling bifurcations, and chaos occur in their simulations. Masoumi et.al. [11] demonstrated symmetry breaking induced by chaotic responses in planetary gears. Li et.al. [49] analyzed the bifurcations and chaos in a two-stage planetary gear train and demonstrated high damping coefficients suppress chaotic behaviors while high value of backlash leads to chaotic responses. Sun and Hu [50] studied nonlinear dynamics of planetary gears with harmonic balance method. Double-sided impact vibration was observed at large resonances. Al-Shyyab and Kahraman [51] used harmonic balance method to investigate nonlinear dynamics of planetary gears. The solutions from the harmonic balance method agreed well with those from numerical integration and finite element simulations. In an another study, Al-Shyyab et.al. [52] extended the model in [51] to multi-stage planetary gear trains. Guo and Parker [53] investigated dynamics of planetary gears with tooth contact loss, bearing clearance, and mesh stiffness variations using harmonic balance methods. A hardening effect caused by the transition from no bearing contact to contact was observed in the dynamic responses. The hardening effect is significant in wind turbine planetary gear sets where gravity plays a dominant role over mesh stiffness fluctuations, as shown by Guo et.al. [54]. Zhu et.al. [55] investigated nonlinear dynamic characteristics of compound planetary gear sets with harmonic balance method. Time-varying mesh stiffness, transmission error, and backlash were considered in their model. Bahk and Parker [56] derived closed-form approximations for the nonlinear dynamics with the method of multiple scales. Their analytical solutions compared well against the solutions from harmonic balance methods, numerical integration, and finite element simulations. From the analytical solutions, they concluded tooth separation occurs even under large torques, which differs from conventional thinking that large torques suppress contact loss. In an another study, Bahk and Parker [57] investigated the effects of tooth profile modification on planetary gear dynamics with a perturbation method. Analytical solutions for the dynamic responses near resonances were derived such that an optimal tooth profile modification can be quickly identified to minimize the vibration.

Planetary gears may have manufacturing or assembly errors such as eccentricity, planet position errors, and tooth profile errors. These errors may drastically alter planetary gear dynamic loads and deflections. The dynamic behaviors of planetary gears with manufacturing and assembly errors were studied in [8, 58–65]. Elastic components, such as thin ring gears, affect planetary gear dynamics as well. Dynamic responses of planetary gears with deformable ring gear or carrier were investigated in [15, 19, 20, 22]. There exist other studies of planetary gear dynamics that focus on time-varying pressure angles and contact ratios [66], statistic dynamics of wind turbine planetary gears subject to random excitation [67], planetary gear dynamics with tooth root crack [68–70], and dynamic load sharing under the effect of gravity [71].

1.3 Scope of Investigation

Chapter 2 develops an analytical dynamic model of planetary gears that combines lumped-parameter models of the sun, carrier, and planets with an elastic continuum ring having bending, extensional, and shear deformations as well as rotary inertia. Coriolis and centripetal accelerations resulting from carrier or/and ring rotation are included. Each ring-planet mesh force acts at a contact point radially away from the neutral axis, creating a concentrated tooth bending moment on the elastic ring. The equations of motion for the hybrid elastic-discrete system are cast into a matrix operator form and then discretized with Galerkin method. Steady deformations are numerically calculated from a quasi-static model reduced from the dynamic one, and they are compared with those from a finite element/contact mechanics model for verification. The effects of the ring extensional deformations, shear deformations, and the concentrated tooth bending moment on the steady deformations are evaluated. Spectra of ring deflections measured by sensors fixed to the rotating ring, the rotating carrier, and ground are examined for in-phase and out-of-phase systems with the quasi-static model. Simple rules are derived that govern the occurrence of spectral content in any measured spectra including the three specific cases listed above for in-phase and out-of-phase systems. Influences of floating a central member on the measured spectra are demonstrated numerically and examined analytically.

Chapter 3 examines natural frequencies and vibration modes of spinning planetary gears with equally-spaced planets using the hybrid elastic-discrete model with gyroscopic effects. Natural frequencies and vibration modes calculated from the analytical model are compared against those from a finite element/contact mechanics model [12, 72, 73] for verification. As mentioned in section 1.2.4, Wu and Parker [21] determined modal structure for stationary planetary gears without gyroscopic effects. This work compares the modal structure between stationary and spinning systems with a numerical example. Mathematical justification of the modal structure is presented for spinning systems with gyroscopic effects. A perturbation analysis details the evolution of vibration modes from stationary to spinning systems. Influences of the concentrated tooth bending moments, extensional deformation, shear deformation, and rotary inertia on the natural frequencies are evaluated.

In Chapter 4, parametric instabilities of planetary gears with gyroscopic effects are analyzed with parametric excitations of sun-planet and ring-planet mesh stiffness variations. The governing equations for the analytical planetary gear model are put in a state-space form and then cast into modal equations. Closed-form expressions for instability boundaries are derived from the modal equations with a perturbation analysis. The analytical results are compared against numerical results from Floquet theory for verification. Using the modal structure for spinning planetary gears with gyroscopic effects in the analytical instability boundary expressions leads to an instability suppression rule. This work compares the suppression rule for spinning systems and that for stationary systems derived by Parker and Wu [44]. Numerical examples illustrate the application of the suppression rule for spinning systems.

In Chapter 5, dynamic responses of planetary gears with gyroscopic effects are numerically simulated with the analytical model considering time-varying mesh stiffness excitations and tooth separation nonlinearity. These results are compared against those from a finite element/contact mechanics simulation [12, 72, 73] for verification. Linear resonances without and nonlinear resonances with tooth contact loss in these numerical simulations are analyzed with knowledge of the modal properties and parametric instabilities. Closed-form expressions for dynamic responses near resonances are derived from the analytical model with the method of multiple scales. The analytical results are compared against results from numerical simulations of the analytical model for verification. Influences of the gyroscopic effects and planet mesh phasing on the dynamic responses are studied numerically and analytically.

Chapter 2

Dynamic Modeling and Mesh Phasing-Based Spectral Analysis of Quasi-Static Deformations of Spinning Planetary Gears with a Deformable Ring

2.1 Introduction

Thin planetary ring gears are desirable in aerospace applications. When transmitting loads, these ring gears experience elastic deformations that consist of steady deformations and vibrations about the steady deformed configurations. The steady deformations in this work refer to quasi-static deflections that arise from transmitted torque and centripetal acceleration effects rather than from vibration. Such quasi-static deformations are time-dependent, however, because of the fluctuating tooth mesh stiffnesses, mesh phase relations between the multiple tooth meshes, and possibly fluctuating torque and speed. Steady deformations require attention because they lead to cyclic stresses that can cause fatigue. Vibration that involves inertial effects is likewise damaging, but steady deformations dominate in non-resonant speed regions where the system is designed to operate. Planetary gear steady deformations include elastic ring deformations as well as motions of the sun, carrier, and planets, which are regarded as rigid bodies.

In order to investigate the steady deformation, this paper first develops an analytical planetary gear dynamic model that includes an elastic ring and gyroscopic and centripetal effects arising from carrier and ring rotation. The elastic ring has bending, extensional, and shear deformations. The ring-planet mesh load acts at a contact point away from the ring neutral axis, creating a concentrated tooth bending moment on the ring. The dynamic model is reduced to a quasi-static one to determine steady deformations, and the important centripetal accelerations are retained. We compare the steady deformations from the analytical model to those from a commercial finite element/contact mechanics (FE/CM) software [12, 72, 73] for verification. Ring tooth bending, extensional, and shear effects on the steady deformations are evaluated.

Some experimental measurements [1–3] of ring deformations demonstrate sidebands near, but not necessarily at, the mesh frequency harmonics, while others just show spectral content at the mesh frequency harmonics. These differing behaviors depend on whether the sensor is rotating with the ring, with the carrier, or fixed to ground. Planet mesh phasing plays a critical role. Understanding these different spectra is of practical significance to planetary gear engineers and researchers. This work demonstrates and explains the differing spectra for quasi-static ring deformations measured by sensors fixed to a material point on the rotating ring, space-fixed ground, or the rotating carrier for in-phase and out-of-phase planet meshes. Simple rules are derived that govern the occurrence of frequency content in any measured spectra including the three specific cases listed above for in-phase and out-of-phase systems.

Steady deformations can be calculated from different planetary gear models, such as lumped parameter models [4–11], FE/CM models [12, 72, 73], and lumped parameter models with elastic components [19–22]. Lumped parameter models [4–11] provide a quick estimate of steady deformations. They need fewer input quantities and can be solved easily. These models, however, do not consider elastic ring deformations. The FE/CM software developed by Vijayakar [12] overcomes the limitations of the lumped-parameter models by modeling each gear as a deformable body with specialized modeling of the tooth contact forces. The FE/CM approach is suitable for steady deformation analysis of one or a few planetary gear configurations, but it does not provide analytical understanding, uses proprietary modeling, and is not suitable for parametric studies that require many parameter variations. A few papers [19–22] have developed hybrid models that combine lumped-parameter models for sun and planet deflections with an elastic ring or carrier. Among them, Abousleiman and Velex [19] presented quasi-static deflections of a lumped-parameter planetary gear coupled with a finite element ring gear. Ref. [20] extended the elastic-discrete model [19] to include a finite element carrier. Instead of using a finite element approach, Wu and Parker [21] incorporated an analytical deformable ring with partial differential equations into a model with rigid sun, carrier, and planets. The model in [21], however, has limitations: the elastic ring is inextensional without extensional or shear deformations; the ring-planet mesh load is applied on the ring neutral axis such that the concentrated tooth bending moment is ignored; the model is stationary without any rotational effects. The current work removes these limitations.

Ring deformations generate unusual sideband behavior near harmonics of mesh frequency that has important implications in practice and for understanding measured spectra. Abousleiman and Velex [19] showed ring displacements at a finite element node have low-frequency fluctuations associated with the frequency at which planets pass the node as well as asymmetric sidebands near mesh frequencies. McFadden and Smith [1] explained the sideband behavior as an outcome of vibrations excited by planets as they move relative to a point on the stationary ring. They identified where the sideband frequencies occur using phaser sums, but did not address sideband amplitudes. McNames [2] employed a continuous-time Fourier series to study the sideband behavior and predicted that dominant sidebands only occur at frequencies that are integer multiples of planet pass frequency relative to a point on the stationary ring. McNames' analysis gives general representations of the sideband amplitudes but does not reveal the ring deformations associated with each sideband, nor does it reveal sideband amplitudes. Inalpolat and Kahraman [3] analytically and experimentally investigated sideband behaviors for planetary gears of any planet spacing condition and any planet phasing condition. All of these studies [1–3] focused on the spectra of ring deflection at a fixed point for planetary gears with a stationary ring gear. In contrast, the present work examines epicyclic/planetary gear systems where any two or all of the ring, carrier, and sun rotate. Furthermore, we explain the differing spectra (including sideband locations, sideband amplitudes, and ring deformation associated with each sideband) of ring deflection measured by sensors fixed to any one of: a material point on the rotating ring (e.g., a strain gauge), space-fixed ground (e.g., a displacement probe), and the rotating carrier. The analytical predictions apply to systems with a stationary carrier or ring gear by specifying zero carrier or ring gear speed.

2.2 Analytical Dynamic Model

2.2.1 Model Description

Figure 2.1 shows the elastic-discrete planetary gear model for motions confined to the plane. The sun, carrier, and N planets are treated as rigid bodies while the ring is elastically deformable. Each of the sun, carrier, and planets has three degrees of freedom: two in-plane translations and one rotation. The supports or bearings for the sun, carrier, and planets are modeled as linear stiffnesses. The sun-planet and ring-planet tooth mesh interactions are represented as linear stiffnesses along the line of action. The carrier and ring have speeds Ω_c and Ω_r, respectively. Speeds of the sun and planets can be derived from kinematics.

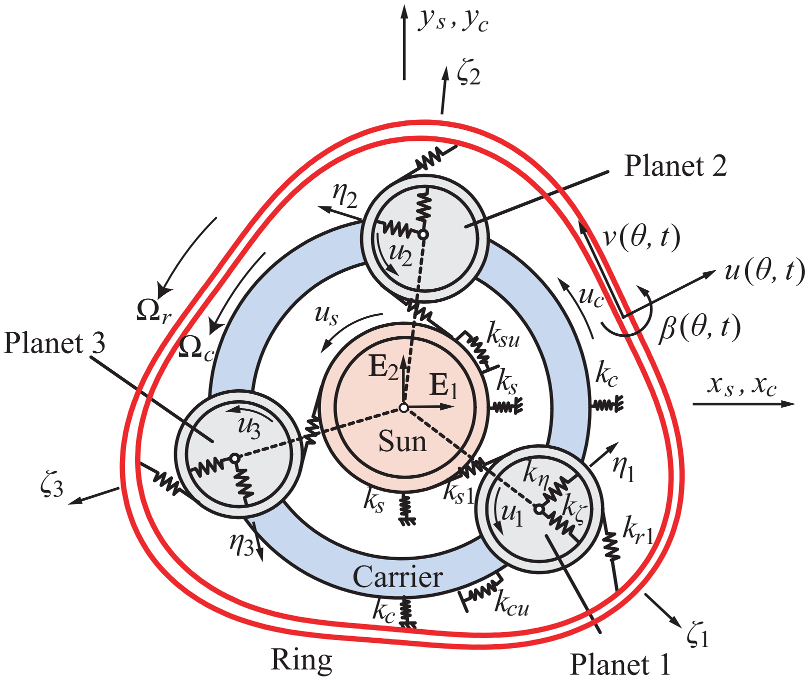

Figure 2.1: Schematic of a planetary gear model with a deformable ring.

A schematic of the elastic ring is shown in Fig. 2.2. The ring is uniform along the circumferential direction with neutral axis radius R and cross-sectional area A. The ring neutral axis is defined by the circle that passes through the centroid of each ring cross section. The ring density, Young's modulus, and shear modulus are ρ, E, and G, respectively. The elastic ring has a rigid body at its center to accommodate an input or output member attached to the ring. The circumference of this circular ring rigid body connects to the ring neutral axis through a uniform elastic foundation with radial (k_u) and tangential (k_v) distributed stiffnesses per unit arclength of ring neutral axis. The ring rigid body has one rotational and two in-plane translational degrees of freedom that are connected to ground by rotational stiffness k_{bu} and isotropic translational stiffness k_b, respectively.

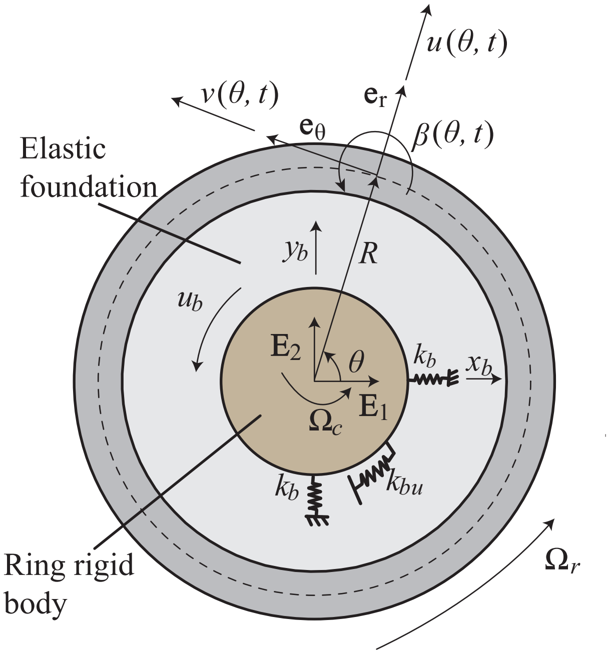

Figure 2.2: Schematic of the rotating ring.

The coordinates are illustrated in Fig. 2.1 and Fig. 2.2. The sun, carrier, and ring rigid body have translations $x_h, y_h,\ h = s, c, b$, with respect to the basis $\{\mathbf{E}_1, \mathbf{E}_2, \mathbf{E}_3\}$ that is fixed to the carrier and rotates with speed Ω_c. Planet translations are described in the radial and tangential directions as $\zeta_n, \eta_n,\ n = 1, 2, \cdots N$, as shown in Fig. 2.1. The rotational displacements u_j for $j = 1, 2, \cdots, N, s, c, b$ are the rotations in radians times the gear base radii R_p and R_s, the center distance R_c for the carrier, and the radius R_b for the ring rigid body. The circumferential planet locations ψ_n are measured with respect to the rotating basis vector $\mathbf{E}_1$. Without loss of generality, $\psi_1 = 0$.

The elastic deformations of particles on the ring neutral axis are represented by radial ($u(\theta, t)$) and tangential ($v(\theta, t)$) deflections, where θ defines a fixed angular position relative to the rotating basis vector $\mathbf{E}_1$ attached to the carrier. The term material point refers to a particle of the elastic ring. Because the ring has a rotation speed relative to the carrier, and so also relative to $\mathbf{E}_1$, the specific ring particles (or material points) instantaneously located at a given value of θ (which include all material points on a radial cross section) change with time. Likewise, the angle θ at which a given material point is located changes with time. The radial and tangential deflections of the material point that is instantaneously located at a specified angular position θ with a radial distance r from the ring neutral axis are

$$U(\theta, r, t) = u(\theta, t), \qquad V(\theta, r, t) = v(\theta, t) + r\beta(\theta, t), \tag{2.1}$$

where $\beta(\theta, t)$ is the cross-sectional rotation angle [74]. This β is introduced to account for the ring shear deformation. The ring shear angle at the neutral axis is $(v - \partial u/\partial\theta)/R - \beta$. When the shear deformation is neglected, then $\beta = (v - \partial u/\partial\theta)/R$. The extensional deformation at the neutral axis is $u + \partial v/\partial\theta$. When the ring neutral axis is assumed to be inextensible, the ring radial and tangential deflections satisfy $u = -\partial v/\partial\theta$. The ring has only inextensible bending deformation when both of the shear and extensional deformations are neglected. If not otherwise indicated, the ring radial and tangential deflections refer to those of the ring neutral axis.

2.2.2 Dynamic Model Derivation

To expand its applicability, the following derivation is for a *dynamic* model that captures steady deformation and vibrations. Later steady deformation results focus on a quasi-static model reduced from the more general dynamic one. The equations of motion for the elastic-discrete system are derived using Hamilton's principle. Energy expressions for the sun, carrier, planets, ring rigid body, and sun-planet meshes are shown in Appendix A.1, while expressions for ring kinetic energy, ring strain energy, strain energy in the elastic foundation, ring-planet mesh energy, and virtual work are derived below.

Ring Kinetic Energy

The deformed state position of the material point on the ring that is instantaneously located at a given θ and radial distance r from the neutral axis is

$$\mathbf{r}_p = [R + r + u(\theta, t)]\mathbf{e}_r + [v(\theta, t) + r\beta(\theta, t)]\mathbf{e}_\theta, \tag{2.2}$$

where $\{\mathbf{e}_r, \mathbf{e}_\theta, \mathbf{e}_z\}$ is a cylindrical basis defined by the coordinate θ (Fig. 2.2), and this basis rotates with speed Ω_c. The velocity of the material point is given by the material time derivative of the position vector that accounts for the fact that the angle θ at which the material point is located changes with time because of the relative angular speed $(\Omega_r - \Omega_c)$ of the ring relative to the carrier-fixed $\{\mathbf{e}_r, \mathbf{e}_\theta, \mathbf{e}_z\}$ and $\{\mathbf{E}_1, \mathbf{E}_2, \mathbf{E}_3\}$ bases. The following examples illustrate material time derivatives:

$$\mathrm{d}u/\mathrm{d}t = \partial u/\partial t + (\partial u/\partial \theta)(\partial \theta/\partial t) = \partial u/\partial t + (\Omega_r - \Omega_c)(\partial u/\partial \theta),$$

$$\mathrm{d}\mathbf{e}_r/\mathrm{d}t = \partial \mathbf{e}_r/\partial t + (\partial \mathbf{e}_r/\partial \theta)(\partial \theta/\partial t) = \Omega_c\mathbf{e}_\theta + (\Omega_r - \Omega_c)\mathbf{e}_\theta = \Omega_r\mathbf{e}_\theta,$$

$$\mathrm{d}\mathbf{e}_\theta/\mathrm{d}t = \partial \mathbf{e}_\theta/\partial t + (\partial \mathbf{e}_\theta/\partial \theta)(\partial \theta/\partial t) = -\Omega_c\mathbf{e}_r - (\Omega_r - \Omega_c)\mathbf{e}_r = -\Omega_r\mathbf{e}_r.$$

The material time derivatives of $v(\theta,t)$ and $\beta(\theta,t)$ are similar. For compact notation, $\partial u/\partial t$ and $\partial u/\partial\theta$ are subsequently replaced by $u_{,t}$ and $u_{,\theta}$, and $\Omega_{rc}=\Omega_r-\Omega_c$. Thus, the time derivative of Eq. (2.2) is

$$\begin{aligned}\dot{\mathbf{r}}_p =&[u_{,t}+\Omega_{rc}u_{,\theta}-\Omega_r(v+r\beta)]\mathbf{e}_r\\&+[v_{,t}+r\beta_{,t}+\Omega_{rc}(v_{,\theta}+r\beta_{,\theta})+\Omega_r(R+r+u)]\mathbf{e}_\theta.\end{aligned}\tag{2.3}$$

The kinetic energy of the elastic ring is

$$\begin{aligned}K_e =&\frac{1}{2}\int_0^{2\pi}\int_A \rho(R+r)\dot{\mathbf{r}}_p\cdot\dot{\mathbf{r}}_p\ \mathrm{d}A\mathrm{d}\theta\\&\frac{1}{2}\int_0^{2\pi}\Big\{J_0[u_{,t}^2+v_{,t}^2+2\Omega_r(v_{,t}u-u_{,t}v)+2\Omega_{rc}(u_{,t}u_{,\theta}+v_{,t}v_{,\theta})\\&+\Omega_r^2(v^2+u^2+2Ru)+\Omega_{rc}^2(u_{,\theta}^2+v_{,\theta}^2)+2\Omega_{rc}\Omega_r(v_{,\theta}u-u_{,\theta}v)]\\&+J_1[2v_{,t}\beta_{,t}-2\Omega_r u_{,t}\beta+2\Omega_{rc}(v_{,t}\beta_{,\theta}+\beta_{,t}v_{,\theta})+2\Omega_r\beta_{,t}u\\&+2\Omega_r^2 v\beta+2\Omega_r^2 u+2\Omega_{rc}^2 v_{,\theta}\beta_{,\theta}+2\Omega_r\Omega_{rc}(\beta_{,\theta}u-\beta u_{,\theta})]\\&+J_2[\beta_{,t}^2+2\Omega_{rc}\beta_{,t}\beta_{,\theta}+\Omega_r^2\beta^2+\Omega_{rc}^2\beta_{,\theta}^2]+\int_A\rho\Omega_r(R+r)^2/R\\&[2(v_{,t}+r\beta_{,t})+2\Omega_{rc}(v_{,\theta}+r\beta_{,\theta})+\Omega_r(R+r)]\ \mathrm{d}A\Big\}\ R\mathrm{d}\theta,\end{aligned}\tag{2.4}$$

$$J_0=\int_A\rho(R+r)/R\ \mathrm{d}A,\quad J_1=\int_A\rho(R+r)r/R\ \mathrm{d}A,$$
$$J_2=\int_A\rho(R+r)r^2/R\ \mathrm{d}A,$$

where J_0 is the mass per unit arclength of the ring neutral axis, and J_1 and J_2 are the first and second mass moments of inertia about the ring neutral axis per unit arclength of the ring neutral axis, respectively. J_2 is also referred to as rotary inertia [74–76]. Terms associated with J_0, J_1, and J_2 survive the energy variation δK_e to yield terms in the final equations of motion, while the terms that do not contribute to the equations of motion are collected into the last term of Eq. (2.4).

Ring Strain Energy

The extensional and shear strains are [74]

$$\epsilon_n = (u + v_{,\theta} + r\beta_{,\theta})/(R + r), \quad \epsilon_s = (u_{,\theta} - v + R\beta)/(R + r). \tag{2.5}$$

A nonlinear extensional strain-displacement relation from Ref. [77] was used in an initial ring model that did not include shear deformations (i.e., $\epsilon_s = 0$). For that model, the nonlinear terms had negligible effects on the steady deformations of planetary gears for practical torques and speeds. When shear deformations are considered, introducing the second-order nonlinear terms $(u_{,\theta}-v-r\beta)^2/[2(R+r)^2]$ and $(v+r\beta-u_{,\theta})(u+v_{,\theta}+r\beta_{,\theta})/(R+r)^2$ [74] to the extensional and shear strains, respectively, results in cumbersome ring equations that we expect to yield similarly negligible differences compared to those obtained using Eq. (2.5). Therefore, these nonlinear strain terms are neglected.

The stresses and strains are related by $\sigma_n = E\epsilon_n$ and $\sigma_s = \kappa G\epsilon_s$, where κ is a shear correction factor [78] that depends on the geometry of the ring cross section. The strain energy of the elastic ring is

$$\begin{aligned} V_e =& \frac{1}{2}\int_0^{2\pi}\int_A (\sigma_n\epsilon_n + \sigma_s\epsilon_s)(R + r)\ \mathrm{d}A\mathrm{d}\theta \\ =& \frac{1}{2}\int_0^{2\pi}\left\{[\alpha_1(u + v_{,\theta})^2 + \alpha_2(u + v_{,\theta})R\beta_{,\theta} + k_\beta(R\beta_{,\theta})^2] + \alpha_3(u_{,\theta} - v + R\beta)^2\right\}\ \mathrm{d}\theta, \end{aligned} \tag{2.6}$$

$$\alpha_1 = EI_0, \quad \alpha_2 = EI_1/R, \quad k_\beta = EI_2/R^2, \quad \alpha_3 = \kappa GI_0,$$

$$I_0 = \int_A 1/(R + r)\ \mathrm{d}A, \quad I_1 = \int_A r/(R + r)\ \mathrm{d}A, \quad I_2 = \int_A r^2/(R + r)\ \mathrm{d}A.$$

Strain Energy in the Elastic Foundation

The elastic foundation connects the ring neutral axis to the circumference of the ring rigid body. The strain energy in the elastic foundation is

$$\begin{aligned} V_f = \frac{1}{2}\int_0^{2\pi} & [k_u(u - x_b\cos\theta - y_b\sin\theta)^2 \\ & + k_v(v + x_b\sin\theta - y_b\cos\theta - Ru_b/R_b)^2]\ R\mathrm{d}\theta. \end{aligned} \tag{2.7}$$

Ring-Planet Mesh Energy

The ring gear tooth contact is shown in Fig. 2.3. The radial distance from the contact point to the ring neutral axis is denoted as $\mathit{\Gamma}$. Although $\mathit{\Gamma}$ varies over a mesh cycle, the value of $\mathit{\Gamma}$ is approximated as a constant equal to the radial distance from the pitch contact point to the ring neutral axis. The tooth mesh force acting at this contact point, as opposed to acting directly on the neutral axis as done in [21], creates a concentrated moment on the ring neutral axis, in addition to the action of the mesh force itself.

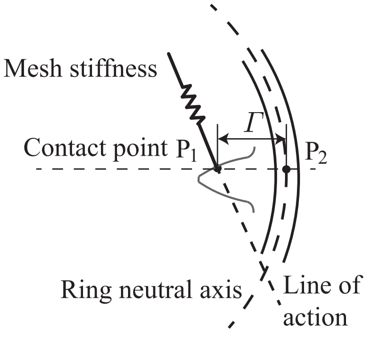

Figure 2.3: Ring gear tooth contact.

The ring-planet mesh deflection is the relative displacement between the ring and planet contact points along the line of action. The expression for the n-th planet is

$$\begin{aligned}\Delta_{rn} =&(\zeta_n \sin\alpha_r - \eta_n \cos\alpha_r - u_n) \\ &+ [-u\sin\alpha_r + v\cos\alpha_r - \mathit{\Gamma}\beta\cos\alpha_r]_{\theta=\psi_n}, \quad n = 1, 2, \cdots, N,\end{aligned} \tag{2.8}$$

where α_r is the ring-planet pressure angle. The last term represents ring gear tooth bending mesh deflection, that is, the displacement of the ring contact point P_1 relative to the point P_2 along the line of action (Fig. 2.3). The ring-planet mesh energy for the n-th planet is

$$V_{rn} = \frac{1}{2}k_{rn}\Delta_{rn}^2, \quad n = 1, 2, \cdots, N. \tag{2.9}$$

Virtual Work

The virtual work done by external torques is

$$\delta W = (T_s/R_s)\delta u_s + (T_c/R_c)\delta u_c + (T_b/R_b)\delta u_b, \tag{2.10}$$

where T_h for $h = s, c, b$ represents the torque applied to the sun, carrier, and ring rigid body.

2.2.3 Dimensionless Equations of Motion

Use of the energy and virtual work expressions in Hamilton's principle leads to ordinary differential equations for the discrete motions of the sun, carrier, planets, and ring rigid body as well as three partial differential equations for the ring elastic deformations. These equations are non-dimensionalized with the quantities

$$\begin{aligned}
&\hat{t} = t\sqrt{k_\zeta/(m_p R)}, \qquad \hat{\Omega}_r, \hat{\Omega}_c = \Omega_r, \Omega_c\sqrt{m_p R/k_\zeta}, \qquad \hat{k}_i = k_i/k_\zeta, \\
&\hat{k}_u = Rk_u/k_\zeta, \qquad \hat{k}_v = Rk_v/k_\zeta, \qquad \hat{\alpha}_1 = \alpha_1/k_\zeta, \qquad \hat{\alpha}_2 = \alpha_2/k_\zeta, \\
&\hat{\alpha}_3 = \alpha_3/k_\zeta, \qquad \hat{u}, \hat{v} = u, v/R, \qquad \hat{\zeta}_n, \hat{\eta}_n, \hat{u}_n = \zeta_n, \eta_n, u_n/R, \\
&\hat{x}_h, \hat{y}_h, \hat{u}_h = x_h, y_h, u_h/R, \qquad \hat{T}_h = (T_h/R_h)/(k_\zeta R), \qquad \hat{\mathit{\Gamma}} = \mathit{\Gamma}/R, \\
&\hat{J}_0 = J_0/m_p, \qquad \hat{J}_1 = J_1/(m_p R), \qquad \hat{J}_2 = J_2/(m_p R^2), \\
&\hat{m}_\varsigma = m_\varsigma/(m_p R), \qquad \hat{I}_\varsigma = I_\varsigma/(m_p R R_h^2), \qquad \hat{R}_\varsigma = R_\varsigma/R,
\end{aligned} \tag{2.11}$$

where the subscripts are

$$i = s, su, c, cu, b, bu, \zeta, \eta, rn, sn, \beta, \qquad n = 1, 2, \cdots, N,$$

$$h = s, c, b, \qquad \varsigma = s, c, b, p.$$

In what follows, the hats on all dimensionless variables are dropped.

The ordinary differential equations for the discrete motions are

$$\mathbf{M}_d\ddot{\mathbf{q}} + \Omega_c\mathbf{G}_d\dot{\mathbf{q}} + \mathbf{K}_d\mathbf{q} - \Omega_c^2\mathbf{C}_d\mathbf{q} + (\mathbf{K}_m + \mathbf{K}_f)\boldsymbol{w} = \mathbf{f}_d, \tag{2.12a}$$

$$\mathbf{q} = \begin{bmatrix}\mathbf{p}_b^T, & \mathbf{p}_c^T, & \mathbf{p}_s^T, & \mathbf{p}_1^T, & \cdots, & \mathbf{p}_N^T\end{bmatrix}^T, \quad \boldsymbol{w} = \begin{bmatrix}u, & v, & \beta\end{bmatrix}^T, \tag{2.12b}$$

$$\mathbf{p}_n = \begin{bmatrix}\zeta_n, & \eta_n, & u_n\end{bmatrix}^T, \quad \mathbf{p}_h = \begin{bmatrix}x_h, & y_h, & u_h\end{bmatrix}^T, \quad h = s, c, b. \tag{2.12c}$$

$\mathbf{M}_d$ and $\mathbf{K}_d$ are non-dimensional mass and stiffness matrices. $\mathbf{G}_d$ and $\mathbf{C}_d$ are non-dimensional gyroscopic and centripetal matrices. Details of these four matrices can be found in Appendix A.2. The vector $\mathbf{f}_d$ represents torque excitations and a constant vector of centripetal acceleration terms acting on the planets from carrier rotation (see Appendix A.2 for detail).

The stiffness coupling terms where the ring elastic deformations influence the discrete motions come from the ring-planet meshes as $\mathbf{K}_m\boldsymbol{w}$ and the connection of the elastic ring to the ring rigid body through the elastic foundation as $\mathbf{K}_f\boldsymbol{w}$. The expressions for $\mathbf{K}_m\boldsymbol{w}$ and $\mathbf{K}_f\boldsymbol{w}$ are

$$\begin{aligned}\mathbf{K}_m\boldsymbol{w} &= \Big[\mathbf{0},\ \ \mathbf{0},\ \ \mathbf{0},\ \ (\mathbf{K}_{m1}\boldsymbol{w})^T,\ \ \cdots,\ \ (\mathbf{K}_{mN}\boldsymbol{w})^T\Big]^T, \\ \mathbf{K}_{mn}\boldsymbol{w} &= k_{rn}\Delta_n\Big[\sin\alpha_r,\ \ -\cos\alpha_r,\ \ -1\Big]^T, \\ \Delta_n &= [-u\sin\alpha_r + v\cos\alpha_r - \mathit{\Gamma}\beta\cos\alpha_r]_{\theta=\psi_n},\end{aligned} \tag{2.13}$$

$$\begin{aligned}\mathbf{K}_f\boldsymbol{w} &= \Big[(\mathbf{K}_{fb}\boldsymbol{w})^T,\ \ \mathbf{0},\ \ \mathbf{0},\ \ \mathbf{0},\ \ \cdots,\ \ \mathbf{0}\Big]^T, \\ \mathbf{K}_{fb}\boldsymbol{w} &= \begin{bmatrix}\int_0^{2\pi}(-k_u u\cos\theta + k_v v\sin\theta)\ \mathrm{d}\theta \\ \int_0^{2\pi}(-k_u u\sin\theta - k_v v\cos\theta)\ \mathrm{d}\theta \\ \int_0^{2\pi} -k_v v/R_b\ \mathrm{d}\theta\end{bmatrix}.\end{aligned} \tag{2.14}$$

Correspondingly, the equations for the ring elastic deformations incorporate coupling with the discrete motions, which is evident from the presence of x_b, y_b, and Δ_{rn} defined in Eq. (2.8). These equations are

$$\begin{aligned}&J_0u_{,tt} + 2J_0(\Omega_{rc}u_{,t\theta} - \Omega_r v_{,t}) - 2J_1\Omega_r\beta_{,t} + \alpha_1(u + v_{,\theta}) + \alpha_2\beta_{,\theta} \\ &+k_u(u - x_b\cos\theta - y_b\sin\theta) - \alpha_3[\beta_{,\theta} - (v_{,\theta} - u_{,\theta\theta})] \\ &-J_0(\Omega_r^2u + 2\Omega_r\Omega_{rc}v_{,\theta} - \Omega_{rc}^2u_{,\theta\theta}) - 2J_1\Omega_r\Omega_{rc}\beta_{,\theta} \\ &+\sum_{n=1}^{N}k_{rn}\Delta_{rn}(-\sin\alpha_r)\delta(\theta - \psi_n) = (J_0 + J_1)\Omega_r^2,\end{aligned} \tag{2.15a}$$

$$\begin{aligned}&J_0v_{,tt} + J_1\beta_{,tt} + 2J_0(\Omega_{rc}v_{,t\theta} + \Omega_r u_{,t}) + 2J_1\Omega_{rc}\beta_{,\theta t} - \alpha_2\beta_{,\theta\theta} \\ &-\alpha_1(u_{,\theta} + v_{,\theta\theta}) + k_v[v + x_b\sin\theta - y_b\cos\theta - u_b/R_b] \\ &-\alpha_3[\beta - (v - u_{,\theta})] - J_0(\Omega_r^2v - 2\Omega_r\Omega_{rc}u_{,\theta} - \Omega_{rc}^2v_{,\theta\theta})\end{aligned}$$

$$-J_1(\Omega_r^2\beta - \Omega_{rc}^2\beta_{,\theta\theta}) + \sum_{n=1}^{N} k_{rn}\Delta_{rn}(\cos\alpha_r)\delta(\theta - \psi_n) = 0, \tag{2.15b}$$

$$\begin{aligned} J_2\beta_{,tt} + J_1 v_{,tt} + 2J_1(\Omega_{rc}v_{,\theta t} + \Omega_r u_{,t}) + 2J_2\Omega_{rc}\beta_{,t\theta} - \alpha_2(u_{,\theta} + v_{,\theta\theta}) \\ -\beta_{,\theta\theta} + \alpha_3[\beta - (v - u_{,\theta})] - J_1(\Omega_r^2 v - 2\Omega_r\Omega_{rc}u_{,\theta} - \Omega_{rc}^2 v_{,\theta\theta}) \\ -J_2(\Omega_r^2\beta - \Omega_{rc}^2\beta_{,\theta\theta}) + \sum_{n=1}^{N} k_{rn}\Delta_{rn}(-\mathit{\Gamma}\cos\alpha_r)\delta(\theta - \psi_n) = 0, \end{aligned} \tag{2.15c}$$

where $\delta(\cdot)$ is the Dirac delta function. The last term on the left side of Eq. (2.15c) is the concentrated tooth bending moment mentioned in section 2.2.2.

Terms associated with the relative speed Ω_{rc} appear in Eq. (2.15) because the rotating ring is modeled in the rotating carrier reference frame. These terms would not appear if the rotating ring was modeled in its own reference frame, as evident in [74]. In order to confirm these terms associated with Ω_{rc}, we re-derived the same rotating ring model in the rotating carrier reference frame by applying the transformation $\theta = \tilde{\theta} + \Omega_{rc}t$ to the rotating ring model in its own reference frame [74], where $\tilde{\theta}$ denotes a fixed angular position in the rotating ring reference frame. In addition, the reverse transformation $\tilde{\theta} = \theta - \Omega_{rc}t$ of the current model (Eq. (2.15)) to the rotating ring model in its own reference frame eliminates these terms. Such a reference frame transformation has been done in Ref. [79] for an inextensional ring without shear deformation, which inspires the idea of using the reference frame transformation to confirm the terms associated with Ω_{rc}.

Focusing on the rotating ring as a component separated from the planetary gear, the present model derived in the rotating carrier reference frame differs from ring models in the literature. Refs. [74, 76, 79–83] presented rotating ring models in the rotating ring reference frame. Some other works [77, 84, 85] formulated rotating ring models in the stationary reference frame. The differences between the three types of rotating ring models lie in the speed-dependent gyroscopic and centripetal terms. The current rotating ring model can be generalized to a rotating ring model in a reference frame with arbitrary rotation speed Ω_a by simply replacing the carrier speed Ω_c with Ω_a. If $\Omega_a = \Omega_r$, the current rotating ring model reduces to a rotating ring model in the rotating ring reference frame. A rotating ring model in the stationary reference frame results from $\Omega_a = \Omega_c = 0$ in the current rotating ring model.

The rotating carrier reference frame has advantages over others as the basis for planetary gears. In any other reference frame, the sun-planet and ring-planet mesh locations are not fixed; instead, their circumferential locations vary with time. Such a change of mesh locations leads to time-varying coefficients in the system equations even if the mesh stiffnesses are constants. Developing the system model in the rotating carrier reference frame avoids this problem.

The complete elastic-discrete model for a spinning planetary gear consists of Eq. (2.12) for the discrete motions and Eq. (2.15) for the ring elastic deformations. With the freedom to independently specify the carrier and ring speeds, the model covers planetary gears of any combination of fixed and/or rotating carrier, sun, and ring gears. This model applies for systems with any planet spacing by simply changing the planet position angles ψ_n, but this work focuses on equally-spaced systems.

The current model has substantial differences compared to the elastic-discrete model in [21]. The model in this work connects the elastic ring to a vibrating ring rigid body, which allows more accurate representation of the total inertia of the ring and any attached input or output member, rather than connecting the elastic ring directly to ground as in [21]. Ref. [21] presents a stationary model that neglects speed-dependent gyroscopic (Coriolis) and centripetal effects that result from carrier and/or ring rotation speeds. The elastic ring in [21] considers only inextensible bending deformation. The present work models bending, extensional, and shear deformations, and later results show extensional deformation is important. Furthermore, the present model includes ring rotary inertia. Ref. [21] neglects the concentrated moment on the ring at the tooth contact point from the mesh force (Fig. 2.3) and the resulting tooth bending mesh deflection (the last term in Eq. (2.8)) because it attaches the ring-planet mesh stiffness directly to the ring neutral axis. These features can be significant for high-speed, lightweight (i.e., thin) gears such as those in aircraft engines.

2.3 Matrix Operator Form and Galerkin Discretization

The coupled partial and ordinary differential equations for the hybrid continuous-discrete system can be collected into a compact form using extended matrix operators similar to what was done in [21]. The vector $\boldsymbol{\chi}$ contains all motions of the system, both elastic and discrete. The extended matrix operator form is

$$\mathbf{M}\ddot{\boldsymbol{\chi}} + (\Omega_r\mathbf{G}_r + \Omega_c\mathbf{G}_c)\dot{\boldsymbol{\chi}} + (\mathbf{K} - \Omega_r^2\mathbf{C}_r - \Omega_c^2\mathbf{C}_c - 2\Omega_r\Omega_c\mathbf{C}_{rc})\boldsymbol{\chi} = \mathbf{f}, \tag{2.16a}$$

$$\boldsymbol{\chi} = \begin{bmatrix} \boldsymbol{w}(\theta,t) \\ \mathbf{q}(t) \end{bmatrix}, \qquad \mathbf{M}\boldsymbol{\chi} = \begin{bmatrix} M\boldsymbol{w} \\ \mathbf{M}_d\mathbf{q} \end{bmatrix}, \qquad \mathbf{G}_r\boldsymbol{\chi} = \begin{bmatrix} G_r\boldsymbol{w} \\ \mathbf{0} \end{bmatrix}, \tag{2.16b}$$

$$\mathbf{G}_c\boldsymbol{\chi} = \begin{bmatrix} G_c\boldsymbol{w} \\ \mathbf{G}_d\mathbf{q} \end{bmatrix}, \quad \mathbf{K}\boldsymbol{\chi} = \begin{bmatrix} L\boldsymbol{w} + (L_m + L_f)\mathbf{q} \\ \mathbf{K}_d\mathbf{q} + (\mathbf{K}_m + \mathbf{K}_f)\boldsymbol{w} \end{bmatrix}, \quad \mathbf{C}_r\boldsymbol{\chi} = \begin{bmatrix} C_r\boldsymbol{w} \\ \mathbf{0} \end{bmatrix}, \tag{2.16c}$$

$$\mathbf{C}_c\boldsymbol{\chi} = \begin{bmatrix} C_c\boldsymbol{w} \\ \mathbf{C}_d\mathbf{q} \end{bmatrix}, \qquad \mathbf{C}_{rc}\boldsymbol{\chi} = \begin{bmatrix} C_{rc}\boldsymbol{w} \\ \mathbf{0} \end{bmatrix}, \qquad \mathbf{f} = \begin{bmatrix} \boldsymbol{f} \\ \mathbf{f}_d \end{bmatrix}, \tag{2.16d}$$

$$M\boldsymbol{w} = \begin{bmatrix} J_0u, & J_0v + J_1\beta, & J_2\beta + J_1v \end{bmatrix}^T, \tag{2.17a}$$

$$G_r\boldsymbol{w} = 2\begin{bmatrix} J_0(u_{,\theta} - v) - J_1\beta \\ J_0(v_{,\theta} + u) + J_1\beta_{,\theta} \\ J_2\beta_{,\theta} + J_1(u + v_{,\theta}) \end{bmatrix}, \quad G_c\boldsymbol{w} = 2\begin{bmatrix} -J_0u_{,\theta} \\ -J_0v_{,\theta} - J_1\beta_{,\theta} \\ -J_2\beta_{,\theta} - J_1v_{,\theta} \end{bmatrix}, \tag{2.17b}$$

$$\begin{aligned} L\boldsymbol{w} = &\begin{bmatrix} \alpha_1(u + v_{,\theta}) + \alpha_2\beta_{,\theta} - \alpha_3[\beta_{,\theta} - (v_{,\theta} - u_{,\theta\theta})] + k_u u \\ -\alpha_1(u_{,\theta} + v_{,\theta\theta}) - \alpha_2\beta_{,\theta\theta} - \alpha_3[\beta - (v - u_{,\theta})] + k_v v \\ -\beta_{,\theta\theta} - \alpha_2(u_{,\theta} + v_{,\theta\theta}) + \alpha_3[\beta - (v - u_{,\theta})] \end{bmatrix} \\ &+ \sum_{n=1}^{N} k_{rn}\Delta_n\delta(\theta - \psi_n)\begin{bmatrix} -\sin\alpha_r, & \cos\alpha_r, & -\mathit{\Gamma}\cos\alpha_r \end{bmatrix}^T, \end{aligned} \tag{2.17c}$$

$$L_m\mathbf{q} = \sum_{n=1}^{N} k_{rn}\tilde{\Delta}_n\delta(\theta - \psi_n)\begin{bmatrix} -\sin\alpha_r, & \cos\alpha_r, & -\mathit{\Gamma}\cos\alpha_r \end{bmatrix}^T, \tag{2.17d}$$

$$\tilde{\Delta}_n = \zeta_n\sin\alpha_r - \eta_n\cos\alpha_r - u_n, \tag{2.17e}$$

$$L_f\mathbf{q} = \begin{bmatrix} k_u(-x_b\cos\theta - y_b\sin\theta) \\ k_v(x_b\sin\theta - y_b\cos\theta - u_b/R_b) \\ 0 \end{bmatrix}, \tag{2.17f}$$

$$C_r\boldsymbol{w} = \begin{bmatrix} J_0(u + 2v_{,\theta} - u_{,\theta\theta}) + 2J_1\beta_{,\theta} \\ J_0(v - 2u_{,\theta} - v_{,\theta\theta}) + J_1(\beta - \beta_{,\theta\theta}) \\ J_1(v - 2u_{,\theta} - v_{,\theta\theta}) + J_2(\beta - \beta_{,\theta\theta}) \end{bmatrix}, \tag{2.17g}$$

$$C_c\boldsymbol{w} = \begin{bmatrix} -J_0u_{,\theta\theta}, \\ -J_0v_{,\theta\theta} - J_1\beta_{,\theta\theta}, \\ -J_1v_{,\theta\theta} - J_2\beta_{,\theta\theta} \end{bmatrix}, \quad C_{rc}\boldsymbol{w} = \begin{bmatrix} J_0(-v_{,\theta} + u_{,\theta\theta}) - J_1\beta_{,\theta} \\ J_0(u_{,\theta} + v_{,\theta\theta}) + J_1\beta_{,\theta\theta} \\ J_1(u_{,\theta} + v_{,\theta\theta}) + J_2\beta_{,\theta\theta} \end{bmatrix}, \tag{2.17h}$$

$$\boldsymbol{f} = \begin{bmatrix} (J_0 + J_1)\Omega_r^2, & 0, & 0 \end{bmatrix}. \tag{2.17i}$$

The operators $\mathbf{M}$, $\mathbf{K}$, $\mathbf{C}_r$, $\mathbf{C}_c$, and $\mathbf{C}_{rc}$ are self-adjoint with the inner product

$$\langle \boldsymbol{\chi}_1,\ \boldsymbol{\chi}_2 \rangle = \int_0^{2\pi} \overline{\boldsymbol{w}}_1^T\boldsymbol{w}_2\mathrm{d}\theta + \overline{\mathbf{q}}_1^T\mathbf{q}_2, \tag{2.18}$$

where the overbar denotes complex conjugate. The gyroscopic operator $\mathbf{G}_r$ is skew self-adjoint with $\langle \boldsymbol{\chi}_1,\ \mathbf{G}_r\boldsymbol{\chi}_2\rangle = -\langle \mathbf{G}_r\boldsymbol{\chi}_1,\ \boldsymbol{\chi}_2\rangle$, and so is the gyroscopic operator $\mathbf{G}_c$.

Casting the hybrid model in the operator form of Eq. (2.16) with the inner product in Eq. (2.18) allows straightforward application of the Galerkin method to discretize the model. The solution of Eq. (2.16) is approximated with a series of linearly independent vectors as

$$\begin{aligned}\boldsymbol{\chi}_a(\theta,t) = &\sum_{l=0}^{L_b} a_{cl}(t)\boldsymbol{\chi}_{1l}(\theta) + \sum_{l=1}^{L_b} a_{sl}(t)\boldsymbol{\chi}_{2l}(\theta) + \sum_{m=0}^{M_b} b_{cm}(t)\boldsymbol{\chi}_{3m}(\theta)\\ &+ \sum_{m=1}^{M_b} b_{sm}(t)\boldsymbol{\chi}_{4m}(\theta) + \sum_{p=0}^{P_b} c_{cp}(t)\boldsymbol{\chi}_{5p}(\theta)\\ &+ \sum_{p=1}^{P_b} c_{sp}(t)\boldsymbol{\chi}_{6p}(\theta) + \sum_{k=1}^{3N+9} d_k(t)\boldsymbol{\chi}_{7k}(\theta),\end{aligned} \tag{2.19a}$$

$$\boldsymbol{\chi}_{1l} = \left[\begin{array}{c}\cos l\theta\\ 0\\ 0\\ \hdashline \mathbf{0}\end{array}\right],\qquad \boldsymbol{\chi}_{2l} = \left[\begin{array}{c}\sin l\theta\\ 0\\ 0\\ \hdashline \mathbf{0}\end{array}\right],\qquad \boldsymbol{\chi}_{3m} = \left[\begin{array}{c}0\\ \cos m\theta\\ 0\\ \hdashline \mathbf{0}\end{array}\right],$$

$$\boldsymbol{\chi}_{4m} = \left[\begin{array}{c}0\\ \sin m\theta\\ 0\\ \hdashline \mathbf{0}\end{array}\right],\ \boldsymbol{\chi}_{5p} = \left[\begin{array}{c}0\\ 0\\ \cos p\theta\\ \hdashline \mathbf{0}\end{array}\right],\ \boldsymbol{\chi}_{6p} = \left[\begin{array}{c}0\\ 0\\ \sin p\theta\\ \hdashline \mathbf{0}\end{array}\right],\ \boldsymbol{\chi}_{7k} = \left[\begin{array}{c}0\\ 0\\ 0\\ \hdashline \mathbf{e}_k\end{array}\right], \tag{2.19b}$$

where the vector $\mathbf{e}_k$, which has dimension equal to the number of discrete degrees of freedom $(3N+9)$, is a unit vector with the k-th element equal to one and all others zero. The $\boldsymbol{\chi}_{1l}, \cdots, \boldsymbol{\chi}_{7k}$ in Eq. (2.19b) form a complete set of basis functions, so the approximate solution $\boldsymbol{\chi}_a$ converges to the true solution $\boldsymbol{\chi}$ as L_b, M_b, and P_b approach infinity. All these basis functions are orthogonal to each other in terms of the inner product in Eq. (2.18). The basis functions $\boldsymbol{\chi}_{1l}, \cdots, \boldsymbol{\chi}_{6p}$ are different nodal diameter (i.e., Fourier series) components of the total ring deformation. The coefficients (a_{ci}, a_{si}), (b_{ci}, b_{si}), and (c_{ci}, c_{si}) represent the magnitude of contribution of the i-th nodal diameter component to the total radial deformation, tangential deformation, and cross-sectional rotation angle, respectively.

Substitution of the approximate solution $\boldsymbol{\chi}_a$ into Eq. (2.16) gives the residual

$$\boldsymbol{\xi}(\theta, t) = \mathbf{M}\ddot{\boldsymbol{\chi}}_a + (\Omega_r \mathbf{G}_r + \Omega_c \mathbf{G}_c)\dot{\boldsymbol{\chi}}_a + (\mathbf{K} - \Omega_r^2 \mathbf{C}_r - \Omega_c^2 \mathbf{C}_c - 2\Omega_r \Omega_c \mathbf{C}_{rc})\boldsymbol{\chi}_a - \mathbf{f}. \quad (2.20)$$

Requiring the residual to be orthogonal to each basis function in Eq. (2.19b) using the inner product in Eq. (2.18) (for example, $\langle \boldsymbol{\xi},\ \boldsymbol{\chi}_{1l} \rangle = 0$ for $l = 1, 2, \cdots, L_b$) gives the matrix equation

$$[\mathbf{M}]\ddot{\mathbf{z}} + (\Omega_r[\mathbf{G}_r] + \Omega_c[\mathbf{G}_c])\dot{\mathbf{z}} + ([\mathbf{K}] - \Omega_r^2[\mathbf{C}_r] - \Omega_c^2[\mathbf{C}_c] - 2\Omega_r\Omega_c[\mathbf{C}_{rc}])\mathbf{z} = \tilde{\mathbf{f}}, \quad (2.21a)$$

$$\begin{aligned} \mathbf{z} = [&a_{c0}, \cdots, a_{cL_b}, a_{s1}, \cdots, a_{sL_b}, b_{c0}, \cdots, b_{cM_b}, \\ &b_{s1}, \cdots, b_{sM_b}, c_{c0}, \cdots, c_{cP_b}, c_{s1}, \cdots, c_{sP_b}, d_1, \cdots, d_{3N+9}]^T, \end{aligned} \quad (2.21b)$$

where $\mathbf{z}$ has dimension $2L_b + 2M_b + 2P_b + 3N + 12$. Once $\mathbf{z}$ is determined, the approximate solution $\boldsymbol{\chi}_a$ can be recovered from Eq. (2.19a).

2.4 Steady Deformations

The planetary gear system deflects into a steady configuration due to applied torques and centripetal excitations. The discretized governing equations for steady deformations $\mathbf{z}_s$ are obtained by eliminating time derivative terms in Eq. (2.21a) to give

$$([\mathbf{K}] - \Omega_r^2[\mathbf{C}_r] - \Omega_c^2[\mathbf{C}_c] - 2\Omega_r\Omega_c[\mathbf{C}_{rc}])\mathbf{z}_s = \tilde{\mathbf{f}}. \quad (2.22)$$

Numerically solving Eq. (2.22) and using the resulting $\mathbf{z}_s$ in Eq. (2.19a) gives the steady deformation.

2.4.1 Steady Deformation Benchmark Comparisons

This section compares the steady deformations calculated from the analytical model with those from two-dimensional finite element/contact mechanics (FE/CM) software [12, 72, 73]. Figure 2.4 shows the FE/CM model. The carrier (not shown) is modeled as a rigid body. For this comparison, the inner surfaces of the sun and planet gears are constrained to remain circular (in practice, stiff bearings and shafts occupy the gear interiors in Fig. 2.4), while the outer surface of the ring gear can deform elastically.

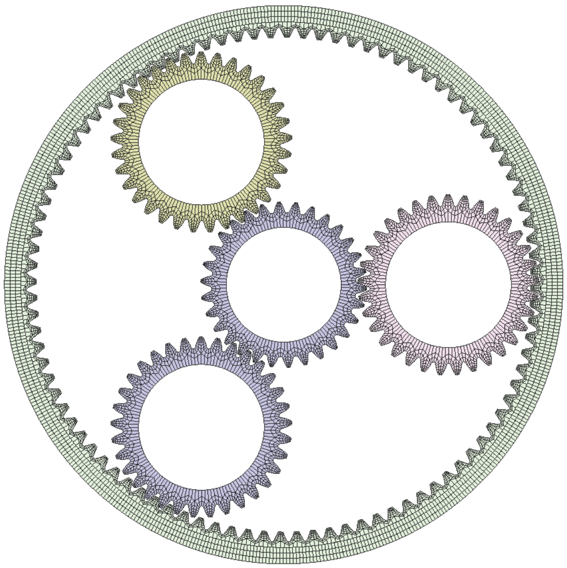

Figure 2.4: FE/CM model

In the FE/CM model, it is not possible to specify a ring rigid body that connects to the ring gear through an elastic foundation as done in the analytical model. Instead, the

FE/CM software admits rigid-body motions of the ring gear according to the definitions

$$\begin{gathered} x_r = \int_0^{2\pi} 2u_o(\theta)\cos\theta \ \mathrm{d}\theta, \qquad y_r = \int_0^{2\pi} 2u_o(\theta)\sin\theta \ \mathrm{d}\theta, \\ u_r = (R_r/R_o)\int_0^{2\pi} v_o(\theta) \ \mathrm{d}\theta, \end{gathered} \tag{2.23}$$

where u_r represents the rigid rotation in radians times the ring gear base radius R_r. u_o and v_o denote the radial and tangential deflections of the ring outer surface, and R_o is the radius of the ring outer surface. The FE/CM model allows that the two translations (x_r and y_r) are resisted by translational stiffnesses and the rotation (u_r) is resisted by a rotational stiffness, but the present example constrains these motions to be zero.

The analytical model must be adjusted to facilitate the comparison because of the above modeling differences. The elastic foundation and ring rigid body are removed. We define rigid-body motions for the analytical ring in the same way as the FE/CM model does in Eq. (2.23) and constrain them to be zero. The analytical model has its speed-dependent centripetal terms in the left side of Eq. (2.22) removed because these terms are not considered in the quasi-static analysis of the FE/CM model. These adjustments apply only for this benchmarking section.

The comparison is conducted on a three-planet system with equal planet spacing. The sun-planet and ring-planet tooth meshes at the three planets are out-of-phase. Table 2.1 shows the parameters for the FE/CM model. The carrier parameters are not shown because it is stationary and fixed to ground. The sun gear is the input, and the ring gear is the output. The input torque and speed are 600 N·m and 10,000 rpm, respectively. The analytical model takes the parameters in Table 2.1 as well as the following parameters. The sun-planet and ring-planet mesh stiffnesses are listed in Table 2.2. They are calculated from single-pair sun-planet and ring-planet FE/CM models using an average slope method [86] at the same

Table 2.1: Parameters of a three-planet FE/CM planetary gear model.

	Sun	Planets	Ring
Number of teeth	29	34	97
Module(mm)	2.868	2.868	2.868
Inner diameter (mm)	60.00	72.00	272.4
Root diameter (mm)	77.14	90.13	284.4
Outer diameter (mm)	89.64	100.9	300.4
Facewidth (mm)	25.40	25.40	25.40
Pressure angle (deg)	24.60	24.60	24.60
Young's modulus (GPa)	202.1	202.1	202.1
Poisson's ratio	0.3	0.3	0.3
Translational stiffness (N/m)	10×10^6	10^9	∞
Rotational stiffness (N/m)	0	0	∞
Center distance (mm)	90.33		

Table 2.2: Sun-planet and ring-planet mesh stiffnesses.

	Planet 1	Planet 2	Planet 3
Sun-planet mesh stiffness (N/m)	409.0×10^6	425.9×10^6	641.6×10^6
Ring-planet mesh stiffness (N/m)	769.3×10^6	516.9×10^6	773.3×10^6

mesh cycle instance where the FE/CM planetary gear steady deformations are evaluated. The ring inner diameter of the analytical model is a tunable parameter that is in between the ring gear inner and root diameters of the FE/CM model. For the FE/CM model, ring gear deformations are measured along a circle that has the same radius as the analytical ring neutral axis.

Figure 2.5 and Table 2.3 show steady deformations predicted by the analytical and FE/CM models. When the ring inner diameter of the analytical model is set to the ring gear root diameter (i.e., 284.4 mm), the elastic ring deformations (overall magnitudes) as well as the sun and planet rotations (absolute values) calculated from the analytical model

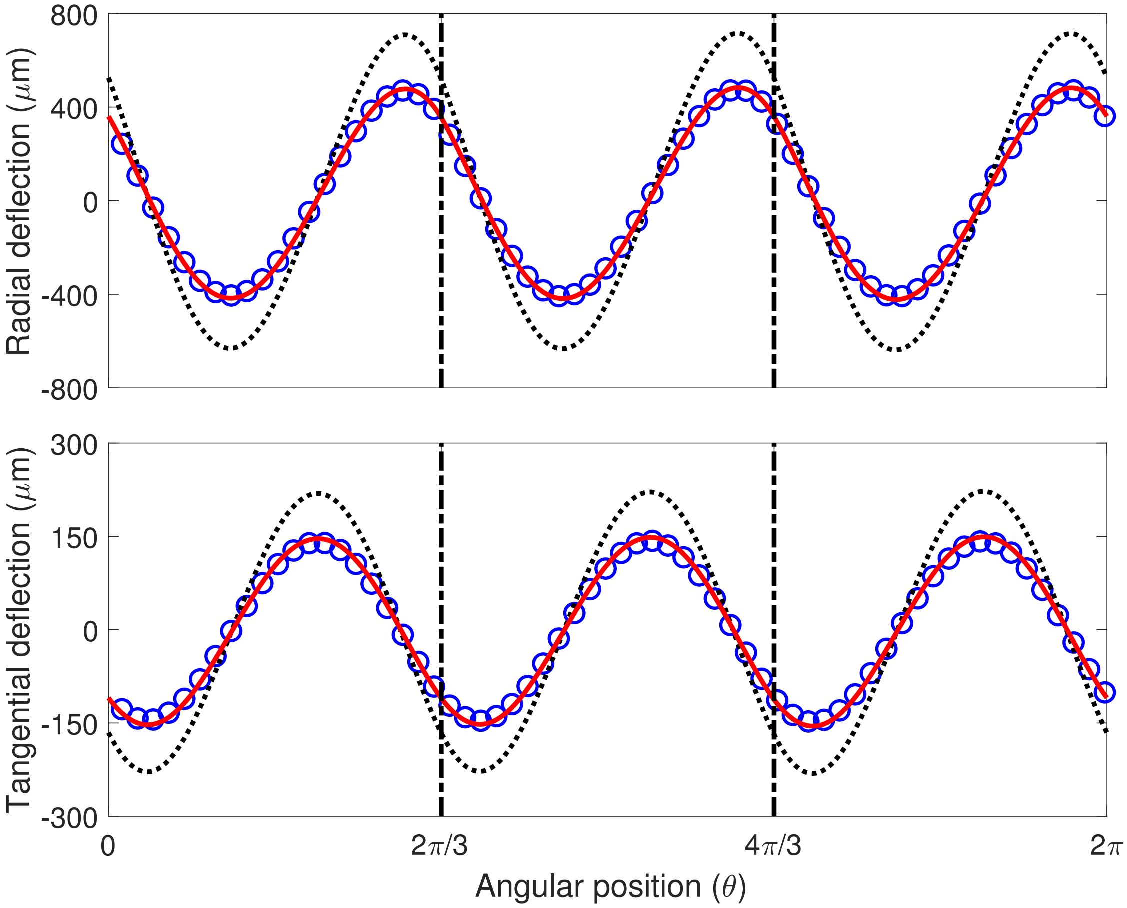

Figure 2.5: Ring (a) radial and (b) tangential deflections for the three-planet system in Table 2.1. The (blue) circles represent the results from the FE/CM model, and the (black) dotted line and (red) solid line represent the results from the analytical model with ring inner diameter equal to 284.4 mm and 282.2 mm, respectively.

Table 2.3: Discrete motions (unit: μm) of the same system used in Fig. 2.5 calculated from the FE/CM model (first row) and analytical model with ring inner diameter equal to 284.4 mm (second row) and 282.2 mm (third row).

x_s	y_s	u_s	ζ_1	η_1	u_1	ζ_2	η_2	u_2	ζ_3	η_3	u_3
-2.58	-1.13	324	0	9.65	-302	0.0215	9.60	-307	-0.0177	9.62	-307
-0.991	0.572	474	0	9.62	-452	0	9.61	-454	0	9.63	-456
-1.29	0.745	327	0	9.62	-305	0	9.60	-307	0	9.64	-308

are larger than those from the FE/CM model. This difference comes from selecting the ring inner diameter to be the root diameter, which neglects ring stiffness from the teeth. This stiffness underestimation leads to an increase of steady deformations. By compensating for the omitted tooth geometry with a smaller ring inner diameter (282.2 mm), the elastic ring deformations, sun rotation, and planet rotations predicted by the analytical model match well with those from the FE/CM model, as shown in Fig. 2.5 and Table 2.3. We do not compare the sun and planet translations between these two models because their values are small relative to the sun and planet rotations, but the quality of the agreement was similar.

For a three-planet system with equal planet spacing, identical bearing stiffnesses for all planets, and in-phase tooth meshes, steady deformations are cyclically symmetric: the sun gear has only rotation, all planets have the same deflections, and the ring elastic deflections are periodic with $N = 3$ periods. The steady deformations for the out-of-phase system in Figure 2.5 and Table 2.3 are not cyclically symmetric due to unequal tooth mesh stiffnesses among the planets. The deviation from cyclical symmetry, however, is small despite the significant differences of the sun-planet and ring-planet mesh stiffnesses among the three planets (Table 2.2). Small differences of the sun-planet and ring-planet mesh loads among the three planets (not shown) account for this small deviation.

2.4.2 Steady Deformation Results and Discussion

This section studies steady deformations of a planetary gear with dimensional parameters shown in Table 2.4. Torque flows into the planetary gear through the carrier and out from the ring. The sun is stationary and fixed to ground. The stiffness k_{cu} vanishes. The ring rigid body is fixed ($k_b, k_{bu} \to \infty$) such that it neither translates nor deviates from its angular orientation determined by its rotation speed. The elastic ring has a rectangular cross-section with radial thickness H and axial thickness B.

Table 2.4: Dimensional parameters of an example planetary gear system with an elastic ring.

Stiffness (N/m)	$k_c = 1.00\times10^9,\ k_{cu} = 0,\ k_\zeta = 200\times10^6,\ k_\eta = 1.00\times10^9,\ Rk_u = Rk_v = 200\times10^6$
Dimensions (mm)	$R_s = 39.1,\ R_c = 90.3,\ R = 147,\ \mathit{\Gamma} = 9.55,\ H = 12.0,\ B = 25.4$
Mass (kg)	$m_c = 5.00,\ m_p = 0.640$
Elastic modulus (GPa)	$E = 202,\ \kappa G = 59.1$
Density (kg/m^3)	$\rho = 7.85\times10^3$
Pressure angle (deg)	$\alpha_s = \alpha_r = 24.6$
Carrier torque (N·m)	$T_c = -1500$
Speed (rpm)	$\Omega_c = -1600,\ \Omega_r = -2100$

Tooth Bending Effects on Steady Deformations

The tooth bending effect relates to the radial distance ($\mathit{\Gamma}$) from the ring contact point to the ring neutral axis (Fig. 2.3). Use of $\mathit{\Gamma} = 0$ indicates no consideration of tooth bending.

Figure 2.6 shows the elastic ring radial and tangential deflections for an out-of-phase system with and without tooth bending. In both cases, the maximum radial deflections occur at the clockwise sides of the contact points for planet mesh forces acting clockwise on the ring, while the maximum tangential deflections occur at the counter-clockwise sides. Neither of the maxima occur at the contact locations. When tooth bending is considered, the radial and tangential deflections (overall magnitudes) increase due to the concentrated moment on the ring at the tooth contact point from the mesh force (Fig. 2.3). Figure 2.6 shows a clockwise shift of the ring radial and tangential deflections from the tooth bending for clockwise mesh forces acting on the ring.

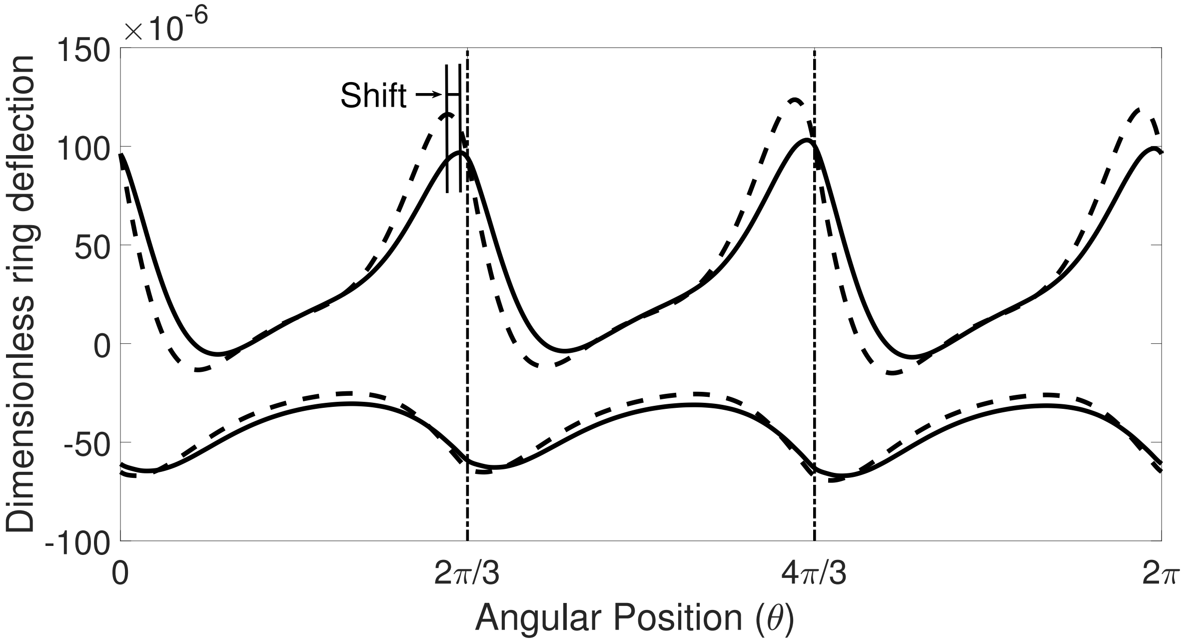

Figure 2.6: Ring radial (upper) and tangential (lower) deflections for a three-planet out-of-phase system with nominal value of Γ (dashed line) from Table 2.4 and zero value of Γ (solid line). The ring-planet contact locations are 0, $2\pi/3$, and $4\pi/3$. Mesh stiffnesses have the values in Table 2.2, and all other parameters are given in Table 2.4.

The ring deformations in Fig. 2.6 are the superposition of several nodal diameter components from a Fourier series, while those in Fig. 2.5 look like nearly pure three nodal diameter sinusoidal deformations. The elastic foundation causes this difference. When the elastic foundation stiffnesses (k_u, k_v) are reduced to 10% of the values in Fig. 2.6, the ring deformations look like those in Fig. 2.5. The elastic foundation stiffnesses are determined by the physical connection of the elastic ring to the ring rigid body or housing. With a weaker connection, the elastic foundation stiffnesses are smaller, and the ring deformations look more like single nodal diameter sinusoidal deformations.

The carrier rotation and planet 1 motions of the system with and without tooth bending are shown in Table 2.5. Introducing tooth bending to the system does not alter the planet radial deflection much because it is mainly determined by the centripetal acceleration of the planet center of mass. The carrier rotation, planet tangential deflection, and, especially, the planet rotation (absolute values) increase due to the tooth bending.

Table 2.5: Dimensionless carrier rotation and planet 1 motions of the same system used in Fig. 2.6 with and without tooth bending.

	u_c	ζ_1	η_1	u_1
Without tooth bending ($\times 10^{-6}$)	-132	57.8	-94.8	-11.8
With tooth bending ($\times 10^{-6}$)	-146	57.6	-109	-25.0
Difference (%)	10.6	-0.346	15.0	112

Tooth bending meaningfully influences the steady deformations, which is evident in Fig. 2.6 and Table 2.5. Additional numerical experiments show that an increase of Γ magnifies the effect of tooth bending on the steady deformations. For systems with high value of Γ and a compliant ring, inclusion of tooth bending in the modeling is necessary.

Ring Extensional and Shear Effects on Steady Deformations

The full elastic ring model considers bending, extension, and shear effects. A simpler bending-extensional ring model (subsequently called the extensional model) results from assuming the shear strain ϵ_s in Eq. (2.5) vanishes, that is, $\beta = (v - u_{,\theta})/R$. Further imposing the inextensional assumption $u = -v_{,\theta}$ leads to a model with only ring bending.

Numerical experiments on an out-of-phase stationary planetary gear system (mesh stiffnesses in Table 2.2 and other parameters in Table 2.4) show that the steady deformations predicted by the three models are close to each other for a range of input torques up to 150,000 N·m, and a range of ring thicknesses ($0.05 < H/R < 0.35$). For these cases, the extensional and shear effects on steady deformations are minimal, and the inextensional model is sufficient.

This result does not apply for the spinning planetary gear system. Results from the extensional and full ring models have negligible differences for a range of thickness ratios at either half (Fig. 2.7a) or four (Fig. 2.7b) times the nominal speeds in Table 2.4. Results of the inextensional model have small but noticeable differences from those of the extensional and full models at half nominal speed (Fig. 2.7a) and large differences at four times nominal speed (Fig. 2.7b). The ring speed causes the large differences because the inextensional model cannot capture the uniform expansion caused by high-speed ring rotation (Eq. (2.17i)). Increasing the ring thickness ratio stiffens the system, yet the maximum ring radial deflection increases for higher thickness ratio at high speed (Fig. 2.7b). This occurs because the centripetal excitation (Eq. (2.17i)) simultaneously increases with the ring thickness through the inertia quantities J_0 and J_1.

The results in Fig. 2.7 show that shear effects in the full model yield negligible differences compared to the extensional model for steady deformations of the present system. The impact of shear effects in dynamic vibrations is not yet known.

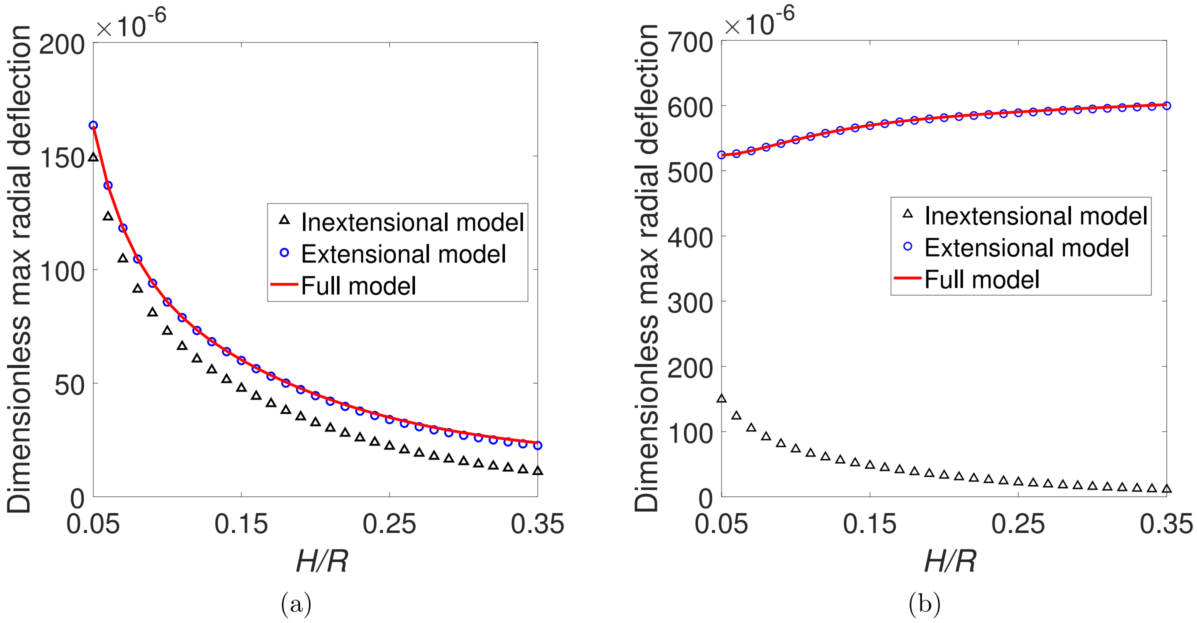

(a)

(b)

Figure 2.7: Maximum ring radial deflection for a three-planet in-phase system with a range of H/R. The value of H is varied, and R is a constant. The results from the system with inextensional, extensional, and full ring model are shown at (a) half and (b) four times of nominal speeds in Table 2.4. Mesh stiffnesses have the values in Table 2.2, and all other parameters are given in Table 2.4.

.

2.5 Spectral Analysis

The previous section focuses on steady deformations evaluated at one mesh instance. The quasi-static steady deformations fluctuate over a mesh cycle, however, because the sun-planet and ring-planet mesh stiffnesses vary periodically at the mesh frequency ω_m. These mesh stiffness variations are shown in Fig. 2.8. All the sun-planet mesh stiffnesses have the same variations over a mesh cycle, but these variations may be in- or out-of-phase (and similarly for the ring-planet meshes).

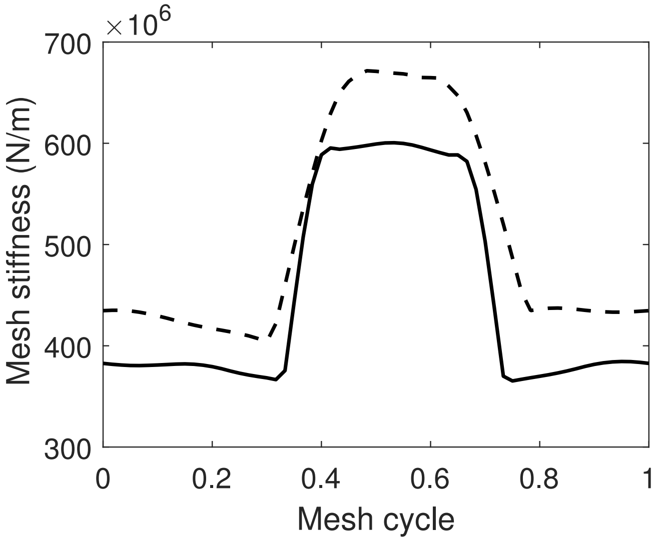

Figure 2.8: Dimensional sun-planet (solid line) and ring-planet (dashed line) mesh stiffnesses.

The phase difference between the sun-planet mesh stiffness for the n-th planet ($k_{sn}(t)$) and that for the first planet ($k_{s1}(t)$) is represented by γ_{sn} such that $k_{sn}(t) = k_{s1}(t - 2\pi\gamma_{sn}/\omega_m)$. Similarly, $k_{rn}(t) = k_{r1}(t - 2\pi\gamma_{rn}/\omega_m)$. Ref. [87] gives

$$\gamma_{sn} = Z_s\psi_n/(2\pi), \quad \gamma_{rn} = -Z_r\psi_n/(2\pi) \tag{2.24}$$

for clockwise planet rotation and

$$\gamma_{sn} = -Z_s\psi_n/(2\pi), \quad \gamma_{rn} = Z_r\psi_n/(2\pi) \tag{2.25}$$

for counter-clockwise planet rotation, where Z_s and Z_r are the sun and ring gear tooth numbers. Ref. [87] presents Eqs. (2.24) and (2.25) under the assumption that one of the sun, carrier, and ring is fixed. For general cases where all of the sun, carrier, and ring can rotate, Eq. (2.24) is valid when $\Omega_c > \Omega_r$ and Eq. (2.25) is valid when $\Omega_c < \Omega_r$. Here and in all subsequent and prior results, Ω_c and Ω_r are positive in the counter-clockwise direction and negative otherwise.

The ring-planet mesh phase in Eq. (2.24) for $\Omega_c > \Omega_r$ and Eq. (2.25) for $\Omega_c < \Omega_r$ is illustrated as follows. In one complete revolution of a planet gear center around the ring gear, Z_r tooth mesh cycles are completed. In other words, when a planet gear center revolves by an angle of 2π as seen by an observer fixed to the ring gear, the tooth mesh advances by a phase of $2\pi Z_r/(2\pi)$. Accordingly, when a planet gear center revolves by an angle of ψ_n as seen by an observer on the ring, the tooth mesh advances a phase of $\psi_n Z_r/(2\pi)$. This establishes the magnitudes of γ_{rn} in Eqs. (2.24) and (2.25). For $\Omega_c > \Omega_r$ where the planet centers revolve counter-clockwise relative to the ring (i.e., the carrier rotates counter-clockwise as seen by an observer on the ring gear), the ring-planet mesh for the n-th planet has a phase lead of $\psi_n Z_r/(2\pi)$ relative to that for the first planet. This yields the minus sign for γ_{rn} in Eq. (2.24). For $\Omega_c < \Omega_r$ where the carrier rotates clockwise as seen by an observer on the ring gear, the ring-planet mesh for the n-th planet has a phase lag of $\psi_n Z_r/(2\pi)$ relative to that for the first planet, so no minus sign appears for γ_{rn} in Eq. (2.25). Similar arguments result in the sun-planet mesh phase in Eq. (2.24) for $\Omega_c > \Omega_r$ and Eq. (2.25) for $\Omega_c < \Omega_r$. The special case $\Omega_c = \Omega_r$ represents a trivial transmission system and is not addressed in this work.

Two mesh phases are identical if their difference is an integer number of mesh cycles. The relation $\gamma_{sn} = \gamma_{rn}$ holds for equally-spaced systems because of the conditions $(Z_s + Z_r)/N =$ integer and $\psi_n = 2\pi(n-1)/N$. According to Eqs. (2.24) and (2.25), $\gamma_{sn} = \gamma_{rn} = 0$ when Z_s/N and Z_r/N are both integers. In this case, all of the sun-planet (ring-planet) mesh stiffnesses are in-phase and have the same values at each instant over a mesh cycle. All other cases are out-of-phase.

Two example three-planet systems are used in the following section with one having in-phase tooth meshes and the other having out-of-phase tooth meshes. The in-phase system has $Z_s = 30$ and $Z_r = 96$. Sun-planet and ring-planet mesh stiffnesses for the first planet are shown in Fig. 2.8, and all other parameters are given in Table 2.4. The out-of-phase planetary gear results from simultaneously increasing the sun tooth number and decreasing the ring tooth number by one relative to the in-phase system (i.e., $Z_s = 31$ and $Z_r = 95$). All other parameters stay the same.

2.5.1 Spectra of Ring Deformation Measured in Different Reference Frames

This section focuses on ring deformation measured by sensors in different reference frames with special attention to the differing frequency content. A sensor attached to the rotating ring, as shown in Fig. 2.9, measures deflection of the material point to which it is attached. One example is a strain gauge fixed to the ring. Ring fatigue lives are related to the deflection or strain at a material point. A sensor fixed in space (on a gearbox housing, for example) and directed at a spinning ring measures deflections of different material points as they pass a fixed spatial location with speed Ω_r. Finally, a sensor rotating with the carrier and directed at the ring captures deflections of different material points passing a carrier-fixed location with speed Ω_{rc}.

Subsequent results examine the spectra of these three possible sensor locations for systems with in-phase and out-of-phase tooth meshes. To illustrate these spectra, we define the following frequencies. The frequency at which the planets pass a fixed material point on the ring is $N|\Omega_{rc}|$, where $|\Omega_{rc}|$ is the absolute value of Ω_{rc}. The frequency at which the planets pass a fixed spatial angular location is $N|\Omega_c|$. Low-frequency content is defined as that involving integer multiples of carrier speed or relative ring-carrier speed; high-frequency

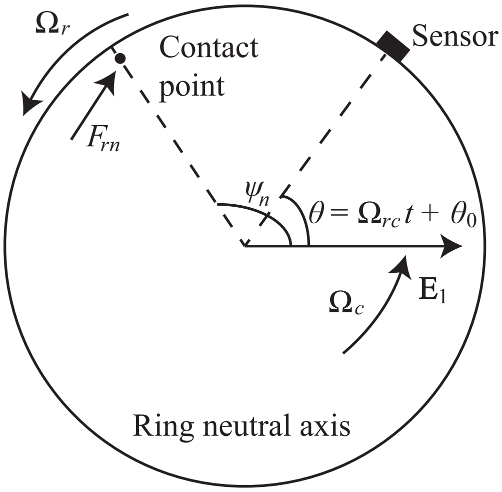

Figure 2.9: Measuring ring deflection with a sensor rotating with the ring.

content is near multiples of the mesh frequency $\omega_m = Z_r|\Omega_{rc}|$.

Figure 2.10 shows spectra of the ring tangential deflection (from the discretized model in Eq. (2.22)) measured by sensors in the three different reference frames for the in-phase system. The measurement in the rotating ring reference frame contains only low-frequency content at multiples of $N|\Omega_{rc}|$, where $N = 3$ for the present example. The measurement in the stationary reference frame has only low-frequency content at multiples of $N|\Omega_c|$. Only a zero-frequency mean value appears when the ring deflection is measured by a sensor fixed to the rotating carrier. For all three measurements, no high-frequency content occurs. In particular, spectral lines at harmonics of mesh frequency are absent.

Figure 2.11 shows spectra analogous to Fig. 2.10 but for the out-of-phase system. The low-frequency spectral content for all three measurements is nearly identical to that of the in-phase system in Fig. 2.10 except for trivial differences in amplitudes. In the out-of-phase case, however, high-frequency content occurs for all three measurements. For the measurements in the rotating ring and stationary reference frames, sidebands occur near the first, second, and fourth mesh frequency harmonics, while the mesh frequency harmonics them-

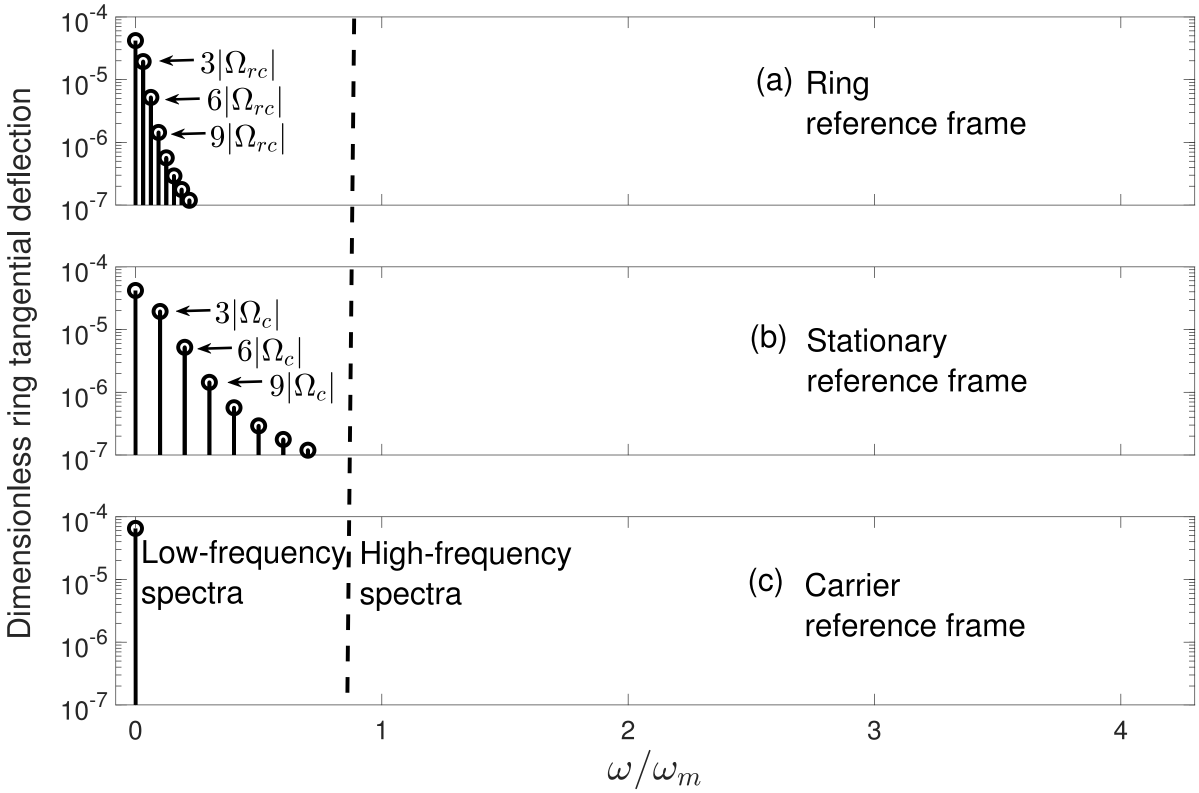

Figure 2.10: Spectra of ring tangential deflection measured by sensors fixed to three different reference frames for the three-planet in-phase system ($Z_s = 30$ and $Z_r = 96$) with $\Omega_r < \Omega_c < 0$. Sun-planet and ring-planet mesh stiffnesses for the first planet are shown in Fig. 2.8, and all other parameters are in Table 2.4.

selves are suppressed. No spectral content occurs near the third mesh frequency harmonic. The high-frequency content for the measurement in the rotating carrier reference frame has only the first, second, and fourth mesh frequency harmonics but with no sidebands near them; again the third mesh frequency harmonic is absent. To explain the phenomena in Figs. 2.10 and 2.11, a spectral analysis is conducted subsequently.

The quasi-static ring-planet mesh loads vary periodically at the mesh frequency ω_m. Similar to mesh stiffnesses, all ring-planet mesh loads at the different planets have the same

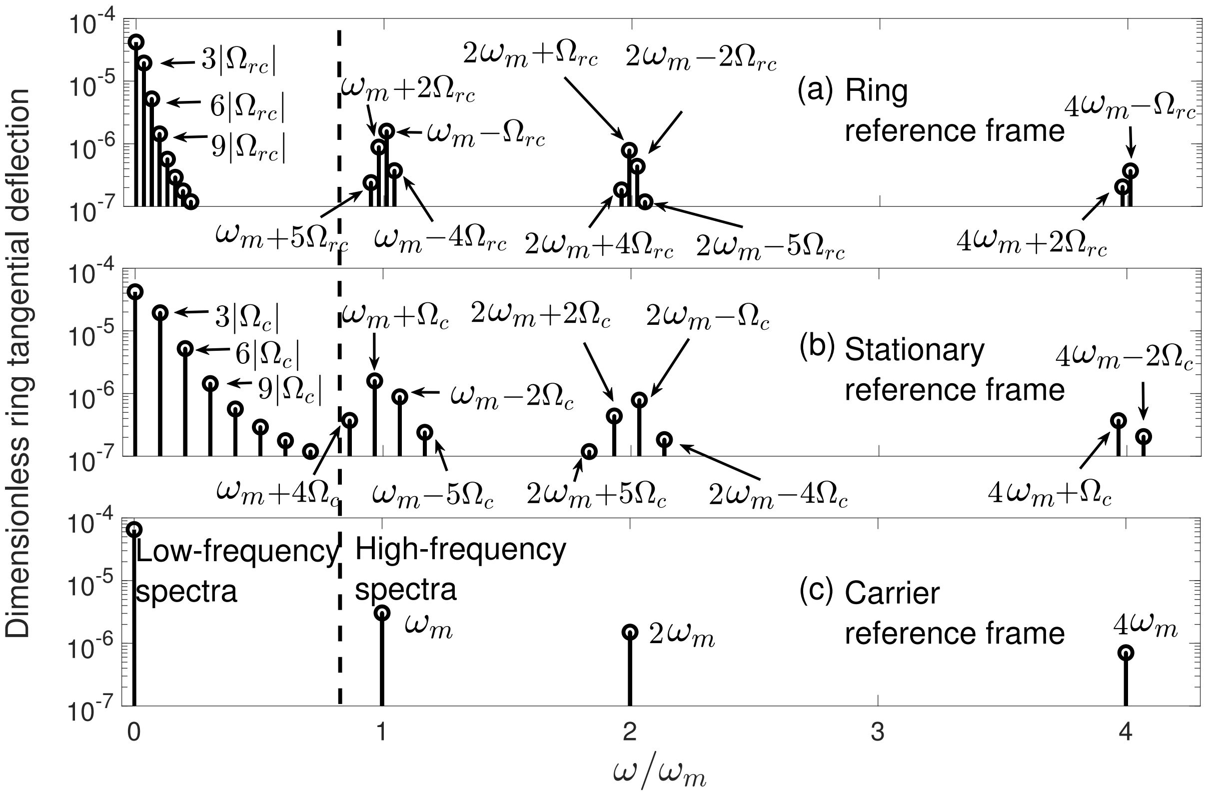

Figure 2.11: Spectra of ring tangential deflection measured by sensors fixed to three different reference frames for the three-planet out-of-phase system ($Z_s = 31$ and $Z_r = 95$) with $\Omega_r < \Omega_c < 0$. Sun-planet and ring-planet mesh stiffnesses for the first planet are shown in Fig. 2.8, and all other parameters are in Table 2.4.

variations, but these variations may be in- or out-of-phase depending on the phase difference γ_{rn}, which has the expression in Eq. (2.24) for $\Omega_c > \Omega_r$ and the expression in Eq. (2.25) for $\Omega_c < \Omega_r$. We first focus on the case $\Omega_c > \Omega_r$. The ring-planet mesh load for the n-th planet reaches the same value as that for the first planet after a time interval of $2\pi\gamma_{rn}/\omega_m$. The Fourier representation of the quasi-static ring-planet mesh load for the n-th planet is therefore

$$\begin{aligned} F_{rn}(t) &= F_{r1}(t - 2\pi\gamma_{rn}/\omega_m) \\ &= \sum_{j=0}^{\infty} D_j \cos[j\omega_m(t - 2\pi\gamma_{rn}/\omega_m) + \phi_j], \quad n = 1, 2, \cdots, N \end{aligned} \tag{2.26}$$

where $\phi_0 = 0$ for the mean mesh load and D_j and ϕ_j for $j > 0$ are the amplitude and phase angle of the j-th mesh load harmonic for the first planet. The term in the parentheses accounts for the phase difference between the mesh load for the n-th planet and that for the first planet. The mean mesh load D_0, the mesh load harmonic amplitudes D_j, and the phases ϕ_j (which would in practice be numerically calculated from $F_{r1}(t)$) are the same for each ring-planet pair (i.e., for each n).

For a unit discrete load applied along the line of action at the contact point at the first planet angular position $\psi_1 = 0$, the tangential deflection of the ring neutral axis is given as the Fourier series

$$V_1(\theta) = \sum_{i=0}^{\infty} C_i \cos(i\theta + \varphi_i), \tag{2.27}$$

where C_i and φ_i are the amplitude and phase angle of the i-th nodal diameter component. Because of ring axisymmetry, a unit discrete load applied at ψ_n results in the same ring deformation as for a unit discrete load at $\psi_1 = 0$, but with the deformed shape rotated by ψ_n, i.e.,

$$V_n(\theta) = V_1(\theta - \psi_n) = \sum_{i=0}^{\infty} C_i \cos[i(\theta - \psi_n) + \varphi_i], \quad n = 1, \cdots, N. \tag{2.28}$$

The total ring tangential deformation is the superposition of deflections from all the ring-planet mesh loads, which gives

$$v(t,\theta) = \sum_{n=1}^{N} F_{rn}(t) V_n(\theta). \tag{2.29}$$

Substitution of Eqs. (2.26) and (2.28) into Eq. (2.29) and invoking the mesh phase γ_{rn} in Eq. (2.24) for $\Omega_c > \Omega_r$ results in

$$\begin{aligned} v(t,\theta) = \frac{1}{2}\sum_{i=0}^{\infty}\sum_{j=0}^{\infty}\sum_{n=1}^{N} C_i D_j \{ & \cos[j\omega_m t - i\theta + \phi_j - \varphi_i]\cos(jZ_r + i)\psi_n \\ & - \sin[j\omega_m t - i\theta + \phi_j - \varphi_i]\sin(jZ_r + i)\psi_n \\ & + \cos[j\omega_m t + i\theta + \phi_j + \varphi_i]\cos(jZ_r - i)\psi_n \\ & - \sin[j\omega_m t + i\theta + \phi_j + \varphi_i]\sin(jZ_r - i)\psi_n \}. \end{aligned} \tag{2.30}$$

Ring radial deformation ($u(t,\theta)$) and cross-sectional rotation angle ($\beta(t,\theta)$) have this same form except the numerical values of the Fourier coefficients analogous to C_i and φ_i are different. Therefore, conclusions regarding spectral content of $v(t,\theta)$ in Eq. (2.30) also apply to $u(t,\theta)$ and $\beta(t,\theta)$.

We now analyze Eq. (2.30) for values of θ corresponding to different sensor locations. Throughout this work, the angular coordinate θ is measured relative to the rotating base vector $\mathbf{E}_1$ fixed to the carrier. Thus, the angular position of a sensor fixed to the ring, as shown in Fig. 2.9, is given in terms of the speed of the ring relative to the carrier as $\theta = \Omega_{rc} t + \theta_0$. Similarly, the angular position of a sensor fixed in space is given by $\theta = -\Omega_c t + \theta_0$. For a sensor fixed to the carrier, $\theta = \theta_0$. In all three cases, we choose $\theta_0 = 0$ without loss of generality in what follows.

For the ring deflection at a material point (measured by a sensor fixed to the rotating ring), substitution of $\theta = \Omega_{rc}t$ into Eq. (2.30) gives

$$
\begin{aligned}
v(t)|_{ring} = \frac{1}{2}\sum_{i=0}^{\infty}\sum_{j=0}^{\infty}\sum_{n=1}^{N} C_i D_j \{ & \cos[(j\omega_m - i\Omega_{rc})t + \phi_j - \varphi_i]\cos(jZ_r + i)\psi_n \\
& - \sin[(j\omega_m - i\Omega_{rc})t + \phi_j - \varphi_i]\sin(jZ_r + i)\psi_n \\
& + \cos[(j\omega_m + i\Omega_{rc})t + \phi_j + \varphi_i]\cos(jZ_r - i)\psi_n \\
& - \sin[(j\omega_m + i\Omega_{rc})t + \phi_j + \varphi_i]\sin(jZ_r - i)\psi_n \},
\end{aligned}
\tag{2.31}
$$

where $\Omega_{rc} < 0$ because $\Omega_c > \Omega_r$ was used to obtain Eq. (2.30). Eq. (2.31) shows that the deflection at a material point is a superposition of different frequency components that depend on ω_m and Ω_{rc}. Each frequency component is associated with a specific harmonic of mesh frequency (i.e., j) and a specific nodal diameter i. This nodal diameter can be quickly identified from Eq. (2.31). For example, a measured frequency component $\omega = j\omega_m - i\Omega_{rc}$ near the j-th mesh frequency harmonic has the associated nodal diameter $i = (\omega - j\omega_m)/|\Omega_{rc}|$. The amplitudes of the frequency components $j\omega_m \pm i\Omega_{rc}$ depend on the product C_iD_j, where the meanings of C_i and D_j are evident in Eqs. (2.26) and (2.27). The frequencies at which the frequency components appear do not depend on C_i and D_j, however, but rather depend on only ω_m and Ω_{rc}.

Most frequency components in Eq. (2.31) are not present and would not be measured by the sensor because the following identities hold for integer values of l:

$$
\sum_{n=1}^{N}\cos l\psi_n = \left\{ \begin{array}{ll} N, & l/N = \text{integer} \\ 0, & l/N \neq \text{integer} \end{array} \right\}, \qquad \sum_{n=1}^{N}\sin l\psi_n = 0. \tag{2.32}
$$

According to Eq. (2.32), the frequency component $j\omega_m - i\Omega_{rc}$ in Eq. (2.31) is present (in general) if $(jZ_r + i)/N =$ integer, and the frequency component $j\omega_m + i\Omega_{rc}$ is present (in general) if $(jZ_r - i)/N =$ integer. Other frequency components are suppressed.

When $j = 0$ and $i \neq 0$, $j\omega_m + i\Omega_{rc}$ as given above is negative. In such cases, the associated frequency component in the measured spectrum is $|j\omega_m + i\Omega_{rc}|$. This prescription applies whenever a frequency component has a negative value.

This frequency occurrence rule explains the spectral content for the in-phase system in Fig. 2.10a and out-of-phase system in Fig. 2.11a. The low-frequency content in Figs. 2.10a and 2.11a are associated with $j = 0$. For $j = 0$, a frequency component $i|\Omega_{rc}|$ can occur only if i is an integer multiple of $N = 3$. The two sidebands $\omega_m + 5\Omega_{rc}$ and $\omega_m + 2\Omega_{rc}$ on the left side of the first mesh harmonic ($j = 1$) for the out-of-phase system ($Z_r = 95$) in Fig. 2.11a are associated with $i = 5$ and $i = 2$, respectively. They satisfy the condition $(jZ_r - i)/N$ = integer. The two sidebands $\omega_m - \Omega_{rc}$ and $\omega_m - 4\Omega_{rc}$ on the right side of the first mesh harmonic are associated with $i = 1$ and $i = 4$, respectively. They satisfy the condition $(jZ_r + i)/N$ = integer. All other frequency components can be explained similarly.

Substitution of $\omega_m = Z_r|\Omega_{rc}|$ and $-\Omega_{rc} = |\Omega_{rc}|$ into the frequency occurrence rule gives that the frequency component $(jZ_r + i)|\Omega_{rc}|$ can occur only if $(jZ_r + i)/N$ = integer, the frequency component $(jZ_r - i)|\Omega_{rc}|$ can occur only if $(jZ_r - i)/N$ = integer, and other frequency components are suppressed. In other words, the frequency components can only occur at integer multiples of $N|\Omega_{rc}|$. For the special case where $\Omega_r = 0$, this rule agrees with that in Refs. [2, 3] stating the sidebands (or frequency components) only occur at integer multiples of $N|\Omega_c|$ for planetary gears with a stationary ring. The present work is not restricted to a stationary ring.

According to the frequency occurrence rule, sidebands near the j-th mesh frequency harmonic have the associated nodal diameters

$$i = |sN \pm \mathrm{mod}(jZ_r, N)|, \qquad s = 0, 1, 2, \cdots, \tag{2.33}$$

where mod(A, B) represents A modulo B. Eq. (2.33) gives a rule of which nodal diameters can be measured for a certain mesh frequency harmonic. For example, the sidebands $\omega_m + 5\Omega_{rc}$, $\omega_m + 2\Omega_{rc}$, $\omega_m - \Omega_{rc}$, and $\omega_m - 4\Omega_{rc}$ near the first mesh frequency harmonic ($j = 1$) for the three-planet ($N = 3$) out-of-phase system ($Z_r = 95$) in Fig. 2.11a are associated with the nodal diameters 5, 2, 1, and 4, respectively. All of them satisfy Eq. (2.33). The sideband at $\omega_m - \Omega_{rc}$ has the highest amplitude among the four sidebands, indicating the ring tangential deflection excited by the first mesh load harmonic is dominated by one nodal diameter deformation.

Eq. (2.31) reveals that the amplitudes of the frequency components $j\omega_m \pm i\Omega_{rc}$ are determined by the product $C_i D_j$. Tables 2.6 and 2.7 show the amplitudes of D_j and C_i, as determined from the analytical model in Eq. (2.22). The mean mesh load D_0 has the same value for the in-phase and out-of-phase systems. As a result, amplitudes of the low-frequency content ($j = 0$) are identical for the in-phase (Fig. 2.10a) and out-of-phase (Fig. 2.11a) systems. The spectral line at $6|\Omega_{rc}|$ for the out-of-phase system, although its associated nodal diameter amplitude C_6 is small (Table 2.7), has relatively higher amplitude than the high-frequency sidebands because the mean mesh load D_0 is large compared to D_j for $j > 0$.

Table 2.6: Dimensionless amplitudes of ring-planet mesh load harmonics for the in-phase system in Fig. 2.10 and the out-of-phase system in Fig. 2.11. They are determined from the analytical model in Eq. (2.22).

	D_0	D_1	D_2	D_3	D_4
In phase ($\times 10^{-6}$)	103	0	0	0	0
Out-of-phase ($\times 10^{-6}$)	103	5.99	2.96	0	1.39

Table 2.6 shows that all mesh load harmonics vanish for the in-phase system, which eliminates all high-frequency content for the in-phase system in Fig. 2.10a. Because the

Table 2.7: Dimensionless nodal diameter amplitudes (unit: 10^{-3}) of ring tangential deflection along the neutral axis for an elastic ring (separated from the planetary gears) subject to a unit discrete load applied at only one mesh along the line of action. The elastic ring is from the system used in Fig. 2.10 and 2.11, and its parameters are assumed to have negligible change for different phasing conditions.

C_0	C_1	C_2	C_3	C_4	C_5	C_6
135	177	98.6	62.7	41.5	26.8	16.8

out-of-phase system has zero amplitude for the third mesh load harmonic (i.e., $D_3 = 0$), sidebands near the third mesh frequency harmonic are absent in Fig. 2.11a. Two sidebands near the fourth mesh frequency harmonic are observed for the out-of-phase system in Fig. 2.11a. The sideband at $4\omega_m - \Omega_{rc}$ (associated with C_1) has higher amplitude than the sideband at $4\omega_m + 2\Omega_{rc}$ (associated with C_2) because $C_1 > C_2$, as shown in Table 2.7. All other sideband amplitudes can be explained similarly.

The reason why certain mesh load harmonics for the in-phase and out-of-phase systems in Table 2.6 vanish is given as follows. Moment balance for the carrier gives

$$\sum_{n=1}^{N} F_{\eta n} = T_c, \tag{2.34}$$

where $F_{\eta n}$ is the bearing force for the n-th planet in the tangential direction. Force balances of the planets in the tangential direction yield

$$F_{sn} \cos\alpha_s + F_{rn} \cos\alpha_r = F_{\eta n}, \tag{2.35}$$

where F_{sn} is the sun-planet mesh force for the n-th planet. Moment balances at the planets give

$$F_{sn} = F_{rn} \cos\alpha_r / \cos\alpha_s, \qquad n = 1, 2, \cdots, N. \tag{2.36}$$

Substitution of Eqs. (2.35), (2.36), and (2.26) into Eq. (2.34) leads to

$$2\cos\alpha_r \sum_{j=0}^{\infty} \sum_{n=1}^{N} D_j [\cos(j\omega_m t + \phi_j) \cos jZ_r\psi_n - \sin(j\omega_m t + \phi_j) \sin jZ_r\psi_n] = T_c. \tag{2.37}$$

Applying Eq. (2.32) to Eq. (2.37) gives that the net torque components for the j-th mesh frequency harmonic in Eq. (2.37) vanish for $jZ_r/N \neq$ integer. The amplitude of the j-th mesh load harmonic

$$D_j = 0, \qquad \text{for } jZ_r/N = \text{integer and } j > 0 \tag{2.38}$$

to satisfy Eq. (2.37). Therefore, $D_1 = D_2 = D_3 = D_4 = 0$ for the three-planet in-phase system ($Z_r = 96$) and $D_3 = 0$ for the three-planet out-of-phase system ($Z_r = 95$), as given in Table 2.6.

For the deflection measured by a sensor fixed in space, $\theta = -\Omega_c t$ is substituted into Eq. (2.30). The result is the same as Eq. (2.31) except Ω_{rc} is replaced by $-\Omega_c$, and, after using Eq. (2.32), gives the following frequency occurrence rule: the frequency component of $j\omega_m - i\Omega_c$ can occur only if $(jZ_r - i)/N =$ integer, and the frequency component of $j\omega_m + i\Omega_c$ can occur only if $(jZ_r + i)/N =$ integer. Other frequency components are suppressed. This frequency occurrence rule applies to systems with any value of Ω_c under the condition $\Omega_c > \Omega_r$. This frequency occurrence rule, the amplitudes D_j in Table 2.6, and the amplitudes C_i in Table 2.7 explain the spectral content of the measurements in the stationary reference frame for the in-phase system in Fig. 2.10b and out-of-phase system in Fig. 2.11b. These explanations are similar to those given for Fig. 2.10a and 2.11a.

For the deflection measured by a sensor fixed to the rotating carrier, substitution of $\theta = 0$ into Eq. (2.30) gives the expression in Eq. (2.31) but with $\Omega_{rc} = 0$. Consequently, the measurement will have frequency content only at integer multiples of mesh frequency. There will be no sidebands near these mesh frequency harmonics. Because the mesh load harmonics D_j for the in-phase system vanish for $j > 0$ (Table 2.6), no non-zero frequencies are present in Fig. 2.10c. The third mesh frequency harmonic does not appear in Fig. 2.11c for the out-of-phase system because $D_3 = 0$ (Table 2.6).

Sidebands appear in the spectra of the measured deflection in the rotating ring and stationary reference frames, but do not appear for a sensor in the rotating carrier reference frame. This phenomenon is shown in Fig. 2.11 and confirmed by the foregoing spectral analysis. Generalizing the spectral analysis answers the question: If a sensor rotating with an arbitrary speed Ω_a measures ring deflection, what frequency content is possible in the measurement? Substitution of $\theta = \Omega_{ac}t$, where $\Omega_{ac} = \Omega_a - \Omega_c$, into Eq. (2.30), and invoking Eq. (2.32) yields the following generalized frequency occurrence rule: the frequency component of $j\omega_m + i\Omega_{ac}$ can occur only if $(jZ_r - i)/N =$ integer; the frequency component of $j\omega_m - i\Omega_{ac}$ can occur only if $(jZ_r + i)/N =$ integer; other frequency components are suppressed. This occurrence rule applies to systems with $\Omega_c > \Omega_r$.

For systems with $\Omega_c < \Omega_r$, substitution of Eq. (2.26), Eq. (2.28), the mesh phase γ_{rn} in Eq. (2.25), and $\theta = \Omega_{ac}t$ into Eq. (2.29) gives

$$\begin{aligned} v(t) = \frac{1}{2}\sum_{i=0}^{\infty}\sum_{j=0}^{\infty}\sum_{n=1}^{N} C_i D_j \{ & \cos[(j\omega_m + i\Omega_{ac})t + \phi_j + \varphi_i]\cos(jZ_r + i)\psi_n \\ & + \sin[(j\omega_m + i\Omega_{ac})t + \phi_j + \varphi_i]\sin(jZ_r + i)\psi_n \\ & + \cos[(j\omega_m - i\Omega_{ac})t + \phi_j - \varphi_i]\cos(jZ_r - i)\psi_n \\ & + \sin[(j\omega_m - i\Omega_{ac})t + \phi_j - \varphi_i]\sin(jZ_r - i)\psi_n \}. \end{aligned} \tag{2.39}$$

For a sensor rotating with an arbitrary speed Ω_a, the measured spectra follow the rule: the frequency component of $j\omega_m - i\Omega_{ac}$ can occur only if $(jZ_r - i)/N =$ integer; the frequency component of $j\omega_m + i\Omega_{ac}$ can occur only if $(jZ_r + i)/N =$ integer; other frequency components are suppressed.

The frequency occurrence rules for the frequency components $j\omega_m - i\Omega_{ac}$ and $j\omega_m + i\Omega_{ac}$ under $\Omega_c > \Omega_r$ and $\Omega_c < \Omega_r$ are summarized in Table 2.8.

Table 2.8: Summary of the frequency occurrence rules of the frequency components for the ring deflection measured by a sensor rotating with speed Ω_a. The frequencies in the upper row are the only possible frequency components, and they occur only when the conditions in the table hold.

	$j\omega_m - i\Omega_{ac}$	$j\omega_m + i\Omega_{ac}$
Systems with $\Omega_c > \Omega_r$	$(jZ_r + i)/N =$ integer	$(jZ_r - i)/N =$ integer
Systems with $\Omega_c < \Omega_r$	$(jZ_r - i)/N =$ integer	$(jZ_r + i)/N =$ integer

2.5.2 Floating Central Members

Central members (sun, carrier, and ring rigid body) have no translations for in-phase planetary gears. Thus, whether a central member floats (very low or zero translational bearing/support stiffnesses) or not does not affect ring elastic deformations for in-phase systems. Considering out-of-phase systems, this section investigates the effects of a floating central member on the spectral content of measured ring deflection for sensors attached to the rotating ring, stationary, and rotating carrier reference frames.

Figure 2.12 shows spectra of ring tangential deflection measured by sensors in the three different reference frames for the same out-of-phase system in Fig. 2.11 but with a floating carrier ($k_c = 0$). All the low-frequency spectral lines for the three different measurements

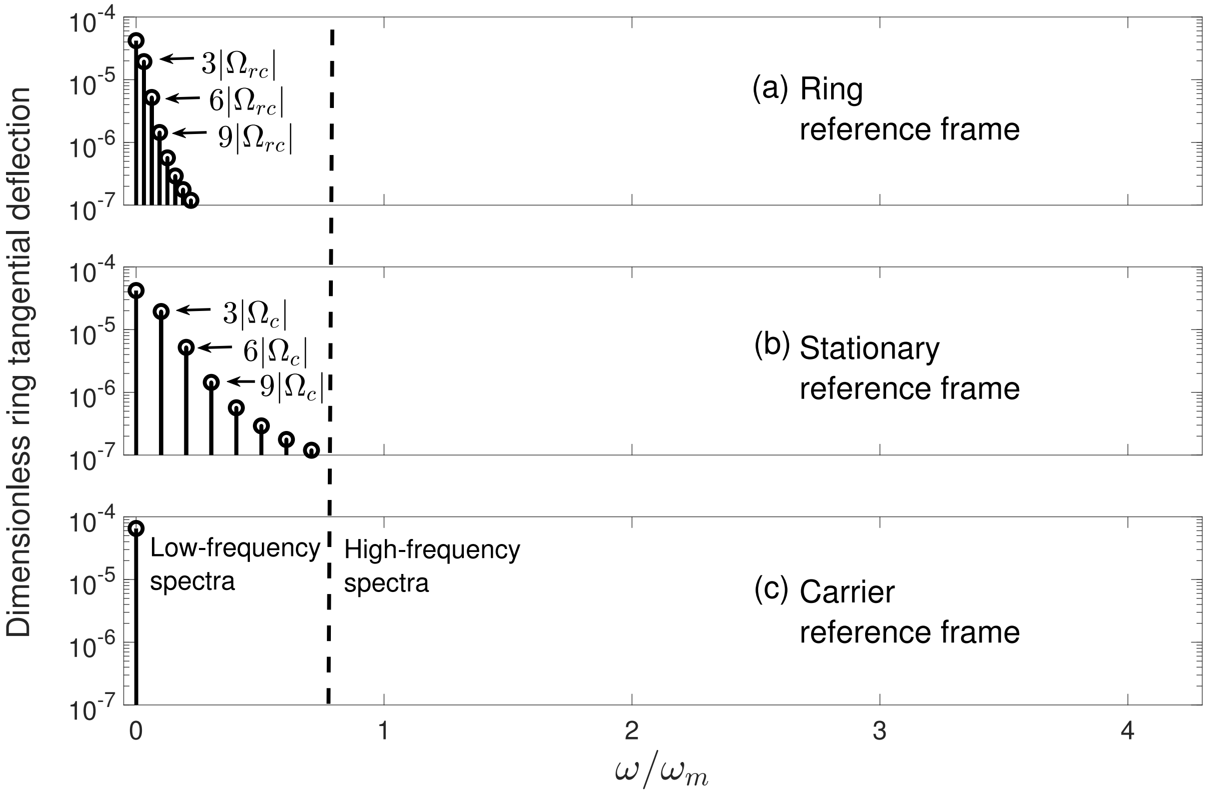

Figure 2.12: Spectra of ring tangential deflection measured by sensors fixed to three different reference frames for the same out-of-phase system ($Z_s = 31$ and $Z_r = 95$) used in Fig. 2.11, but with a floating carrier.

have trivial changes compared with Fig. 2.11, but all the high-frequency spectral lines disappear. Similar behavior happens for the out-of-phase system with a floating sun or ring.

Force equilibrium balances for a floating carrier give

$$\sum_{n=1}^{N} F_{sn}\sin(\psi_n - \alpha_s) + \sum_{n=1}^{N} F_{rn}\sin(\psi_n + \alpha_r) = 0, \tag{2.40a}$$

$$\sum_{n=1}^{N} F_{sn}\cos(\psi_n - \alpha_s) + \sum_{n=1}^{N} F_{rn}\cos(\psi_n + \alpha_r) = 0. \tag{2.40b}$$

Substitution of Eqs. (2.36) and (2.26) into Eqs. (2.40) and considering the mesh phase γ_{rn} in Eq. (2.24) for $\Omega_c > \Omega_r$ gives

$$\begin{aligned}\frac{1}{2}\sum_{j=0}^{\infty}\sum_{n=1}^{N} D_j\{&[\sin(j\omega_m t+\phi_j-\alpha_s)\frac{\cos\alpha_r}{\cos\alpha_s}+\sin(j\omega_m t+\phi_j+\alpha_r)]\cos(jZ_r+1)\psi_n\\ &+[\cos(j\omega_m t+\phi_j-\alpha_s)\frac{\cos\alpha_r}{\cos\alpha_s}+\cos(j\omega_m t+\phi_j+\alpha_r)]\sin(jZ_r+1)\psi_n\\ &-[\sin(j\omega_m t+\phi_j+\alpha_s)\frac{\cos\alpha_r}{\cos\alpha_s}+\sin(j\omega_m t+\phi_j-\alpha_r)]\cos(jZ_r-1)\psi_n\\ &+[\cos(j\omega_m t+\phi_j+\alpha_s)\frac{\cos\alpha_r}{\cos\alpha_s}+\cos(j\omega_m t+\phi_j-\alpha_r)]\sin(jZ_r-1)\psi_n\}=0,\end{aligned} \tag{2.41a}$$

$$\begin{aligned}\frac{1}{2}\sum_{j=0}^{\infty}\sum_{n=1}^{N} D_j\{&[\cos(j\omega_m t+\phi_j-\alpha_s)\frac{\cos\alpha_r}{\cos\alpha_s}+\cos(j\omega_m t+\phi_j+\alpha_r)]\cos(jZ_r+1)\psi_n\\ &-[\sin(j\omega_m t+\phi_j-\alpha_s)\frac{\cos\alpha_r}{\cos\alpha_s}+\sin(j\omega_m t+\phi_j+\alpha_r)]\sin(jZ_r+1)\psi_n\\ &+[\cos(j\omega_m t+\phi_j+\alpha_s)\frac{\cos\alpha_r}{\cos\alpha_s}+\cos(j\omega_m t+\phi_j-\alpha_r)]\cos(jZ_r-1)\psi_n\\ &-[\sin(j\omega_m t+\phi_j+\alpha_s)\frac{\cos\alpha_r}{\cos\alpha_s}+\sin(j\omega_m t+\phi_j-\alpha_r)]\sin(jZ_r-1)\psi_n\}=0.\end{aligned} \tag{2.41b}$$

Considering Eq. (2.32), the net force components for the j-th mesh frequency harmonic in Eq. (2.41) vanish for $(jZ_r \pm 1)/N \neq$ integer. For values of j where $(jZ_r \pm 1)/N =$ integer, the amplitude of the j-th mesh load harmonic D_j must vanish to satisfy Eq. (2.41). The same conclusion results for the case $\Omega_c < \Omega_r$. Similar analyses for a floating sun or ring lead to the same conclusion as for a floating carrier.

The foregoing analysis yields $D_1 = D_2 = D_4 = 0$ for the three-planet system with $Z_r = 95$. Therefore, the spectral content near and including the first, second, and fourth mesh frequency harmonics disappear for all three measurements in Fig. 2.12. No spectral content near the third mesh frequency harmonic could occur no matter whether any of the carrier, sun, and ring float or not (Figs. 2.11 and 2.12) because $D_3 = 0$ (Eq. (2.38)).

Because the ring deflection at a material point (measured by a sensor fixed to the rotating ring) affects ring fatigue life, a floating central member design can reduce fatigue failure by eliminating some of the high-frequency fluctuations in a quasi-static view.

2.6 Conclusions

This paper investigates steady deformations and measured spectra of spinning planetary gears with a deformable ring and equally-spaced planets. A dynamic model is derived in the carrier reference frame with gyroscopic and centripetal effects from carrier and ring rotation. The elastic ring model includes bending, extensional, and shear deformations. Each ring-planet mesh force acts at a contact point radially away from the ring neutral axis and thus imposes a concentrated tooth bending moment on the elastic ring.

Steady deformations are numerically calculated from a quasi-static model reduced from the dynamic one, and the results match well with those from a finite element/contact mechanics model. The concentrated tooth bending moments can significantly influence the steady deformations depending on the radial distance from the ring contact point to the ring neutral axis and on ring compliance. Ring extensional effect on steady deformations can be significant at high-speed ring rotation, while ring shear effect is minimal in this study.

In-phase and out-of-phase systems have much different spectral content for the ring deflection measured by sensors fixed to one of: a material point on the rotating ring, space-fixed ground, or the rotating carrier. For all three measurements, an in-phase system has only low-frequency content associated with the mean value of the ring-planet mesh load. In contrast, an out-of-phase system has high-frequency spectral lines near multiples of mesh frequency in addition to the low-frequency content. For an out-of-phase system, sidebands in the measured spectra occur near harmonics of the mesh frequency for a sensor fixed to a point on the rotating ring or fixed to ground. In contrast, spectra of the ring deflection measured by a sensor fixed to the rotating carrier have only mesh frequency harmonics and no neighboring sidebands. Simple rules are derived that govern the occurrence of all frequency components (including low-frequency and high-frequency content) of the ring deflection measured by a sensor rotating at an arbitrary speed (which includes the three specific cases listed above) for in-phase and out-of-phase systems.

A floating central member eliminates high-frequency content associated with certain mesh frequency harmonics for out-of-phase systems, potentially reducing fatigue failure.

Appendix A

A.1 Energy Expressions for the Sun, Carrier, Planets, Ring Rigid Body, and Sun-Planet Meshes

The kinetic energies for the sun, carrier, and ring rigid body are

$$K_h = \frac{1}{2}m_h[(\dot{x}_h - \Omega_c y_h)^2 + (\dot{y}_h + \Omega_c x_h)^2] + \frac{1}{2}(I_h/R_h^2)\dot{u}_h^2, \quad h = s, c, b,$$

where m_h and I_h represent mass and moment of inertia.

The kinetic energy of the n-th planet is

$$\begin{aligned} K_n =& \frac{1}{2}m_p\{(\dot{\zeta}_n - \Omega_c\eta_n)^2 + [\dot{\eta}_n + \Omega_c(R_c + \zeta_n)]^2\} \\ &+ \frac{1}{2}(I_p/R_p^2)\dot{u}_n^2, \quad n = 1, 2, \cdots, N, \end{aligned}$$

where m_p and I_p are planet mass and moment of inertia.

The strain energies in the sun, carrier, and ring rigid body supports/bearings are

$$V_h = \frac{1}{2}[k_h(x_h^2 + y_h^2) + k_{hu}u_h^2], \quad h = s, c, b.$$

The strain energy in each carrier-planet bearing is

$$\begin{aligned} V_n =& \frac{1}{2}[k_\zeta(\zeta_n - x_c\cos\psi_n - y_c\sin\psi_n)^2 \\ & + k_\eta(\eta_n + x_c\sin\psi_n - y_c\cos\psi_n - u_c)^2], \quad n = 1, 2, \cdots, N. \end{aligned}$$

The sun-planet mesh stiffness strain energy for the n-th planet is

$$V_{sn} = \frac{1}{2}k_{sn}\Delta_{sn}^2, \quad n = 1, 2, \cdots, N,$$

$$\Delta_{sn} = (-x_s\sin\psi_{sn} + y_s\cos\psi_{sn} + u_s) + (-\zeta_n\sin\alpha_s - \eta_n\cos\alpha_s + u_n),$$

where α_s is the sun-planet pressure angle and $\psi_{sn} = \psi_n - \alpha_s$.

A.2 Nondimensional Matrices and Vectors: $\mathbf{M}_d$, $\mathbf{G}_d$, $\mathbf{K}_d$, $\mathbf{C}_d$, and $\mathbf{f}_d$

$$\mathbf{M}_d = \mathrm{diag}(\mathbf{M}_b, \mathbf{M}_c, \mathbf{M}_s, \mathbf{M}_1, \cdots, \mathbf{M}_N)$$

$$\mathbf{M}_j = \mathrm{diag}(m_j, m_j, I_j), \quad j = s, c, b, 1, \cdots, N$$

$$\mathbf{G}_d = \mathrm{diag}(\mathbf{G}_b, \mathbf{G}_c, \mathbf{G}_s, \mathbf{G}_1, \cdots, \mathbf{G}_N)$$

$$\mathbf{G}_j = \begin{bmatrix} 0 & -2m_j & 0 \\ 2m_j & 0 & 0 \\ 0 & 0 & 0 \end{bmatrix}, \quad j = s, c, b, 1, \cdots, N$$

$$\mathbf{K}_d = \begin{bmatrix} \mathbf{K}_b & \mathbf{0} & \mathbf{0} & \mathbf{0} & \mathbf{0} & \cdots & \mathbf{0} \\ & \sum \mathbf{K}_{c1}^n + \mathbf{K}_c & \mathbf{0} & \mathbf{K}_{c2}^1 & \mathbf{K}_{c2}^2 & \cdots & \mathbf{K}_{c2}^N \\ & & \sum \mathbf{K}_{s1}^n + \mathbf{K}_s & \mathbf{K}_{s2}^1 & \mathbf{K}_{s2}^2 & \cdots & \mathbf{K}_{s2}^N \\ & & & \mathbf{K}_{pp}^1 & \mathbf{0} & \cdots & \mathbf{0} \\ & & & & \mathbf{K}_{pp}^2 & \cdots & \mathbf{0} \\ & & & & & & \ddots \\ \text{symmetric} & & & & & & \mathbf{K}_{pp}^N \end{bmatrix}$$

$$\mathbf{K}_b = \mathrm{diag}\Big(k_b + \pi(k_u + k_v), k_b + \pi(k_u + k_v), k_{bu} + 2\pi k_v / R_b^2\Big)$$

$$\mathbf{K}_h = \mathrm{diag}(k_h, k_h, k_{hu}), \quad h = s, c$$

$$\mathbf{K}_{pp}^n = \mathbf{K}_{s3}^n + \mathbf{K}_{c3}^n + \mathbf{K}_{r3}^n$$

$$\mathbf{K}_{c1}^n = \begin{bmatrix} k_\zeta \cos^2\psi_n + k_\eta \sin^2\psi_n & (k_\zeta - k_\eta)\sin\psi_n\cos\psi_n & -k_\eta \sin\psi_n \\ & k_\zeta \sin^2\psi_n + k_\eta \cos^2\psi_n & k_\eta \cos\psi_n \\ \text{symmetric} & & k_\eta \end{bmatrix}$$

$$\mathbf{K}_{c2}^n = \begin{bmatrix} -k_\zeta \cos\psi_n & k_\eta \sin\psi_n & 0 \\ -k_\zeta \sin\psi_n & -k_\eta \cos\psi_n & 0 \\ 0 & -k_\eta & 0 \end{bmatrix}$$

$$\mathbf{K}_{c3}^n = \mathrm{diag}(k_\zeta, k_\eta, 0)$$

$$\mathbf{K}_{r3}^n = k_{rn} \begin{bmatrix} \sin^2\alpha_r & -\sin\alpha_r\cos\alpha_r & -\sin\alpha_r \\ & \cos^2\alpha_r & \cos\alpha_r \\ \text{symmetric} & & 1 \end{bmatrix}$$

$$\mathbf{K}_{s1}^{n} = k_{sn} \begin{bmatrix} \sin^2\psi_{sn} & -\sin\psi_{sn}\cos\psi_{sn} & -\sin\psi_{sn} \\ & \cos^2\psi_{sn} & \cos\psi_{sn} \\ \text{symmetric} & & 1 \end{bmatrix}$$

$$\mathbf{K}_{s2}^{n} = k_{sn} \begin{bmatrix} \sin\psi_{sn}\sin\alpha_s & \sin\psi_{sn}\cos\alpha_s & -\sin\psi_{sn} \\ -\cos\psi_{sn}\sin\alpha_s & -\cos\psi_{sn}\cos\alpha_s & \cos\psi_{sn} \\ -\sin\alpha_s & -\cos\alpha_s & 1 \end{bmatrix}$$

$$\mathbf{K}_{s3}^{n} = k_{sn} \begin{bmatrix} \sin^2\alpha_s & \sin\alpha_s\cos\alpha_s & -\sin\alpha_s \\ & \cos^2\alpha_s & -\cos\alpha_s \\ \text{symmetric} & & 1 \end{bmatrix}$$

$$\mathbf{C}_d = \mathrm{diag}(\mathbf{C}_b, \mathbf{C}_c, \mathbf{C}_s, \mathbf{C}_1, \cdots, \mathbf{C}_N)$$

$$\mathbf{C}_j = \mathrm{diag}(m_j, m_j, 0), \quad j = s, c, b, 1, \cdots, N$$

$$\mathbf{f}_d = \begin{bmatrix} \mathbf{f}_b^T, & \mathbf{f}_c^T, & \mathbf{f}_s^T, & \mathbf{f}_1^T, & \cdots, & \mathbf{f}_N^T \end{bmatrix}^T$$

$$\mathbf{f}_h = \begin{bmatrix} 0 & 0 & T_h \end{bmatrix}^T, \quad h = s, c, b$$

$$\mathbf{f}_n = \begin{bmatrix} m_p\Omega_c^2 R_c & 0 & 0 \end{bmatrix}^T, \quad n = 1, 2, \cdots, N$$

Chapter 3

Free Vibrations of Spinning Epicyclic/Planetary Gears with a Deformable Ring

3.1 Introduction

Throughout this work, the term planetary gear is used even though the model and analysis allow for arrangements where all or any two of the sun gear, carrier, and ring gear spin.

Planetary gears in aerospace applications have thin ring gears to reduce weight. These thin ring gears, as demonstrated in experiments [88–91], deform elastically when transmitting power. Gyroscopic and centripetal effects that arise from carrier and/or ring gear rotation become significant at the high speeds of aerospace applications. This work investigates the natural frequencies and vibration modes of planetary gears with an elastic ring and gyroscopic (i.e., Coriolis) and centripetal acceleration effects.

Planetary gears have highly structured modal properties due to their cyclic symmetry. The modal structure was observed first from lumped-parameter models where the sun, carrier, planets, and ring are treated as rigid bodies. Botman [5] and Kahraman [6] identified modal structures for three-planet and four-planet systems, respectively. No general conclusions were derived. Lin and Parker [9] identified the modal structure for planetary gears with equally-spaced planets and proved there exist exactly three types of modes: rotational, translational, and planet modes. Planet modes do not occur for three-planet systems. For a rotational mode, the central components (the sun, carrier, and ring) have only rotations, and all planets have the same motions that are all in-phase. In a translational mode, the central components have only translations, and the planets vibrate with a known phase relationship. In a planet mode, the central components have no motions, and only the planets vibrate, again with a specified phase relationship but different than that for translational modes. Ericson and Parker [31] confirmed this modal structure in experiments. Cooley and Parker [10] proved that the modal structure persists for planetary gears with gyroscopic effects, but the real-valued modes evolve into complex-valued ones. Shi and Parker [92] derived modal properties of general cyclically symmetric structures with central components having planar vibrations, which include planetary gears. Dong and Parker [93] extended that derivation [92] to cyclically symmetric systems with central components vibrating as three-dimensional rigid bodies.

The modal properties of planetary gears that have lumped-parameter sun, carrier, and planets coupled to an elastically deformable ring gear were investigated by Wu and Parker [21]. They grouped vibration modes of the elastic-discrete system into rotational, translational, planet, and purely ring modes. The discrete motions for the rotational, translational, and planet modes are similar to those in [9], and the elastic ring has unique deformations associated with each of the three types of modes. The purely ring modes have only ring deformations, and all the discrete motions vanish. Ref. [21], however, ignored the gyroscopic and centripetal effects that make the vibration modes complex-valued. The elastic ring model has only inextensible bending deformation.

An elastic-discrete planetary gear model developed in Chapter 2 is adopted in this study. Gyroscopic and centripetal effects are included for all spinning components. The elastic ring model includes bending, extensional, and shear deformations as well as rotary inertia. Some studies [21, 80, 94, 95] considered only the inextensible bending deformation for an elastic ring, and a few studies [77, 82] employed extensional ring models that have bending and extensional deformations. Fewer studies [74] considered all three deformation components. For planetary gears with an elastic ring, whether the ring extensional deformation, shear deformation, and rotary inertia change the modal structure or not is unknown.

The model in Chapter 2 includes a concentrated tooth bending moment on the ring resulting from the ring-planet mesh forces acting at a contact point radially away from the ring neutral axis. Most literature [21, 77, 79, 96–98] that modeled gears as elastic rings ignored this concentrated tooth bending moment by applying the mesh force directly on the ring neutral axis. The effects of the concentrated tooth bending moment on the modal structure are unknown.

This work investigates free vibrations of spinning planetary gears with a deformable ring. The eigenvalue problem of the elastic-discrete model from Chapter 2 is solved for the natural frequencies and vibration modes. Predictions from the analytical model are compared against those from a finite element/contact mechanics model [12, 72, 73] for verification. A numerical example illustrates the modal structure, followed by a generalization of the structured modal properties to planetary gears with an arbitrary number of equally-spaced planets. A perturbation analysis illustrates the evolution of vibration modes from stationary to spinning planetary gears.

3.2 Model Overview and Eigenvalue Problem

Figure 3.1 shows the elastic-discrete planetary gear model for planar motions from Chapter 2, which is summarized below. The ring gear is modeled as an elastic ring with neutral axis radius R, cross-sectional area A, density ρ, Young's modulus E, shear modulus G, and shear correction factor κ [78]. The sun, carrier, and N planets are treated as rigid bodies with masses m_s, m_c, and m_p and moments of inertia I_s, I_c, and I_p. The elastic ring has a rigid body (mass m_b and moment of inertia I_b) at its center to accommodate an input or output member attached to the ring. This ring rigid body is depicted by the large, shaded circle in Fig. 3.1. The ring rigid body connects to the ring neutral axis through a uniform elastic foundation with radial (k_u) and tangential (k_v) distributed stiffnesses per unit arclength of ring neutral axis.

Each of the central components (sun, carrier, and ring rigid body) has one rotational and two in-plane translational degrees of freedom that are constrained by rotational and isotropic translational stiffnesses representing the bearings and supporting structures. All planets are identical and equally spaced, and each of them has one rotation and two translations, which are constrained by two radially and tangentially oriented linear stiffnesses that are identical for all planets. The sun-planet and ring-planet mesh interactions are modeled as linear stiffnesses along the line of action. Although these mesh stiffnesses change periodically over a mesh cycle, the free vibration (i.e., eigenvalue) analysis uses the average values of the mesh stiffnesses over a mesh cycle. These constant mesh stiffnesses k_{sp} and k_{rp} are the same for all planets (but $k_{sp} \neq k_{rp}$). The sun-planet and ring-planet pressure angles are denoted as α_s and α_r. Each ring-planet mesh force acts at a contact point with a radial distance Γ

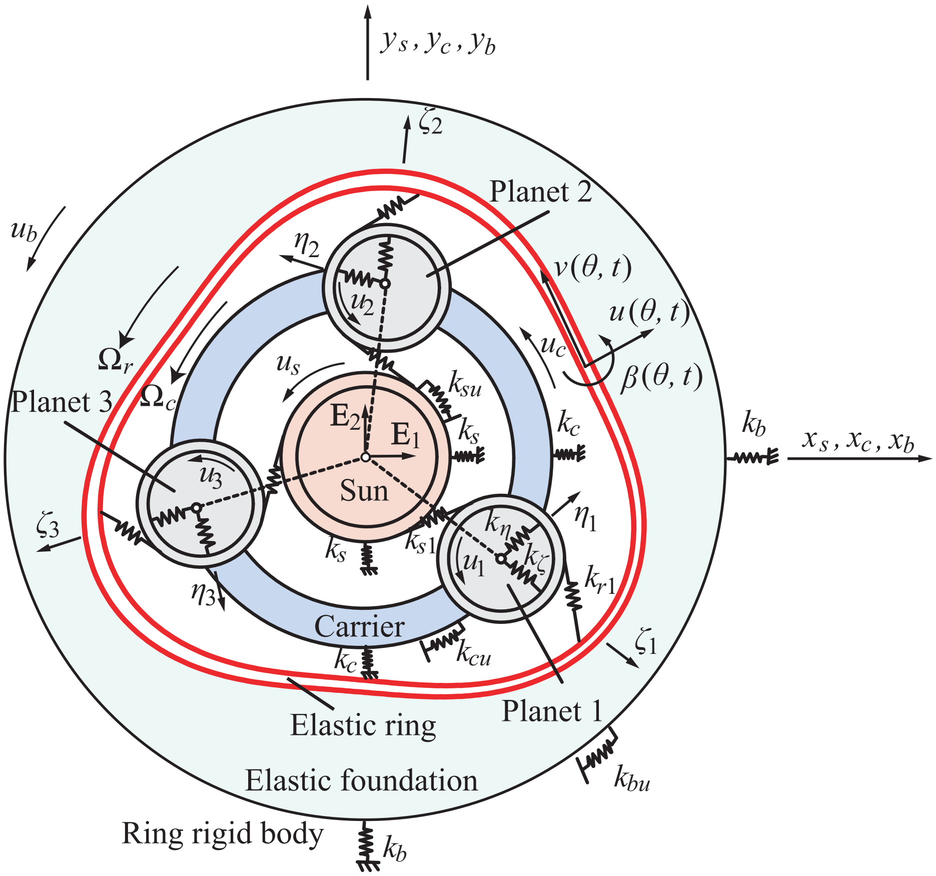

Figure 3.1: Schematic of a planetary gear model with a deformable ring.

away from the ring neutral axis, creating a concentrated moment on the ring neutral axis, as shown in Fig. 2.3 in Chapter 2. The carrier and ring have speeds Ω_c and Ω_r, respectively. Speeds of the sun and planets can be derived from kinematics. There is no constraint that any central component be stationary.

The elastic ring has the inertia quantities

$$\begin{gathered}J_0 = \int_A \rho(R+r)/R \,\mathrm{d}A, \quad J_1 = \int_A \rho(R+r)r/R \,\mathrm{d}A, \\ J_2 = \int_A \rho(R+r)r^2/R \,\mathrm{d}A\end{gathered} \tag{3.1}$$

and stiffness quantities

$$\begin{gathered}\alpha_1 = EI_0, \quad \alpha_2 = EI_1/R, \quad k_\beta = EI_2/R^2, \quad \alpha_3 = \kappa G I_0, \\ I_0 = \int_A 1/(R+r)\,\mathrm{d}A, \quad I_1 = \int_A r/(R+r)\,\mathrm{d}A, \quad I_2 = \int_A r^2/(R+r)\,\mathrm{d}A,\end{gathered} \tag{3.2}$$

where r is the radial distance from the ring neutral axis to a material point on the ring.

The deflection of the whole system is represented by the vector $\boldsymbol{\chi}(\theta, t)$ that combines the elastic ring deformations $u(\theta,t)$, $v(\theta,t)$, and $\beta(\theta,t)$ and the discrete motions $\mathbf{q}(t)$ of the sun, carrier, planets, and ring rigid body as

$$\boldsymbol{\chi} = \begin{bmatrix}\boldsymbol{w}^T & \mathbf{q}^T\end{bmatrix}^T, \tag{3.3a}$$

$$\boldsymbol{w} = \begin{bmatrix}u & v & \beta\end{bmatrix}^T, \quad \mathbf{q} = \begin{bmatrix}\mathbf{p}_b^T & \mathbf{p}_c^T & \mathbf{p}_s^T & \mathbf{p}_1^T & \dots & \mathbf{p}_N^T\end{bmatrix}^T, \tag{3.3b}$$

$$\mathbf{p}_h = \begin{bmatrix}x_h & y_h & u_h\end{bmatrix}^T, \qquad h = s, c, b, \tag{3.3c}$$

$$\mathbf{p}_n = \begin{bmatrix}\zeta_n & \eta_n & u_n\end{bmatrix}^T, \qquad n = 1, \dots, N. \tag{3.3d}$$

All the coordinates in $\boldsymbol{\chi}$ are described in the rotating carrier reference frame with speed Ω_c. $\{\mathbf{E}_1, \mathbf{E}_2, \mathbf{E}_3\}$ (Fig. 3.1) defines the carrier-fixed basis. The vector $\boldsymbol{w}(\theta,t)$ contains the elastic ring deformations consisting of the radial ($u(\theta,t)$) and tangential ($v(\theta,t)$) deflections of the ring neutral axis and its cross-sectional rotation angle ($\beta(\theta,t)$), where θ defines an angular position relative to the rotating basis vector $\mathbf{E}_1$. A given value of θ defines an angular orientation in the carrier reference frame but not a specific point on the ring gear; because the ring rotates relative to the carrier, different points on the ring rotate past an angular orientation defined by a given value of θ. The translations of the central components are represented by x_h, y_h for $h = s, c, b$ in the $\mathbf{E}_1$ and $\mathbf{E}_2$ directions. Planet translations are described using radial (ζ_n) and tangential (η_n) coordinates. The rotational displacements

u_j for $j = 1, \ldots, N, s, c, b$ are the rotations in radians times the gear base radii R_p and R_s, the center distance R_c for the carrier, and the radius R_b for the ring rigid body. The planets are positioned at ψ_n with respect to the rotating basis vector $\mathbf{E}_1$. Without loss of generality, the first planet has angular position $\psi_1 = 0$.

Nondimensionalization of the system deflections and parameters follows that in Chapter 2. The dimensionless eigenvalue problem of the elastic-discrete model is written in extended operator form as

$$\lambda^2 \mathbf{M}\boldsymbol{\chi} + \lambda(\Omega_r \mathbf{G}_r + \Omega_c \mathbf{G}_c)\boldsymbol{\chi} + (\mathbf{K} - \Omega_r^2 \mathbf{C}_r - \Omega_c^2 \mathbf{C}_c - 2\Omega_r \Omega_c \mathbf{C}_{rc})\boldsymbol{\chi} = \mathbf{0}, \tag{3.4}$$

where λ is the eigenvalue; $\mathbf{M}$ and $\mathbf{K}$ are extended mass and stiffness operators, respectively; $\mathbf{G}_r$ and $\mathbf{G}_c$ are extended gyroscopic operators; and, $\mathbf{C}_r$, $\mathbf{C}_c$, and $\mathbf{C}_{rc}$ are extended centripetal operators. All these operators are identical to those in Chapter 2. The operators $\mathbf{M}$, $\mathbf{K}$, $\mathbf{C}_r$, $\mathbf{C}_c$, and $\mathbf{C}_{rc}$ are self-adjoint with the inner product

$$\langle \boldsymbol{\chi}_1,\ \boldsymbol{\chi}_2 \rangle = \int_0^{2\pi} \overline{\boldsymbol{w}}_1^T \boldsymbol{w}_2 \mathrm{d}\theta + \overline{\mathbf{q}}_1^T \mathbf{q}_2, \tag{3.5}$$

where the overbar denotes complex conjugate. The gyroscopic operators $\mathbf{G}_r$ and $\mathbf{G}_c$ are skew self-adjoint with the inner product in Eq. (3.5).

The model in Eq. (3.4) differs from the elastic-discrete model in [21]. The current model has a vibrating ring rigid body that models an additional component connecting to the elastic ring, while Ref. [21] just connects the elastic ring to ground. Gyroscopic and centripetal effects are present in Eq. (3.4) for spinning systems, but these effects are not considered in [21] for stationary systems. The present model considers ring bending deformation, extensional deformation, shear deformation, and rotary inertia as well as a concentrated tooth bending moment resulting from each ring-planet mesh force acting at a contact point radially away from the ring neutral axis. In contrast, Ref. [21] considers only inextensible bending deformation and neglects the other features listed above.

Galerkin's method is used to discretize the eigenvalue problem in Eq. (3.4). The eigenmode $\boldsymbol{\chi}$ is approximated as a truncated series of basis functions as

$$\boldsymbol{\chi}_a(\theta) = \sum_{l=-L_b}^{L_b} a_l \boldsymbol{\chi}_{1l}(\theta) + \sum_{m=-M_b}^{M_b} b_m \boldsymbol{\chi}_{2m}(\theta) + \sum_{p=-P_b}^{P_b} c_p \boldsymbol{\chi}_{3p}(\theta) + \sum_{k=1}^{3N+9} d_k \boldsymbol{\chi}_{4k}(\theta), \tag{3.6a}$$

$$\boldsymbol{\chi}_{1l} = \left[\begin{array}{c} e^{jl\theta} \\ 0 \\ 0 \\ \hdashline \mathbf{0} \end{array}\right], \quad \boldsymbol{\chi}_{2m} = \left[\begin{array}{c} 0 \\ e^{jm\theta} \\ 0 \\ \hdashline \mathbf{0} \end{array}\right], \quad \boldsymbol{\chi}_{3p} = \left[\begin{array}{c} 0 \\ 0 \\ e^{jp\theta} \\ \hdashline \mathbf{0} \end{array}\right], \quad \boldsymbol{\chi}_{4k} = \left[\begin{array}{c} 0 \\ 0 \\ 0 \\ \hdashline \mathbf{e}_k \end{array}\right], \tag{3.6b}$$

where $\mathbf{e}_k$ is a unit vector of dimension $3N+9$ (i.e., the number of discrete degrees of freedom) with the k-th element equal to one and all others zero. The ring radial deflection, tangential deflection, and cross-sectional rotation angle have the complex-valued nodal diameter (i.e., Fourier series) expansions

$$u(\theta) = \sum_{l=-L_b}^{L_b} a_l e^{jl\theta}, \qquad v(\theta) = \sum_{m=-M_b}^{M_b} b_m e^{jm\theta}, \qquad \beta(\theta) = \sum_{p=-P_b}^{P_b} c_p e^{jp\theta}. \tag{3.7}$$

The discretization error in Eq. (3.6a) approaches zero as the integers L_b, M_b, $P_b \to \infty$.

Substitution of Eq. (3.6a) into Eq. (3.4) and requiring that the inner product of the residual (i.e., the result of the substitution) with each of the basis functions in Eq. (3.6b) vanishes gives the matrix eigenvalue problem

$$\lambda^2[\mathbf{M}]\mathbf{z} + \lambda(\Omega_r[\mathbf{G}_r] + \Omega_c[\mathbf{G}_c])\mathbf{z} + ([\mathbf{K}] - \Omega_r^2[\mathbf{C}_r] - \Omega_c^2[\mathbf{C}_c] - 2\Omega_r\Omega_c[\mathbf{C}_{rc}])\mathbf{z} = \mathbf{0}, \tag{3.8a}$$

$$\mathbf{z} = [a_{-L_b} \ \dots \ a_{L_b} \ b_{-M_b} \ \dots \ b_{M_b} \ c_{-P_b} \ \dots \ c_{P_b} \ d_1 \ \dots \ d_{3N+9}]^T \tag{3.8b}$$

where the eigenvector $\mathbf{z}$ has dimension $2L_b + 2M_b + 2P_b + 3N + 12$. Numerically solving the discretized eigenvalue problem yields the natural frequencies $\omega_i = \mathrm{Im}(\lambda_i)$ (imaginary part of λ_i) and eigenvectors $\mathbf{z}_i$. Vibration modes are determined by substitution of the corresponding elements of $\mathbf{z}_i$ into Eq. (3.6a). The dimensionless natural frequencies ω_i are related to the dimensional natural frequencies $\tilde{\omega}_i$ according to $\tilde{\omega}_i = \omega_i\sqrt{k_\zeta/(m_p R)}$.

3.3 Verification of the Free Vibration Model

This section compares natural frequencies and vibration modes calculated from the analytical model with those from two-dimensional finite element/contact mechanics (FE/CM) software [12, 72, 73]. In general, the sun, carrier, ring, and planets can all deform elastically in the FE/CM approach, but this work only allows elastic deformation of the ring and restricts the sun, carrier, and planets to have only rigid-body motions. The sun and planet gears have rigid inner circles at a diameter close to the root diameter with the FE/CM mesh being used only for the gear teeth and tooth root regions.

Chapter 2 successfully compared steady deformations from the analytical model to those from the FE/CM model. Because of the difference between the analytical and FE/CM models, the analytical model was adjusted for that comparison. Steady deformations are independent of inertia terms. Difference of the inertia terms between these two models is not discussed in Chapter 2. This work details both the difference in Chapter 2 and that of inertia terms between these two models.

The FE/CM model does not allow a ring rigid body or an elastic foundation. Instead, the ring gear can have a lumped mass/moment of inertia attached to it, and motions of the lumped inertia equal the rigid-body motion components of the elastic ring gear having the expressions

$$\begin{gathered}x_r(t) = \int_0^{2\pi} 2u_o(\theta,t)\cos\theta\ \mathrm{d}\theta, \qquad y_r(t) = \int_0^{2\pi} 2u_o(\theta,t)\sin\theta\ \mathrm{d}\theta, \\ u_r(t) = (R_r/R_o)\int_0^{2\pi} v_o(\theta,t)\ \mathrm{d}\theta,\end{gathered} \tag{3.9}$$

where u_r represents the rigid rotation in radians times the ring gear base radius R_r. u_o and v_o denote the radial and tangential deflections of the FE/CM model's ring outer surface, and R_o is the radius of the ring outer surface. The two translations are resisted by isotropic translational stiffness k_r, and the rotation is resisted by a rotational stiffness k_{ru}.

To facilitate the comparison of natural frequencies and mode shapes, the analytical model is adjusted because of the above modeling differences. The elastic foundation is removed, and motions of the ring rigid body (which resembles the lumped inertia attached to the FE/CM ring gear as discussed above) equal the rigid-body motions for the analytical ring that are defined in the same way as the FE/CM model does in Eq. (3.9), i.e., $x_b = x_r$, $y_b = y_r$, and $u_b/R_b = u_r/R_r$. The support/bearing stiffnesses k_b and k_{bu}/R_b of the ring rigid body equal the stiffnesses k_r and k_{ru}/R_r for the FE/CM model, respectively. These adjustments apply only for the present section.

We adopt Eq. (3.9) to compare with the FE/CM software. If the rigid-body motions of the elastic ring are instead defined as the translations of the center of mass of the ring and the average rotation of all ring particles, the alternative relations are

$$\begin{aligned}x_r &= \int_0^{2\pi}\int_A \rho(R+r)[u\cos\theta - (v+r\beta)\sin\theta]\ \mathrm{d}A\mathrm{d}\theta \bigg/ \int_0^{2\pi}\int_A \rho(R+r)\ \mathrm{d}A\mathrm{d}\theta, \\ y_r &= \int_0^{2\pi}\int_A \rho(R+r)[u\sin\theta + (v+r\beta)\cos\theta]\ \mathrm{d}A\mathrm{d}\theta \bigg/ \int_0^{2\pi}\int_A \rho(R+r)\ \mathrm{d}A\mathrm{d}\theta, \\ u_r &= R_r\int_0^{2\pi}\int_A \rho(R+r)^2(v+r\beta)\ \mathrm{d}A\mathrm{d}\theta \bigg/ \int_0^{2\pi}\int_A \rho(R+r)^3\ \mathrm{d}A\mathrm{d}\theta.\end{aligned}$$

The comparison is conducted on a three-planet system with equal planet spacing. The sun-planet and ring-planet tooth meshes at the three planets are in-phase. The parameters of the FE/CM model are shown in Table 3.1. Natural frequencies and vibration modes of the FE/CM model are obtained from impulse tests, which are conducted at zero speed so

Table 3.1: Parameters of a three-planet FE/CM planetary gear model.

	Sun	Planets	Ring	Carrier
Number of teeth	30	33	96	-
Module (mm)	2.868	2.868	2.868	-
Inner diameter (mm)	63.00	69.00	271.4	-
Root diameter (mm)	79.14	86.13	282.4	-
Outer diameter (mm)	91.14	99.13	326.4	-
Facewidth (mm)	25.40	25.40	25.40	-
Pressure angle (deg)	24.60	24.60	24.60	-
Young's modulus (GPa)	202.1	202.1	202.1	-
Poisson's ratio	0.3	0.3	0.3	-
Mass (kg)	1	2	15	20
Moment of inertia (kg·m^2)	2×10^{-3}	5×10^{-3}	160×10^{-3}	200×10^{-3}
Translational stiffness (N/m)	50×10^3	$\zeta : 200 \times 10^6$ $\eta : 1 \times 10^9$	200×10^6	2×10^9
Rotational stiffness (N/m)	6.537×10^6	0	63.84×10^6	612.7×10^6
Center distance (mm)	90.33			

Note: sun, carrier, and ring translational stiffnesses are specified in X and Y direction, while planet translational stiffnesses are in radial and tangential directions.

that the impulse test response is free from the contamination of tooth mesh excitations. For a stationary planetary gear, four types of modes exist: rotational, translational, planet, and purely ring modes [21]. Planet modes do not occur for three-planet systems. Two different impulse tests are conducted, with a torque impulse on the sun gear capturing the rotational modes of the three-planet system and a force impulse on the sun gear capturing the translational modes. Purely ring modes are not captured in the impulse tests. LMS Test.Lab [99] is used to process the impulse responses and generate natural frequencies and mode shapes.

The analytical model takes the parameters in Table 3.1 as well as the following parameters. The sun-planet and ring-planet mesh stiffnesses are 400.6×10^6 N/m and 457.4×10^6 N/m, respectively. They are calculated from single-pair sun-planet and ring-planet FE/CM models using a local slope method [86] at the same mesh cycle instance where the FE/CM planetary gear impulse tests are conducted. The ring inner diameter of the analytical model is a tunable parameter that is bounded between the ring gear inner and root diameters of the FE/CM model. Gyroscopic and centripetal effects vanish for the analytical model at zero speed.

Three different values of the ring inner diameter of the analytical model were considered: (a) ring gear root diameter, (b) ring gear inner diameter, and (c) mean value of ring gear root and inner diameters of the FE/CM model. Case (a) gives the best comparison with the FE/CM model in terms of natural frequencies among the three cases.

Table 3.2 shows natural frequencies from the analytical model of case (a) and the FE/CM model for the first nineteen modes occurring in the impulse tests. The analytical model captures the first eighteen modes with errors less than 6%, most of which are less than 1%. The error of the last mode reaches 10%.

Table 3.2: Natural frequencies of the FE/CM model and analytical model (case (a)) with parameters in Table 3.1.

Frequency index	Mode type	FE/CM (Hz)	Analytical (Hz)	Multiplicity	Error (%)
1	Rotational	293.3	293.5	1	0.068
2	Translational	386.4	369.0	2	-4.5
3	Translational	586.7	582.9	2	-0.65
4	Rotational	651.2	649.9	1	-0.20
5	Translational	1152	1155	2	0.26
6	Rotational	1202	1144	1	-4.8
7	Rotational	1571	1573	1	0.13
8	Translational	1582	1574	2	-0.51
9	Translational	2175	2118	2	-2.6
10	Rotational	2858	2869	1	0.38
11	Translational	3157	3183	2	0.82
12	Translational	3990	3937	2	-1.3
13	Rotational	4297	4331	1	0.79
14	Translational	4951	4990	2	0.79
15	Rotational	5166	5457	1	5.6
16	Translational	5231	5302	2	1.4
17	Rotational	5776	5930	1	2.7
18	Translational	6038	6211	2	2.9
19	Rotational	6834	7539	1	10

Figure 3.2 and Figure 3.3 compare a rotational mode (mode 10 in Table 3.2) and a translational mode (mode 11 in Table 3.2) from the analytical model with the corresponding modes from the FE/CM model. The analytical predictions match those from the FE/CM model in both comparisons.

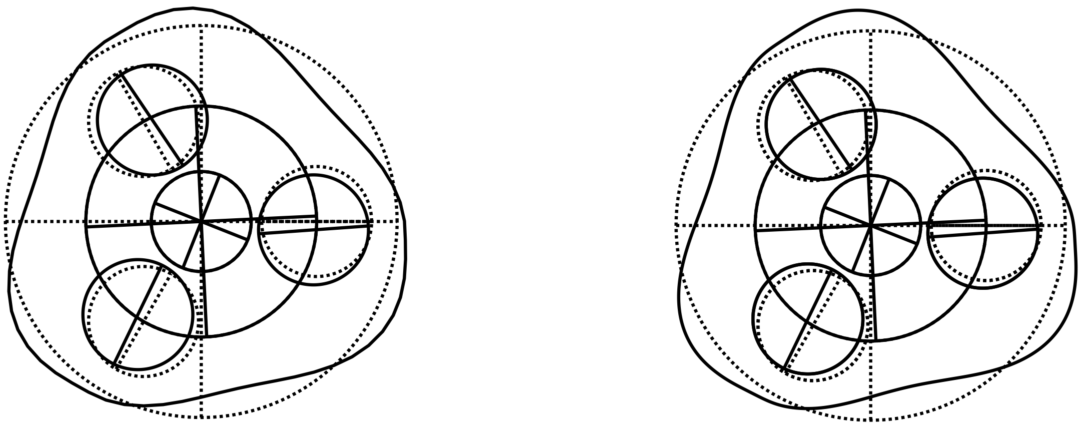

(a)

(b)

Figure 3.2: Rotational mode shapes (mode 10 in Table 3.2) from (a) the FE/CM model and (b) the analytical model. The dotted lines represent undeformed positions.

3.4 Natural Frequencies and Vibration Modes of Gyroscopic Planetary Gears

Numerical experiments on the discretized eigenvalue problem in Eq. (3.8a) show that the gyroscopic effects alter the modal structure of planetary gears with equally-spaced planets. The vibration modes of stationary planetary gears without gyroscopic effects, presented by Wu and Parker [21], are real-valued and fall into four categories: rotational, translational, planet, and purely ring modes. The gyroscopic effects considered in the current model render the vibration modes as complex-valued quantities, and these modes fall into three categories:

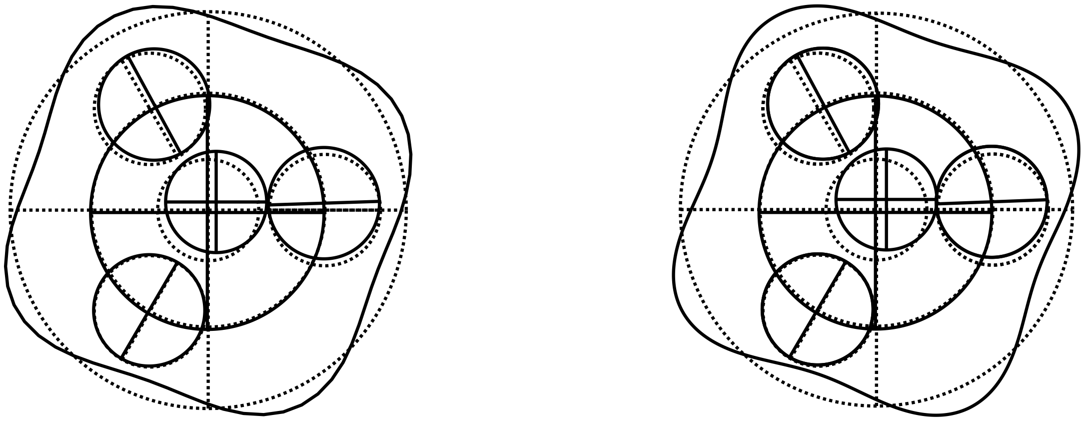

(a) (b)

Figure 3.3: Translational mode shapes (mode 11 in Table 3.2) from (a) the FE/CM model and (b) the analytical model. The dotted lines represent undeformed positions.

rotational, translational, and planet modes. Purely ring modes do not appear. In addition to the gyroscopic effects, the current model includes centripetal effects, ring extensional and shear effects, effects of ring rotary inertia, and effects of concentrated tooth bending moments, all of which do not exist in [21]. These effects, however, do not alter the modal structure.

For stationary planetary gears, the mass ($\mathbf{M}$) and stiffness ($\mathbf{K}$) operators in Eq. (3.4) are self-adjoint. Thus, all vibration modes are real-valued. When gyroscopic effects are included, the skew self-adjoint operators $\mathbf{G}_r$ and $\mathbf{G}_c$ in Eq. (3.4) lead to complex-valued modes [100]. Complex-valued modes are those where different degrees of freedom vibrate out-of-phase with each other; different points achieve their maximum displacements at different times over an oscillation at the corresponding natural frequency.

Real-valued modes are standing wave modes. For the response of a single real-valued mode, the ring radial deflection can be expressed as $u(\theta, t) = [a_0 + \sum_{l=1}^{L_b}(a_l e^{jl\theta} + c.c.)]\cos(\omega_i t + \phi_i)$, where a_0 is real-valued, ω_i is the natural frequency, and ϕ_i is the phase angle. The motions of different points on the ring are either in-phase or 180 degree out-of-phase. Complex-valued modes are traveling wave modes [77, 85]. The ring radial deflection for the response of a single complex-valued mode has the expression $u(\theta,t) = \sum_{l=-L_b}^{L_b}(a_l e^{jl\theta} e^{j\omega_i t} + c.c.) = \sum_{l=-L_b}^{L_b} 2|a_l|\cos(l\theta + \omega_i t + \varphi_l)$, where $\varphi_l = \tan^{-1}(\mathrm{Im}(a_l)/\mathrm{Re}(a_l))$ is the phase of a_l. In general, $a_l \neq \bar{a}_{-l}$. The positive l nodal diameter component is a backward wave that travels in the negative θ direction, while the negative l nodal diameter component is a forward wave that travels in the positive θ direction. The ring deflection is a summation of backward and forward waves.

An example planetary gear with six equally-spaced planets illustrates the gyroscopically-altered modal structure. The system parameters are listed in Table 3.3. The carrier is stationary (i.e., $\Omega_c = 0$) while the ring rotates. The elastic ring has a rectangular cross-section with radial thickness H and axial thickness B. Table 3.4 gives the natural frequencies of the system without gyroscopic effects ($\Omega_r = 0$) for each type of modes appearing in Ref. [21] and their counterparts of the same system with gyroscopic effects at dimensionless ring speed $\Omega_r = -0.05$, which corresponds to a dimensional speed of $-11,414$ rpm. Figure 3.4 shows representative mode shapes for the system with gyroscopic effects. The following paragraphs summarize the observations from the numerical experiments on spinning planetary gears with gyroscopic effects and the modal properties of stationary planetary gears from Ref. [21].

Rotational modes. Because the central components have only rotations for this type of modes, they are called rotational modes. Rotational modes are, in general, distinct for spinning systems with gyroscopic effects. All planets have identical motions that are in-phase, i.e., $\mathbf{p}_n = \mathbf{p}_1 e^{j0\psi_n}$. The individual components in $\mathbf{p}_n$ for the planet n, however, are out-of-phase with each other. The ring deformations contain only $sN + 0$ nodal diameter components, where $s = 0, \pm1, \pm2, \ldots$. In other words, all coefficients a_l, b_m, and c_p vanish except for $l, m, p = sN$ for integer s. The rotational modes are also called type 0 modes.

Table 3.3: Dimensional parameters of an example planetary gear with an elastic ring.

Stiffness (N/m)	$k_s = k_{su} = 100 \times 10^6,\ k_c = k_{cu} = k_b = k_{bu} = 10^{12},\ k_\zeta = 200 \times 10^6,\ k_\eta = 10^9,\ Rk_u = Rk_v = 20.0 \times 10^6,\ k_{sp} = k_{rp} = 500 \times 10^6$
Inertia (kg)	$I_s/R_s^2 = 0.654,\ I_p/R_p^2 = 0.490,\ I_c/R_c^2 = 4.69,\ I_b/R_b^2 = 9.77$
Mass (kg)	$m_s = 0.640,\ m_p = 0.350,\ m_c = 3.00,\ m_b = 3.20$
Dimensions (mm)	$R_b = 64.0,\ R = 148,\ \Gamma = 10.4,\ H = 12.0,\ B = 25.4$
Elastic modulus (GPa)	$E = 202,\ \kappa G = 61.3$
Density (kg/m^3)	$\rho = 7.85 \times 10^3$
Pressure angle (deg)	$\alpha_s = \alpha_r = 24.6$

Rotational modes for stationary systems have the same properties with those for spinning systems except that stationary systems have real-valued rotational modes while spinning systems have complex-valued ones.

Translational modes. For this type of modes, the central components have only translations. Translational modes for spinning systems with gyroscopic effects are distinct. These gyroscopic translational modes are classified into two subtypes with one designated as type 1 modes and the other called type $N-1$ modes. For a type 1 mode, the two translations of the central components are related by $y_h = jx_h$ $(h = s, c, b)$, the planet motions are related by $\mathbf{p}_n = \mathbf{p}_1 e^{j\psi_n}$ for $n = 1, 2, \ldots, N$, and the ring deformations have only $sN + 1$ nodal diameter components, where $s = 0, \pm 1, \pm 2, \ldots$. In contrast, a type $N-1$ translational mode has $y_h = -jx_h$, $\mathbf{p}_n = \mathbf{p}_1 e^{-j\psi_n}$, and only $sN - 1$ nodal diameter ring deformations.

Translational modes for spinning systems differ significantly from those for stationary systems. Translational modes for stationary systems are degenerate with multiplicity two. The two translations of the central components in a single translational mode have no special

Table 3.4: Dimensionless natural frequencies of a planetary gear with six equally-spaced planets. The system parameters are listed in Table 3.3. Example natural frequencies are shown for different mode types at $\Omega_r = 0$, and the counterpart natural frequencies at $\Omega_r = -0.05$ follow those at $\Omega_r = 0$ in each row.

$\Omega_r = 0$		$\Omega_r = -0.05$	
Mode type	Natural frequency	Mode type	Natural frequency
Rotational	$\omega_{18} = 1.04$	Rotational	$\omega_{18} = 0.996$
Translational	$\omega_8 = 0.716$	Translational	$\omega_7 = 0.613$
	$\omega_9 = 0.716$	Translational	$\omega_{10} = 0.755$
Degenerate planet	$\omega_{10} = 0.718$	Planet	$\omega_8 = 0.633$
	$\omega_{11} = 0.718$	Planet	$\omega_{12} = 0.807$
Distinct planet	$\omega_7 = 0.638$	Planet	$\omega_9 = 0.676$
Type 0 purely ring	$\omega_{21} = 1.32$	Rotational	$\omega_{20} = 1.23$
Type 3 purely ring	$\omega_4 = 0.413$	Planet	$\omega_4 = 0.363$

relations. Translational modes cannot be further classified into different subtypes. The motion of each planet in two orthogonal (with respect to $\mathbf{M}$) degenerate modes is related to the motion of the first planet by a rotation matrix [21]. The ring deformations contain only $sN \pm 1$ nodal diameter components, where $s = 0, \pm 1, \pm 2, \ldots$.

Planet modes. No central components vibrate in a planet mode. Planet modes exist only for systems with $N > 3$ planets. All planet modes, in general, are distinct for spinning systems with gyroscopic effects. The gyroscopic planet modes are classified into $(N - 3)$ subtypes. Each subtype is associated with an integer $d \in \{2, 3, \ldots, N - 2\}$ and called a type

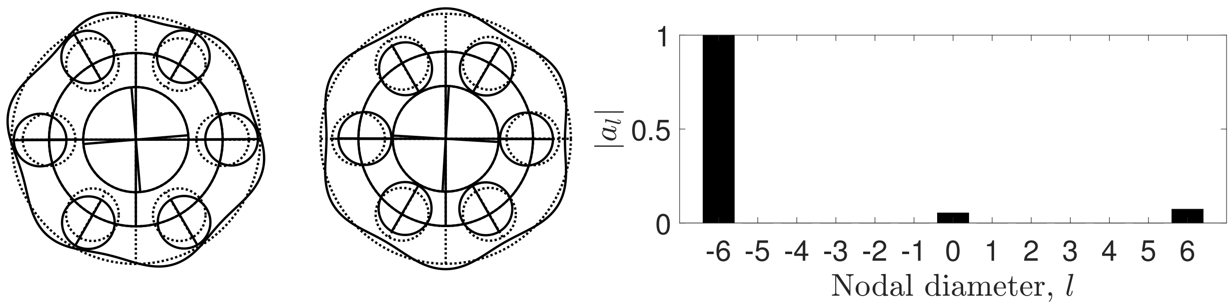

(a) Rotational mode, $\omega_{18} = 0.996$

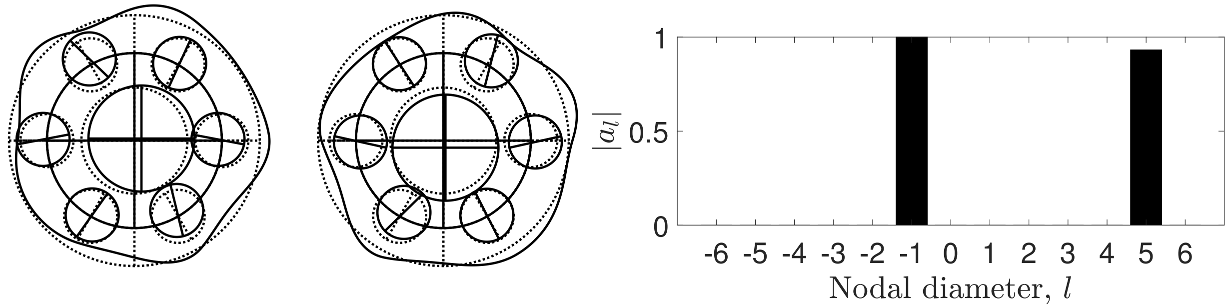

(b) Translational mode, $\omega_{10} = 0.755$

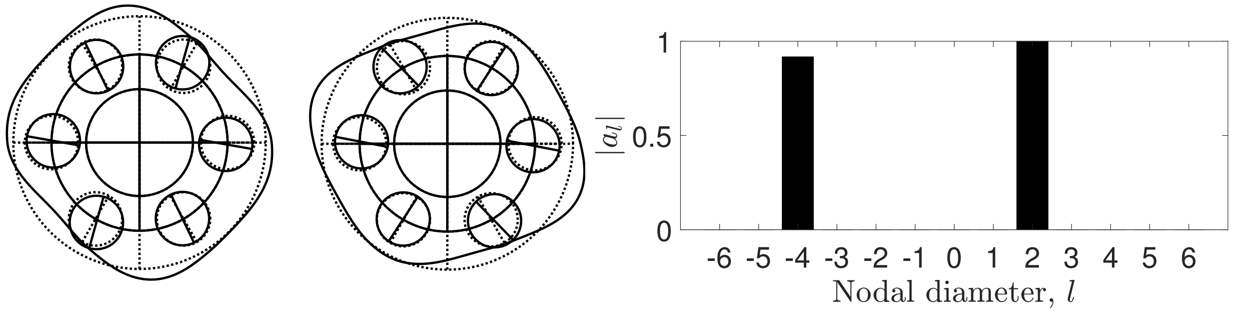

(c) Planet mode, $\omega_8 = 0.633$

Figure 3.4: Real part (left), imaginary part (middle), and ring radial nodal diameter amplitudes a_l from Eq. (3.7) (right) of vibration modes for a six-planet system with parameters in Table 3.3 at non-dimensional speed $\Omega_r = -0.05$. The dotted lines represent undeformed positions. The ring rigid body is not shown. The ring radial nodal diameter amplitudes are normalized by their maximum value. The ring tangential deflection and cross-sectional rotation angle (not shown) have the same non-trivial nodal diameter components but with different amplitudes.

d mode. For that subtype, the elastic ring deformations contain only $sN + d$ nodal diameter components, where $s = 0, \pm 1, \pm 2, \ldots$, and planet motions are related by $\mathbf{p}_n = \mathbf{p}_1 e^{jd\psi_n}$ for $n = 1, 2, \ldots, N$.

Substantial difference exists between planet modes for spinning and stationary systems. Planet modes in stationary systems are classified into two sub-categories according to the degeneracy of their natural frequencies. Degenerate planet modes appear in systems with five or more planets, and their multiplicity is two, while distinct planet modes exist only for systems with an even number of planets. For all planet modes, the motion of each planet is a scalar multiple of any other planet's motion. Each of the degenerate planet modes is associated with a particular integer $d \in \{2, 3, \ldots, \mathrm{int}((N-1)/2)\}$. For that particular d, the ring deformations contain only $sN \pm d$ nodal diameter components, where $s = 0, \pm 1, \pm 2, \ldots$. All distinct planet modes are associated with an integer $N/2$ for even N, and the ring deformations contain only $sN + N/2$ nodal diameter components, where $s = 0, \pm 1, \pm 2, \ldots$.

Purely ring modes. For this type of modes, all discrete motions vanish and only the elastic ring vibrates. Purely ring modes do not occur in spinning systems, but exist in stationary systems. Purely ring modes are distinct. The real-valued elastic ring deformations contain only a single complex conjugate pair of nodal diameter components, i.e.,

$$u(\theta) = a_g e^{jg\theta} + c.c., \qquad v(\theta) = b_g e^{jg\theta} + c.c., \qquad \beta(\theta) = c_g e^{jg\theta} + c.c.. \tag{3.10}$$

The purely ring modes have two subtypes. In one subtype (type 0), $g = sN$ for $s = 1, 2, \ldots$. In the other subtype (type $N/2$), $g = sN + N/2$ for $s = 0, 1, 2, \ldots$. The latter ones occur only for systems with an even number of planets. Table 3.4 shows that the type 0 purely ring modes evolve into rotational modes and the type $N/2$ purely ring modes evolve into planet modes when gyroscopic effects are introduced. Section 3.6.2 details this evolution of purely ring modes.

3.5 Generalization of Modal Properties to Planetary Gears with Arbitrary Number of Equally-Spaced Planets

The gyroscopic rotational, translational, and planet modes result from the cyclic symmetry of planetary gears. Shi and Parker [92] proved the modal structure for general lumped-parameter cyclically symmetric systems with central components having planar vibrations. That derivation was extended to central components with general rigid-body motions [93]. This work applies their proof to planetary gears with an elastic ring.

Figure 3.5 shows decompositions of a planetary gear into substructures and central components. The elastic ring is divided into N identical sectors such that the n-th sector has the domain $D_n = \{\theta | \theta_0 + \psi_n \leq \theta < \theta_0 + \psi_{n+1}\}$. Without loss of generality, $\theta_0 = 0$. Each ring sector, its connecting planet, and the ring-planet mesh stiffness connecting them compose of a substructure (Fig. 3.5b). The first substructure is the one that has the first planet and ring sector in it. The sun, carrier, and ring rigid body are central components. Substructures connect to the central components through sun-planet mesh stiffnesses for the sun, carrier-planet bearing stiffnesses for the carrier, and elastic foundation stiffnesses for the ring rigid body.

To use the proof in [92], all ring sectors are identically discretized with an arbitrary discretization method (Fig. 3.5). An example uniform finite difference discretization of the

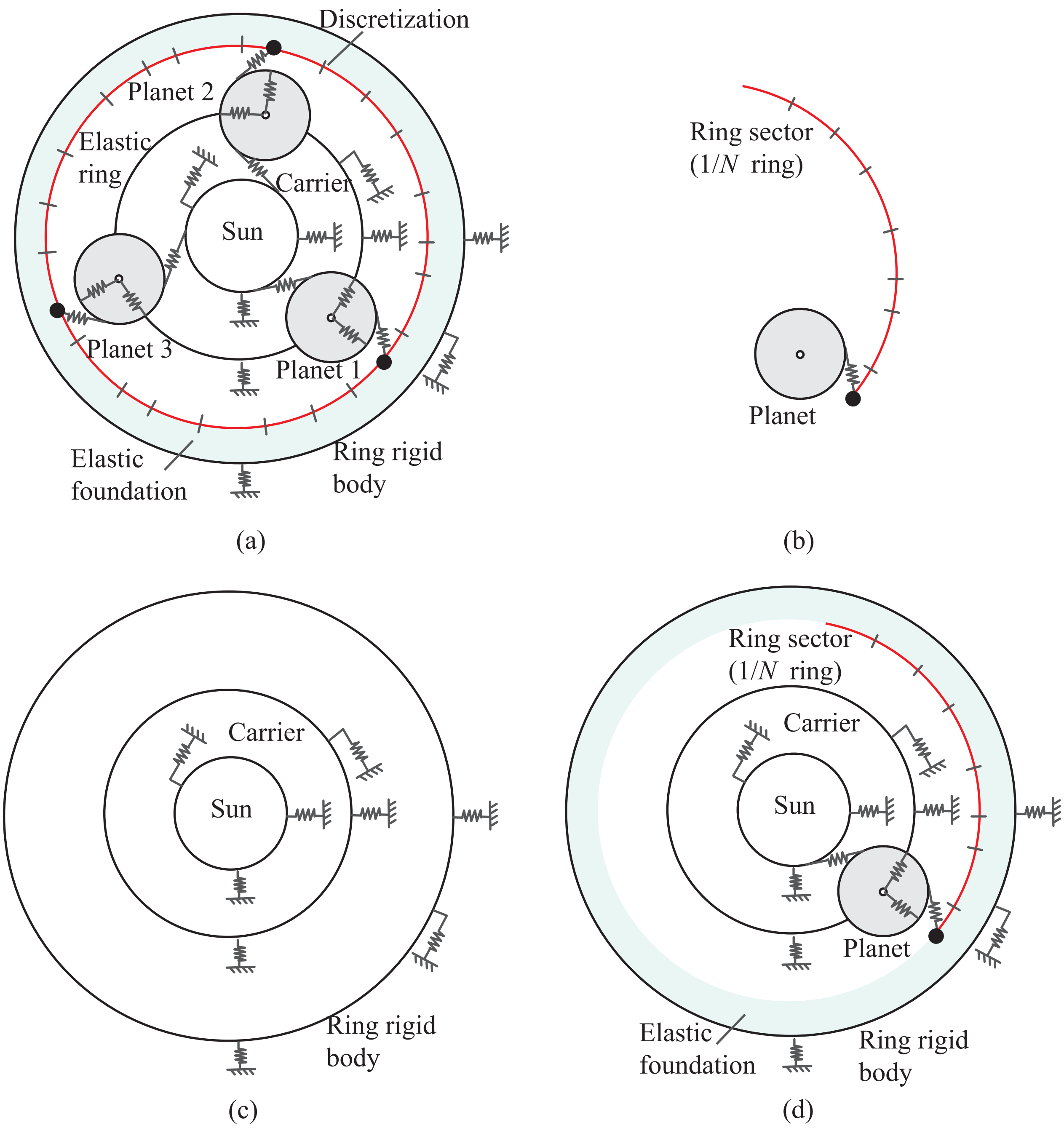

Figure 3.5: Planetary gears as a cyclically symmetric structure with central components in (a). The substructure, central components, and coupling between them are illustrated in (b-d), respectively.

first and second derivatives of $u(\theta)$ with respect to θ is given as

$$\frac{\partial u}{\partial \theta} = \frac{u(\theta_{i+1}) - u(\theta_i)}{\Delta\theta}, \qquad \frac{\partial^2 u}{\partial \theta^2} = \frac{u(\theta_{i+1}) - 2u(\theta_i) + u(\theta_{i-1})}{\Delta\theta^2}, \tag{3.11}$$

where $\Delta\theta$ is the step size. The finite difference discretization of the first and second derivatives of $v(\theta)$ and $\beta(\theta)$ with respect to θ is similar. For compact notation, $u(\theta_i)$ is subsequently replaced by u_i.

The eigenvalue problem of discretized equations for the elastic ring together with equations for the sun, carrier, ring rigid body, and planets, is represented as

$$\lambda^2[\mathbf{M}]^*\boldsymbol{\phi} + \lambda[\mathbf{G}]^*\boldsymbol{\phi} + ([\mathbf{K}]^* - [\mathbf{C}]^*)\boldsymbol{\phi} = \mathbf{0} \tag{3.12a}$$

$$[\mathbf{M}]^* = \begin{bmatrix} [\mathbf{M}_c] & [\mathbf{M}_{cs}] \\ [\mathbf{M}_{cs}]^T & [\mathbf{M}_s] \end{bmatrix}, \qquad [\mathbf{G}]^* = \begin{bmatrix} [\mathbf{G}_c] & [\mathbf{G}_{cs}] \\ -[\mathbf{G}_{cs}]^T & [\mathbf{G}_s] \end{bmatrix},$$

$$[\mathbf{K}]^* = \begin{bmatrix} [\mathbf{K}_c] & [\mathbf{K}_{cs}] \\ [\mathbf{K}_{cs}]^T & [\mathbf{K}_s] \end{bmatrix}, \qquad [\mathbf{C}]^* = \begin{bmatrix} [\mathbf{C}_c] & [\mathbf{C}_{cs}] \\ [\mathbf{C}_{cs}]^T & [\mathbf{C}_s] \end{bmatrix}. \tag{3.12b}$$

The mass matrix $[\mathbf{M}]^*$ and stiffness matrix $[\mathbf{K}]^*$ correspond to the mass operator $\mathbf{M}$ and stiffness operator $\mathbf{K}$ in Eq. (3.4), and the gyroscopic matrix $[\mathbf{G}]^*$ and centripetal matrix $[\mathbf{C}]^*$ correspond to the gyroscopic operator $\Omega_r\mathbf{G}_r + \Omega_c\mathbf{G}_c$ and centripetal operator $\Omega_r^2\mathbf{C}_r + \Omega_c^2\mathbf{C}_c + 2\Omega_r\Omega_c\mathbf{C}_{rc}$. The subscripts c and s indicate that the submatrices associate with the central components, substructures or both of them. The eigenvector $\boldsymbol{\phi}$ associated with the eigenvalue λ is

$$\boldsymbol{\phi} = \begin{bmatrix} \boldsymbol{\phi}_c^T & \boldsymbol{\phi}_s^T \end{bmatrix}^T, \tag{3.13a}$$

$$\boldsymbol{\phi}_c = \begin{bmatrix} \mathbf{p}_s^T & \mathbf{p}_c^T & \mathbf{p}_b^T \end{bmatrix}^T, \qquad \mathbf{p}_h = \begin{bmatrix} x_h & y_h & u_h \end{bmatrix}, \qquad h = s, c, b, \tag{3.13b}$$

$$\boldsymbol{\phi}_s = \begin{bmatrix} \boldsymbol{\phi}_1^T & \boldsymbol{\phi}_2^T & \dots & \boldsymbol{\phi}_N^T \end{bmatrix}^T,$$

$$\boldsymbol{\phi}_n = \begin{bmatrix} \mathbf{p}_n^T & (\boldsymbol{\varphi}_n^{(1)})^T & (\boldsymbol{\varphi}_n^{(2)})^T & \dots & (\boldsymbol{\varphi}_n^{(M)})^T \end{bmatrix}^T, \qquad n = 1, 2, \dots, N,$$

$$\mathbf{p}_n = \begin{bmatrix} \zeta_n & \eta_n & u_n \end{bmatrix}^T, \qquad \boldsymbol{\varphi}_n^{(m)} = \begin{bmatrix} u_n^{(m)} & v_n^{(m)} & \beta_n^{(m)} \end{bmatrix}^T, \qquad m = 1, 2, \dots, M, \tag{3.13c}$$

where M is the total number of discretized points in each ring sector. The vector $\boldsymbol{\varphi}_n^{(m)}$ includes radial deflection ($u_n^{(m)}$), tangential deflection ($v_n^{(m)}$), and cross-sectional rotational angle ($\beta_n^{(m)}$) at the m-th discretized point in the n-th ring sector.

A compact form of Eq. (3.12) is

$$\mathbf{A}^* \boldsymbol{\phi} = \mathbf{0}, \tag{3.14a}$$

$$\mathbf{A}^* = \begin{bmatrix} \mathbf{A}_c & \mathbf{A}_{cs} \\ \mathbf{A}_{sc} & \mathbf{A}_s \end{bmatrix} = \lambda^2[\mathbf{M}]^* + \lambda[\mathbf{G}]^* + ([\mathbf{K}]^* - [\mathbf{C}]^*). \tag{3.14b}$$

We now demonstrate the submatrices $\mathbf{A}_c$, $\mathbf{A}_s$, and $\mathbf{A}_{cs}$ in Eq. (3.14) have the structure considered in [92].

The matrix $\mathbf{A}_c$ is only associated with the translations and rotations of the sun, carrier, and ring rigid body. No discretized ring deflections are involved. Therefore, the property of $\mathbf{A}_c$ discussed in [92] holds here.

The substructure system (which includes the discretized ring and all the planets) is cyclically symmetric. The matrix $\mathbf{A}_s$ has the same block circulant structure as that in [92].

The matrix $\mathbf{A}_{cs}$ can be expressed as

$$\mathbf{A}_{cs} = \begin{bmatrix} \mathbf{A}_{cs}^{(1)} & \mathbf{A}_{cs}^{(2)} & \dots & \mathbf{A}_{cs}^{(N)} \end{bmatrix}, \tag{3.15}$$

where each $9 \times 3(M+1)$-dimensional matrix $\mathbf{A}_{cs}^{(n)}$ captures the coupling between the central components and n-th substructure. The submatrix $\mathbf{A}_{cs}^{(n)}$ has the form

$$\mathbf{A}_{cs}^{(n)} = \begin{bmatrix} \mathbf{B}_{sp}^{(n)} & \mathbf{B}_{s1}^{(n)} & \dots & \mathbf{B}_{sM}^{(n)} \\ \mathbf{B}_{cp}^{(n)} & \mathbf{B}_{c1}^{(n)} & \dots & \mathbf{B}_{cM}^{(n)} \\ \mathbf{B}_{bp}^{(n)} & \mathbf{B}_{b1}^{(n)} & \dots & \mathbf{B}_{bM}^{(n)} \end{bmatrix}, \tag{3.16}$$

where $\mathbf{B}_{hp}^{(n)}$ and $\mathbf{B}_{hm}^{(n)}$ for $h = s, c, b$ represent the coupling of each central component (the sun, carrier, and ring rigid body) with the n-th planet and the m-th discretized point in the n-th ring sector. We now show the following property in [92]

$$\mathbf{A}_{cs}^{(n)} = \mathrm{diag}(\mathbf{R}_n, \mathbf{R}_n, \dots, \mathbf{R}_n)\mathbf{A}_{cs}^{(1)}, \tag{3.17a}$$

$$\mathbf{R}_n = \begin{bmatrix} \cos\psi_n & -\sin\psi_n & 0 \\ \sin\psi_n & \cos\psi_n & 0 \\ 0 & 0 & 1 \end{bmatrix} \tag{3.17b}$$

still holds here.

Ref. [92] presented the following property

$$\mathbf{B}_{hp}^{(n)} = \mathbf{R}_n \mathbf{B}_{hp}^{(1)}, \qquad h = s, c, b. \tag{3.18}$$

The sun and carrier do not directly interact with the elastic ring, indicating $\mathbf{B}_{sm}^{(n)} = \mathbf{B}_{cm}^{(n)} = \mathbf{0}$ for $m = 1, 2, \dots N$. The matrix $\mathbf{B}_{bm}^{(n)}$ is expressed as

$$\mathbf{B}_{bm}^{(n)} = \lambda^2 \mathbf{M}_{bm}^{(n)} + \lambda \mathbf{G}_{bm}^{(n)} + (\mathbf{K}_{bm}^{(n)} - \mathbf{C}_{bm}^{(n)}) \tag{3.19}$$

where $\mathbf{M}_{bm}^{(n)} = \mathbf{G}_{bm}^{(n)} = \mathbf{C}_{bm}^{(n)} = \mathbf{0}$ because the motion of the ring rigid body does not couple the elastic ring deformation in the mass, gyroscopic, and centripetal operators in Eq. (3.4). The matrix $\mathbf{K}_{bm}^{(n)}$ has the expression

$$\mathbf{K}_{bm}^{(n)} = \begin{bmatrix} -k_u \cos\theta_m^{(n)} & k_v \sin\theta_m^{(n)} & 0 \\ -k_u \sin\theta_m^{(n)} & -k_v \cos\theta_m^{(n)} & 0 \\ 0 & -k_v/R_b & 0 \end{bmatrix}. \tag{3.20}$$

This matrix satisfies $\mathbf{K}_{bm}^{(n)} = \mathbf{R}_n \mathbf{K}_{bm}^{(1)}$ with $\theta_m^{(n)} = \theta_m^{(1)} + \psi_n$. Therefore, the property of $\mathbf{A}_{cs}$ in Eq. (3.17) holds.

The matrices $\mathbf{A}_c$, $\mathbf{A}_s$, and $\mathbf{A}_{cs}$ have the same properties as those in [92]. The vibration mode structure for general lumped-parameter cyclically symmetric systems with central components derived in [92] applies, therefore. According to Ref. [92], rotational modes with type (or phase index [92]) $d = 0$, translational modes with type $d = 1$ and $d = N - 1$, and substructure (planet) modes with type $d = 2, 3, \ldots, N-2$ result for the planetary gear system. For each phase index d, the substructure degrees of freedom have the form

$$\boldsymbol{\phi}_s = \begin{bmatrix} \underbrace{e^{jd\psi_1}\hat{\boldsymbol{\phi}}_s^T}_{\boldsymbol{\phi}_1} & \underbrace{e^{jd\psi_2}\hat{\boldsymbol{\phi}}_s^T}_{\boldsymbol{\phi}_2} & \cdots & \underbrace{e^{jd\psi_N}\hat{\boldsymbol{\phi}}_s^T}_{\boldsymbol{\phi}_N} \end{bmatrix}^T, \tag{3.21}$$

where $\boldsymbol{\phi}_n$ is a vector of the degrees of freedom for the n-th substructure, $\hat{\boldsymbol{\phi}}_s$ has dimension equal to the number of degrees of freedom for a single substructure, and $\hat{\boldsymbol{\phi}}_s = \boldsymbol{\phi}_1$ due to $\psi_n = 2\pi(n-1)/N$.

Therefore, the radial deflection at $\theta + \psi_n$ in the n-th ring sector relates to that at θ in the first sector according to

$$u(\theta + \psi_n) = e^{jd\psi_n} u(\theta). \tag{3.22}$$

Use of Eq. (3.7) gives

$$u(\theta) = \sum_{l=-L_b}^{L_b} a_l e^{jl\theta}, \qquad u(\theta + \psi_n) = \sum_{l=-L_b}^{L_b} a_l e^{jl\theta} e^{jl\psi_n}. \tag{3.23}$$

Substitution of Eq. (3.23) into Eq. (3.22) yields

$$a_l = 0, \qquad \text{for } l \neq sN + d, \tag{3.24}$$

where $s = 0, \pm 1, \pm 2, \ldots$. Thus, for type d gyroscopic modes, the ring radial deflection $u(\theta)$ has only $sN + d$ nodal diameter components. The same conclusion results for the ring tangential deflection $v(\theta)$ and cross-sectional rotation angle $\beta(\theta)$. A modal combination of the discrete motions of the sun, carrier, ring rigid body, and planets (resulting from the proof in Ref. [92]) and the elastic ring deformations for each phase index d gives the modal structure for the gyroscopic elastic-discrete system. A summary of the modal structure is given in Table 3.5.

The distinctive modal properties can be used for mode identification in dynamic responses. For example, if a resonant mode for a five-planet system has dominant four nodal diameter ring deformation (i.e., $e^{\pm j4\theta}$), this mode is a translational mode with phase index $d = 1$ or $d = 4$. Zero amplitudes of the rotations for the central components are expected.

3.6 Evolution of Vibration Modes due to Gyroscopic Effects

Purely ring modes of stationary planetary gears disappear when gyroscopic effects are introduced. Degenerate translational and planet natural frequencies (multiplicity two) of

Table 3.5: Modal structure of gyroscopic planetary gears with an elastic ring and N equally-spaced planets. The subscripts $h = s, c, b$ and $n = 1, 2, \ldots, N$, and the deflection for the first planet $\mathbf{p}_1 = [\zeta_1 \ \eta_1 \ u_1]^T$. All the modal deflection quantities are in general complex-valued.

Mode type	Phase index	Modal representation
Rotational	0	$\boldsymbol{w} = \sum_{s=-\infty}^{\infty} \begin{bmatrix} a_{sN} & b_{sN} & c_{sN} \end{bmatrix}^T e^{jsN\theta},$ $\mathbf{p}_h = \begin{bmatrix} 0 & 0 & u_h \end{bmatrix}^T, \qquad \mathbf{p}_n = \mathbf{p}_1$
Translational	1	$\boldsymbol{w} = \sum_{s=-\infty}^{\infty} \begin{bmatrix} a_{sN+1} & b_{sN+1} & c_{sN+1} \end{bmatrix}^T e^{j(sN+1)\theta}$ $\mathbf{p}_h = \begin{bmatrix} x_h & jx_h & 0 \end{bmatrix}^T, \qquad \mathbf{p}_n = e^{j\psi_n}\mathbf{p}_1$
	$N-1$	$\boldsymbol{w} = \sum_{s=-\infty}^{\infty} \begin{bmatrix} a_{sN-1} & b_{sN-1} & c_{sN-1} \end{bmatrix}^T e^{j(sN-1)\theta}$ $\mathbf{p}_h = \begin{bmatrix} x_h & -jx_h & 0 \end{bmatrix}^T, \qquad \mathbf{p}_n = e^{-j\psi_n}\mathbf{p}_1$
Planet	$d \in \{2, \ldots, N-2\}$	$\boldsymbol{w} = \sum_{s=-\infty}^{\infty} \begin{bmatrix} a_{sN+d} & b_{sN+d} & c_{sN+d} \end{bmatrix}^T e^{j(sN+d)\theta}$ $\mathbf{p}_h = \begin{bmatrix} 0 & 0 & 0 \end{bmatrix}^T, \qquad \mathbf{p}_n = e^{jd\psi_n}\mathbf{p}_1$

stationary planetary gears split due to the gyroscopic effects (Fig. 3.6). The degenerate translational modes for stationary systems have only one type that is associated with both phase indices 1 and $N-1$, while the gyroscopic translational modes have two different subtypes with each of phase index 1 or $N-1$, not both of them. Whether a pair of degenerate

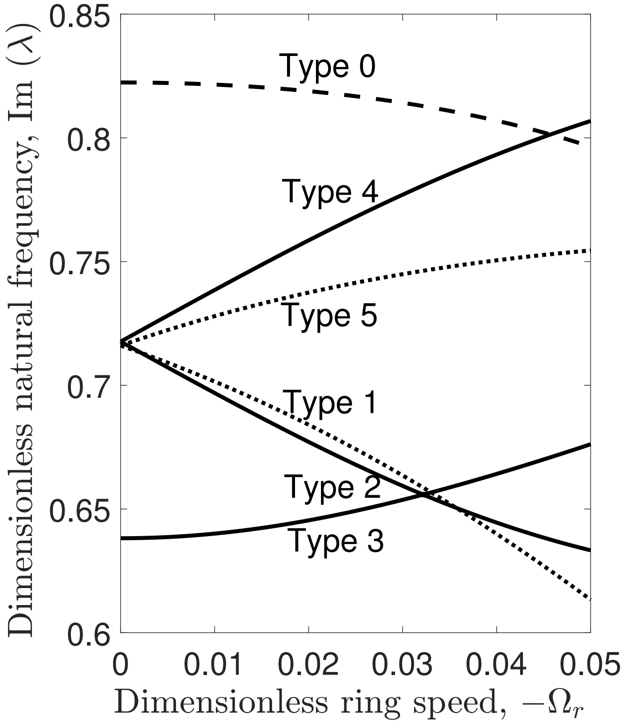

Figure 3.6: Eigenvalue loci of a six-planet system with parameters in Table 3.3 for varying ring speed. The dashed, dotted, and solid lines represent rotational, translational, and planet natural frequencies, respectively.

translational modes splits into two modes of the same subtype or different subtypes is unclear. The same question arises for the splitting of the degenerate planet modes. This section discusses the evolution of these distinct modes and degenerate modes with multiplicity two using eigenvalue perturbation approaches from Ref. [101, 102].

3.6.1 Perturbation Analysis

Considering evolution from zero to non-zero speeds, we let $\Omega_c = \epsilon\hat{\Omega}_c$ and $\Omega_r = \epsilon\hat{\Omega}_r$, where ϵ is a small parameter and $\hat{\Omega}_c$ and $\hat{\Omega}_r$ are $O(1)$. Eq. (3.4) becomes

$$\lambda^2\mathbf{M}\boldsymbol{\chi} + \epsilon\lambda\mathbf{G}\boldsymbol{\chi} + \mathbf{K}\boldsymbol{\chi} - \epsilon^2\mathbf{C}\boldsymbol{\chi} = \mathbf{0}, \tag{3.25}$$

$$\mathbf{G} = \hat{\Omega}_r\mathbf{G}_r + \hat{\Omega}_c\mathbf{G}_c, \qquad \mathbf{C} = \hat{\Omega}_r^2\mathbf{C}_r + \hat{\Omega}_c^2\mathbf{C}_c + 2\hat{\Omega}_r\hat{\Omega}_c\mathbf{C}_{rc}.$$

The eigenvalues and eigenvectors of Eq. (3.25) are expressed as

$$\lambda_i = \hat{\lambda}_i + \epsilon\mu_i + O(\epsilon^2), \qquad \boldsymbol{\chi}_i = \boldsymbol{\chi}_i^{(0)} + \epsilon\boldsymbol{\chi}_i^{(1)} + O(\epsilon^2), \qquad i = 1, 2, \ldots. \tag{3.26}$$

Solving Eq. (3.8) with $\Omega_r = \Omega_c = 0$ (i.e., $\epsilon = 0$) gives the eigenvalue $\hat{\lambda}_i$ and real-valued eigenvector $\boldsymbol{\chi}_i^{(0)}$. We normalize $\boldsymbol{\chi}_i^{(0)}$ with $\langle\boldsymbol{\chi}_i^{(0)},\ \mathbf{M}\boldsymbol{\chi}_i^{(0)}\rangle = 1$.

Following the perturbation approach in [101, 102], the first-order eigenvalue and eigenvector perturbation (μ_i, $\boldsymbol{\chi}_i^{(1)}$) for a pair of distinct eigenvalue and eigenvector ($\hat{\lambda}_i$, $\boldsymbol{\chi}_i^{(0)}$) is given as

$$\mu_i = -\frac{1}{2}\langle\boldsymbol{\chi}_i^{(0)},\ \mathbf{G}\boldsymbol{\chi}_i^{(0)}\rangle \tag{3.27a}$$

$$\boldsymbol{\chi}_i^{(1)} = \sum_{k\neq i}\nu_{ki}\boldsymbol{\chi}_k^{(0)}, \tag{3.27b}$$

$$\nu_{ki} = \frac{\hat{\lambda}_i}{\hat{\lambda}_k^2 - \hat{\lambda}_i^2}\langle\boldsymbol{\chi}_k^{(0)},\ \mathbf{G}\boldsymbol{\chi}_i^{(0)}\rangle, \qquad k \neq i. \tag{3.27c}$$

For a degenerate eigenvalue $\hat{\lambda}_i = \hat{\lambda}_{i+1}$ with multiplicity two, the unperturbed eigenvectors $\boldsymbol{\chi}_i^{(0)}$ and $\boldsymbol{\chi}_{i+1}^{(0)}$ are linear combinations of any set of linearly independent eigenvectors $\boldsymbol{\chi}_{il}^{(0)}$ ($l = 1, 2$) associated with this degenerate value. In addition to the normalization mentioned above, these $\boldsymbol{\chi}_{il}^{(0)}$ are made orthogonal with respect to $\mathbf{M}$ such that $\langle \boldsymbol{\chi}_{i1}^{(0)}, \mathbf{M}\boldsymbol{\chi}_{i2}^{(0)} \rangle = 0$. Using the perturbation approach for degenerate eigenvalues in [101, 102] gives the first order eigenvalue perturbations μ_i and μ_{i+1} , the unperturbed eigenvectors $\boldsymbol{\chi}_i^{(0)}$ and $\boldsymbol{\chi}_{i+1}^{(0)}$, and the first order eigenvector perturbations $\boldsymbol{\chi}_i^{(1)}$ and $\boldsymbol{\chi}_{i+1}^{(1)}$ associated with this degenerate eigenvalue $\hat{\lambda}_i$. They are

$$\mu_i = j\frac{1}{2}\langle \boldsymbol{\chi}_{i1}^{(0)},\ \mathbf{G}\boldsymbol{\chi}_{i2}^{(0)} \rangle, \qquad \mu_{i+1} = -j\frac{1}{2}\langle \boldsymbol{\chi}_{i1}^{(0)},\ \mathbf{G}\boldsymbol{\chi}_{i2}^{(0)} \rangle, \tag{3.28a}$$

$$\boldsymbol{\chi}_i^{(0)} = \frac{\sqrt{2}}{2}(\boldsymbol{\chi}_{i1}^{(0)} - j\boldsymbol{\chi}_{i2}^{(0)}), \qquad \boldsymbol{\chi}_{i+1}^{(0)} = \frac{\sqrt{2}}{2}(\boldsymbol{\chi}_{i1}^{(0)} + j\boldsymbol{\chi}_{i2}^{(0)}), \tag{3.28b}$$

$$\boldsymbol{\chi}_m^{(1)} = \mathbf{v}_m + \sum_{k=i\neq m}^{i+1} \nu_{km}\boldsymbol{\chi}_k^{(0)}, \qquad m = i, i+1, \tag{3.28c}$$

$$\mathbf{v}_m = \sum_{k\neq i,i+1} \nu_{km}\boldsymbol{\chi}_k^{(0)}, \qquad m = i, i+1, \tag{3.28d}$$

$$\nu_{km} = \frac{\hat{\lambda}_m}{\hat{\lambda}_k^2 - \hat{\lambda}_m^2}\langle \boldsymbol{\chi}_k^{(0)},\ \mathbf{G}\boldsymbol{\chi}_m^{(0)} \rangle, \qquad m = i, i+1,\ k \neq i, i+1, \tag{3.28e}$$

$$\nu_{km} = \frac{-\hat{\lambda}_m\langle \boldsymbol{\chi}_k^{(0)},\ \mathbf{G}\mathbf{v}_m \rangle + \langle \boldsymbol{\chi}_k^{(0)},\ \mathbf{C}\boldsymbol{\chi}_m^{(0)} \rangle}{4\hat{\lambda}_m\mu_m}, \qquad m, k = i, i+1,\ m \neq k. \tag{3.28f}$$

We now analytically evaluate Eqs. (3.27) and (3.28) to determine the evolution of distinct and degenerate modes when gyroscopic effects are introduced. This evaluation requires general representations of rotational, translational, planet, and purely ring modes for stationary planetary gears without gyroscopic effects from Ref. [21]. For distinct modes (i.e., rotational, distinct planet, and purely ring modes), these representations serve as general forms of the unperturbed eigenvectors $\boldsymbol{\chi}_i^{(0)}$. For degenerate modes (i.e., translational and degenerate planet modes), use of Eq. (3.28b) together with the representations from [21] leads to general forms of the unperturbed eigenvectors $\boldsymbol{\chi}_i^{(0)}$ and $\boldsymbol{\chi}_{i+1}^{(0)}$.

For the unperturbed distinct eigenvectors, rotational modes have phase index 0, distinct planet modes (which exist for even number of planets N) have phase index $N/2$, and, purely ring modes are associated with either phase index 0 or $N/2$ for even N. For the unperturbed eigenvectors for a pair of degenerate translational modes, one is of phase index 1 and the other is of phase index $N-1$. Similarly, one of the unperturbed eigenvectors for a pair of degenerate planet modes is associated with phase index $d \in \{2, 3, \ldots, \mathrm{int}((N-1)/2)\}$ and the other is associated with phase index $N-d$.

Each unperturbed eigenvector is associated with a phase index $d \in \{0, 1, 2 \ldots, N-1\}$. The coefficients ν_{ki} in Eq. (3.27c) for distinct mode perturbation vanish when $\boldsymbol{\chi}_k^{(0)}$ and $\boldsymbol{\chi}_i^{(0)}$ have different phase indices. Similarly, the coefficients ν_{km} in Eqs. (3.28e) and (3.28f) for degenerate mode perturbation vanish when $\boldsymbol{\chi}_k^{(0)}$ and $\boldsymbol{\chi}_m^{(0)}$ have different phase indices.

3.6.2 Evolution of Purely Ring Modes

The evolution of purely ring modes from the stationary to spinning systems follows Eq. (3.27) because they are distinct modes. Purely ring modes of phase index 0 and those of phase index $N/2$ evolve differently.

For a purely ring mode $\boldsymbol{\chi}_i^{(0)}$ with phase index 0, the coefficients ν_{ki} in Eq. (3.27c) vanish for $\boldsymbol{\chi}_k^{(0)}$ being any of a translational, planet, or purely ring mode of phase index $N/2$. Nontrivial ν_{ki} is possible only for $\boldsymbol{\chi}_k^{(0)}$ being a rotational mode or another purely ring mode of phase index 0. Therefore, the linear combination in Eq. (3.27b) that defines the eigenvector perturbation $\boldsymbol{\chi}_i^{(1)}$ contains only contributions from rotational and purely ring modes of phase index 0. The perturbed eigenvector $\boldsymbol{\chi}_i$, as a linear combination of the unperturbed purely ring mode $\boldsymbol{\chi}_i^{(0)}$ with phase index 0 and the eigenvector perturbation $\boldsymbol{\chi}_i^{(1)}$, has the structure of rotational modes in Table 3.5. Therefore, this purely ring mode of phase index 0 evolves into a rotational mode. Figure 3.7 shows an example of this evolution.

For a purely ring mode $\boldsymbol{\chi}_i^{(0)}$ with phase index $N/2$ (N even), the coefficients ν_{ki} can be

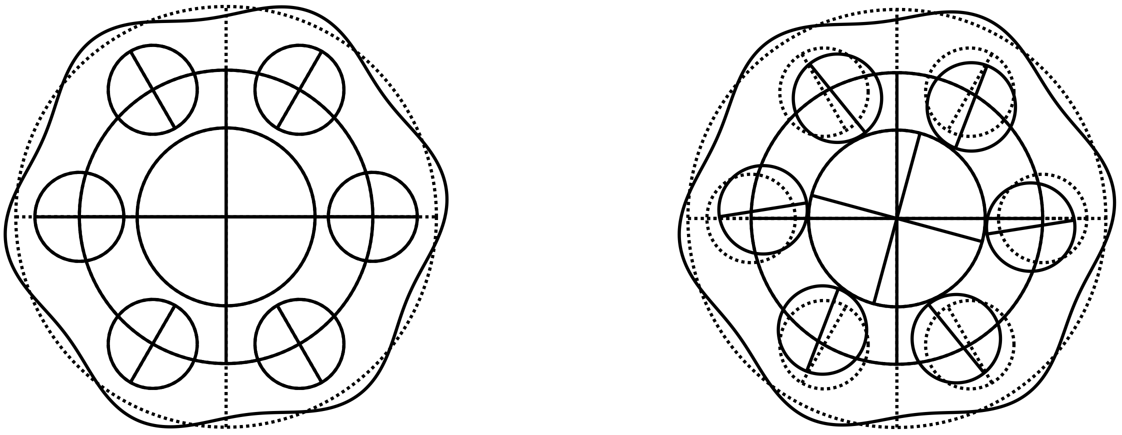

(a) (b)

Figure 3.7: (a) Purely ring mode with natural frequency ω_{21} at $\Omega_r = 0$ (without gyroscopic effect) in Table 3.4. (b) Real part of rotational mode with natural frequency ω_{20} at $\Omega_r = -0.05$ (with gyroscopic effect) in Table 3.4. The dotted lines represent undeformed positions. The ring rigid body is not shown. For visualization, the discrete deflections are amplified 20 times relative to the elastic ring deflections in both (a) and (b).

non-trivial only for $\boldsymbol{\chi}_k^{(0)}$ being a distinct planet mode or another purely ring mode of phase index $N/2$. The eigenvector perturbation $\boldsymbol{\chi}_i^{(1)}$ in Eq. (3.27b) contains only contributions from distinct planet or purely ring modes of phase index $N/2$. The linear combination of the unperturbed purely ring mode $\boldsymbol{\chi}_i^{(0)}$ with phase index $N/2$ and the eigenvector perturbation $\boldsymbol{\chi}_i^{(1)}$ in Eq. (3.26) yields the perturbed eigenvector $\boldsymbol{\chi}_i$ that has the structure of a planet mode with phase index $N/2$ in Table 3.5. Thus, this purely ring mode become a planet mode with phase index $N/2$ when gyroscopic effects are introduced. Figure 3.8 illustrates this evolution.

Physically, purely ring modes, in which the ring has fixed nodes at all ring-planet mesh locations [21], cannot exist in the gyroscopic system. Vibration modes of gyroscopic systems are traveling waves [77, 85], in which purely ring modes with fixed nodes cannot stand.

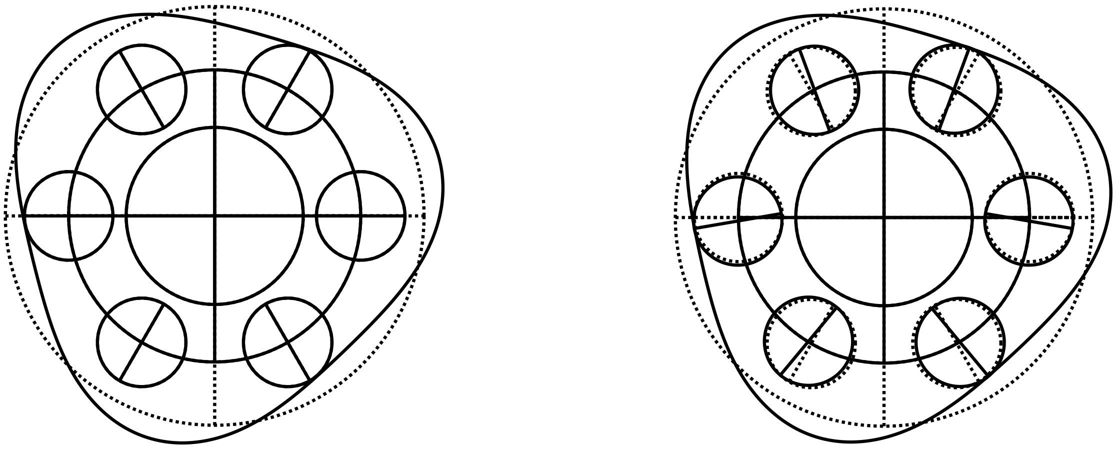

(a) (b)

Figure 3.8: (a) Purely ring mode with natural frequency ω_4 at $\Omega_r = 0$ (without gyroscopic effect) in Table 3.4. (b) Real part of planet mode with natural frequency ω_4 at $\Omega_r = -0.05$ (with gyroscopic effect) in Table 3.4. The dotted lines represent undeformed positions. The ring rigid body is not shown. For visualization, the discrete deflections are amplified 20 times relative to the elastic ring deflections in both (a) and (b).

3.6.3 Evolution of Degenerate Modes

Translational modes and planet modes with phase index other than $N/2$ are degenerate with multiplicity two for stationary systems. The evolution of these degenerate modes follows Eqs. (3.28c) – (3.28f). This section discusses first the evolution of a pair of translational modes and then the evolution of a pair of planet modes.

For a pair of degenerate translational modes $\boldsymbol{\chi}_i^{(0)}$ (phase index 1) and $\boldsymbol{\chi}_{i+1}^{(0)}$ (phase index $N-1$), only translational modes of phase index 1 contribute to the eigenvector perturbation $\boldsymbol{\chi}_i^{(1)}$ and only translational modes of phase index $N-1$ contribute to $\boldsymbol{\chi}_{i+1}^{(1)}$ because the coefficients ν_{km} in Eqs. (3.28e) and (3.28f) vanish when $\boldsymbol{\chi}_k^{(0)}$ and $\boldsymbol{\chi}_m^{(0)}$ have different phase indices. The linear combination of $\boldsymbol{\chi}_i^{(0)}$ and $\boldsymbol{\chi}_i^{(1)}$ in Eq. (3.26) gives the perturbed eigenvector $\boldsymbol{\chi}_i$ having phase index 1. According to the modal structure in Table 3.5, $\boldsymbol{\chi}_i$ is a translational mode of phase index 1. Similarly, the linear combination of $\boldsymbol{\chi}_{i+1}^{(0)}$ and $\boldsymbol{\chi}_{i+1}^{(1)}$ in Eq. (3.26) results in a translational mode $\boldsymbol{\chi}_{i+1}$ of phase index $N-1$. Figure 3.6 shows a pair of degenerate translational modes splits into two gyroscopic translational modes with one of type 1 (i.e., phase index 1) and the other of type 5 for a six-planet ($N = 6$) system.

A similar analysis as for the degenerate translational mode evolution works for the evolution of degenerate planet modes. For a pair of degenerate planet modes, the unperturbed eigenvectors $\boldsymbol{\chi}_i^{(0)}$ and $\boldsymbol{\chi}_{i+1}^{(0)}$ are of phase indices d and $N-d$ respectively, where $d \in \{2, 3, \ldots, \text{int}((N-1)/2)\}$. The unperturbed eigenvector $\boldsymbol{\chi}_i^{(0)}$ evolves into a planet mode $\boldsymbol{\chi}_i$ of phase index d, and $\boldsymbol{\chi}_{i+1}^{(0)}$ evolves into a planet mode $\boldsymbol{\chi}_{i+1}$ of phase index $N-d$. Figure 3.6 demonstrates a pair of degenerate planet modes splits into two gyroscopic planet modes with one of type 2 and the other of type 4 for a six-planet ($N = 6$) system.

3.7 Conclusions

This paper investigates the natural frequencies and vibration modes of spinning planetary gears with equally-spaced planets and a deformable ring. An analytical model is used with the sun, carrier, and planets modeled as rigid bodies coupled to an elastic ring having bending deformation, extensional deformation, shear deformation, rotary inertia, and a concentrated tooth bending moment resulting from each ring-planet mesh force acting at a contact point radially away from the ring neutral axis. Gyroscopic and centripetal effects from carrier and ring rotation are included. Any of the sun, carrier, or ring can be stationary, or all three can spin. Natural frequencies and vibration modes are numerically calculated from the analytical model, and the results agree well with those from a finite element/contact mechanics model.

The centripetal effects, ring extensional and shear effects, effects of ring rotary inertia, and effects of concentrated tooth bending moments do not alter the modal structure of planetary gears defined in [21], but the gyroscopic effects do. Vibration modes for stationary systems without gyroscopic effects are real-valued standing wave modes, while those for spinning systems are complex-valued traveling wave modes. There exist only four types of modes for stationary systems, i.e., rotational, translational, planet, and purely ring modes, while only three types of modes exist for spinning systems: rotational, translational, and planet modes. Planet modes only exist for systems with four or more planets no matter the systems are stationary or spinning.

Rotational modes for stationary and spinning systems are similar except that rotational modes for stationary systems are real-valued while those for spinning systems are complex-valued. Translational modes for stationary systems are degenerate with multiplicity two and cannot be classified into different subtypes. In contrast, translational modes for spinning systems are distinct in general and can be classified into two different subtypes. Both distinct and degenerate (multiplicity two) planet modes can exist for stationary systems. The distinct planet modes exist only for systems with even number of planets and they have only one type. The degenerate planet modes exist only for systems with five or more planets and they can have different subtypes depending on the number of planets. Planet modes for spinning systems are distinct in general and different subtypes can exist depending on the number of planets.

For spinning systems, each type/subtype of modes are associated with a phase index. The elastic ring deformation has unique nodal diameter components associated with each phase index. The planet deflections have unique phase relationships between different planets for each phase index.

Purely ring modes, present in stationary planetary gears, evolve into rotational or one subtype of planet modes when gyroscopic effects are introduced. Degenerate translational or planet modes with multiplicity two for stationary planetary gears split into two different subtypes of translational or planet modes, respectively.

Chapter 4

Parametric Instability of Spinning Planetary Gears with a Deformable Ring

4.1 Introduction

The primary source of gear vibration is changing mesh interaction as gear rotates. This change is modeled as time-varying mesh stiffness that parametrically excites the gear system.

Parametric instabilities, in general, occur when the excitation frequency or one of its harmonics is near twice a natural frequency or combinations of two natural frequencies. Not every pair of modes can cause parametric instabilities in planetary gears, however. Lin and Parker [43] revealed that certain parametric instabilities vanish under particular mesh phasing conditions regardless of any form of mesh stiffness variations when analyzing parametric instabilities of lumped-parameter planetary gears with a purely rotational model.

Parker and Wu [44] derived an instability existence rule for any two modes (which can be the same) in their study of parametric instabilities of planetary gears with an elastic ring. The instability existence rule depends only on mesh phasing parameters (i.e., sun/ring tooth number and number of planets) and the mode types defined in [21] for stationary planetary gears with a deformable ring. Both of these two studies [43, 44] used stationary models without gyroscopic (i.e., Coriolis) and centripetal effects that arise from carrier and/or ring gear rotation.

This work investigates parametric instabilities of spinning planetary gears with an elastic ring and equally-spaced planets. We adopt the elastic-discrete model from Chapter 2 that includes gyroscopic and centripetal effects from carrier and ring rotation. By using the method of multiple scales and the structured modal properties defined in Chapter 3 for spinning planetary gears with an elastic ring, closed-form expressions for instability boundaries are derived, and an instability existence rule is revealed.

4.2 Mathematical Formulation

Details of the model in Fig. 4.1 including dimensional parameters and variables, nondimensionalization, and equations of motion are given in Chapter 2 and adopted here. The elastic ring has radial ($u(\theta,t)$) and tangential ($v(\theta,t)$) deformation of the ring neutral axis and cross-sectional rotation angle ($\beta(\theta,t)$). These ring deformations are collected into a vector as $\boldsymbol{w} = [u\ v\ \beta]^T$.

The deflection of the whole system is represented by the extended vector

$$\boldsymbol{\chi}(\theta,t) = [\boldsymbol{w}(\theta,t)^T,\ \mathbf{q}(t)] \tag{4.1}$$

with the vector $\mathbf{q}(t)$ given as

$$\mathbf{q} = [\ \underbrace{x_b\ y_b\ u_b}_{\mathbf{p}_b}\ \underbrace{x_c\ y_c\ u_c}_{\mathbf{p}_c}\ \underbrace{x_s\ y_s\ u_s}_{\mathbf{p}_s}\ \underbrace{\zeta_1\ \eta_1\ u_1}_{\mathbf{p}_1}\ \cdots\ \underbrace{\zeta_N\ \eta_N\ u_N}_{\mathbf{p}_N}\ ]^T,$$

where $\mathbf{p}_l$ for $l = b, c, s, 1, \ldots, N$ represent discrete motions of the ring rigid body (which is depicted by the largest circle in Fig. 4.1), carrier, sun, and planets. Refer to Chapter 2 for more details of this ring rigid body. The carrier and ring gear have speeds Ω_c and Ω_r, respectively. Speeds of the sun and planets can be derived from kinematics. The N planets are identical and equally spaced. Without loss of generality, the first planet is positioned at $\psi_1 = 0$ relative to the rotating basis vector $\mathbf{E}_1$ fixed to the carrier (Fig. 4.1). The n-th planet has an angular position of $\psi_n = 2\pi(n-1)/N$, therefore.

The sun-planet and ring-planet mesh stiffnesses change periodically with mesh frequency ω_m. They parametrically excite the planetary gear system. Dimensionless sun-planet and ring-planet mesh stiffnesses for the n-th planet are represented as

$$k_{sn}(t) = k_{sp} + k_{1n}(t), \qquad k_{rn}(t) = k_{rp} + k_{2n}(t), \tag{4.2}$$

where k_{sp}, k_{rp} are mean values and $k_{1n}(t)$, $k_{2n}(t)$ are mesh stiffness variations with zero means. Fourier series representations of $k_{1n}(t)$, $k_{2n}(t)$ are

$$k_{1n}(t) = 2\mu k_{sp} \sum_{L=1}^{\infty} [C_{sn}^{(L)} e^{jL\omega_m t} + c.c.] \tag{4.3a}$$

$$k_{2n}(t) = 2\epsilon k_{rp} \sum_{L=1}^{\infty} [C_{rn}^{(L)} e^{jL\omega_m t} + c.c.] \tag{4.3b}$$

where $2\mu k_{sp}$ and $2\epsilon k_{rp}$ are peak-to-peak values of $k_{1n}(t)$ and $k_{2n}(t)$. The complex-valued Fourier coefficients $C_{sn}^{(L)}$ and $C_{rn}^{(L)}$ are the L-th harmonics of the sun-planet and ring-planet

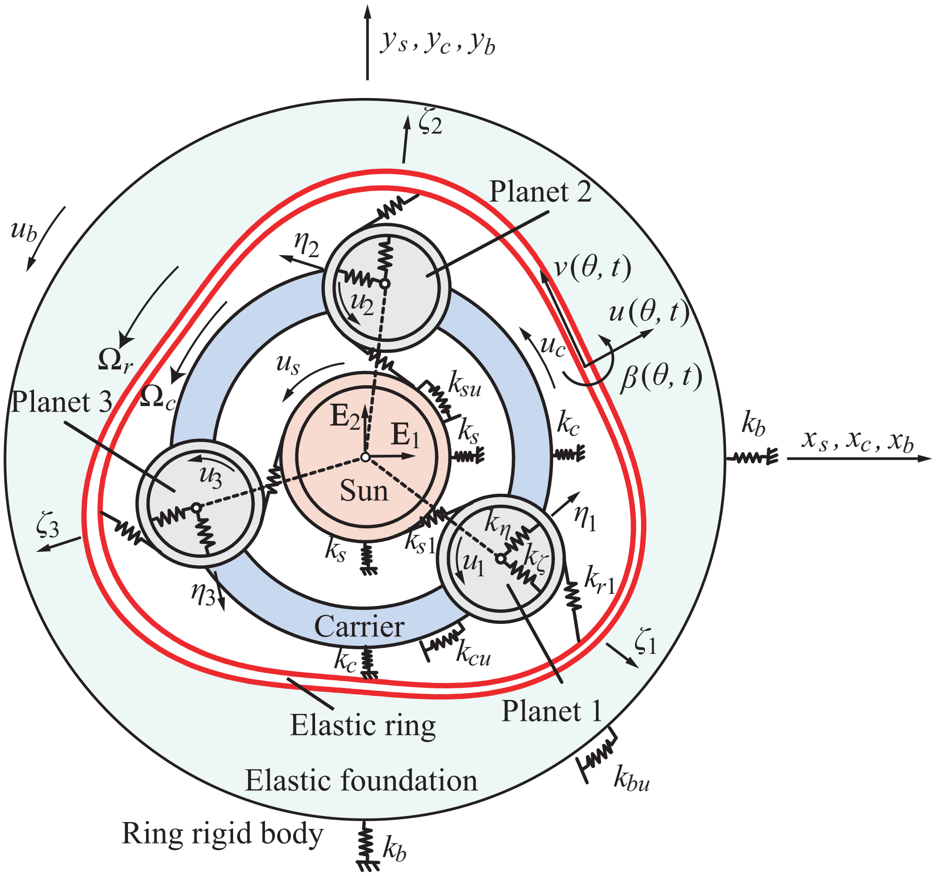

Figure 4.1: Schematic of a planetary gear model with a deformable ring.

mesh stiffnesses for the n-th planet normalized by the peak-to-peak values, respectively. The term *c.c.* represents the complex conjugate of its preceding term.

The sun-planet and ring-planet mesh stiffnesses between planets differ only by a time translation, that is,

$$k_{sn}(t) = k_{s1}(t - \gamma_{sn} T_m), \qquad k_{rn}(t) = k_{r1}(t - \gamma_{rn} T_m), \tag{4.4}$$

where $T_m = 2\pi/\omega_m$ denotes mesh period and γ_{sn} (γ_{rn}) is the mesh phase between the n-th and first sun-planet (ring-planet) meshes. In Chapter 2, we show

$$\gamma_{sn} = Z_s\psi_n/(2\pi), \quad \gamma_{rn} = -Z_r\psi_n/(2\pi) \tag{4.5}$$

for counter-clockwise rotation of the carrier relative to the ring gear (i.e., $\Omega_c > \Omega_r$) and

$$\gamma_{sn} = -Z_s\psi_n/(2\pi), \quad \gamma_{rn} = Z_r\psi_n/(2\pi) \tag{4.6}$$

for clockwise rotation of the carrier relative to the ring gear (i.e., $\Omega_c < \Omega_r$), where Z_s and Z_r are the sun and ring gear tooth numbers. The relation $\gamma_{sn} = \gamma_{rn}$ holds for equally-spaced systems [87]. With the phase relations in Eq. (4.4), the Fourier coefficients $C_{sn}^{(L)}$, $C_{rn}^{(L)}$ between different planets are related by

$$C_{sn}^{(L)} = C_{s1}^{(L)} e^{-j2\pi L\gamma_{rn}}, \qquad C_{rn}^{(L)} = C_{r1}^{(L)} e^{-j2\pi L\gamma_{rn}}. \tag{4.7}$$

The ratios of the amplitudes of sun-planet and ring-planet mesh stiffness variations to their mean values are μ and ϵ. We assume μ is of the same order as ϵ, i.e., $\mu = g\epsilon$, where $g = O(1)$. To facilitate the following perturbation analysis, ϵ is assumed to be small. This assumption is verified by comparing the analytical perturbation results with numerical results.

The dimensionless equation of motion for the time-varying planetary gear system from Chapter 2 is

$$\mathbf{M}\ddot{\boldsymbol{\chi}} + (\Omega_r\mathbf{G}_r + \Omega_c\mathbf{G}_c)\dot{\boldsymbol{\chi}} + (\mathbf{K}(t) - \Omega_r^2\mathbf{C}_r - \Omega_c^2\mathbf{C}_c - 2\Omega_r\Omega_c\mathbf{C}_{rc})\boldsymbol{\chi} = \mathbf{0}, \tag{4.8}$$

where $\mathbf{M}$ is extended mass operator; $\mathbf{G}_r$ and $\mathbf{G}_c$ are extended gyroscopic operators; $\mathbf{K}(t)$ is extended stiffness operator; and, $\mathbf{C}_r$, $\mathbf{C}_c$, and $\mathbf{C}_{rc}$ are extended centripetal operators. The operators $\mathbf{M}$, $\mathbf{G}_r$, $\mathbf{G}_c$, $\mathbf{C}_r$, $\mathbf{C}_c$, and $\mathbf{C}_{rc}$ are identical to those in Chapter 2. The operator $\mathbf{K}(t)$ is the same with $\mathbf{K}$ in Chapter 2 with k_{sn}, k_{rn} replaced by the time-varying sun-planet and ring-planet mesh stiffnesses $(k_{sn}(t),\ k_{rn}(t))$. The operators $\mathbf{M}$, $\mathbf{K}(t)$, $\mathbf{C}_r$, $\mathbf{C}_c$, and $\mathbf{C}_{rc}$ are self-adjoint with the inner product

$$\langle \boldsymbol{\chi}_1,\ \boldsymbol{\chi}_2\rangle = \int_0^{2\pi} \overline{\boldsymbol{w}}_1^T \boldsymbol{w}_2 \mathrm{d}\theta + \overline{\mathbf{q}}_1^T \mathbf{q}_2, \tag{4.9}$$

where the overbar denotes complex conjugate. The gyroscopic operator $\mathbf{G}_r$ and $\mathbf{G}_c$ are skew self-adjoint with respect to Eq. (4.9).

Separation of the stiffness operator $\mathbf{K}(t)$ into time-varying and time-invariant parts gives

$$\mathbf{K}(t) = \mathbf{K}_0 + 2\epsilon \sum_{L=1}^{\infty} [(\mathbf{K}_{sp}^{(L)} + \mathbf{K}_{rp}^{(L)}) e^{jL\omega_m t} + c.c.], \tag{4.10}$$

where $\mathbf{K}_0$ is the same with $\mathbf{K}(t)$ with $k_{sn}(t),\ k_{rn}(t)$ replaced by the mean values of sun-planet and ring-planet mesh stiffnesses $(k_{sp},\ k_{rp})$. The Fourier coefficient operators $\mathbf{K}_{sp}^{(L)}$ and $\mathbf{K}_{rp}^{(L)}$ have the same form as $\mathbf{K}(t)$ with substitutions that all stiffnesses other than mesh stiffnesses are zero and that sun-planet and ring-planet mesh stiffnesses for the n-th planet in $\mathbf{K}(t)$ are substituted by $gk_{sp}C_{s1}^{(L)} e^{-j2\pi L\gamma_{rn}}$ and $k_{rp}C_{r1}^{(L)} e^{-j2\pi L\gamma_{rn}}$.

Natural frequencies and vibration modes of the unperturbed time-invariant system are necessary for the parametric instability analysis. The eigenvalue problem for the unperturbed $(\epsilon \to 0)$ system of Eq. (4.8) is

$$\lambda_k^2 \mathbf{M}\boldsymbol{\chi}_k + \lambda_k(\Omega_r \mathbf{G}_r + \Omega_c \mathbf{G}_c)\boldsymbol{\chi}_k + (\mathbf{K}_0 - \Omega_r^2 \mathbf{C}_r - \Omega_c^2 \mathbf{C}_c - 2\Omega_r\Omega_c \mathbf{C}_{rc})\boldsymbol{\chi}_k = \mathbf{0}, \tag{4.11}$$

where λ_k and $\boldsymbol{\chi}_k(\theta)$ are the eigenvalue and eigenfunction of the k-th mode. The gyroscopic system gives purely imaginary eigenvalues (i.e. $\lambda_k = j\omega_k$) and complex-valued modes $\boldsymbol{\chi}_k(\theta)$ when operating at speeds below the first critical speed [100]. The eigenvalue problem in Eq. (4.11) is solved in Chapter 3.

Substitution of Eq. (4.10) into Eq. (4.8) and putting the resulting equation into state space form give

$$\mathbf{A}\dot{\boldsymbol{\phi}} + \mathbf{B}\boldsymbol{\phi} + 2\epsilon\mathbf{D}(t)\boldsymbol{\phi} = \mathbf{0}, \qquad \boldsymbol{\phi} = \begin{bmatrix} \dot{\boldsymbol{\chi}}^T & \boldsymbol{\chi}^T \end{bmatrix}^T, \tag{4.12a}$$

$$\mathbf{A} = \begin{pmatrix} \mathbf{M} & \mathbf{0} \\ \mathbf{0} & \mathbf{K}_0 - \Omega_r^2\mathbf{C}_r - \Omega_c^2\mathbf{C}_c - 2\Omega_r\Omega_c\mathbf{C}_{rc} \end{pmatrix}, \tag{4.12b}$$

$$\mathbf{B} = \begin{pmatrix} \Omega_r\mathbf{G}_r + \Omega_c\mathbf{G}_c & \mathbf{K} - \Omega_r^2\mathbf{C}_r - \Omega_c^2\mathbf{C}_c - 2\Omega_r\Omega_c\mathbf{C}_{rc} \\ -(\mathbf{K} - \Omega_r^2\mathbf{C}_r - \Omega_c^2\mathbf{C}_c - 2\Omega_r\Omega_c\mathbf{C}_{rc}) & \mathbf{0} \end{pmatrix}, \tag{4.12c}$$

$$\mathbf{D}(t) = \begin{pmatrix} \mathbf{0} & \sum_{L=1}^{\infty}[(\mathbf{K}_{sp}^{(L)} + \mathbf{K}_{rp}^{(L)})e^{jL\omega_m t} + c.c.] \\ \mathbf{0} & \mathbf{0} \end{pmatrix}. \tag{4.12d}$$

An inner product defined in the state space is

$$(\mathbf{a},\ \mathbf{b}) = \langle \mathbf{a}_1,\ \mathbf{b}_1 \rangle + \langle \mathbf{a}_2,\ \mathbf{b}_2 \rangle, \tag{4.13}$$

where $\mathbf{a} = \begin{bmatrix} \mathbf{a}_1^T & \mathbf{a}_2^T \end{bmatrix}^T$ and $\mathbf{b} = \begin{bmatrix} \mathbf{b}_1^T & \mathbf{b}_2^T \end{bmatrix}^T$ are two elements in the state space, and $\mathbf{a}_i$ and $\mathbf{b}_i$ $(i = 1, 2)$ are extended vectors having the same form of $\boldsymbol{\chi}$ in Eq. (4.1). The state space formulation in Eq. (4.12) gives the advantage that the eigenfunctions $\boldsymbol{\phi}_k(\theta)$ of the state space eigenvalue problem

$$j\omega_k\mathbf{A}\boldsymbol{\phi}_k + \mathbf{B}\boldsymbol{\phi}_k = \mathbf{0}, \qquad \boldsymbol{\phi}_k = \begin{bmatrix} j\omega_k\boldsymbol{\chi}_k^T & {\boldsymbol{\chi}_k}^T \end{bmatrix}^T, \qquad k = 1, 2, \cdots \tag{4.14}$$

are orthogonal with respect to $\mathbf{A}$ and $\mathbf{B}$ such that

$$\big(\boldsymbol{\phi}_l,\ \mathbf{A}\boldsymbol{\phi}_k\big) = \delta_{lk}, \qquad \big(\boldsymbol{\phi}_l,\ \mathbf{B}\boldsymbol{\phi}_k\big) = -j\omega_l\delta_{lk}, \tag{4.15}$$

where δ_{lk} is the Kronecker delta.

The state space formulation in Eq. (4.12) and the eigenfunction orthogonality in Eq. (4.15) facilitate a perturbation analysis that yields closed-form expressions for parametric instability boundaries. The derivation is not shown because it is similar to that in Ref. [103].

Parametric instabilities occur when a mesh frequency harmonic is close to the sum of two natural frequencies, that is,

$$L\omega_m = \omega_l + \omega_k + \epsilon\sigma, \qquad L = 1, 2, \dots, \tag{4.16}$$

where $\sigma = O(1)$ is a real-valued detuning parameter and l and k can be the same. When a mesh frequency harmonic is close to the difference of two natural frequencies, i.e., $L\omega_m = \omega_l - \omega_k + \epsilon\sigma$, it can be shown that difference type parametric instabilities cannot occur.

Following the perturbation approach in Ref. [103], we derive instability boundaries for the two modes $\boldsymbol{\phi}_l$ and $\boldsymbol{\phi}_k$ as

$$\omega_m = \frac{\omega_l + \omega_k}{L} \pm \frac{4\epsilon\sqrt{\omega_l\omega_k}}{L}\left|D_L^{(lk)}\right|, \tag{4.17a}$$

$$D_L^{(lk)} = \sum_{n=1}^{N}\Big(gk_{sp}C_{s1}^{(L)}\bar{\Delta}_{sn}^{(l)}\bar{\Delta}_{sn}^{(k)} + k_{rp}C_{r1}^{(L)}\bar{\Delta}_{rn}^{(l)}\bar{\Delta}_{rn}^{(k)}\Big)e^{-j2\pi L\gamma_{rn}}, \tag{4.17b}$$

where $\Delta_{sn}^{(l)}$ and $\Delta_{rn}^{(l)}$ are the sun-planet and ring-planet mesh deflections for the n-th planet for the mode $\boldsymbol{\chi}_l$, and $\Delta_{sn}^{(k)}$ and $\Delta_{rn}^{(k)}$ are for the mode $\boldsymbol{\chi}_k$. These mesh deflections for a given mode $\boldsymbol{\chi}_k$ are given as

$$\begin{aligned}\Delta_{sn}^{(k)} =&(-x_s^{(k)}\sin\psi_{sn}+y_s^{(k)}\cos\psi_{sn}+u_s^{(k)})\\&+(-\zeta_n^{(k)}\sin\alpha_s-\eta_n^{(k)}\cos\alpha_s+u_n^{(k)}),\end{aligned}\tag{4.18a}$$

$$\begin{aligned}\Delta_{rn}^{(k)} =&[-u^{(k)}\sin\alpha_r+v^{(k)}\cos\alpha_r-\Gamma\beta^{(k)}\cos\alpha_r]_{\theta=\psi_n}\\&+(\zeta_n^{(k)}\sin\alpha_r-\eta_n^{(k)}\cos\alpha_r-u_n^{(k)}),\end{aligned}\tag{4.18b}$$

where α_s and α_r are the sun-planet and ring-planet pressure angle and $\psi_{sn}=\psi_n-\alpha_s$. Γ is the radial distance from the ring contact point to the ring neutral axis (see Fig. 2.3 in Chapter 2).

Eq. (4.17a) gives the upper and lower boundaries of mesh frequencies for the parametric instability between the modes $\boldsymbol{\chi}_l$ and $\boldsymbol{\chi}_k$ induced by the L-th harmonic. The mesh frequency bandwidth between the two boundaries is

$$\Delta\omega_m=\frac{8\epsilon\sqrt{\omega_l\omega_k}}{L}\left|\sum_{n=1}^{N}\left(gk_{sp}C_{s1}^{(L)}\bar{\Delta}_{sn}^{(l)}\bar{\Delta}_{sn}^{(k)}+k_{rp}C_{r1}^{(L)}\bar{\Delta}_{rn}^{(l)}\bar{\Delta}_{rn}^{(k)}\right)e^{-j2\pi L\gamma_{rn}}\right|\tag{4.19}$$

Eq. (4.19) shows the instability bandwidth depends on the natural frequencies, mesh stiffness Fourier coefficients, mesh phase, and modal gear mesh deflections. We now simplify Eq. (4.19) by studying the modal gear mesh deflections with the modal properties of the gyroscopic planetary gear system in Chapter 3.

4.3 Modal Properties and Gear Mesh Deflections

Chapter 3 shows the gyroscopic system has only three types of modes: rotational, translational, and planet modes. Planet modes exist only for systems with $N>3$ planets.

Each mode is associated with an integer or phase index $d \in \{0, 1, 2, \ldots, N-1\}$. A rotational mode has phase index 0; a translational mode is associated with phase index 1 or $N-1$; and, a planet mode is of phase index $d \in \{2, 3, \ldots, N-2\}$. We will show the gear mesh deflections for a mode $\boldsymbol{\chi}_k$ satisfy

$$\Delta_{sn}^{(k)} = e^{jT_k\psi_n}\Delta_{s1}^{(k)}, \qquad \Delta_{rn}^{(k)} = e^{jT_k\psi_n}\Delta_{r1}^{(k)}, \tag{4.20}$$

where T_k is its phase index.

A rotational mode (phase index 0) has the form

$$\boldsymbol{\chi}_k = \begin{bmatrix} \boldsymbol{w}_{rot}^T & \mathbf{q}_{rot}^T \end{bmatrix}^T, \tag{4.21a}$$

$$\boldsymbol{w}_{rot} = \sum_{s=-\infty}^{\infty} \begin{bmatrix} a_{sN}^{(k)} & b_{sN}^{(k)} & c_{sN}^{(k)} \end{bmatrix}^T e^{jsN\theta}, \tag{4.21b}$$

$$\mathbf{q}_{rot} = \begin{bmatrix} 0 \; 0 \; u_b^{(k)} \; 0 \; 0 \; u_c^{(k)} \; 0 \; 0 \; u_s^{(k)} \; \zeta_1^{(k)} \; \eta_1^{(k)} \; u_1^{(k)} \; \ldots \; \zeta_1^{(k)} \; \eta_1^{(k)} \; u_1^{(k)} \end{bmatrix}^T. \tag{4.21c}$$

According to Eqs. (4.21b) and (4.21c), the central components (sun, carrier, and ring rigid body) have only rotation, all planets have identical motions, and the elastic ring deformations contain only sN nodal diameter components. Substitution of Eqs. (4.21b) and (4.21c) into Eqs. (4.18a) and (4.18b) yields

$$\Delta_{sn}^{(k)} = \Delta_{s1}^{(k)} = u_s^{(k)} - \zeta_1^{(k)} \sin\alpha_s - \eta_1^{(k)} \cos\alpha_s + u_1^{(k)}, \tag{4.22a}$$

$$\begin{aligned} \Delta_{rn}^{(k)} = \Delta_{r1}^{(k)} = & \sum_{s=-\infty}^{\infty} \left(-a_{sN}^{(k)} \sin\alpha_r + b_{sN}^{(k)} \cos\alpha_r - \Gamma c_{sN}^{(k)} \cos\alpha_r\right) \\ & + \left(\zeta_1^{(k)} \sin\alpha_r - \eta_1^{(k)} \cos\alpha_r - u_1^{(k)}\right). \end{aligned} \tag{4.22b}$$

Therefore, Eqs. (4.22a) and (4.22b) satisfy Eq. (4.20) with $T_k = 0$.

For a translational mode $\boldsymbol{\chi}_k = [\boldsymbol{w}_{trn,1}^T \quad \mathbf{q}_{trn,1}^T]^T$ of phase index 1, the elastic ring deformations $\boldsymbol{w}_{trn,1}$ contain only $sN+1$ nodal diameter components, the central components have deflections $\mathbf{p}_h = [x_h^{(k)} \ jx_h^{(k)} \ 0]$ for $h = s, c, b$, and the motions for the n-th planet relate to those for the first planet as $\mathbf{p}_n = \mathbf{p}_1 e^{j\psi_n}$. These properties ensure the sun-planet and ring-planet mesh deflections satisfy Eq. (4.20) with $T_k = 1$. In contrast, a translational mode $\boldsymbol{\chi}_l$ of phase index $N-1$ has $\mathbf{p}_h = [x_h^{(l)} \ -jx_h^{(l)} \ 0]$, $\mathbf{p}_n = \mathbf{p}_1 e^{-j\psi_n}$, and only $sN-1$ nodal diameter ring deformation. The mesh deflections for this mode satisfy Eq. (4.20) with $T_l = N-1$.

A planet mode of phase index $d \in \{2, 3, \ldots, N-2\}$ has the structure

$$\boldsymbol{\chi}_k = \begin{bmatrix} \boldsymbol{w}_{plt}^T & \mathbf{q}_{plt}^T \end{bmatrix}^T, \tag{4.23a}$$

$$\boldsymbol{w}_{plt} = \sum_{s=-\infty}^{\infty} \begin{bmatrix} a_{sN+d}^{(k)} & b_{sN+d}^{(k)} & c_{sN+d}^{(k)} \end{bmatrix}^T e^{j(sN+d)\theta}, \tag{4.23b}$$

$$\mathbf{q}_{plt} = \begin{bmatrix} \mathbf{0} & \mathbf{0} & \mathbf{0} & e^{jd\psi_1}\mathbf{p}_1^T & \cdots & e^{jd\psi_N}\mathbf{p}_1^T \end{bmatrix}^T. \tag{4.23c}$$

Substitution of Eqs. (4.23b) and (4.23c) into Eqs. (4.18a) and (4.18b) gives

$$\Delta_{sn}^{(k)} = e^{jd\psi_n}\Delta_{s1}^{(k)} = (-\zeta_1^{(k)} \sin\alpha_s - \eta_1^{(k)} \cos\alpha_s + u_1^{(k)})e^{jd\psi_n}, \tag{4.24a}$$

$$\begin{aligned} \Delta_{rn}^{(k)} = e^{jd\psi_n}\Delta_{r1}^{(k)} = \Bigg[& \sum_{s=-\infty}^{\infty} (-a_{sN+d}^{(k)} \sin\alpha_r + b_{sN+d}^{(k)} \cos\alpha_r - \Gamma c_{sN+d}^{(k)} \cos\alpha_r) \\ & + (\zeta_1^{(k)} \sin\alpha_r - \eta_1^{(k)} \cos\alpha_r - u_1^{(k)}) \Bigg] e^{jd\psi_n}. \end{aligned} \tag{4.24b}$$

The sun-planet and ring-planet mesh deflections in Eqs. (4.24a) and (4.24b) satisfy Eq. (4.20) with $T_k = d$.

4.4 Parametric Instabilities

The mesh phase γ_{rn} affects the instability bandwidth, as shown in Eq. (4.19). This γ_{rn} has different expressions in Eqs. (4.5) and (4.6) for $\Omega_c > \Omega_r$ and $\Omega_c < \Omega_r$, respectively. We proceed with $\Omega_c > \Omega_r$, and discuss the other case later.

Substitution of Eq. (4.20) into Eq. (4.19) and simultaneously invoking γ_{rn} in Eq. (4.5) for $\Omega_c > \Omega_r$ lead to

$$\Delta\omega_m = \frac{8\epsilon\sqrt{\omega_l\omega_k}}{L}\left|\left(gk_{sp}C_{s1}^{(L)}\bar{\Delta}_{s1}^{(l)}\bar{\Delta}_{s1}^{(k)} + k_{rp}C_{r1}^{(L)}\bar{\Delta}_{r1}^{(l)}\bar{\Delta}_{r1}^{(k)}\right)\sum_{n=1}^{N} e^{-j(T_l+T_k-LZ_r)\psi_n}\right|. \tag{4.25}$$

The parametric instability between the modes $\boldsymbol{\chi}_l$ and $\boldsymbol{\chi}_k$ for the L-th harmonic may not occur because the following identities hold for integer values of m:

$$\sum_{n=1}^{N} e^{jm\psi_n} = \left\{\begin{array}{ll} N, & m/N = \text{integer} \\ 0, & m/N \neq \text{integer} \end{array}\right\}. \tag{4.26}$$

According to Eq. (4.26), the instability bandwidth $\Delta\omega_m$ vanishes when

$$(T_l + T_k - LZ_r)/N \neq \text{integer}, \tag{4.27}$$

which indicates a suppression of the parametric instability between the mode $\boldsymbol{\chi}_l$ and $\boldsymbol{\chi}_k$ for the L-th mesh harmonic.

The suppression rule in Eq. (4.27) applies to both in-phase ($Z_s, Z_r/N$ = integer) and out-of-phase ($Z_s, Z_r/N \neq$ integer) planetary gears. For in-phase systems, the suppression rule in Eq. (4.27) reduces to $(T_l + T_k)/N \neq$ integer, independent of the harmonic number L. Parametric instabilities can only occur between two rotational modes, between two translational modes with one of phase index 1 and the other of phase index $N - 1$, and between two planet modes with one of phase index d and the other of phase index $N-d$, where $d \in \{2, 3, \cdots, N-2\}$. Parametric instabilities between two modes of different types (for example, a rotational mode and a translational mode) are not possible. For out-of-phase planetary gears, there is no simple reduction of Eq. (4.27). The suppression rule depends on which mesh frequency harmonic L drives the parametric instability.

When $(T_l + T_k - LZ_r)/N =$ integer, the instability bandwidth in Eq. (4.25) are

$$\Delta\omega_m = \frac{8\epsilon\sqrt{\omega_l\omega_k}}{L}\left|N\left(gk_{sp}C_{s1}^{(L)}\bar{\Delta}_{s1}^{(l)}\bar{\Delta}_{s1}^{(k)} + k_{rp}C_{r1}^{(L)}\bar{\Delta}_{r1}^{(l)}\bar{\Delta}_{r1}^{(k)}\right)\right|. \tag{4.28}$$

The mesh stiffness Fourier coefficients $C_{s1}^{(L)}$ and $C_{r1}^{(L)}$ and the gear mesh deflections $\Delta_{s1}^{(l)}$, $\Delta_{r1}^{(l)}$, $\Delta_{s1}^{(k)}$, and $\Delta_{r1}^{(k)}$ are in general complex-valued quantities. Both the amplitudes and phases of these complex-valued quantities affect the instability bandwidth.

For systems with $\Omega_c < \Omega_r$, substitution of Eq. (4.20) and the mesh phase γ_{rn} in Eq. (4.6) into Eq. (4.19) yields

$$\Delta\omega_m = \frac{8\epsilon\sqrt{\omega_l\omega_k}}{L}\left|\left(gk_{sp}C_{s1}^{(L)}\bar{\Delta}_{s1}^{(l)}\bar{\Delta}_{s1}^{(k)} + k_{rp}C_{r1}^{(L)}\bar{\Delta}_{r1}^{(l)}\bar{\Delta}_{r1}^{(k)}\right)\sum_{n=1}^{N} e^{-j(T_l+T_k+LZ_r)\psi_n}\right|. \tag{4.29}$$

The parametric instabilities between the mode $\boldsymbol{\chi}_l$ and $\boldsymbol{\chi}_k$ for the L-th mesh harmonic are suppressed when

$$(T_l + T_k + LZ_r)/N \neq \text{integer}. \tag{4.30}$$

A summary of the parametric instability suppression rules for systems with $\Omega_c > \Omega_r$ and $\Omega_c < \Omega_r$ is given in Table 4.1.

Table 4.1: Summary of the suppression conditions for parametric instabilities between two modes $\boldsymbol{\chi}_l$ (phase index T_l) and $\boldsymbol{\chi}_k$ (phase index T_k) for the L-th harmonic.

Systems with $\Omega_c > \Omega_r$	Systems with $\Omega_c < \Omega_r$
$(T_l + T_k - LZ_r)/N \neq$ integer	$(T_l + T_k + LZ_r)/N \neq$ integer

4.5 Comparison of Instability Suppression Rules for Stationary and Spinning Systems

Parker and Wu [44] derived an instability suppression rule for stationary planetary gears without gyroscopic effects. Their derivation depends on the modal structure for stationary planetary gears defined in [21]. Four types of modes exist for stationary planetary gears: rotational, translational, planet, and purely ring modes. Purely ring modes cannot cause parametric instabilities because they have trivial mesh deflections [44]. Each mode $\boldsymbol{\chi}_k$ (purely ring modes excluded) is associated with an integer $T_k \in \{0, 1, \ldots, \text{int}(N/2)\}$ such that its mesh deflections for the n-th planet satisfy [44]

$$\Delta_{jn}^{(k)} = c_{j1}^{(k)} \cos T_k\psi_n + c_{j2}^{(k)} \sin T_k\psi_n, \qquad j = s, r, \tag{4.31}$$

where $c_{j1}^{(k)}$ and $c_{j2}^{(k)}$ are coefficients independent of the planet index n. Mesh deflections of this form are called type T_k deflections. These type T_k mesh deflections are associated with phase indices T_k and $N - T_k$ if $T_k \neq 0$ and only T_k otherwise. A rotational mode has type 0 mesh deflections (phase index 0), a translational mode has type 1 (phase indices 1 and $N-1$), and a planet mode has type d (phase indices d and $N-d$), where d is an integer from $\{2, 3, \ldots, \text{int}(N/2)\}$.

The suppression rule for stationary planetary gears [44] gives that parametric instabilities between two modes $\boldsymbol{\chi}_l$ and $\boldsymbol{\chi}_k$ for the L-th harmonic are suppressed when

$$(T_l \pm T_k \pm LZ_r)/N \neq \text{integer}. \tag{4.32}$$

This instability suppression rule in Eq. (4.32) are different from those for spinning systems with either $\Omega_c > \Omega_r$ or $\Omega_c < \Omega_r$ in Table 4.1 because of different modal structures for stationary and spinning systems. The following two examples illustrate the differences between the instability suppression rules for stationary and spinning systems.

The first example is an in-phase system where $Z_s, Z_r/N =$ integer. The suppression rule in Eq. (4.32) predicts that only two rotational, translational, or planet modes having the same type of mesh deflections can cause a parametric instability. In contrast, the suppression rules in Table 4.1 for systems with either $\Omega_c > \Omega_r$ or $\Omega_c < \Omega_r$ (they are the same for in-phase systems) give that parametric instabilities between two translational or planet modes having the same phase index (except for planet modes with phase index $N/2$ for even N) are suppressed.

The second example is a six-planet ($N = 6$) system with out-of-phase tooth meshes. The sun and ring tooth numbers are $Z_s = 6n_s - 2$ and $Z_r = 6n_r + 2$ respectively, where n_s and n_r are integers. According to Eq. (4.32), parametric instabilities for the first harmonic ($L = 1$) can occur between one rotational mode and one planet mode having type 2 mesh deflections (phase indices 2 and 4), two translational modes (phase indices 1 and 5), one translational mode (phase indices 1 and 5) and one planet mode having type 3 mesh deflections (phase index 3), and two planet modes both having type 2 mesh deflections (phase indices 2 and 4). The suppression rule for systems with $\Omega_c > \Omega_r$ in Table 4.1 predicts existence of instabilities for the first harmonic ($L = 1$) between one rotational mode and one planet mode having phase index 2, two translational modes both having phase index 1, one planet mode of phase index 3 and one translational mode of phase index 5, and two planet modes both having phase index 4. According to the suppression rule for systems with $\Omega_c < \Omega_r$ in Table 4.1, the instabilities for the first harmonic ($L = 1$) between one rotational mode and one planet mode having phase index 4, two translational modes both having phase index 5, one planet mode of phase index 3 and one translational mode of phase index 1, and two planet modes both having phase index 2 can exist.

4.6 Results

This section investigates the parametric instabilities of a planetary gear with dimensional parameters in Table 4.2. The carrier is stationary (i.e., $\Omega_c = 0$), and the ring gear rotates. The periodically changing sun-planet and ring-planet mesh stiffnesses are calculated from a single pair of sun-planet/ring-planet finite element/contact mechanics models [12] using a local slope method [86]. Figure 4.2 shows these sun-planet and ring-planet mesh stiffnesses within one mesh cycle.

Table 4.2: Dimensional parameters of an example planetary gear with an elastic ring.

Stiffness (N/m)	$k_c = k_{cu} = 10^6,\ k_s = k_{su} = k_b = k_{bu} = 10^{12},\ k_\zeta = 200\times10^6,\ k_\eta = 10^9,\ Rk_u = Rk_v = 20.0 \times 10^6$
Inertia (kg)	$I_s/R_s^2 = 0.654,\ I_p/R_p^2 = 0.490,\ I_c/R_c^2 = 4.69,\ I_b/R_b^2 = 9.77$
Mass (kg)	$m_s = 0.640,\ m_p = 0.350,\ m_c = 3.00,\ m_b = 3.20$
Dimensions (mm)	$R_b = 64.0,\ R = 148,\ \Gamma = 10.4,\ H = 14.0,\ B = 25.4$
Elastic modulus (GPa)	$E = 202,\ \kappa G = 61.3$
Density (kg/m^3)	$\rho = 7.85 \times 10^3$
Pressure angle (deg)	$\alpha_s = \alpha_r = 24.6$

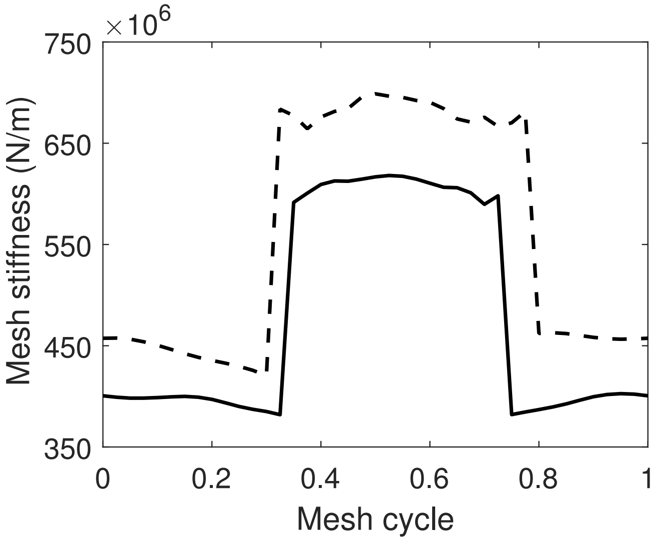

Figure 4.2: Dimensional sun-planet (solid line) and ring-planet (dashed line) mesh stiffnesses.

Two five-planet systems with different planet phasing conditions in Table 4.3 are considered. Case I has in-phase tooth meshes because $Z_s, Z_r/N =$ integer, and Case II has out-of-phase tooth meshes. The two systems have the same parameters in Table 4.2 and mesh stiffness variations for the first planet in Fig. 4.2. In other words, the two systems are identical except for a small change of gear tooth numbers.

Table 4.3: Selection of different planet phasing conditions (i.e., different gear tooth numbers) to examine the parametric instability suppression rules in Table 4.1.

Case I	Case II
$Z_s = 40,\ Z_r = 80$	$Z_s = 39,\ Z_r = 81$

Figure 4.3 shows the natural frequencies $\omega_{19} \sim \omega_{24}$ for the five-planet system in Table 4.2 over a range of negative ring speeds. The negative ring speeds means clockwise rotation of the ring. In this case, $\Omega_c > \Omega_r$ because $\Omega_c = 0$. The maximum dimensionless ring speed $\Omega_r = -0.05$ in Fig. 4.3 corresponds to a dimensional speed of $-11,414$ rpm. The natural frequencies are calculated from the eigenvalue problem in Eq. (4.11) using the average sun-

planet (k_{sp}) and ring-planet (k_{rp}) mesh stiffnesses in Fig. 4.2. Table 4.4 shows the phase indices for the natural frequencies $\omega_{19} \sim \omega_{24}$.

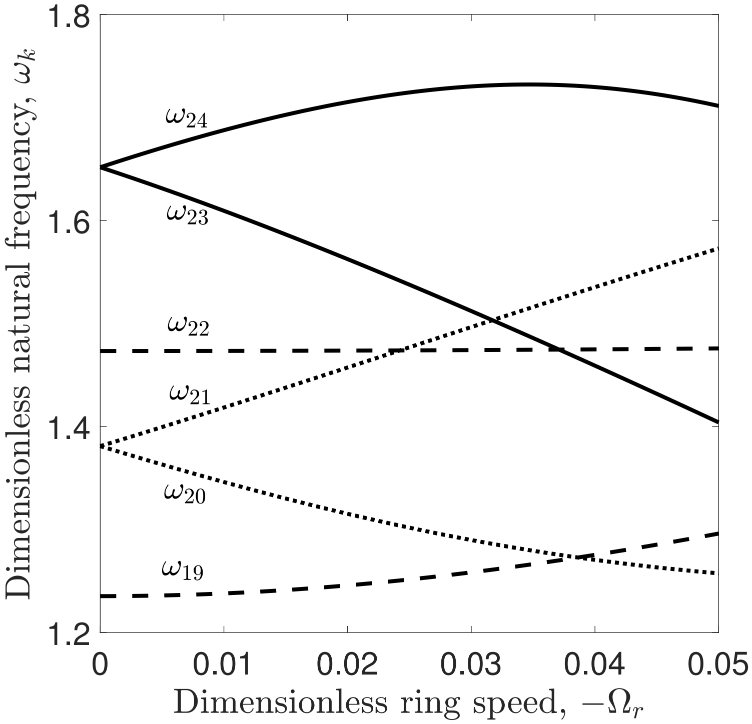

Figure 4.3: Dimensionless natural frequencies of a five-planet system in Table 4.2 for a range of ring speeds. The sun-planet and ring-planet mesh stiffnesses take the mean values in Fig. 4.2. The dashed (ω_{19}, ω_{22}), dotted (ω_{20}, ω_{21}), and solid lines (ω_{23}, ω_{24}) represent natural frequencies of rotational, translational, and planet modes, respectively.

A pair of degenerate translational or planet modes (multiplicity two) splits into two translational or planet modes with one of phase index $d \in \{1, 2, \ldots, \text{int}((N-1)/2)\}$ and the other of phase index $N-d$ from stationary to spinning planetary gears, as shown in Chapter 3. The frequency splitting phenomenon is demonstrated in Fig. 4.3 as the degenerate translational mode frequencies ω_{20} and ω_{21} and planet mode frequencies ω_{23} and ω_{24} split at non-zero ring speed. The phase indices for the split natural frequencies ω_{20} and ω_{21} are different and similarly for ω_{23} and ω_{24} (Table 4.4).

Table 4.4: Phase indices for the natural frequencies $\omega_{19} \sim \omega_{24}$ in Fig. 4.3. The system has speed $\Omega_c > \Omega_r$.

Natural frequency	ω_{19}	ω_{20}	ω_{21}	ω_{22}	ω_{23}	ω_{24}
Phase index	0	4	1	0	3	2

Figure 4.4 shows the instability region boundaries from the analytical solution in Eq. (4.17a) and numerical solutions from Floquet theory for Case I. For a range of peak-to-peak amplitudes of the mesh stiffnesses (i.e., ϵ), the analytical and numerical predictions match well. When the mesh frequency ω_m lies within an instability region, responses for this linear undamped system will go unbounded. In practice, damping and nonlinearities would bound

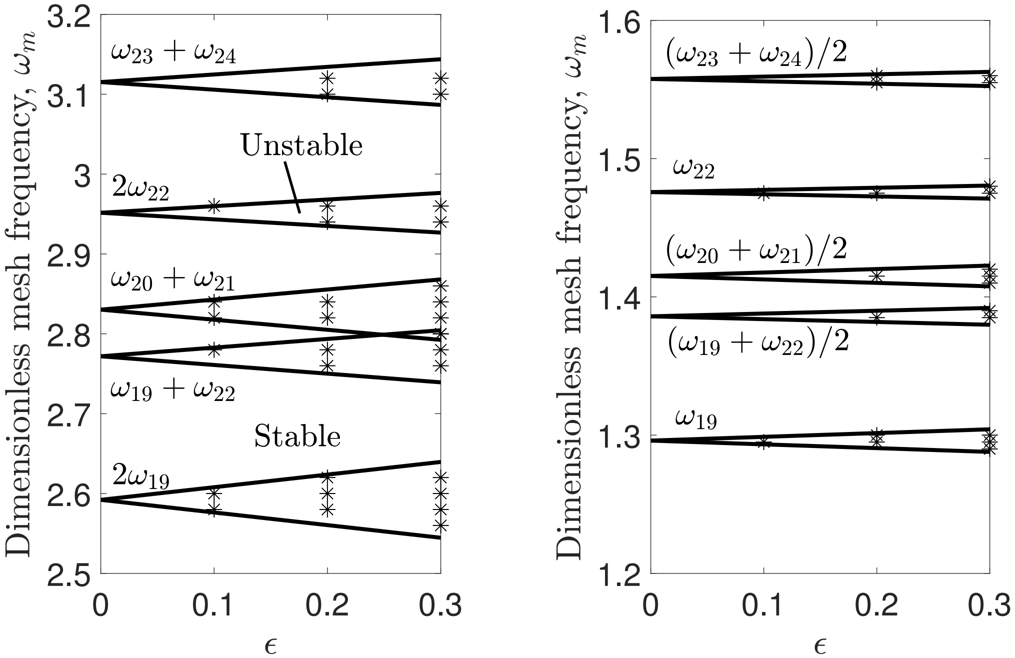

(a) (b)

Figure 4.4: Instability regions for Case I at dimensionless ring speed $\Omega_r = -0.05$. The solid lines are perturbation solutions from Eq. (4.17a), and the asterisks are numerical solutions from Floquet theory. (a) $L = 1$, (b) $L = 2$.

the responses as resonant vibrations.

For this in-phase system (i.e., Case I), single mode parametric instabilities occur only for rotational modes, such as $2\omega_{19}$ and $2\omega_{22}$ for the first harmonic ($L = 1$) and ω_{19} and ω_{22} for the second harmonic ($L = 2$). The parametric instabilities for a single translational or planet modes are suppressed. For example, the instability regions for $2\omega_{20}$ and $2\omega_{23}$ are absent in Fig. 4.4a. This occurs because only the rotational modes $\boldsymbol{\chi}_k$ with phase index $T_k = 0$ satisfy $2T_k/5 =$ integer. For an in-phase system having an even number of planets, single mode parametric instability can occur for planet modes $\boldsymbol{\chi}_k$ having phase index $T_k = N/2$ as well because $2T_k = N$. This result is different from the instability suppression rule for stationary planetary gears in Eq. (4.32) that gives parametric instabilities can occur for a single mode for in-phase systems no matter this mode is a rotational, translational, or planet mode.

Figure 4.4 shows combination parametric instabilities for two split translational $(\omega_{20}, \omega_{21})$ or planet $(\omega_{23}, \omega_{24})$ modes for both the first and second harmonics. For in-phase systems, a pair of split modes interact with each other to cause a parametric instability because the sum of their phase index equals the number of planets N. Single one of them cannot cause parametric instabilities because twice of their phase index cannot equal integer multiples of N.

Figure 4.5 shows the instability regions analogous to Fig. 4.4 but for Case II. This out-of-phase system has sun and ring tooth numbers $Z_s = 39$ and $Z_r = 81$, respectively. The instability suppression rule for $\Omega_c > \Omega_r$ in Table 4.1 gives that parametric instabilities between two modes $\boldsymbol{\chi}_l$ and $\boldsymbol{\chi}_k$ can occur only if their phase indices satisfy $(T_l + T_k + 81L)/N =$ integer. This suppression rule and the phase indices for the natural frequencies $\omega_{19} \sim \omega_{24}$ in Table 4.4 explain the occurrence of parametric instabilities in Fig. 4.5a for $L = 1$ and Fig. 4.5b for $L = 2$.

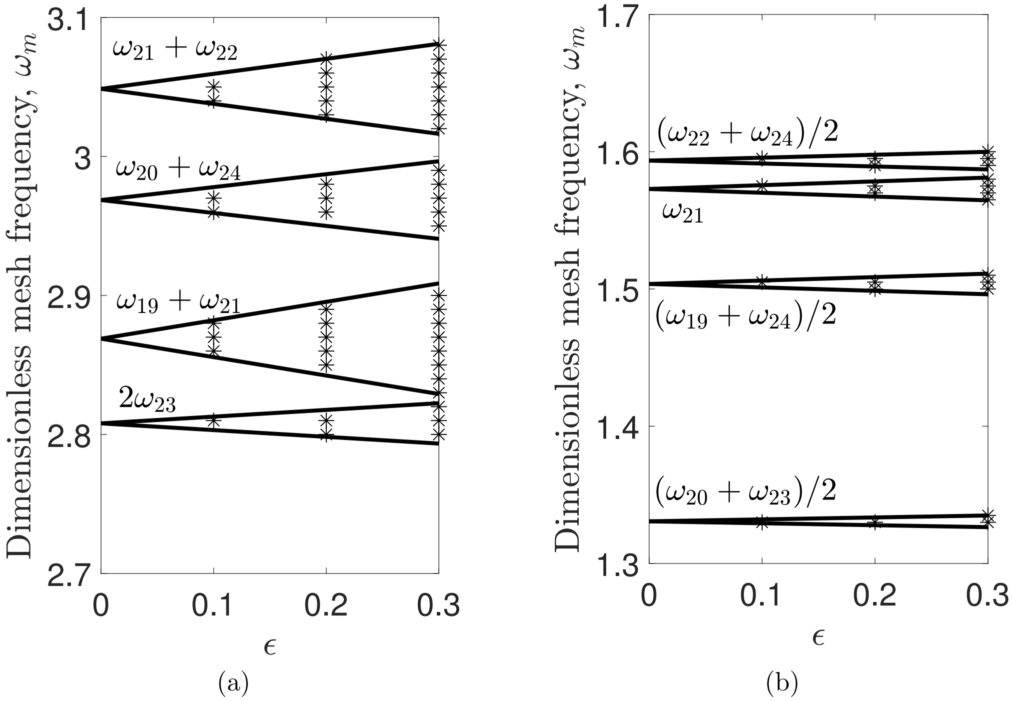

Figure 4.5: Instability regions for Case II at dimensionless ring speed $\Omega_r = -0.05$. The solid lines are perturbation solutions from Eq. (4.17a), and the asterisks are numerical solutions from Floquet theory. (a) $L = 1$, (b) $L = 2$.

For an out-of-phase system, combination instabilities between a pair of split modes $\boldsymbol{\chi}_l$ and $\boldsymbol{\chi}_k$ are suppressed for the L-th harmonic with $L/N \neq$ integer because the condition $(T_l + T_k + LZ_r)/N \neq$ integer holds. Absence of the parametric instabilities $\omega_{20} + \omega_{21}$ and $\omega_{23} + \omega_{24}$ in Fig. 4.5a and $(\omega_{20} + \omega_{21})/2$ and $(\omega_{23} + \omega_{24})/2$ in Fig. 4.5b confirms the foregoing statement.

Single mode parametric instabilities for the mode $\boldsymbol{\chi}_k$ for the L-th harmonic can occur when $(2T_k - LZ_r)/N =$ integer according to the instability suppression rule for $\Omega_c > \Omega_r$ in Table 4.1. These parametric instabilities are not possible for $L = 1$ even N and odd Z_r because $(2T_k - Z_r)/N \neq$ integer for any integer T_k. Single mode parametric instabilities for $L = 2$ always exist for modes having phase index $\mathrm{mod}(Z_r, N)$ or $\mathrm{mod}(Z_r + N/2, N)$ for even

N, where $\mathrm{mod}(A, B)$ represents A modulo B. Parametric instabilities of ω_{19} and ω_{22} in Fig. 4.4b for the in-phase system of Case I and ω_{21} in Fig. 4.5b for the out-of-phase system of Case II agree with the foregoing prediction.

According to the instability suppression rule for $\Omega_c > \Omega_r$ in Table 4.1, only one of a pair of split modes $\boldsymbol{\chi}_l$ and $\boldsymbol{\chi}_k$ can interact with a mode $\boldsymbol{\chi}_a$ (which can be the same with $\boldsymbol{\chi}_l$ or $\boldsymbol{\chi}_k$) to cause parametric instabilities for the L-th harmonic because their phase indices cannot satisfy the conditions $T_l + T_k = N$, $(T_l + T_a - LZ_r)/N =$ integer, and $(T_k + T_a - LZ_r)/N =$ integer simultaneously. This applies for both in-phase and out-of-phase systems. For example, the parametric instabilities for $\omega_{20} + \omega_{21}$ occur in Fig. 4.4a, but $2\omega_{20}$ or $2\omega_{21}$ are suppressed for the in-phase system of Case I, where ω_{20} and ω_{21} are a pair of splitting frequencies (Fig. 4.3). Similarly, instabilities occur for $\omega_{19} + \omega_{21}$ but not for $\omega_{19} + \omega_{20}$ in Fig. 4.5a for the out-of-phase system of Case II.

Figure 4.4 and Figure 4.5 show completely different behaviors of parametric instabilities for Case I and II although these two systems are nearly identical with minimal difference of gear tooth numbers (Table 4.3). This provides a way to suppress some large-bandwidth parametric instabilities occurring at operating speeds by slightly changing the gear tooth numbers with the natural frequencies and mesh frequency minimally changed.

The parametric instabilities for Case I in Fig. 4.4 and Case II in Fig. 4.5 follow the suppression rule for systems with $\Omega_c > \Omega_r$ in Table 4.1. If the planetary gear system reverses rotation but with all other parameters unchanged, the parametric instabilities for Case I and II stay the same with those in Fig. 4.4 and Fig. 4.5. The natural frequency loci for the reversed rotation are identical to those in Fig. 4.3, except that a translational or planet mode natural frequency that has phase index d becomes a translational or planet mode natural frequency with phase index $N - d$ for the reversed rotation (Table 4.5). Because of $\Omega_c < \Omega_r$ for the reversed rotation, the suppression rule for systems with $\Omega_c < \Omega_r$ in Table 4.1 applies.

Table 4.5: Phase indices for the natural frequencies $\omega_{19} \sim \omega_{24}$ in Fig. 4.3 with reversed rotation of the system (i.e., $\Omega_c < \Omega_r$).

Natural frequency	ω_{19}	ω_{20}	ω_{21}	ω_{22}	ω_{23}	ω_{24}
Phase index	0	1	4	0	2	3

4.7 Conclusions

This paper investigates parametric instabilities of spinning planetary gears with a deformable ring and equally-spaced planets. Closed-form expressions for instability boundaries are derived with the method of multiple scales. Instability suppression rules are identified with the structured modal properties for spinning planetary gears with gyroscopic effects.

The instability suppression rules for counter-clockwise and clockwise rotation of the carrier relative to the ring gear are different. Both of them differ from the instability suppression rule for stationary planetary gears. Each mode is associated with a phase index. For counter-clockwise rotation of the carrier relative to the ring gear, parametric instabilities between two modes $\boldsymbol{\chi}_l$ and$\boldsymbol{\chi}_k$ for the L-th harmonic are suppressed when their phase indices satisfy $(T_l + T_k - LZ_r)/N \neq$ integer. For clockwise rotation of the carrier relative to the ring gear, the parametric instabilities are suppressed when $(T_l + T_k + LZ_r)/N \neq$ integer.

A pair of degenerate translational or planet modes (multiplicity two) splits into two translational or planet modes having different phase indices from stationary to spinning planetary gears. For in-phase systems, instabilities can occur for combinations of a pair of split modes, but single one of them cannot cause parametric instabilities. For out-of-phase systems, combination instabilities between a pair of splitting modes are not possible for the L-th harmonic unless $L/N =$ integer. For both in-phase and out-phase systems, only one in a pair of split modes can interact with a mode (which can be the same with one of the split modes) to cause parametric instabilities for a given harmonic.

For in-phase systems, single mode parametric instabilities are possible only for rotational modes or planet modes having phase index $N/2$ (N even) for any harmonic. For out-of-phase systems, single mode parametric instabilities for the first harmonic are not possible for even number of planets and odd number of ring gear teeth. Single mode parametric instabilities for the second harmonic can occur only for modes having phase index $\mathrm{mod}(Z_r, N)$ or $\mathrm{mod}(Z_r + N/2, N)$ for even N.

Planetary gears with different planet phasing conditions (which depend on sun and ring tooth numbers and the number of planets) can have significantly different behaviors of parametric instabilities. Slightly changing the gear tooth numbers can suppress certain parametric instabilities with minimal change in the natural frequencies and mode shapes.

Chapter 5

Nonlinear Dynamics of Spinning Planetary Gears with a Deformable Ring

5.1 Introduction

Planetary gears are widely used in aerospace systems due to their compactness, high power density, and large transmission ratio. Their vibrations lead to larger dynamic tooth mesh and bearing loads than the quasi-static ones, influencing fatigue lives of gears and bearings negatively. The periodically changing sun-planet and ring-planet mesh stiffnesses are the vibration source. Near resonances where a harmonic of the time-varying mesh stiffnesses coincides with a natural frequency or twice a natural frequency, vibrations can become large enough that gear teeth that are normally in contact separate. Tooth contact loss is a strong nonlinearity that can induce jump, period-doubling, and chaos in the dynamic response. Such nonlinear behaviors have been demonstrated in experiments and finite element simulations [16, 48].

Most literature [11, 16, 49–52, 55–57] studied the nonlinear dynamics of planetary gears using lumped parameter models where the sun, carrier, planets, and ring gear are treated as rigid bodies. The elastic deformations of each component including the thin ring gear are ignored. A few studies [15, 19, 20, 22] considered elastic ring or carrier in the dynamic simulations of planetary gears, but nonlinear behaviors due to gear tooth contact loss are not investigated in these studies.

Coriolis and centripetal acceleration effects arise from carrier or ring rotation. They alter natural frequencies and vibration modes of planetary gears [10]. Real-valued standing-wave modes become complex-valued traveling-wave modes due to the gyroscopic (i.e., Coriolis) effects. Degenerate natural frequencies split for planetary gears with an elastic ring, as shown in Chapter 3. At high speed, divergence and flutter instabilities can occur [104]. The gyroscopic and centripetal effects on the nonlinear dynamics of planetary gears are rarely touched, however. Most literature [11, 15, 16, 19, 49–52, 55–57] ignored them without any justification. Whether these effects have meaningful influences on the nonlinear dynamics of planetary gears or not needs investigation.

Planet mesh phasing plays an important role in planetary gear dynamics. A few papers [6, 105–110] have used the planet mesh phasing to suppress translational and rotational vibrations of central members (the sun gear, carrier, and ring gear). Among them, Parker [110] identified mesh phasing rules to suppress certain harmonics of translational and rotational vibration modes [9]. Ambarisha and Parker [111] extended the mesh phasing rules in [110] to suppress certain harmonics of planet mode responses [9]. Planet mesh phasing can also suppress parametric instabilities [43, 44]. The above studies [6, 43, 44, 105–111], however, did not consider the gyroscopic effects.

Numerical simulations and harmonic balance method with arclength continuation are two common approaches to solve the nonlinear dynamics of planetary gears. Ambarisha and Parker [16] simulated nonlinear dynamics of planetary gears with an analytical model and successfully correlated them to those from a finite element/contact mechanics model. Jumps, period-doubling bifurcations, and chaotic behaviors occur in their simulations. Masoumi et.al. [11] demonstrated symmetry breaking induced by chaotic response in their simulations. Li et.al. [49] numerically simulated the nonlinear dynamics of a two-stage planetary gear train. Numerical simulations give only stable solutions, while harmonic balance method with arclength continuation yields both stable and unstable solutions. Sun and Hu [50] studied nonlinear dynamics of planetary gears with single-term harmonic balance method. Al-Shyyab and Kahraman [51] investigated nonlinear dynamics of planetary gears using multi-term harmonic balance method. The harmonic balance solutions agreed with those from numerical integration and finite element simulations. Ref. [52] extended the model and solution method in [51] to multi-stage planetary gear trains. Zhu et.al. [55] investigated nonlinear dynamic characteristics of compound planetary gear sets with single-term harmonic balance method. Neither of numerical simulations or harmonic balance method gives closed-form solutions that explicitly show parameter dependence of the nonlinear dynamic response. Bahk and Parker [56] derived closed-form approximations for the nonlinear dynamics of planetary gears with the method of multiple scales. Their analytical solutions compared well against the solutions from harmonic balance methods, numerical integration, and finite element simulations. From the analytical solutions, they concluded tooth separation occurs even under large torques, which differs from conventional thinking that large torques suppress contact loss. In a different study, Bahk and Parker [57] investigated the effects of tooth profile modification on the nonlinear dynamics of planetary gears with analytical solutions.

This work investigates nonlinear dynamics of spinning planetary gears with a deformable ring and equally-spaced planets using the dynamic model from Chapter 2. Speed-dependent gyroscopic and centripetal effects are included. The sun-planet and ring-planet meshes include time-varying mesh stiffnesses and tooth separation nonlinearity. Numerical integration of the model gives the dynamic response. We compare the dynamic response to those from a commercial finite element/contact mechanics (FE/CM) software [12, 72, 73] for verification. Use of the method of multiple scales yields closed-form approximations for the frequency response functions near resonances. The analytical results are compared against results from numerical integration for verification. Influences of the planet mesh phasing and gyroscopic effects on the dynamics are studied numerically and analytically.

5.2 Modeling of Planetary Gear Dynamics

The two-dimensional planetary gear model developed in Chapter 2, extended to include tooth separation nonlinearity, is adopted here. Figure 5.1 shows the hybrid elastic-discrete model that includes an elastic ring, rigid bodies of the sun, carrier, and planets, and a circular rigid body (which is depicted by the largest circle in Fig. 5.1) that connects the elastic ring through a uniform elastic foundation. The gear mesh is modeled as a periodically changing stiffness in the line of action. The tooth separation nonlinearity is included such that the mesh stiffness acts only when compressed and exerts no force when the mesh separates. All other stiffnesses in Fig. 5.1 are linear. All components can rotate. The carrier and ring have speeds Ω_c and Ω_r, respectively. The sun and planet speeds can be derived from kinematics.

The dimensional equation of motion for a planetary gear with N planets from Chapter 2 is

$$\mathbf{M}\ddot{\boldsymbol{\chi}} + (\Omega_r \mathbf{G}_r + \Omega_c \mathbf{G}_c)\dot{\boldsymbol{\chi}} + [\mathbf{K}(\boldsymbol{\chi}, t) - \Omega_r^2 \mathbf{C}_r - \Omega_c^2 \mathbf{C}_c - 2\Omega_r \Omega_c \mathbf{C}_{rc}]\boldsymbol{\chi} = \mathbf{f}, \tag{5.1a}$$

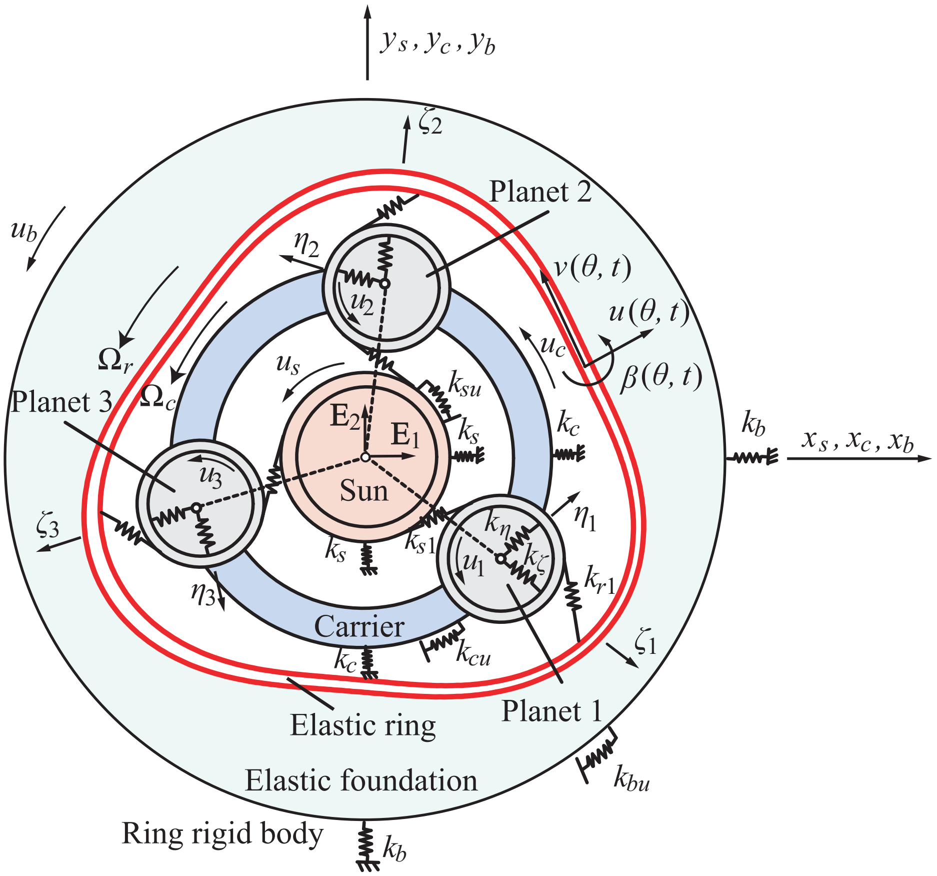

Figure 5.1: Schematic of a planetary gear model with a deformable ring.

$$\boldsymbol{\chi} = \begin{bmatrix} \boldsymbol{w}(\theta, t)^T & \mathbf{q}(t)^T \end{bmatrix}^T, \tag{5.1b}$$

$$\boldsymbol{w} = \begin{bmatrix} u & v & \beta \end{bmatrix}^T, \tag{5.1c}$$

$$\mathbf{q} = \begin{bmatrix} \underbrace{x_b \ y_b \ u_b}_{\mathbf{p}_b} & \underbrace{x_c \ y_c \ u_c}_{\mathbf{p}_c} & \underbrace{x_s \ y_s \ u_s}_{\mathbf{p}_s} & \underbrace{\zeta_1 \ \eta_1 \ u_1}_{\mathbf{p}_1} & \cdots & \underbrace{\zeta_N \ \eta_N \ u_N}_{\mathbf{p}_N} \end{bmatrix}^T, \tag{5.1d}$$

The extended vector $\boldsymbol{\chi}$ includes both elastic ($\boldsymbol{w}(\theta, t)$) and discrete ($\mathbf{q}(t)$) motions. These coordinates are described in the rotating carrier reference frame with speed Ω_c. x_h, y_h for $h = s, c, b$ represent the translations of the sun, carrier, and ring rigid body in the $\mathbf{E}_1$ and $\mathbf{E}_2$ directions, where $\{\mathbf{E}_1, \mathbf{E}_2, \mathbf{E}_3\}$ (Fig. 5.1) is a carrier-fixed basis. ζ_n, η_n are the radial and tangential deflections for the n-th planet at an angular position ψ_n with respect to the rotating basis vector $\mathbf{E}_1$. Without loss of generality, $\psi_1 = 0$. u_j for $j = 1, 2, \cdots, N, s, c, b$ are the rotational deflections (rotation in radians times the gear base radii R_p and R_s, the center distance R_c for the carrier, and the radius R_b for the ring rigid body). The elastic ring deformations $\boldsymbol{w}(\theta, t)$ include the radial ($u(\theta, t)$) and tangential ($v(\theta, t)$) deflections of the ring neutral axis and its cross-sectional rotation angle ($\beta(\theta, t)$), where θ defines an angular position relative to the carrier-fixed basis vector $\mathbf{E}_1$.

The extended mass ($\mathbf{M}$), gyroscopic ($\mathbf{G}_r$ and $\mathbf{G}_c$), and centripetal ($\mathbf{C}_r$, $\mathbf{C}_c$, and $\mathbf{C}_{rc}$) operators and also the forcing vector $\mathbf{f}$ in Eq. (5.1a) are identical to those in Chapter 2 except that Chapter 2 presented them in dimensionless form. The extended stiffness operator $\mathbf{K}(\boldsymbol{\chi}, t)$ is the same with the dimensional form of $\mathbf{K}$ in Chapter 2 with k_{sn}, k_{rn} in $\mathbf{K}$ substituted by the nonlinear, time-varying mesh stiffnesses

$$
\begin{aligned}
k_{sn}(\boldsymbol{\chi}, t) &= k_{sn}(t) H(\Delta_{sn}) = \begin{cases} k_{sn}(t), & \Delta_{sn} > 0, \\ 0, & \Delta_{sn} \leq 0, \end{cases} \\
k_{rn}(\boldsymbol{\chi}, t) &= k_{rn}(t) H(\Delta_{rn}) = \begin{cases} k_{rn}(t), & \Delta_{rn} > 0, \\ 0, & \Delta_{rn} \leq 0, \end{cases} \\
\Delta_{sn} &= (-x_s \sin\psi_{sn} + y_s \cos\psi_{sn} + u_s) + (-\zeta_n \sin\alpha_s - \eta_n \cos\alpha_s + u_n), \\
\Delta_{rn} &= (\zeta_n \sin\alpha_r - \eta_n \cos\alpha_r - u_n) \\
&\qquad + [-u \sin\alpha_r + v \cos\alpha_r - \Gamma\beta \cos\alpha_r]_{\theta=\psi_n}, \qquad n = 1, 2, \ldots, N,
\end{aligned}
\tag{5.2}
$$

where α_s and α_r are the sun-planet and ring-planet pressure angle, $\psi_{sn} = \psi_n - \alpha_s$, and Γ is the radial distance from the ring contact point to the ring neutral axis (See Fig. 2.3 in Chapter 2).

The nonlinear stiffness operator $\mathbf{K}(\boldsymbol{\chi}, t)$ in Eq. (5.1) is separated into linear time-invariant and nonlinear time-varying parts as

$$\mathbf{K}(\boldsymbol{\chi},t)=\mathbf{K}_0+\sum_{n=1}^{N}\Big[k_{sn}(t)\mathbf{K}_{sn}H(\Delta_{sn})+k_{rn}(t)\mathbf{K}_{rn}H(\Delta_{rn})\Big], \tag{5.3}$$

where $\mathbf{K}_0$ is the same with $\mathbf{K}(\boldsymbol{\chi},t)$ with vanishing sun-planet and ring-planet mesh stiffnesses for all planets. The linear mesh stiffness operator $\mathbf{K}_{sn}$ ($\mathbf{K}_{rn}$) has the same form with $\mathbf{K}(\boldsymbol{\chi},t)$ with all stiffnesses other than $k_{sn}(t)H(\Delta_{sn})$ ($k_{rn}(t)H(\Delta_{rn})$) vanishing and the mesh stiffnesses $k_{sn}(t)H(\Delta_{sn})$ ($k_{rn}(t)H(\Delta_{rn})$) replaced by one.

The mesh stiffnesses $k_{sn}(t)$ and $k_{rn}(t)$ vary periodically with mesh frequency ω_m. Fourier representations of the mesh stiffnesses are

$$k_{sn}(t)=k_{sp}+\sum_{L=1}^{\infty}[k_{sn}^{(L)}e^{jL\omega_m t}+c.c.], \tag{5.4a}$$

$$k_{rn}(t)=k_{rp}+\sum_{L=1}^{\infty}[k_{rn}^{(L)}e^{jL\omega_m t}+c.c.], \tag{5.4b}$$

where $c.c.$ denotes the complex conjugate of the preceding term. Chapter 4 shows the Fourier coefficients $k_{sn}^{(L)}$ and $k_{rn}^{(L)}$ are related to $k_{s1}^{(L)}$ and $k_{r1}^{(L)}$ by

$$k_{sn}^{(L)}=k_{s1}^{(L)}e^{-j2\pi L\gamma_{sn}}, \qquad k_{rn}^{(L)}=k_{r1}^{(L)}e^{-j2\pi L\gamma_{rn}}, \tag{5.5}$$

where γ_{sn} and γ_{rn} are the mesh phases between sun-planet and ring-planet meshes for the n-th planet and those for the first planet, respectively. For equally-spaced planets, Chapter 2 gives

$$\gamma_{sn}=\gamma_{rn}=Z_s\psi_n/(2\pi)=-Z_r\psi_n/(2\pi) \tag{5.6}$$

for counter-clockwise rotation of the carrier relative to the ring gear (i.e., $\Omega_c>\Omega_r$), where Z_s and Z_r are the sun and ring gear tooth numbers. The signs of γ_{sn} and γ_{rn} are reversed for systems with clockwise rotation of the carrier relative to the ring gear (i.e., $\Omega_c < \Omega_r$).

The eigenvalue problem of Eq. (5.1) with linear time-invariant mesh stiffnesses k_{sp} and k_{rp} is

$$\lambda_i^2 \mathbf{M}\boldsymbol{\chi}_i + \lambda_i(\Omega_r \mathbf{G}_r + \Omega_c \mathbf{G}_c)\boldsymbol{\chi}_i + (\mathbf{K} - \Omega_r^2 \mathbf{C}_r - \Omega_c^2 \mathbf{C}_c - 2\Omega_r \Omega_c \mathbf{C}_{rc})\boldsymbol{\chi}_i = \mathbf{0}, \tag{5.7a}$$

$$\mathbf{K} = \mathbf{K}_0 + \sum_{n=1}^{N} k_{sp}\mathbf{K}_{sn} + \sum_{n=1}^{N} k_{rp}\mathbf{K}_{rn}. \tag{5.7b}$$

where the eigenvalue $\lambda_i = j\omega_i$ is purely imaginary and the vibration mode $\boldsymbol{\chi}_i(\theta)$ is complex-valued when the gyroscopic system operates at speeds below the first critical speed [100]. When the gyroscopic effects are neglected, $\boldsymbol{\chi}_i(\theta)$ is real-valued. The inner product of two arbitrary extended vectors $\boldsymbol{\chi}_1 = [\boldsymbol{w}_1^T \ \mathbf{q}_1^T]^T$ and $\boldsymbol{\chi}_2 = [\boldsymbol{w}_2^T \ \mathbf{q}_2^T]^T$ is defined as

$$\langle \boldsymbol{\chi}_1, \ \boldsymbol{\chi}_2 \rangle = \int_0^{2\pi} \overline{\boldsymbol{w}}_1^T \boldsymbol{w}_2 \mathrm{d}\theta + \overline{\mathbf{q}}_1^T \mathbf{q}_2, \tag{5.8}$$

where the overbar denotes complex conjugate. The linear operators $\mathbf{M}$, $\mathbf{K}$, $\mathbf{C}_r$, $\mathbf{C}_c$, and $\mathbf{C}_{rc}$ are self-adjoint and $\mathbf{G}_r$ and $\mathbf{G}_c$ are skew self-adjoint with respect to the inner product in Eq. (5.8).

The discretization method from Chapter 2 is adopted here to discretize Eq. (5.1a) to give

$$[\mathbf{M}]\ddot{\mathbf{z}} + (\Omega_r[\mathbf{G}_r] + \Omega_c[\mathbf{G}_c])\dot{\mathbf{z}} + ([\mathbf{K}](\mathbf{z}, t) - \Omega_r^2[\mathbf{C}_r] - \Omega_c^2[\mathbf{C}_c] - 2\Omega_r\Omega_c[\mathbf{C}_{rc}])\mathbf{z} = \tilde{\mathbf{f}}, \tag{5.9}$$

where $\mathbf{z}$ is the discretized coordinates. The discretized matrices $[\mathbf{M}]$, $[\mathbf{G}_r]$, $[\mathbf{G}_c]$, $[\mathbf{K}](\mathbf{z}, t)$, $[\mathbf{C}_r]$, $[\mathbf{C}_c]$, and $[\mathbf{C}_{rc}]$ and vector $\tilde{\mathbf{f}}$ correspond to the extended operators $\mathbf{M}$, $\mathbf{G}_r$, $\mathbf{G}_c$, $\mathbf{K}(\boldsymbol{\chi}, t)$, $\mathbf{C}_r$, $\mathbf{C}_c$, and $\mathbf{C}_{rc}$ and vector $\mathbf{f}$ in Eq. (5.1a), respectively. The corresponding discretized eigenvalue problem of Eq. (5.9) is

$$\lambda_i^2[\mathbf{M}]\mathbf{z}_i + \lambda_i(\Omega_r[\mathbf{G}_r] + \Omega_c[\mathbf{G}_c])\mathbf{z}_i + ([\mathbf{K}] - \Omega_r^2[\mathbf{C}_r] - \Omega_c^2[\mathbf{C}_c] - 2\Omega_r\Omega_c[\mathbf{C}_{rc}])\mathbf{z}_i = \mathbf{0}, \quad (5.10)$$

where the discretized matrix $[\mathbf{K}]$ corresponds to the extended operator $\mathbf{K}$ in Eq. (5.7b).

A damping matrix $[\mathbf{D}]$ is introduced to the discretized model in Eq. (5.9) with $[\mathbf{D}] = [\mathbf{\Psi}]^{-T} diag(2\nu_i\omega_i)[\mathbf{\Psi}]^{-1}$, where $[\mathbf{\Psi}]$ is the orthonormalized modal matrix with respect to $[\mathbf{M}]$ from the eigenvalue problem in Eq. (5.10) without gyroscopic and centripetal terms and ν_i is the modal damping ratio. The final equation including damping for numerical simulation is

$$[\mathbf{M}]\ddot{\mathbf{z}} + (\Omega_r[\mathbf{G}_r] + \Omega_c[\mathbf{G}_c] + [\mathbf{D}])\dot{\mathbf{z}} + ([\mathbf{K}](\mathbf{z}, t) - \Omega_r^2[\mathbf{C}_r] - \Omega_c^2[\mathbf{C}_c] - 2\Omega_r\Omega_c[\mathbf{C}_{rc}])\mathbf{z} = \tilde{\mathbf{f}}. \quad (5.11)$$

5.3 Nonlinear Dynamics Benchmarking Comparisons

The analytical model has been successfully compared to a finite element/contact mechanics (FE/CM) model [12, 72, 73] on natural frequencies and vibration modes in Chapter 3. Because of the differences between the analytical and FE/CM models, the analytical model was adjusted for that comparison. This work makes the same adjustment of the analytical model to compare the nonlinear dynamics from the analytical and FE/CM models. For this comparison, the gyroscopic and centripetal terms in Eq. (5.11) are eliminated because these terms are not considered in the dynamic analysis of the FE/CM model.

The comparison is conducted on the same three-planet in-phase system with equal planet spacing used in Chapter 3. Refer to Table 3.1 in Chapter 3 for detailed system parameters. The input and output members are the sun and ring gears, respectively. The carrier is stationary. The input torque on the sun is 300 N·m. The time-varying sun-planet ($k_{sn}(t)$) and ring-planet ($k_{rn}(t)$) mesh stiffnesses for the analytical model are calculated from single-pair sun-planet and ring-planet FE/CM models using a local slope method [86]. Figure 5.2 shows the mesh stiffnesses for the first planet over one mesh cycle. Because the present example has in-phase tooth meshes, all of the sun-planet (ring-planet) mesh stiffnesses have the same values at each instant over a mesh cycle.

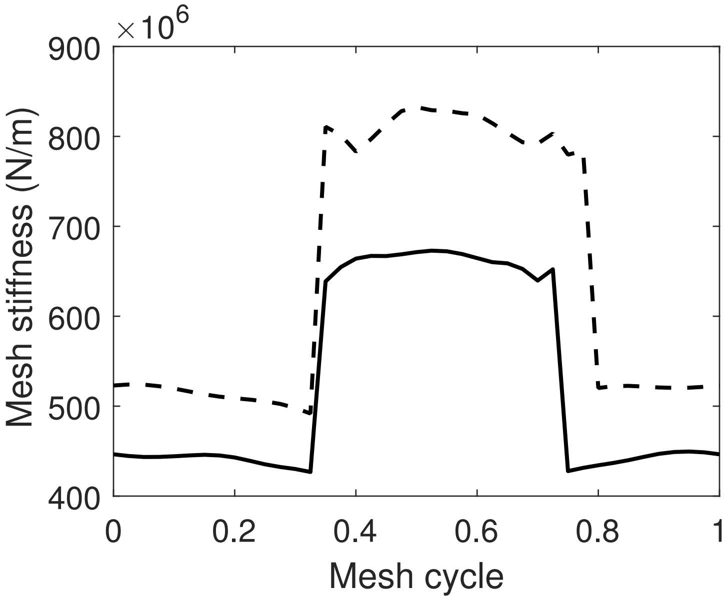

Figure 5.2: Dimensional sun-planet (solid line) and ring-planet (dashed line) mesh stiffnesses.

Non-gyroscopic planetary gears with equally-spaced planets and a deformable ring in general have four sets of natural frequencies and vibration modes: rotational, translational, planet, and purely ring modes [21]. Planet modes exist only for systems with $N > 3$ planets. The first thirty-one natural frequencies for the present three-planet example system, grouped into rotational, translational, and purely ring modes, are shown in Table 5.1. These natural frequencies are calculated from the analytical discretized eigenvalue problem in Eq. (5.10) without gyroscopic and centripetal terms, and they match those from the FE/CM model except that the two purely ring mode natural frequencies ω_{13}, ω_{30} are not captured from

Table 5.1: Natural frequencies of the example system from Chapter 3.

Mode types	Natural frequencies (Hz)
Rotational	$\omega_1 = 293.8$, $\omega_6 = 650.6$, $\omega_7 = 1156$, $\omega_{10} = 1574$, $\omega_{16} = 2981$, $\omega_{21} = 4543$, $\omega_{24} = 5522$, $\omega_{29} = 6705$, $\omega_{31} = 7827$
Translational	$\omega_2, \omega_3 = 370.4$, $\omega_4, \omega_5 = 582.9$, $\omega_8, \omega_9 = 1160$, $\omega_{11}, \omega_{12} = 1595$, $\omega_{14}, \omega_{15} = 2173$, $\omega_{17}, \omega_{18} = 3216$, $\omega_{19} = \omega_{20} = 4071$, $\omega_{22}, \omega_{23} = 5013$, $\omega_{25}, \omega_{26} = 5918$, $\omega_{27}, \omega_{28} = 6554$
Purely ring	$\omega_{13} = 1636$, $\omega_{30} = 6858$

impulse tests of the FE/CM model. Higher natural frequencies are not concerned in the nonlinear dynamics comparison because they are hardly excited.

The FE/CM model uses Rayleigh damping $[\mathbf{D}]_{fe} = \alpha_{fe}[\mathbf{M}]_{fe} + \beta_{fe}[\mathbf{K}]_{fe}$ for the finite element mesh and 3×3 viscous damping matrix for bearings. For the present example, the damping matrix for each bearing has only diagonal components. Table 5.2 shows the damping values for the FE/CM model. Processing the impulse responses of the FE/CM

Table 5.2: Bearing damping and Rayleigh damping for the FE/CM model.

Bearing damping	Translational (N·s/m)	Rotational (N·m·s)
Sun-ground	1	5
Carrier-ground	8	50
Ring-ground	5	20
Planet-carrier	radial: 2 tangential: 8	5
Rayleigh damping	$\alpha_{fe} = 479\ s$, $\beta_{fe} = 1.2 \times 10^{-7}\ s^{-1}$	

model with LMS Test.Lab [99] gives modal damping ratios associated with each of the rotational and translational natural frequencies in Table 5.1. These modal damping ratios were used in the analytical model. Modal damping ratios for the two purely ring natural frequencies are arbitrarily chosen. They do not affect the dynamic response of the non-gyroscopic planetary gear much because these two purely ring modes are hardly excited by the mesh excitations in the analytical model. Table 5.3 shows the modal damping ratios for all the natural frequencies in Table 5.1.

Table 5.3: Modal damping ratios for the analytical model.

Rotational	$\nu_1 = 25.7\%,\ \nu_6 = 6.93\%,\ \nu_7 = 3.72\%,\ \nu_{10} = 5.00\%,\ \nu_{16} = 5.50\%,\ \nu_{21} = 3.60\%,\ \nu_{24} = 0.990\%,\ \nu_{29} = 3.75\%,\ \nu_{31} = 1.30\%$
Translational	$\nu_2, \nu_3 = 18.2\%,\ \nu_4, \nu_5 = 6.55\%,\ \nu_8, \nu_9 = 3.62\%,\ \nu_{11}, \nu_{12} = 5.44\%,\ \nu_{14}, \nu_{15} = 3.63\%,\ \nu_{17}, \nu_{18} = 3.61\%,\ \nu_{19}, \nu_{20} = 3.05\%,\ \nu_{22}, \nu_{23} = 0.980\%,\ \nu_{25}, \nu_{26} = 3.44\%, \nu_{27}, \nu_{28} = 1.03\%$
Purely ring	$\nu_{13} = 5.48\%,\ \nu_{30} = 1.30\%$

Figure 5.3 shows the rms (mean-removed) values of steady-state planet 1 tangential deflection from the FE/CM model and numerical integration (NI) of the analytical discretized model in Eq. (5.11). The results from NI agree well with those from the FE/CM model. The spectra of the planet 1 tangential deflection for decreasing speed sweeps from FE/CM and NI in Fig. 5.4a and 5.4b show agreements between these two solutions at each mesh frequency harmonic.

A nonlinear jump occurs at the resonance of $2\omega_m \approx \omega_{29} = 6705$ Hz. Bending of the rms resonance curve to the left indicates softening nonlinearity induced by tooth contact loss. The rms response jumps up for increasing mesh frequency and jumps down at a lower frequency for decreasing mesh frequency. Multiple steady-state solutions are possible in between the jump up and jump down frequencies. A resonance at $\omega_m \approx \omega_{16} = 2981$ Hz

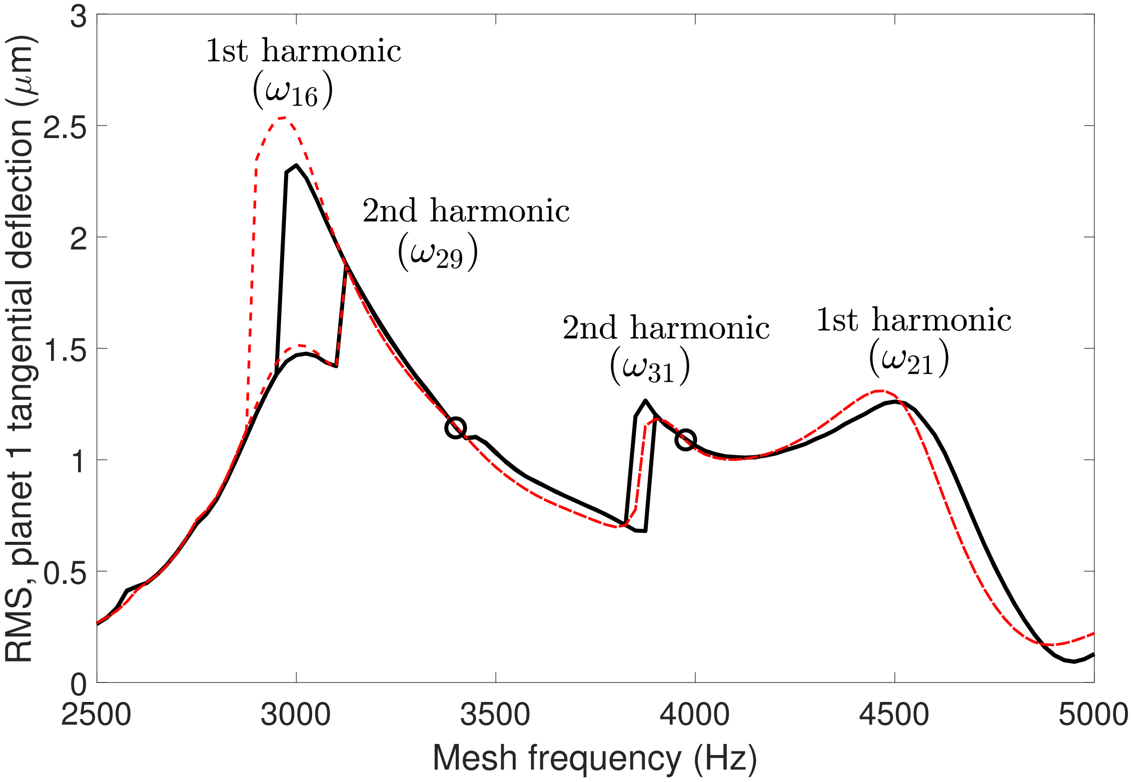

Figure 5.3: Steady state rms values (mean removed) of planet 1 tangential deflection for increasing and decreasing speed sweeps for the example system from Chapter 3. (———) FE/CM model; (- - - - -) analytical model.

coincides with the jump zone (Fig. 5.3). Because of the contribution of the resonance of ω_{16}, the rms curve reaches a peak before jumping up and down for increasing and decreasing mesh frequency, respectively. Another jump occurs at the resonances of $2\omega_m \approx \omega_{31} = 7827$ Hz for the FE/CM solution. The mesh frequency range between the jump up and jump down frequencies is small. At the jump down frequency, the system experiences quasi periodic-$3T_m$ vibrations (Fig. 5.4a), where $T_m = 2\pi/\omega_m$ is the mesh period. The analytical model predicts sharp amplitude change for this resonance instead.

Tooth separation starts from 3400 Hz and 3975 Hz (indicated by the open circles in Fig.

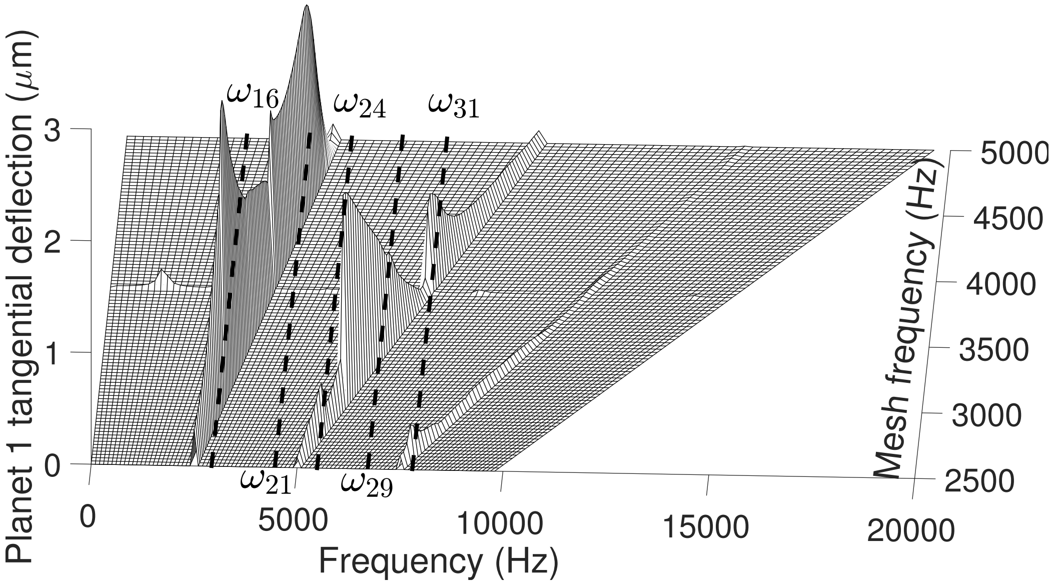

(a)

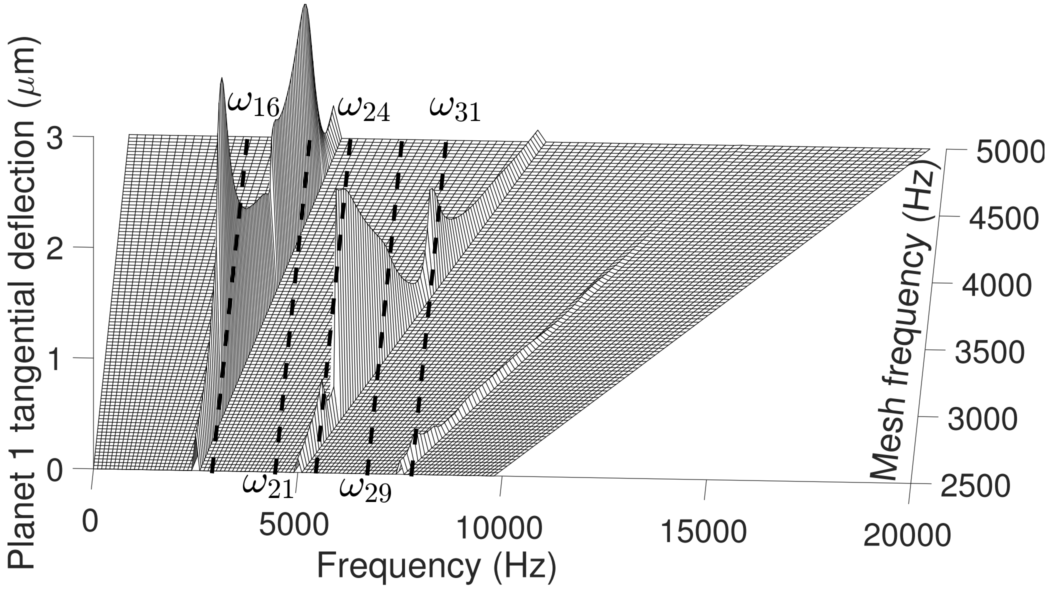

(b)

Figure 5.4: Waterfall spectra of planet 1 tangential deflection for decreasing speeds in (a) FE/CM and (b) analytical models for the same system used in Fig. 5.3.

5.3) and continues for decreasing mesh frequency until the amplitude jumps down. Figure 5.5 and Figure 5.6 show the mesh forces at the mesh frequencies 3200 Hz and 3900 Hz for the two zones of tooth separation, respectively. At ω_m = 3200 Hz, the sun-planet 1 mesh loses contact while the ring-planet 1 mesh does not. In contrast, the ring-planet 1 mesh loses contact while the sun-planet 1 mesh keeps in contact at $\omega_m = 3900$ Hz. This difference is related to the resonant modes at the two mesh frequencies. The resonant mode ω_{29} (not shown) at 3200 Hz has much higher sun-planet 1 mesh force than ring-planet 1 mesh force, while the ring-planet 1 mesh force is much higher for the resonant mode ω_{31} (not shown) at 3900 Hz. The mesh forces for the analytical and FE/CM models in Fig. 5.5 and Fig. 5.6 match well with each other.

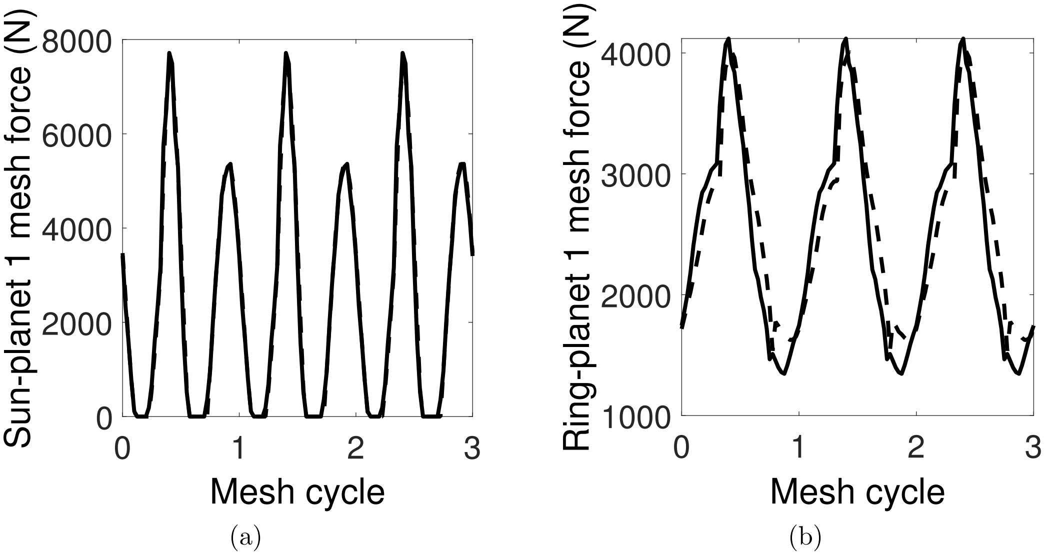

(a) (b)

Figure 5.5: Steady state (a) sun-planet 1 and (b) ring-planet 1 mesh loads at mesh frequency 3200 Hz for the same system used in Fig. 5.3. The solid and dashed lines represent results from the FE/CM and analytical models, respectively.

Figure 5.4 shows the resonances of ω_{16} and ω_{21} excited by the first harmonic of mesh frequency, ω_{24} and ω_{29} by the second harmonic, and ω_{31} by the second and third harmonics. All of these excited modes are rotational modes. No resonances of the translational modes (for example, ω_{17} and ω_{18}) occur. This agrees with the mesh phasing rule in [110, 111] that gives only rotational modes are excited by all harmonics of mesh frequency for an in-phase system with period-T_m vibrations.

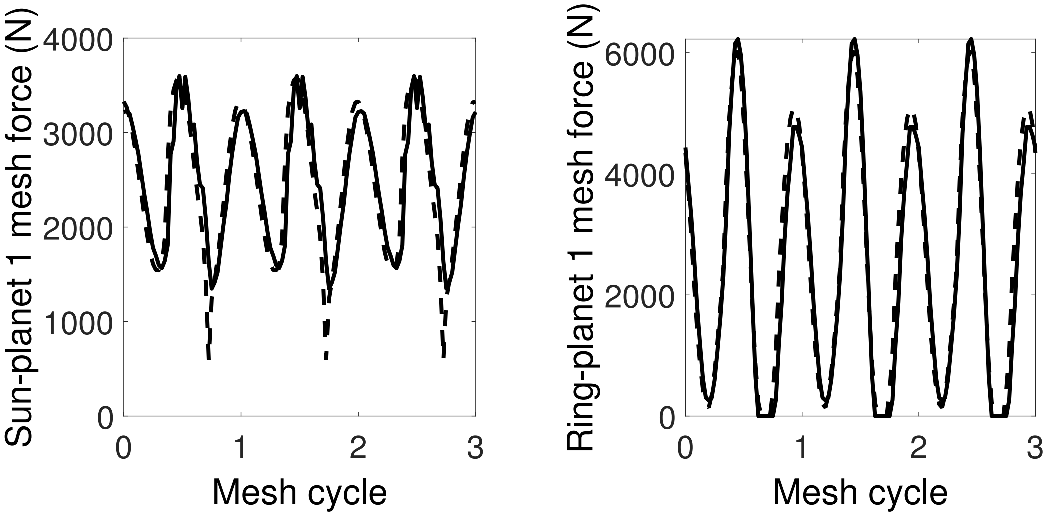

(a) (b)

Figure 5.6: Steady state (a) sun-planet 1 and (b) ring-planet 1 mesh loads at mesh frequency 3900 Hz for the same system used in Fig. 5.3. The solid and dashed lines represent results from the FE/CM and analytical models, respectively.

5.4 Analytical Solutions for Nonlinear Dynamics near Resonances

Numerical simulations provide limited understanding of the nonlinear dynamics. For example, one may not be able to find the answer from numerical results to the question why tooth separation occurs for certain resonances but does not for some others. Conclusions derived from numerical simulations of several cases may not generalize well to other cases. Refs. [56, 112] derived analytical solutions for the dynamics of idler gears and planetary gears using the method of multiple scales. These analytical solutions reveal how system parameters (for example, mesh stiffness variations) affect the nonlinear dynamics. Lumped-parameter models without speed-dependent gyroscopic effects are used in these two studies [56, 112], however. This work derives closed-form approximations for the dynamics of planetary gears with an elastic ring and gyroscopic and centripetal effects using multiple scale perturbation method.

We define two small parameters $\epsilon = |k_{r1}^{(1)}|/k_{rp}$ and $\mu = |k_{s1}^{(1)}|/k_{sp}$ with $\mu = g\epsilon$, where $g = O(1)$. Use of ϵ and μ in Eq. (5.4) yields

$$k_{sn}(t) = k_{sp} + \mu k_{sp} \sum_{L=1}^{\infty} [C_{sn}^{(L)} e^{jL\omega_m t} + c.c.], \tag{5.12a}$$

$$k_{rn}(t) = k_{rp} + \epsilon k_{rp} \sum_{L=1}^{\infty} [C_{rn}^{(L)} e^{jL\omega_m t} + c.c.], \tag{5.12b}$$

$$C_{sn}^{(L)} = k_{sn}^{(L)}/|k_{s1}^{(1)}|, \qquad C_{rn}^{(L)} = k_{rn}^{(L)}/|k_{r1}^{(1)}|. \tag{5.12c}$$

The time of tooth separation is small, i.e., $O(\epsilon)$, compared to one mesh period, as shown in Fig. 5.5 and Fig. 5.6. As a result, the tooth separation functions can be expressed as

$$H(\Delta_{sn}) = 1 + \mu h_{sn}, \qquad H(\Delta_{rn}) = 1 + \epsilon h_{rn}. \tag{5.13}$$

Substitution of Eq. (5.3) into Eq. (5.1a) and invoking Eqs. (5.12) and (5.13) give

$$\begin{aligned} \mathbf{M}\ddot{\boldsymbol{\chi}} + \mathbf{G}\dot{\boldsymbol{\chi}} + \Bigg[\mathbf{K}_0 &+ \sum_{n=1}^{N} k_{sp}(1 + \mu \hat{Q}_{sn})\mathbf{K}_{sn}(1 + \mu h_{sn}) \\ &+ \sum_{n=1}^{N} k_{rp}(1 + \epsilon \hat{Q}_{rn})\mathbf{K}_{rn}(1 + \epsilon h_{rn}) - \mathbf{C}\Bigg]\boldsymbol{\chi} = \mathbf{f}, \end{aligned} \tag{5.14a}$$

$$\mathbf{G} = (\Omega_r \mathbf{G}_r + \Omega_c \mathbf{G}_c), \qquad \mathbf{C} = \Omega_r^2 \mathbf{C}_r + \Omega_c^2 \mathbf{C}_c + 2\Omega_r \Omega_c \mathbf{C}_{rc}, \tag{5.14b}$$

$$\hat{Q}_{sn} = \sum_{L=1}^{\infty} [C_{sn}^{(L)} e^{jL\omega_m t} + c.c.], \qquad \hat{Q}_{rn} = \sum_{L=1}^{\infty} [C_{rn}^{(L)} e^{jL\omega_m t} + c.c.]. \tag{5.14c}$$

The state space form of Eq. (5.14a) is

$$\mathbf{A}\dot{\boldsymbol{\phi}} + \mathbf{B}\boldsymbol{\phi} + \epsilon \sum_{n=1}^{N} \Big[g k_{sp} Q_{sn} \mathbf{E}_{sn} + k_{rp} Q_{rn} \mathbf{E}_{rn}\Big]\boldsymbol{\phi} + O(\epsilon^2) = \hat{\mathbf{f}}, \tag{5.15a}$$

$$\boldsymbol{\phi} = \begin{bmatrix} \dot{\boldsymbol{\chi}}^T & \boldsymbol{\chi}^T \end{bmatrix}^T, \tag{5.15b}$$

$$\mathbf{A} = \begin{pmatrix} \mathbf{M} & \mathbf{0} \\ \mathbf{0} & \mathbf{K}-\mathbf{C} \end{pmatrix}, \qquad \mathbf{B} = \begin{pmatrix} \mathbf{G} & \mathbf{K}-\mathbf{C} \\ -(\mathbf{K}-\mathbf{C}) & \mathbf{0} \end{pmatrix}, \tag{5.15c}$$

$$\mathbf{E}_{sn} = \begin{pmatrix} \mathbf{0} & \mathbf{K}_{sn} \\ \mathbf{0} & \mathbf{0} \end{pmatrix}, \qquad \mathbf{E}_{rn} = \begin{pmatrix} \mathbf{0} & \mathbf{K}_{rn} \\ \mathbf{0} & \mathbf{0} \end{pmatrix}, \tag{5.15d}$$

$$\hat{\mathbf{f}} = \begin{bmatrix} \mathbf{f}^T & \mathbf{0} \end{bmatrix}^T, \tag{5.15e}$$

$$Q_{sn} = \hat{Q}_{sn} + h_{sn}, \qquad Q_{rn} = \hat{Q}_{rn} + h_{rn}. \tag{5.15f}$$

We define the inner product of two elements $\mathbf{a} = \begin{bmatrix} \mathbf{a}_1^T & \mathbf{a}_2^T \end{bmatrix}^T$ and $\mathbf{b} = \begin{bmatrix} \mathbf{b}_1^T & \mathbf{b}_2^T \end{bmatrix}^T$ in the state space as

$$(\mathbf{a},\ \mathbf{b}) = \langle \mathbf{a}_1,\ \mathbf{b}_1 \rangle + \langle \mathbf{a}_2,\ \mathbf{b}_2 \rangle, \tag{5.16}$$

where $\mathbf{a}_i$ and $\mathbf{b}_i$ $(i = 1, 2)$ have the same form of $\boldsymbol{\chi}$ in Eq. (5.1b) and $\langle \cdot,\ \cdot \rangle$ is the configuration space inner product defined in Eq. (5.8). The eigenvalue problem of Eq. (5.15a) considering linear time-invariant mesh stiffnesses is

$$\lambda_i \mathbf{A} \boldsymbol{\phi}_i + \mathbf{B} \boldsymbol{\phi}_i = \mathbf{0}, \qquad \boldsymbol{\phi}_i = \begin{bmatrix} \lambda_i \boldsymbol{\chi}_i^T & \boldsymbol{\chi}_i^T \end{bmatrix}^T. \tag{5.17}$$

The eigenfunctions $\boldsymbol{\phi}_i(\theta)$ are orthogonal with respect to $\mathbf{A}$ and $\mathbf{B}$ such that

$$\big(\boldsymbol{\phi}_l,\ \mathbf{A}\boldsymbol{\phi}_i\big) = \delta_{li}, \qquad \big(\boldsymbol{\phi}_l,\ \mathbf{B}\boldsymbol{\phi}_i\big) = -j\omega_i \delta_{li}, \tag{5.18}$$

where δ_{li} is the Kronecker delta.

The solution of Eq. (5.15a) is expanded in modal coordinates as

$$\boldsymbol{\phi}(\theta, t) = \sum_{i=1}^{\infty} [a_i(t)\boldsymbol{\phi}_i(\theta) + \bar{a}_i(t)\bar{\boldsymbol{\phi}}_i(\theta)]. \tag{5.19}$$

Substitution of Eq. (5.19) into Eq. (5.15a), taking the inner product of the resulting equation with the eigenfunctions $\boldsymbol{\phi}_l(\theta)$, and invoking the orthogonality conditions in Eq. (5.18) give

$$\dot{a}_l + \epsilon\rho_l a_l - j\omega_l a_l + \epsilon \sum_{i=1}^{\infty}\sum_{n=1}^{N} \Big\{ g k_{sp} Q_{sn} \big[\big(\boldsymbol{\phi}_l,\ \mathbf{E}_{sn}\boldsymbol{\phi}_i\big) a_i + \big(\boldsymbol{\phi}_l,\ \mathbf{E}_{sn}\bar{\boldsymbol{\phi}}_i\big)\bar{a}_i \big]$$

$$+ k_{rp} Q_{rn} \big[\big(\boldsymbol{\phi}_l,\ \mathbf{E}_{rn}\boldsymbol{\phi}_i\big) a_i + \big(\boldsymbol{\phi}_l,\ \mathbf{E}_{rn}\bar{\boldsymbol{\phi}}_i\big)\bar{a}_i \big] \Big\} = f_l, \qquad l = 1, 2, \ldots, \tag{5.20a}$$

$$f_l = \big(\boldsymbol{\phi}_l,\ \hat{\mathbf{f}}\big), \tag{5.20b}$$

where modal damping $\epsilon\rho_l = 2\nu_l\omega_l$ is introduced.

By introducing the multiple time scales $t_n = \epsilon^n t$, we expand the modal coordinates in an asymptotic power series of ϵ as

$$a_l(t;\epsilon) = a_{l0}(t_0, t_1) + \epsilon a_{l1}(t_0, t_1) + O(\epsilon^2), \qquad l = 1, 2, \ldots. \tag{5.21}$$

Substitution of Eq. (5.21) into Eq. (5.20a), using $d/dt \to \partial/\partial t_0 + \epsilon\partial/\partial t_1$, and collecting like powers of ϵ give

$$\frac{\partial a_{l0}}{\partial t_0} - j\omega_l a_{l0} = f_l, \tag{5.22a}$$

$$\frac{\partial a_{l1}}{\partial t_0} - j\omega_l a_{l1} = -\frac{\partial a_{l0}}{\partial t_1} - \rho_l a_{l0} - \sum_{i=1}^{\infty}\sum_{n=1}^{N} \Big\{ g k_{sp} Q_{sn} \big[\big(\boldsymbol{\phi}_l,\ \mathbf{E}_{sn}\boldsymbol{\phi}_i\big) a_{i0}$$

$$+ \big(\boldsymbol{\phi}_l,\ \mathbf{E}_{sn}\bar{\boldsymbol{\phi}}_i\big)\bar{a}_{i0} \big] + k_{rp} Q_{rn} \big[\big(\boldsymbol{\phi}_l,\ \mathbf{E}_{rn}\boldsymbol{\phi}_i\big) a_{i0} + \big(\boldsymbol{\phi}_l,\ \mathbf{E}_{rn}\bar{\boldsymbol{\phi}}_i\big)\bar{a}_{i0} \big] \Big\}. \tag{5.22b}$$

Substitution of Eq. (5.15d) into $\big(\boldsymbol{\phi}_l,\ \mathbf{E}_{sn}\boldsymbol{\phi}_i\big)$, $\big(\boldsymbol{\phi}_l,\ \mathbf{E}_{sn}\bar{\boldsymbol{\phi}}_i\big)$, $\big(\boldsymbol{\phi}_l,\ \mathbf{E}_{rn}\boldsymbol{\phi}_i\big)$, and $\big(\boldsymbol{\phi}_l,\ \mathbf{E}_{rn}\bar{\boldsymbol{\phi}}_i\big)$

and expansion of these four quantities give

$$\big(\boldsymbol{\phi}_l,\ \mathbf{E}_{sn}\boldsymbol{\phi}_i\big) = -j\omega_l \bar{\Delta}^{[l]}_{sn}\Delta^{[i]}_{sn}, \qquad \big(\boldsymbol{\phi}_l,\ \mathbf{E}_{sn}\bar{\boldsymbol{\phi}}_i\big) = -j\omega_l \bar{\Delta}^{[l]}_{sn}\bar{\Delta}^{[i]}_{sn}, \tag{5.23a}$$

$$\big(\boldsymbol{\phi}_l,\ \mathbf{E}_{rn}\boldsymbol{\phi}_i\big) = -j\omega_l \bar{\Delta}^{[l]}_{rn}\Delta^{[i]}_{rn}, \qquad \big(\boldsymbol{\phi}_l,\ \mathbf{E}_{rn}\bar{\boldsymbol{\phi}}_i\big) = -j\omega_l \bar{\Delta}^{[l]}_{rn}\bar{\Delta}^{[i]}_{rn}, \tag{5.23b}$$

$$\begin{aligned}\Delta^{[l]}_{sn} &= (-x^{[l]}_s \sin\psi_{sn} + y^{[l]}_s \cos\psi_{sn} + u^{[l]}_s)\\ &\qquad + (-\zeta^{[l]}_n \sin\alpha_s - \eta^{[l]}_n \cos\alpha_s + u^{[l]}_n),\end{aligned} \tag{5.23c}$$

$$\begin{aligned}\Delta^{[l]}_{rn} &= (\zeta^{[l]}_n \sin\alpha_r - \eta^{[l]}_n \cos\alpha_r - u^{[l]}_n)\\ &\qquad + [-u^{[l]} \sin\alpha_r + v^{[l]} \cos\alpha_r - \Gamma\beta^{[l]} \cos\alpha_r]_{\theta=\psi_n},\end{aligned} \tag{5.23d}$$

where $\Delta^{[l]}_{sn}$ and $\Delta^{[l]}_{rn}$ are the n-th sun-planet and ring-planet mesh deflections for the mode $\boldsymbol{\chi}_l$. Chapter 4 shows these modal mesh deflections satisfy

$$\Delta^{[l]}_{sn} = e^{jT_l\psi_n}\Delta^{[l]}_{s1}, \qquad \Delta^{[l]}_{rn} = e^{jT_l\psi_n}\Delta^{[l]}_{r1}, \tag{5.24}$$

where $T_l \in \{0, 1, 2, \ldots, N-1\}$ is an integer or phase index associated with the mode $\boldsymbol{\chi}_l$. Planetary gears with gyroscopic effects have three types of modes: rotational, translational, and planet modes. Planet modes only exist for systems with $N > 3$ planets. All rotational modes have phase index 0. A translational mode is associated with phase index 1 or $N-1$ (not both), and a planet mode has phase index $d \in \{2, \ldots, N-2\}$.

We assume that a single mode dominates the response near resonances. The response is nearly harmonic [16, 113, 114] and has the form

$$\boldsymbol{\chi} = \hat{\boldsymbol{\chi}} + [a_l\boldsymbol{\chi}_l e^{j\omega t} + c.c.], \tag{5.25}$$

where $\omega \approx \omega_l$ is the response frequency. For primary resonances, the response frequency equals the mesh frequency, i.e., $\omega = \omega_m$. For subharmonic, superharmonic, and second harmonic resonances, $\omega = \omega_m/2$, $\omega = 2\omega_m$, and $\omega = 2\omega_m$, respectively. The limitations of the assumption of single mode dominance are discussed later.

5.4.1 Primary Resonance

Primary resonance occurs when the mesh frequency is close to a natural frequency, i.e., $\omega_m = \omega_k + \epsilon\sigma$, where σ is a detuning parameter. The solution of Eq. (5.22a) is

$$a_{l0} = A_l(t_1)e^{j\omega_l t_0} + jf_l/\omega_l, \qquad l = 1, 2, \ldots. \tag{5.26}$$

Substitution of Eq. (5.26) into Eq. (5.22b) and vanishing the secular terms on the right hand side of the resulting equation lead to

$$\partial A_l/\partial t_1 + \rho A_l + \sum_{n=1}^{N} \Big[g k_{sp} h_{sn}\big(\boldsymbol{\phi}_l,\ \mathbf{E}_{sn}\boldsymbol{\phi}_l\big) + +k_{rp} h_{rn}\big(\boldsymbol{\phi}_l,\ \mathbf{E}_{rn}\boldsymbol{\phi}_l\big) \Big] A_l = 0 \tag{5.27}$$

for $l \neq k$. According to Ref. [56], the steady state solution of Eq. (5.27) is $A_l = 0$. The solution for $l = k$ in Eq. (5.26) is

$$a_{k0} = A_k(t_1)e^{j(\omega_m - \epsilon\sigma)t_0} + jf_k/\omega_k = B_k(t_1)e^{j\omega_m t_0} + jf_k/\omega_k, \tag{5.28}$$

where $B_k(t_1) = A_k(t_1)e^{-j\sigma t_1}$. Therefore, the leading order solution is periodic with mesh frequency. Substitution of $A_k(t_1) = 1/2d_k(t_1)e^{j\phi_k(t_1)}$ into Eq. (5.28) yields

$$a_{k0} = 1/2d_k(t_1)e^{j(\omega_m t_0 - \gamma_k(t_1))} + jf_k/\omega_k, \tag{5.29}$$

where $\gamma_k(t_1) = \sigma t_1 - \phi_k(t_1)$.

The sun-planet and ring-planet mesh deflections are

$$\begin{aligned}\Delta_{sn} &= \Delta_{sn,0} + 1/2 d_k (\Delta_{sn}^{[k]} e^{j(\omega_m t_0 - \gamma_k)} + c.c.) \\ &= \Delta_{sn,0} + d_k |\Delta_{sn}^{[k]}| \cos(\omega_m t_0 - \gamma_k + \theta_{sn}^{[k]}), \qquad (5.30a) \\ \Delta_{rn} &= \Delta_{rn,0} + 1/2 d_k (\Delta_{rn}^{[k]} e^{j(\omega_m t_0 - \gamma_k)} + c.c.) \\ &= \Delta_{rn,0} + d_k |\Delta_{rn}^{[k]}| \cos(\omega_m t_0 - \gamma_k + \theta_{rn}^{[k]}), \qquad (5.30b)\end{aligned}$$

$$\Delta_{sn,0} = \sum_{i=1}^{\infty} (j f_i/\omega_i) \Delta_{sn}^{[i]} + c.c., \qquad \Delta_{rn,0} = \sum_{i=1}^{\infty} (j f_i/\omega_i) \Delta_{rn}^{[i]} + c.c., \qquad (5.30c)$$

where $\theta_{sn}^{[k]}$ and $\theta_{rn}^{[k]}$ are the phase angles of the complex-valued modal mesh deflections $\Delta_{sn}^{[k]}$ and $\Delta_{rn}^{[k]}$, respectively. In general, $\Delta_{sn}^{[k]} \neq \Delta_{rn}^{[k]}$ for complex-valued gyroscopic modes. Therefore, the sun-planet and ring-planet mesh deflections for a single planet are out-of-phase. This differs from the case for non-gyroscopic planetary gears where the sun-planet and ring-planet mesh deflections for a single planet are either in-phase or 180 degree out-of-phase.

Figure 5.7 depicts the relationship between the tooth separation function $H(\Delta_{jn})$ and the corresponding mesh deflection Δ_{jn}, where $j = s, r$. They are in-phase with each other. Fourier expansions of the tooth separation functions are

$$H(\Delta_{sn}) = 1 + \mu \Big\{ h_{sn}^{(0)} + \sum_{q=1}^{\infty} [h_{sn}^{(q)} e^{jq(\omega_m t_0 - \gamma_k + \theta_{sn}^{[k]})} + c.c.] \Big\}, \qquad (5.31a)$$

$$H(\Delta_{rn}) = 1 + \epsilon \Big\{ h_{rn}^{(0)} + \sum_{q=1}^{\infty} [h_{rn}^{(q)} e^{jq(\omega_m t_0 - \gamma_k + \theta_{rn}^{[k]})} + c.c.] \Big\}, \qquad (5.31b)$$

The time of separation during one period of response is denoted by ξ_{jn}/ω_m. The Fourier coefficients in Eq. (5.31) in terms of ξ_{jn} are

$$h_{sn}^{(0)} = -\frac{\xi_{sn}}{2\pi\mu}, \qquad h_{rn}^{(0)} = -\frac{\xi_{rn}}{2\pi\epsilon}, \qquad (5.32a)$$

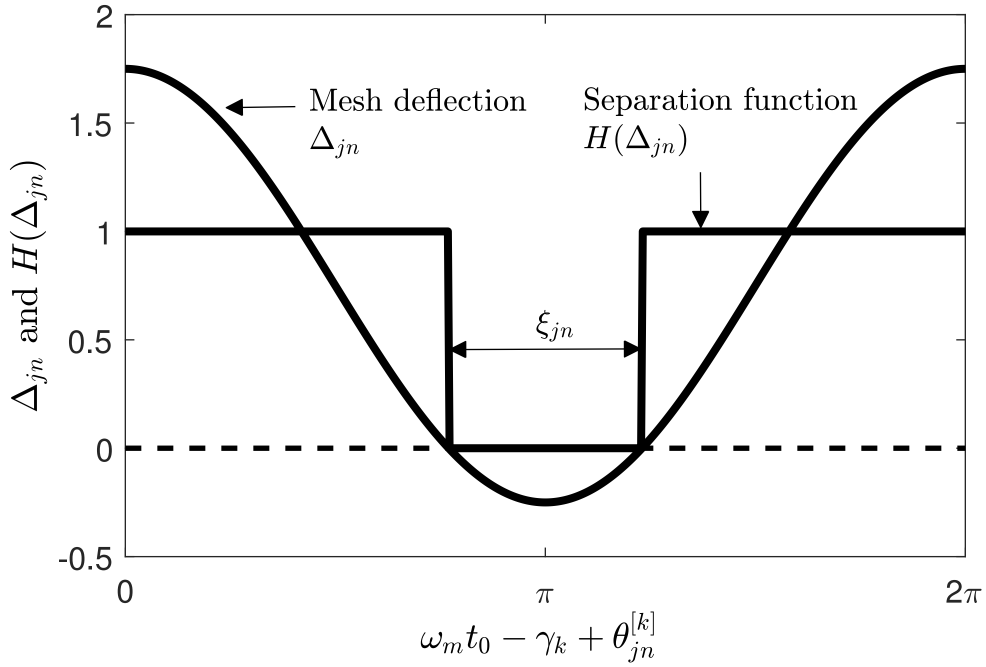

Figure 5.7: Tooth separation function and mesh deflection.

$$h_{sn}^{(q)} = \frac{\sin q(\pi - \xi_{sn}/2)}{q\pi\mu}, \qquad h_{rn}^{(q)} = \frac{\sin q(\pi - \xi_{rn}/2)}{q\pi\epsilon}, \qquad q = 1, 2, \ldots. \tag{5.32b}$$

Substitution of Eqs. (5.26) and (5.31) into the k-th modal equation of Eq. (5.22b) and use of $\omega_m = \omega_k + \epsilon\sigma$ yield the solvability condition

$$\begin{aligned}
&\frac{\partial A_k}{\partial t_1} + \rho_k A_k + \sum_{n=1}^{N} k_{rp} C_{rn}^{(2)} e^{j2\sigma t_1} \big(\boldsymbol{\phi}_k,\ \mathbf{E}_{rn}\bar{\boldsymbol{\phi}}_k\big)\bar{A}_k \\
&+ \sum_{i=1}^{\infty}\sum_{n=1}^{N} k_{rp} C_{rn}^{(1)} e^{j\sigma t_1} \big[\big(\boldsymbol{\phi}_k,\ \mathbf{E}_{rn}\boldsymbol{\phi}_i\big)(j\frac{f_i}{\omega_i}) + \big(\boldsymbol{\phi}_k,\ \mathbf{E}_{rn}\bar{\boldsymbol{\phi}}_i\big)(-j\frac{\bar{f}_i}{\omega_i})\big] \\
&+ \sum_{i=1}^{\infty}\sum_{n=1}^{N} k_{rp} h_{rn}^{(1)} e^{j(\sigma t_1 - \varphi_{rn})} \big[\big(\boldsymbol{\phi}_k,\ \mathbf{E}_{rn}\boldsymbol{\phi}_i\big)(j\frac{f_i}{\omega_i}) + \big(\boldsymbol{\phi}_k,\ \mathbf{E}_{rn}\bar{\boldsymbol{\phi}}_i\big)(-j\frac{\bar{f}_i}{\omega_i})\big] \\
&+ \sum_{n=1}^{N} k_{rp} \big[h_{rn}^{(0)} \big(\boldsymbol{\phi}_k,\ \mathbf{E}_{rn}\boldsymbol{\phi}_k\big)A_k + h_{sn}^{(2)} e^{j2(\sigma t_1 - \varphi_{rn})} \big(\boldsymbol{\phi}_k,\ \mathbf{E}_{rn}\bar{\boldsymbol{\phi}}_k\big)\bar{A}_k\big] \\
&+ (r \to s) = 0,
\end{aligned} \tag{5.33}$$

where $r \to s$ denotes corresponding terms for the sun-planet mesh with k_{rp} replaced by gk_{sp}. Substitution of $A_k(t_1) = 1/2d_k(t_1)e^{j\phi_k(t_1)}$ into Eq. (5.33), separation of the resulting equation into real and imaginary parts, considering only the first mesh stiffness harmonic terms, and invoking Eqs. (5.23) and (5.30c) give

$$\frac{\partial d_k}{\partial t_1} = -\rho_k d_k - 2\omega_k|\hat{R}_3|\sin(\gamma_k + \psi), \tag{5.34a}$$

$$d_k\frac{\partial \gamma_k}{\partial t_1} = \sigma d_k - 2\omega_k\hat{R}_1 - 2\omega_k\hat{R}_2 d_k - 2\omega_k|\hat{R}_3|\cos(\gamma_k + \psi), \tag{5.34b}$$

$$\hat{R}_1 = \sum_{n=1}^{N} k_{rp}h_{rn}^{(1)}|\Delta_{rn}^{[k]}|\Delta_{rn,0} + (r \to s), \tag{5.34c}$$

$$\hat{R}_2 = \sum_{n=1}^{N} \frac{k_{rp}}{2}(h_{rn}^{(0)} + h_{rn}^{(2)})|\Delta_{rn}^{[k]}|^2 + (r \to s), \tag{5.34d}$$

$$\hat{R}_3 = \sum_{n=1}^{N} k_{rp}C_{rn}^{(1)}\bar{\Delta}_{rn}^{[k]}\Delta_{rn,0} + (r \to s), \tag{5.34e}$$

where ψ is the phase angle of $\hat{R}_3$. We discuss the error of neglecting the second and higher mesh stiffness harmonic later.

For steady state periodic response, $\partial d_k/\partial t_1 = \partial\gamma_k/\partial t_1 = 0$ in Eqs. (5.34a) and (5.34b) yields the frequency response function

$$\omega_m = \omega_k + \frac{2\omega_k}{d_k}\left[R_1 + R_2 d_k \pm \sqrt{|R_3|^2 - (\nu_k d_k)^2}\right], \tag{5.35a}$$

$$R_1 = \sum_{n=1}^{N}\left[|k_{s1}^{(1)}|h_{sn}^{(1)}|\Delta_{sn}^{[k]}|\Delta_{sn,0} + |k_{r1}^{(1)}|h_{rn}^{(1)}|\Delta_{rn}^{[k]}|\Delta_{rn,0}\right], \tag{5.35b}$$

$$R_2 = \sum_{n=1}^{N}\frac{1}{2}\left[|k_{s1}^{(1)}|(h_{sn}^{(0)} + h_{sn}^{(2)})|\Delta_{sn}^{[k]}|^2 + |k_{r1}^{(1)}|(h_{rn}^{(0)} + h_{rn}^{(2)})|\Delta_{rn}^{[k]}|^2\right], \tag{5.35c}$$

$$R_3 = \sum_{n=1}^{N}\left[k_{sn}^{(1)}\bar{\Delta}_{sn}^{[k]}\Delta_{sn,0} + k_{rn}^{(1)}\bar{\Delta}_{rn}^{[k]}\Delta_{rn,0}\right]. \tag{5.35d}$$

The steady state phase γ_k is

$$\gamma_k = \tan^{-1}\left[\frac{\rho_k d_k}{2\omega_k \hat{R}_1 + 2\omega_k \hat{R}_2 d_k - \sigma d_k}\right] - \psi. \tag{5.36}$$

Requiring $\Delta_{sn} = \Delta_{rn} = 0$ in Eq. (5.30) leads to the tooth separation angle

$$\xi_{jn} = 2\cos^{-1}\left[\frac{\Delta_{jn,0}}{d_k|\Delta_{jn}^{[k]}|}\right], \qquad j = s, r. \tag{5.37}$$

The quantities $\Delta_{sn,0}$ and $\Delta_{rn,0}$ in Eq. (5.30c) are identical for different planets (i.e., different n) because the modal external force $f_i \neq 0$ only for modes with phase index $T_i = 0$ and modes of this type have identical mesh deflections for each planet (Eq. (5.24)). According to Eq. (5.24), the amplitudes of the mesh deflections for an arbitrary mode $\boldsymbol{\chi}_k$ are identical for each planet, i.e., $|\Delta_{jn}^{[k]}| = |\Delta_{j1}^{[k]}|$ for $j = s, r$. Therefore, the tooth separation angles ξ_{jn} in Eq. (5.37) are independent of the planet index n. With $\xi_{jn} = \xi_{j1}$, the tooth separation Fourier coefficients $h_{jn}^{(q)}$ in Eq. (5.32) for $j = s, r$ and $q = 0, 1, 2, \ldots$ are identical for different n.

Following the above discussions and using Eq. (5.5) with the mesh phase in Eq. (5.6) for $\Omega_c > \Omega_r$ and Eq. (5.24), the R_l in Eq. (5.35) are

$$R_1 = N\Big[|k_{s1}^{(1)}|h_{s1}^{(1)}|\Delta_{s1}^{[k]}|\Delta_{s1,0} + |k_{r1}^{(1)}|h_{r1}^{(1)}|\Delta_{r1}^{[k]}|\Delta_{r1,0}\Big], \tag{5.38a}$$

$$R_2 = \frac{N}{2}\Big[|k_{s1}^{(1)}|(h_{s1}^{(0)} + h_{s1}^{(2)})|\Delta_{s1}^{[k]}|^2 + |k_{r1}^{(1)}|(h_{r1}^{(0)} + h_{r1}^{(2)})|\Delta_{r1}^{[k]}|^2\Big], \tag{5.38b}$$

$$R_3 = \Big[k_{s1}^{(1)}\bar{\Delta}_{s1}^{[k]}\Delta_{s1,0} + k_{r1}^{(1)}\bar{\Delta}_{r1}^{[k]}\Delta_{r1,0}\Big]\sum_{n=1}^{N} e^{j(Z_r - T_k)\psi_n}. \tag{5.38c}$$

Because the identity

$$\sum_{n=1}^{N} e^{jm\psi_n} = \begin{Bmatrix} N, & m/N = \text{integer} \\ 0, & m/N \neq \text{integer} \end{Bmatrix} \tag{5.39}$$

holds for integer value of m, R_3 vanishes for $(Z_r - T_k)/N \neq$ integer. From Eq. (5.35), the peak resonant amplitude for the k-th mode is

$$d_k^{\text{peak}} = |R_3|/\nu_k. \tag{5.40}$$

Because $R_3 = 0$ for the mode $\boldsymbol{\chi}_k$ with its phase index satisfying $(Z_r - T_k)/N \neq$ integer, no resonance occurs for the mode $\boldsymbol{\chi}_k$.

Eq. (5.38) applies to systems with $\Omega_c > \Omega_r$. For systems with $\Omega_c < \Omega_r$, use of $-\gamma_{rn}$ from Eq. (5.6) as the mesh phase in Eq. (5.35) leads to the same R_1 and R_2 as those in Eq. (5.38) but a different R_3 as

$$R_3 = \Big[k_{s1}^{(1)}\bar{\Delta}_{s1}^{[k]}\Delta_{s1,0} + k_{r1}^{(1)}\bar{\Delta}_{r1}^{[k]}\Delta_{r1,0}\Big]\sum_{n=1}^{N} e^{-j(Z_r+T_k)\psi_n}. \tag{5.41}$$

From Eq. (5.41), the primary resonance of the mode $\boldsymbol{\chi}_k$ is suppressed if its phase index satisfies $(Z_r + T_k)/N \neq$ integer.

If $(Z_r - T_k)/N =$ integer for systems with $\Omega_c > \Omega_r$ or $(Z_r + T_k)/N =$ integer for systems with $\Omega_c < \Omega_r$, the term R_3 has the expression

$$R_3 = N\Big[k_{s1}^{(1)}\bar{\Delta}_{s1}^{[k]}\Delta_{s1,0} + k_{r1}^{(1)}\bar{\Delta}_{r1}^{[k]}\Delta_{r1,0}\Big]. \tag{5.42}$$

According to Eqs. (5.40) and (5.42), the peak amplitude depends only on known quantities and is immediately calculable. From Eq. (5.35), the peak frequency is

$$\omega_m^{\text{peak}} = \omega_k + \frac{2\omega_k}{|R_3|}(\nu_k R_1 + R_2|R_3|). \tag{5.43}$$

To calculate this quantity, we determine the tooth separation angle ξ_{jn} using Eq. (5.37) and calculate tooth separation Fourier coefficients $h_{jn}^{(q)}$ for $q = 0, 1, 2$ using Eq. (5.32) so that R_1 and R_2 can be computed.

The condition $\xi_{jn} = 0$ marks the onset of contact loss for sun-planet ($j = s$) and ring-planet ($j = r$) meshes. The amplitudes for the contact loss initiation points are

$$d_{k,j} = \frac{\Delta_{j1,0}}{|\Delta_{j1}^{[k]}|}, \qquad j = s, r. \tag{5.44}$$

The corresponding frequencies that bound the range of contact loss are determined from Eq. (5.35) as

$$\omega_{m,j} = \omega_k \pm \frac{2\omega_k}{d_{k,j}}\sqrt{|R_3|^2 - (\nu_k d_{k,j})^2}, \qquad j = s, r. \tag{5.45}$$

Whether contact loss occurs or not depends on the peak and contact loss initiation point amplitudes. When $d_k^{\text{peak}} > \max(d_{k,s}, d_{k,r})$, contact loss occurs for both sun-planet and ring-planet meshes. When $d_k^{\text{peak}} \leq \max(d_{k,s}, d_{k,r})$ and $d_k^{\text{peak}} > \min(d_{k,s}, d_{k,r})$, only one of the two meshes that has lower contact loss initiation point amplitude experience contact loss. Otherwise, no contact loss occurs.

Stability of the analytical solution in Eq. (5.35) is determined by the eigenvalues of Eqs. (5.34a) and (5.34b) linearized about an equilibrium.

5.4.2 Subharmonic Resonance

Subharmonic resonance with period-$2T_m$ motion occurs when the mesh frequency is close to twice a natural frequency, i.e., $\omega_m = 2\omega_k + \epsilon\sigma$. A similar procedure as for primary resonance gives the frequency response relation for subharmonic resonance as

$$\omega_m = 2\omega_k + 4\omega_k \left[\frac{R_1}{d_k} + R_2 \pm \sqrt{|R_3|^2 - \nu_k^2} \right], \tag{5.46a}$$

$$R_1 = N\Big[|k_{s1}^{(1)}| h_{s1}^{(1)} |\Delta_{s1}^{[k]}| \Delta_{s1,0} + |k_{r1}^{(1)}| h_{r1}^{(1)} |\Delta_{r1}^{[k]}| \Delta_{r1,0} \Big], \tag{5.46b}$$

$$R_2 = \frac{N}{2}\Big[|k_{s1}^{(1)}| (h_{s1}^{(0)} + h_{s1}^{(2)}) |\Delta_{s1}^{[k]}|^2 + |k_{r1}^{(1)}| (h_{r1}^{(0)} + h_{r1}^{(2)}) |\Delta_{r1}^{[k]}|^2 \Big], \tag{5.46c}$$

$$R_3 = \frac{1}{2}\Big[k_{s1}^{(1)} \bar{\Delta}_{s1}^{[k]} \bar{\Delta}_{s1}^{[k]} + k_{r1}^{(1)} \bar{\Delta}_{r1}^{[k]} \bar{\Delta}_{r1}^{[k]} \Big] \sum_{n=1}^{N} e^{j(Z_r - 2T_k)\psi_n}. \tag{5.46d}$$

According to Eq. (5.39), $R_3 = 0$ for modes $\boldsymbol{\chi}_k$ with phase index satisfying $(Z_r - 2T_k)/N \neq$ integer, and, therefore, subharmonic resonance does not occur. Otherwise,

$$R_3 = \frac{N}{2}\Big[k_{s1}^{(1)} \bar{\Delta}_{s1}^{[k]} \bar{\Delta}_{s1}^{[k]} + k_{r1}^{(1)} \bar{\Delta}_{r1}^{[k]} \bar{\Delta}_{r1}^{[k]} \Big]. \tag{5.47}$$

If the absolute value of R_3 is smaller than the modal damping ratio ν_k, subharmonic resonance is suppressed by the damping. Otherwise, subharmonic resonance occurs. Because R_3 depends on only the number of planets, mesh stiffness variations, and modal deflections, the occurrence of subharmonic resonance can be quickly identified.

The mesh phase γ_{rn} in Eq. (5.6) for $\Omega_c > \Omega_r$ is used in the derivation of Eq. (5.46). For systems with $\Omega_c < \Omega_r$, the term R_3 in Eq. (5.46) becomes

$$R_3 = \frac{1}{2}\Big[k_{s1}^{(1)} \bar{\Delta}_{s1}^{[k]} \bar{\Delta}_{s1}^{[k]} + k_{r1}^{(1)} \bar{\Delta}_{r1}^{[k]} \bar{\Delta}_{r1}^{[k]} \Big] \sum_{n=1}^{N} e^{-j(Z_r + 2T_k)\psi_n}, \tag{5.48}$$

while other terms in Eq. (5.46) stay the same. Eq. (5.48) yields the suppression of the subharmonic resonance for the mode $\boldsymbol{\chi}_k$ with phase index satisfying $(Z_r + 2T_k)/N \neq$ integer.

5.4.3 Second Harmonic Excitation and Superharmonic Resonances

When twice the mesh frequency is near a natural frequency $\omega_m = \omega_k/2 + \epsilon\sigma$, second harmonic excitation and superharmonic resonances can occur. The former one (i.e., second harmonic excitation resonance) is similar to the primary resonance case except the second harmonic of the mesh stiffnesses is the excitation, and the latter one (i.e., superharmonic resonance) results from the first harmonic of the mesh stiffnesses. It is difficult to identify their separate contributions to the dynamic response from numerical results. This work investigates the second harmonic excitation and nonlinear superharmonic resonances separately using perturbation analysis instead.

Using a similar procedure as for primary resonance but considering the second harmonic of mesh stiffnesses gives the frequency response function for second harmonic excitation resonance as

$$\omega_m = \frac{\omega_k}{2} + \frac{\omega_k}{d_k}\Big[R_1 + R_2 d_k \pm \sqrt{|R_3|^2 - (\nu_k d_k)^2}\Big], \tag{5.49a}$$

$$R_1 = N\Big[|k_{s1}^{(1)}||h_{s1}^{(1)}||\Delta_{s1}^{[k]}|\Delta_{s1,0} + |k_{r1}^{(1)}||h_{r1}^{(1)}||\Delta_{r1}^{[k]}|\Delta_{r1,0}\Big], \tag{5.49b}$$

$$R_2 = \frac{N}{2}\Big[|k_{s1}^{(1)}|(h_{s1}^{(0)} + h_{s1}^{(2)})|\Delta_{s1}^{[k]}|^2 + |k_{r1}^{(1)}|(h_{r1}^{(0)} + h_{r1}^{(2)})|\Delta_{r1}^{[k]}|^2\Big], \tag{5.49c}$$

$$R_3 = \Big[k_{s1}^{(2)}\bar{\Delta}_{s1}^{[k]}\Delta_{s1,0} + k_{r1}^{(2)}\bar{\Delta}_{r1}^{[k]}\Delta_{r1,0}\Big]\sum_{n=1}^{N} e^{j(2Z_r - T_k)\psi_n}. \tag{5.49d}$$

According to Eq. (5.39), the second harmonic excitation resonance is suppressed when $(2Z_r - T_k)/N \neq$ integer.

The analytical solution in Eq. (5.49) applies to systems with $\Omega_c > \Omega_r$. For systems with

$\Omega_c < \Omega_r$, the analytical solution is the same with that in Eq. (5.49) except that R_3 becomes

$$R_3 = \left[k_{s1}^{(2)}\bar{\Delta}_{s1}^{[k]}\Delta_{s1,0} + k_{r1}^{(2)}\bar{\Delta}_{r1}^{[k]}\Delta_{r1,0}\right]\sum_{n=1}^{N} e^{-j(2Z_r+T_k)\psi_n}. \tag{5.50}$$

From this equation, the second harmonic excitation resonance of the mode $\boldsymbol{\chi}_k$ is suppressed when its phase index satisfies $(2Z_r + T_k)/N \neq$ integer.

For the superharmonic resonance, substitution of $\omega_m = \omega_k/2 + \epsilon\sigma$ into Eq. (5.22b) but only including the first harmonic of mesh stiffnesses yields $A_k(t_1) = 0$. Therefore, the leading order solution of Eq. (5.22a) is

$$a_{l0} = jf_l/\omega_l, \qquad l = 1, 2, \ldots. \tag{5.51}$$

With substitution of Eq. (5.51) into Eq. (5.22b), the solution of Eq. (5.22b) for systems with $\Omega_c > \Omega_r$ is

$$\begin{aligned} a_{l1} = P_l(t_1)e^{j\omega_l t_0} + \frac{\rho_l f_l}{\omega_l^2} + (S_{l1}e^{j\omega_m t})\sum_{n=1}^{N} e^{j(Z_r-T_l)\psi_n} \\ +(S_{l2}e^{-j\omega_m t})\sum_{n=1}^{N} e^{-j(Z_r+T_l)\psi_n}, \qquad l = 1, 2, \ldots \end{aligned} \tag{5.52a}$$

$$S_{l1} = \frac{\omega_l}{\omega_m - \omega_l}\left[gk_{sp}C_{s1}^{(1)}\bar{\Delta}_{s1}^{[l]}\Delta_{s1,0} + k_{rp}C_{r1}^{(1)}\bar{\Delta}_{r1}^{[l]}\Delta_{r1,0}\right], \tag{5.52b}$$

$$S_{l2} = \frac{-\omega_l}{\omega_m + \omega_l}\left[gk_{sp}\bar{C}_{s1}^{(1)}\bar{\Delta}_{s1}^{[l]}\Delta_{s1,0} + k_{rp}\bar{C}_{r1}^{(1)}\bar{\Delta}_{r1}^{[l]}\Delta_{r1,0}\right]. \tag{5.52c}$$

From Eq. (5.39), S_{l1} and S_{l2} contribute to the first order solution a_{l1} only for $(Z_r - T_l)/N =$ integer and $(Z_r + T_l)/N =$ integer, respectively. The equation for the second order perturbation is necessary for the perturbation analysis and it gives

$$\begin{aligned}\frac{\partial a_{l2}}{\partial t_0} - j\omega_l a_{l2} = & -\frac{\partial a_{l1}}{\partial t_1} - \frac{\partial a_{l0}}{\partial t_2} - \rho_l a_{l1} \\ & -\sum_{i=1}^{\infty}\sum_{n=1}^{N}\Big\{ g k_{sp} Q_{sn}\big[(\boldsymbol{\phi}_l,\ \mathbf{E}_{sn}\boldsymbol{\phi}_i)a_{i1} + (\boldsymbol{\phi}_l,\ \mathbf{E}_{sn}\bar{\boldsymbol{\phi}}_i)\bar{a}_{i1}\big] \\ & + k_{rp} Q_{rn}\big[(\boldsymbol{\phi}_l,\ \mathbf{E}_{rn}\boldsymbol{\phi}_i)a_{i1} + (\boldsymbol{\phi}_l,\ \mathbf{E}_{rn}\bar{\boldsymbol{\phi}}_i)\bar{a}_{i1}\big]\Big\} \\ & -\sum_{i=1}^{\infty}\sum_{n=1}^{N}\Big\{ g^2 k_{sp} \hat{Q}_{sn} h_{sn}\big[(\boldsymbol{\phi}_l,\ \mathbf{E}_{sn}\boldsymbol{\phi}_i)a_{i0} + (\boldsymbol{\phi}_l,\ \mathbf{E}_{sn}\bar{\boldsymbol{\phi}}_i)\bar{a}_{i0}\big] \\ & + k_{rp} \hat{Q}_{rn} h_{rn}\big[(\boldsymbol{\phi}_l,\ \mathbf{E}_{rn}\boldsymbol{\phi}_i)a_{i0} + (\boldsymbol{\phi}_l,\ \mathbf{E}_{rn}\bar{\boldsymbol{\phi}}_i)\bar{a}_{i0}\big]\Big\}, \\ & l = 1, 2, \ldots . \end{aligned} \tag{5.53}$$

With substitution of Eqs. (5.51) and (5.52) into Eq. (5.53) for $l = k$, the solvability condition for the resulting equation with $\omega_m = \omega_k/2 + \epsilon\sigma$ yields the frequency response function for superharmonic resonance for systems with $\Omega_c > \Omega_r$ as

$$\omega_m = \frac{\omega_k}{2} + \frac{\omega_k}{d_k}\Big[R_1 d_k \pm \sqrt{|R_2|^2 - (\nu_k d_k)^2}\Big], \tag{5.54a}$$

$$R_1 = \frac{N}{2}\Big[|k_{s1}^{(1)}|(h_{s1}^{(0)} + h_{s1}^{(2)})|\Delta_{s1}^{[k]}|^2 + |k_{r1}^{(1)}|(h_{r1}^{(0)} + h_{r1}^{(2)})|\Delta_{r1}^{[k]}|^2\Big], \tag{5.54b}$$

$$\begin{aligned} R_2 = \sum_{i=1}^{\infty}\Big[& (k_{s1}^{(1)}\bar{\Delta}_{s1}^{[k]}\Delta_{s1}^{[i]} + k_{r1}^{(1)}\bar{\Delta}_{r1}^{[k]}\Delta_{r1}^{[i]})S_{i1}\sum_{n=1}^{N} e^{j(Z_r - T_k + T_i)\psi_n}\sum_{n=1}^{N} e^{j(Z_r - T_i)\psi_n} \\ & + (k_{s1}^{(1)}\bar{\Delta}_{s1}^{[k]}\bar{\Delta}_{s1}^{[i]} + k_{r1}^{(1)}\bar{\Delta}_{r1}^{[k]}\bar{\Delta}_{r1}^{[i]})\bar{S}_{i2}\sum_{n=1}^{N} e^{j(Z_r - T_k - T_i)\psi_n}\sum_{n=1}^{N} e^{j(Z_r + T_i)\psi_n}\Big]. \end{aligned} \tag{5.54c}$$

According to Eq. (5.39), the contribution from S_{i1} to R_2 can be nontrivial only for $(Z_r - T_i)/N =$ integer and $(Z_r - T_k + T_i)/N =$ integer, and $\bar{S}_{i2}$ can contribute to R_2 only for $(Z_r + T_i)/N =$ integer and $(Z_r - T_k - T_i)/N =$ integer. In other words, R_2 can be nontrivial only for $(2Z_r - T_k)/N =$ integer, and the contribution from S_{i1} and $\bar{S}_{i2}$ to R_2 can be nontrivial only for $(Z_r - T_i)/N =$ integer and $(Z_r + T_i)/N =$ integer, respectively. For the case $(2Z_r - T_k)/N \neq$ integer, $R_2 = 0$ and the superharmonic resonance is suppressed. This suppression rule applies to systems with $\Omega_c > \Omega_r$.

For systems with $\Omega_c < \Omega_r$, superharmonic resonance is suppressed for the mode $\boldsymbol{\chi}_k$ with phase index satisfying $(2Z_r + T_k)/N \neq$ integer. The derivation for this suppression rule is similar to that for systems with $\Omega_c > \Omega_r$ discussed above.

5.5 Results and Discussions

This section discusses the results from the analytical frequency response functions derived in the previous section and numerical simulations with a five-planet planetary gear in Table 5.4. The sun and ring gears are the input and output, respectively. The carrier is stationary and fixed to ground. The ring rigid body is fixed such that it cannot deviate from the position determined by its kinematics. Planet bearing stiffnesses k_ζ, k_η are infinitely high such that planets cannot translate. The input torque on the sun gear is 500 N·m.

Table 5.4: Dimensional parameters of an example planetary gear with an elastic ring.

Stiffness (N/m)	$k_s = k_{su} = 0,\ Rk_u = Rk_v = 10.0 \times 10^6,\ k_{sp} = 529 \times 10^6,\ k_{rp} = 647 \times 10^6$
Inertia (kg)	$I_s/R_s^2 = 0.654,\ I_p/R_p^2 = 0.490$
Mass (kg)	$m_s = 0.640$
Dimensions (mm)	$R = 150,\ \Gamma = 12.4,\ H = 18.0,\ B = 25.4$
Elastic modulus (GPa)	$E = 202,\ \kappa G = 62.4$
Density (kg/m^3)	$\rho = 7.85 \times 10^3$
Pressure angle (deg)	$\alpha_s = \alpha_r = 24.6$

Two different planet phasing conditions are considered. One has in-phase tooth meshes with sun and ring tooth numbers $Z_s = 30$ and $Z_r = 100$, and the other has out-of-phase tooth meshes with $Z_s = 29$ and $Z_r = 101$. These two cases have identical parameters in Table 5.4 and identical mesh stiffness variations for the first planet in Fig. 5.2. The Fourier coefficients of these mesh stiffness variations are given in Table 5.5.

Table 5.5: Fourier coefficients of sun-planet and ring-planet mesh stiffnesses in Fig. 5.2.

Harmonics, L	k_{s1}^L (10^6 N/m)	k_{r1}^L (10^6 N/m)
1	-64.2 +j15.3	-85.1+j36.8
2	23.0 -j10.4	16.8-j11.9
3	7.99-j7.57	7.64 -j23.2
4	-9.97+j14.6	-0.146+j11.9
5	0.675 -j0.148	4.86+j11.9

Figure 5.8 shows the natural frequencies $\omega_{11} \sim \omega_{22}$ for the five-planet in-phase system over a range of mesh frequencies. They are calculated from the discretized eigenvalue problem in Eq. (5.10). The natural frequencies for the out-of-phase system are slightly different from those in Fig. 5.8, and this small difference is neglected in the following study. Table 5.6 shows the phase indices for the natural frequencies $\omega_{11} \sim \omega_{22}$ for the system with counter-clockwise rotation of the carrier relative to the ring gear (i.e., $\Omega_c > \Omega_r$). If not otherwise indicated, the carrier rotates counter-clockwise relative to the ring gear in the following results.

Table 5.6: Phase indices for the natural frequencies $\omega_{11} \sim \omega_{22}$ in Fig. 5.8. The system has counter-clockwise rotation of the carrier relative to the ring gear (i.e., $\Omega_c > \Omega_r$).

ω_{11}	ω_{12}	ω_{13}	ω_{14}	ω_{15}	ω_{16}	ω_{17}	ω_{18}	ω_{19}	ω_{20}	ω_{21}	ω_{22}
1	4	2	3	0	4	1	0	0	4	1	0

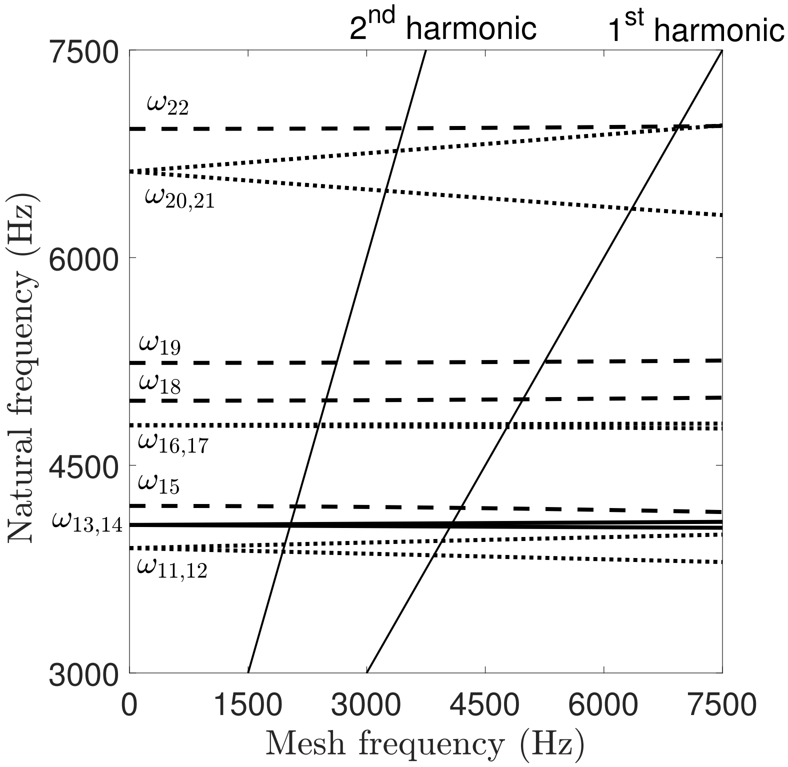

Figure 5.8: Natural frequencies of a five-planet system in Table 5.4 for a range of mesh frequencies. The dashed, dotted, and solid lines represent natural frequencies of rotational, translational, and planet modes, respectively.

5.5.1 Comparison of numerical and analytical results

Figure 5.9 shows the primary resonance of mode ω_{18} from numerical integration (NI) with the first and full mesh stiffness harmonics and multiple scale perturbation for the in-phase system. The mode ω_{18} has damping ratio $\nu_{18} = 2.40\%$, and all other modes are suppressed by high damping. The results from NI with the first harmonic have slight difference from those from NI with full harmonics, justifying the truncation of mesh stiffness harmonics to the first order in the perturbation analysis. The analytical solutions from perturbation agree well with those from NI with the first harmonic except for large amplitudes where tooth contact loss is so significant that the first order perturbation is not sufficient.

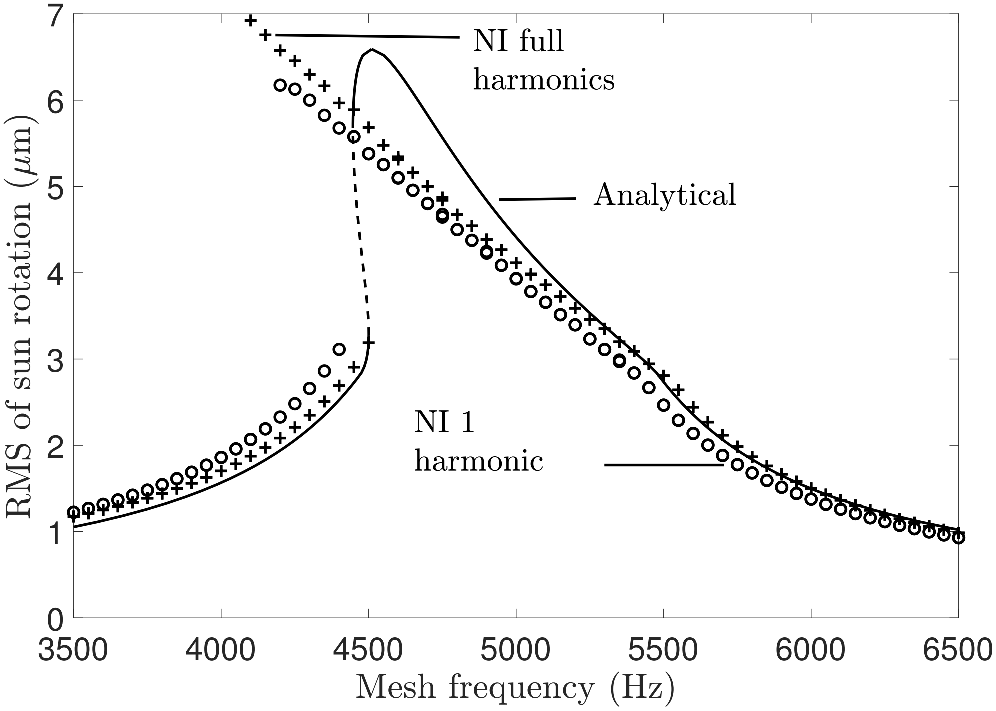

Figure 5.9: RMS of sun rotation for the primary resonance of mode ω_{18} from numerical integration (NI) with full and the first mesh stiffness harmonics and the analytical approximation in Eq. (5.35) for the in-phase system. The dashed line represents unstable solutions.

Extending to higher order perturbation might increase the accuracy of the analytical solutions but with increased complexity. The sun-planet meshes lose contact, and the ring-planet meshes do not. The analytical and numerical solutions agree on this point.

The subharmonic resonance of mode ω_{18} from NI and perturbation is shown in Fig. 5.10 for the in-phase system. The modal damping ratios are the same with those for Fig. 5.9. For increasing mesh frequency, the numerical result follows the period-T_m solution branch, jumps up at 9700 Hz, follows the period-$2T_m$ solution branch, and jumps down to the period-T_m solution at 10100 Hz. For decreasing mesh frequency, the numerical result jumps up at 10200 Hz, follows the period-$2T_m$ solution branch, and jumps down to the period-T_m solution at the peak frequency. The analytical solution successfully captures the vertical jumping up

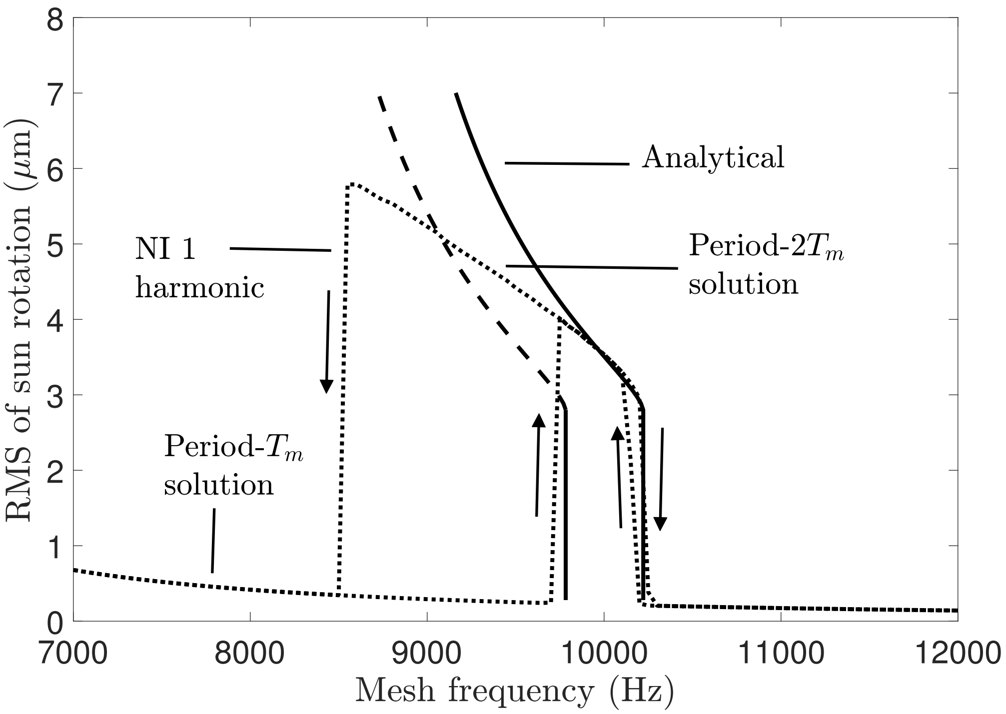

Figure 5.10: RMS of sun rotation for the subharmonic resonance of mode ω_{18} from NI and the analytical approximation in Eq. (5.46) for the in-phase system. The dashed line represents unstable solutions.

and down branches for increasing mesh frequency. For decreasing mesh frequency, the jump up and stable period-$2T_m$ solution branches are successfully identified by perturbation, but it does not capture the jumping down branch at the peak frequency. The analytical solution yields open solution branches because of absence of the amplitude d_k in the square root in Eq. (5.46). The mesh frequency interval bounded by the two vertical branches from perturbation is the parametric instability region for the corresponding linear system. From Eq. (5.46), this instability interval is

$$\Delta\omega_m = 8\omega_k\sqrt{|R_3|^2 - \nu_k^2}. \tag{5.55}$$

Eq. (5.55) shows an increase of damping can narrow the instability region and even eliminate it.

Figure 5.11a and Figure 5.11b show the second harmonic excitation and superharmonic resonances of mode ω_{18} from NI and perturbation for the in-phase system. The damping ratio for this mode is 2%. Only the second harmonic of mesh stiffnesses is considered for the NI solution in Fig. 5.11a, while only the first harmonic is included in Fig. 5.11b. This separates the contributions from different sources to the resonance. The response components at twice mesh frequency from NI are compared to the analytical solutions from perturbation in Fig. 5.11a and Fig. 5.11b. The analytical solutions agree well with the numerical ones for both the second harmonic excitation and superharmonic resonances. The larger amplitude of the second harmonic excitation resonance relative to the superharmonic resonance indicates the second harmonic excitation contributes more to the resonance at twice mesh frequency.

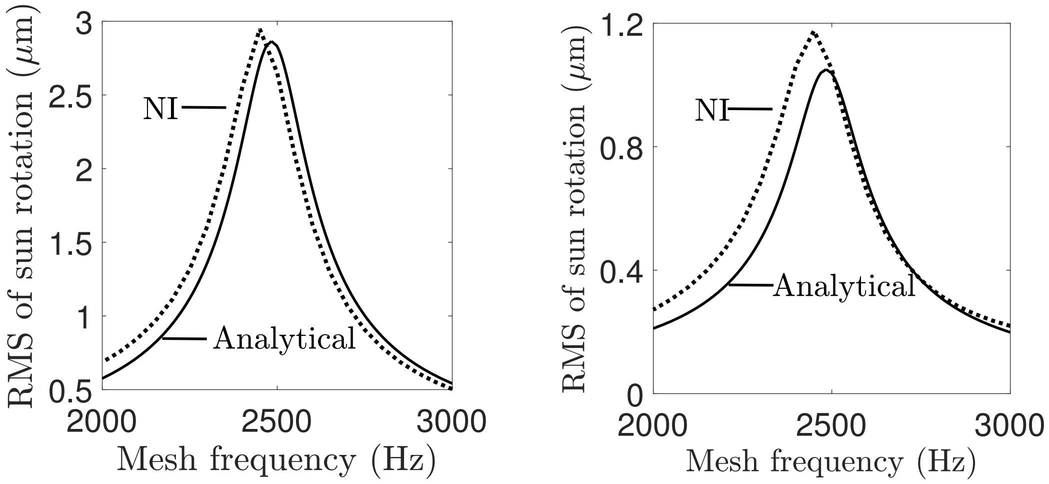

(a)

(b)

Figure 5.11: RMS of sun rotation for (a) second harmonic excitation and (b) superharmonic resonance of mode ω_{18} from NI and perturbation for the in-phase system.

5.5.2 Mesh Phasing Effect

Figure 5.12a and Figure 5.12b show the dynamic response in the mesh frequency range $6000 \sim 8000$ Hz from NI and perturbation for the in-phase and out-of-phase systems, respectively. The natural frequencies $\omega_{20} \sim \omega_{22}$ fall into this frequency range, as shown in Fig. 5.8. The damping ratios for these three modes are $\nu_{20} = \nu_{21} = 0.5\%$, and $\nu_{22} = 1\%$. All other modes are suppressed by high damping. Figure 5.8 shows the natural frequencies ω_{21} and ω_{22} are close to each other. If resonance occurred for both ω_{21} and ω_{22} simultaneously, the assumption that one mode dominates the response near a resonance was not valid and the analytical solutions would not work.

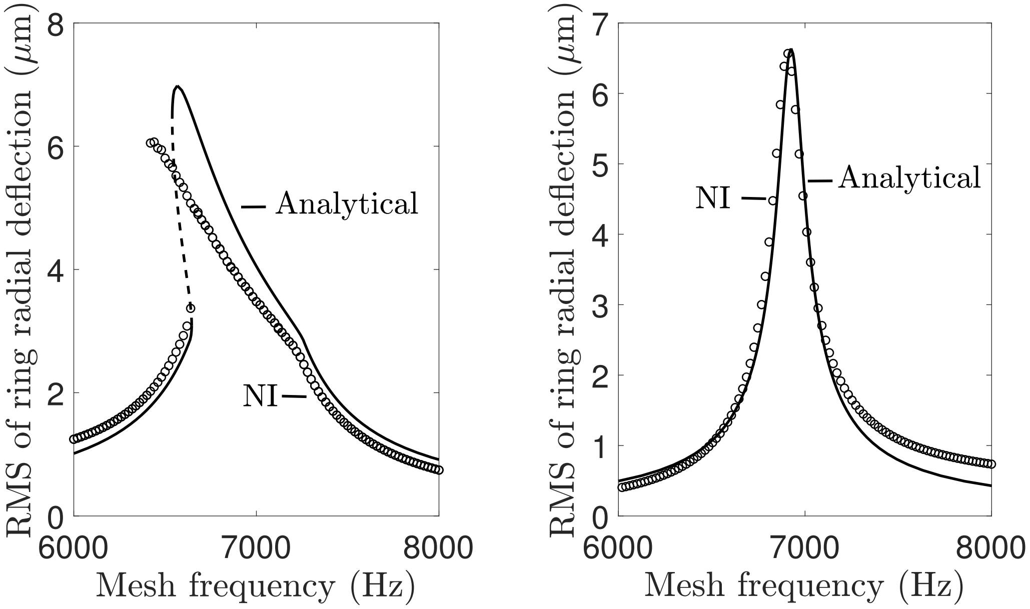

(a)

(b)

Figure 5.12: RMS of ring radial deflection at $\theta = 0$ for the (a) in-phase and (b) out-of-phase systems from NI and perturbation.

The numerical results in Fig. 5.12a show that resonance occurs only for the rotational mode ω_{22} for the in-phase system. For the out-of-phase system in Fig. 5.12b, only the translational mode ω_{21} with phase index 1 causes a resonance. As a result, the assumption that one mode dominates the response near a resonance holds. The agreements between the analytical and numerical results in both Fig. 5.12a and Fig. 5.12b confirm this point.

From the analytical solution in Section 5.4.1, a primary resonance occurs only for the mode $\boldsymbol{\chi}_k$ with phase index satisfying $(Z_r - T_k)/N$ = integer. For the in-phase system, only rotational modes with phase index 0 can cause resonances. Therefore, the resonances for the translational modes ω_{20} and ω_{21} are suppressed in Fig. 5.12a. For the five-planet ($N = 5$) out-of-phase system with $Z_r = 101$, resonance occurs only for translational modes with phase index 1. This explains the resonance only for the mode ω_{21} in Fig. 5.12b. This mesh phasing effect leads to suppression of certain modes, making the assumption that one mode dominates the response near a resonance still valid for the case where multiple natural frequencies are close to a primary resonant frequency but have different phase indices.

The above discussion is limited to primary resonances. In general, the assumption that one mode dominates the response is not valid when multiple modes are excited to resonances simultaneously. For example, a primary resonance of one mode coincides with a subharmonic resonance of another different mode. Neither the analytical solutions for primary resonances in Eq. (5.35) nor those for subharmonic resonances in Eq. (5.46) work for this case. If one of the two resonances (for example, the primary resonance) is suppressed by the mesh phasing effect, the assumption that one mode dominates the response holds and the analytical solutions in Eq. (5.46) works for this case.

The results for the in-phase system in Fig. 5.12a and out-of-phase system in Fig. 5.12b follow the suppression conditions for systems with $\Omega_c > \Omega_r$. If the planetary gear system reverses rotation but keeps all other parameters unchanged, the dynamic response for the in-phase and out-of-phase systems stay the same with those in Fig. 5.12a and Fig. 5.12b. The natural frequency loci for the reversed rotation are identical to those in Fig.

5.8, except that a translational or planet mode natural frequency that has phase index d becomes a translational or planet mode natural frequency with phase index $N - d$ for the reversed rotation (Table 5.7). Because of $\Omega_c < \Omega_r$ for the reversed rotation, the suppression conditions for systems with $\Omega_c < \Omega_r$ apply.

Table 5.7: Phase indices for the natural frequencies $\omega_{11} \sim \omega_{22}$ in Fig. 5.8. The system has clockwise rotation of the carrier relative to the ring gear (i.e., $\Omega_c < \Omega_r$).

ω_{11}	ω_{12}	ω_{13}	ω_{14}	ω_{15}	ω_{16}	ω_{17}	ω_{18}	ω_{19}	ω_{20}	ω_{21}	ω_{22}
4	1	3	2	0	1	4	0	0	1	4	0

5.5.3 Gyroscopic Effects

Figure 5.13 shows the dynamic response near ω_{15} from NI for the in-phase system with and without gyroscopic effects. The damping ratio for the mode ω_{15} is 0.65%. Resonance occurs for the system with gyroscopic effects but is suppressed for the case without gyroscopic effects. The mode ω_{15} for the non-gyroscopic system is a purely ring mode where sun-planet and ring-planet mesh deflections vanish [21]. Therefore, the term $R_3 = 0$ in Eq. (5.35), leading to the suppression of the resonance of mode ω_{15} for the non-gyroscopic case. Non-gyroscopic systems with odd number of planets (for example, the current five-planet system) have only one type of purely ring modes that are associated with phase index 0 [21]. A purely ring mode of this type (for example, the mode ω_{15}) evolves into a rotational mode when gyroscopic effects are introduced, as shown in Chapter 3. The nontrivial sun-planet and ring-planet modal mesh deflections lead to non-zero R_3 for the rotational mode ω_{15}. Thus, resonance of mode ω_{15} occurs for the system with gyroscopic effects.

For non-gyroscopic systems with even number of planets (i.e., even N), a different

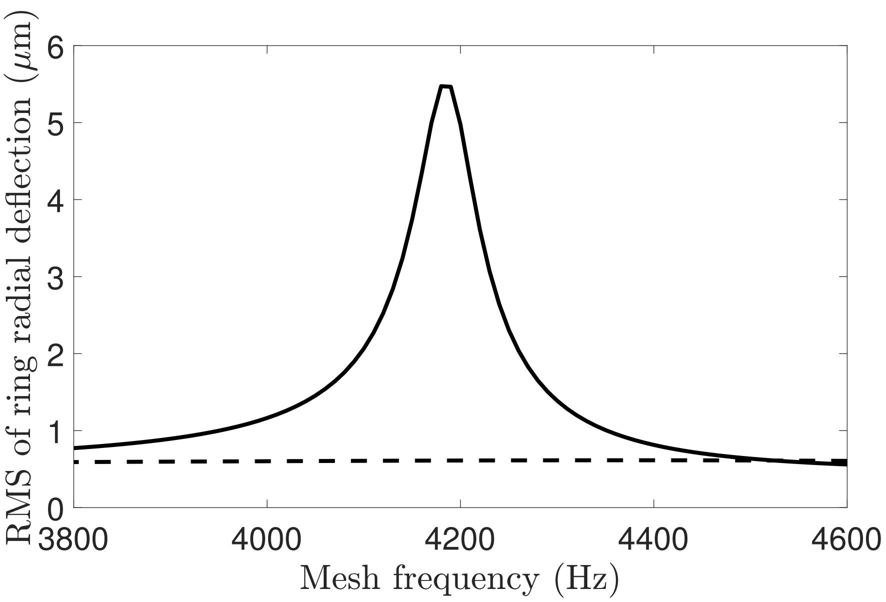

Figure 5.13: RMS of ring radial deflection at $\theta = \pi/5$ for the primary resonance of mode ω_{15} from NI for the in-phase system with (solid line) and without (dashed line) gyroscopic effect.

type of purely ring modes with phase index $N/2$ exist in addition to those of phase index 0 [21]. Chapter 3 shows a purely ring mode of phase index $N/2$ becomes a planet mode having phase index $N/2$ when gyroscopic effects are introduced. This planet mode for the gyroscopic system can be excited, while the corresponding purely ring mode is suppressed for the non-gyroscopic system.

Figure 5.14 shows the influence of the gyroscopic effects on the resonance of the translational modes ω_{20}, ω_{21}. The damping ratios for these two modes are $\nu_{20} = \nu_{21} = 0.5\%$, and all other modes are suppressed by high damping. The modes ω_{20}, ω_{21} are degenerate for the case without gyroscopic effects, as shown in Fig. 5.8 at zero mesh frequency where the speed-dependent gyroscopic effect vanishes. Therefore, only one resonant peak occurs for this pair of degenerate modes in Fig. 5.14. When the gyroscopic effects are introduced, the degenerate modes ω_{20}, ω_{21} split (Fig. 5.8). The mode ω_{21} causes the resonance in Fig. 5.14, but no resonance occurs near ω_{20}. As shown in Table 5.6, the two modes ω_{20} and ω_{21} have phase indices $T_{20} = 4$ and $T_{21} = 1$, respectively. Because $(Z_r - T_{20})/N = (101 - 4)/5 \neq$ integer, the term R_3 in Eq. (5.38c) vanishes for ω_{20}. Thus, no resonance occurs near ω_{20}. The resonance near ω_{21} occurs because $(Z_r - T_{21})/N = (101 - 1)/5 =$ integer. The peak amplitude for the case with gyroscopic effects is smaller than that without gyroscopic effects in Fig. 5.14. From Eqs. (5.38c) and (5.40), the gyroscopic effects alter the peak amplitude through changing modal mesh deflections. For the case in Fig. 5.14, the modal mesh deflections for the gyroscopic system results in smaller amplitude of R_3 than those for the non-gyroscopic system.

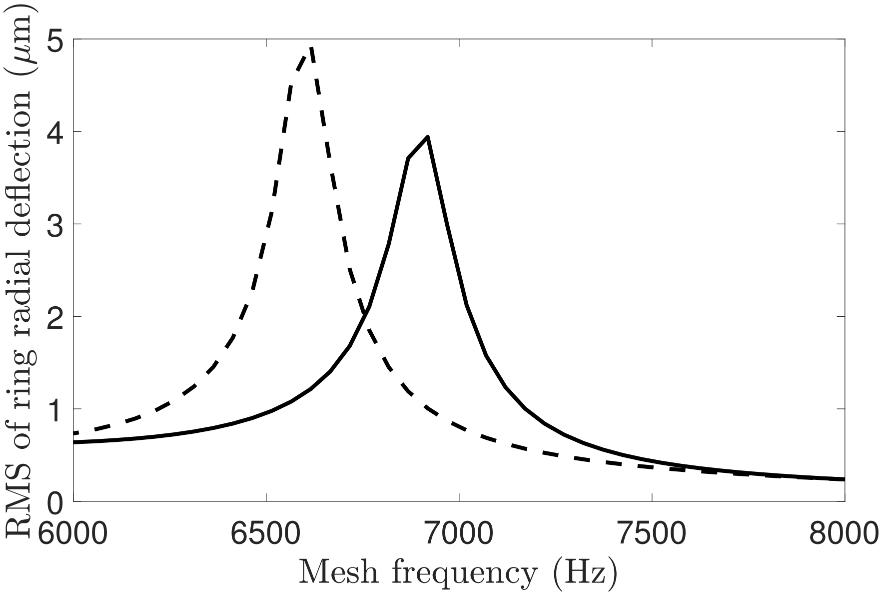

Figure 5.14: RMS of ring radial deflection at $\theta = \pi/5$ for the dynamic response near ω_{20}, ω_{21} from NI for the out-of-phase system with (solid line) and without (dashed line) gyroscopic effect.

Chapter 3 gives a pair of degenerate planet modes with multiplicity two splits into two planet modes having different phase indices when gyroscopic effects are introduced. For example, the planet modes ω_{13} and ω_{14} in Fig. 5.8 are degenerate at zero mesh frequency and split for non-zero mesh frequency. The mode ω_{13} has phase index 2, and ω_{14} has phase index 3 (Table 5.6). Similar to the translational mode resonance for ω_{20} and ω_{21}, only one of the modes ω_{13} and ω_{14} can cause resonance because the conditions $(Z_r - T_{13})/N =$ integer and $(Z_r - T_{14})/N =$ integer cannot hold simultaneously.

5.6 Conclusions

This paper investigates nonlinear dynamics of planetary gears with an elastically deformable ring and equally-spaced planets. An analytical model with rigid sun, carrier, and planets coupled to an elastic ring is used. The model includes gyroscopic and centripetal effects from carrier and ring gear rotation. The sun-planet and ring-planet mesh interactions are modeled as time-varying stiffnesses with tooth separation nonlinearity. Numerical integration of the model gives the dynamic responses and they agree well with those from a finite element/contact mechanics model.

With the assumption that one mode dominates the response near resonances, the method of multiple scales yields closed-form solutions for primary, subharmonic, superharmonic, and second harmonic resonances. The analytical solutions are verified against the solutions from numerical integration. These analytical solutions explicitly show the parameter dependence of the dynamic responses. The main conclusions are :

- Planet mesh phasing, determined by the sun and ring gear tooth numbers (Z_s and Z_r) and the number of planets N, plays an important role in the occurrence of resonances. For systems with counter-clockwise rotation of the carrier relative to the ring gear, primary resonance can occur only for modes with phase index T_k satisfying $(Z_r - T_k)/N =$ integer; subharmonic resonance can occur only for modes satisfying $(Z_r -$

$2T_k)/N =$ integer; and, superharmonic and second harmonic excitation resonances can occur only for modes satisfying $(2Z_r - T_k)/N =$ integer. In contrast, systems with clockwise rotation of the carrier relative to the ring gear can have primary resonance only for modes satisfying $(Z_r + T_k)/N =$ integer, subharmonic resonance only for modes satisfying $(Z_r + 2T_k)/N =$ integer, and superharmonic and second harmonic excitation resonances only for modes satisfying $(2Z_r + T_k)/N =$ integer.

- The assumption that one mode dominates the response is in general not valid when multiple modes are excited to resonances simultaneously. The mesh phasing effect can suppresses certain resonances, making this assumption and the analytical solutions still valid.

- Different from non-gyroscopic planetary gears where the sun-planet and ring-planet mesh deflections for a single planet are either in-phase or 180 degree out-of-phase, those for gyroscopic planetary gears are in general out-of-phase. Purely ring modes for non-gyroscopic systems are not excited. When gyroscopic effects are included, these modes become rotational or planet modes and can cause resonances. Degenerate translational or planet modes with multiplicity two for non-gyroscopic systems split with gyroscopic effects introduced. Only one of the split modes can cause primary resonances. The gyroscopic effects alter the resonant amplitudes through changing modal mesh deflections.

Chapter 6

Future Recommendations

6.1 Mesh Phasing Rule for the Dynamics of Planetary Gears with a Deformable Ring Gear

Numerical experiments show the elastic ring has only certain nodal diameter (ND) deformation for a specified harmonic of periodic responses with mesh frequency ω_m. Take a five-planet ($N = 5$) system with sun and ring tooth numbers $Z_s = 28$, $Z_r = 92$ for example. When its carrier rotates counter-clockwise relative to its ring gear (i.e. $\Omega_c > \Omega_r$), the system has only $sN + 2$ ND (i.e., $e^{j(sN+2)\theta}$) ring deformation for the first mesh frequency harmonic (i.e., $e^{j\omega_m t}$), $sN + 4$ ND for the second harmonic, and $sN + 1$ ND for the third harmonic, where $s = 0, \pm1, \pm2 \ldots$. If the five-planet system reverses its rotation (i.e., its carrier rotates clockwise relative to its ring gear), the ring deformation contains only $sN+3$ ND components for the first harmonic, $sN+1$ ND for the second harmonic, $sN+4$ ND for the third harmonic.

The modal structure defined in Chapter 3 gives that a mode with phase index $d \in \{0, 1, \ldots, N - 1\}$ contain only $sN + d$ ND ring deformation. Therefore, the five-planet system has only modes with phase index $d = 2$ excited for the first harmonic, $d = 4$ for the second harmonic, and $d = 1$ for the third harmonic when $\Omega_c > \Omega_r$. In contrast, the five-planet system has only modes with phase index $d = 3$ excited for the first harmonic, $d = 1$ for the second harmonic, and $d = 4$ for the third harmonic when $\Omega_c < \Omega_r$.

The excited ring deformation and modes for any harmonic and any planet mesh phasing are summarized in Table 6.1. These rules are observed from numerical simulations. Mathematical justification is necessary.

Table 6.1: Summary of the rules of the excited ring deformation and modes by the l-th mesh frequency harmonic.

	Systems with $\Omega_c > \Omega_r$	Systems with $\Omega_c < \Omega_r$
Excited ND ring deformation	$sN + \mathrm{mod}(lZ_r, N)$	$sN + \mathrm{mod}(lZ_s, N)$
Phase index of excited modes	$\mathrm{mod}(lZ_r, N)$	$\mathrm{mod}(lZ_s, N)$

6.2 Three Dimensional Vibrations of Helical Planetary Gears with a Deformable Ring Gear

The analytical model in this work only considers in-plane vibration for each component in a planetary gear system. This model applies to spur planetary gears. For helical planetary gears, both in-plane and out-of-plane motions are significant. The sun, carrier, and planets should be modeled as rigid bodies with each having six degrees of freedom: two in-plane translations, one in-plane rotation, one axial translation, and two tilting motions. The elastic ring gear should have radial, tangential, axial, in-plane bending, out-of-plane bending, and twisting deflections (Fig. 6.1). The mesh interaction can be modeled as a stiffness normal to the tooth profile.

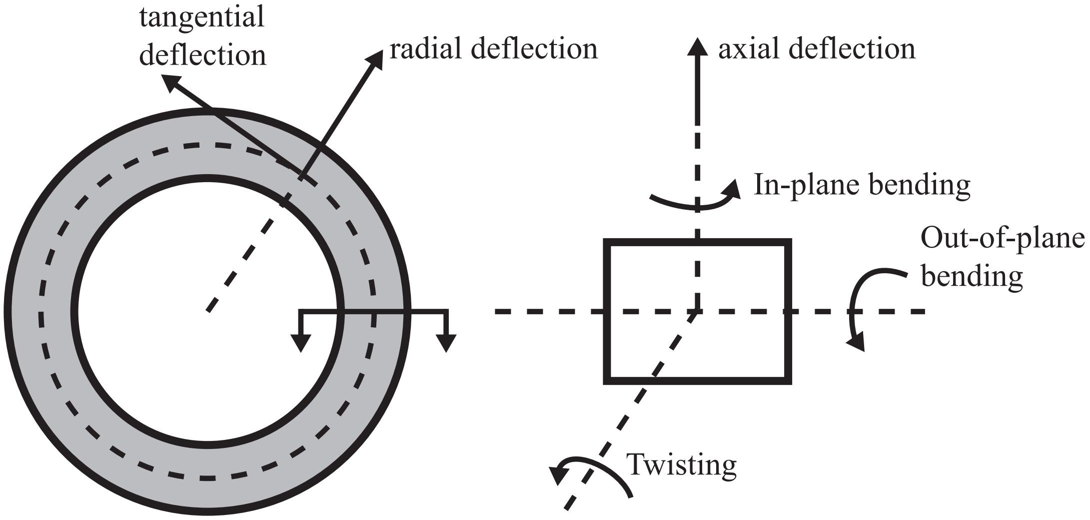

Figure 6.1: Schematic of an elastic ring with three dimensional motions.

Because of cyclic symmetry, helical planetary gears are expected to have structured modal properties like spur planetary gears do. Vibration modes can be classified into different types, but the modal properties for each type need to be investigated. In particular, how out-of-plane motions couple with in-plane motions for each type of modes is unknown. Parametric instabilities of helical planetary gears can be investigated with the three dimensional model. An instability suppression rule is expected to exist. Dynamic responses can be numerically simulated, and analytical solutions for dynamic responses near resonances can be derived.

6.3 Nonlinear Dynamics of Compound Planetary Gears with a Deformable Ring Gear

The current work deals with single-stage planetary gears where sun-planet and ring-planet meshes have the same frequency. For a compound planetary gear in Fig. 6.2, the mesh frequency of the sun and stage-1 planet differs from that of the ring and stage-2 planet. Both frequencies parametrically excite the compound planetary gear system.

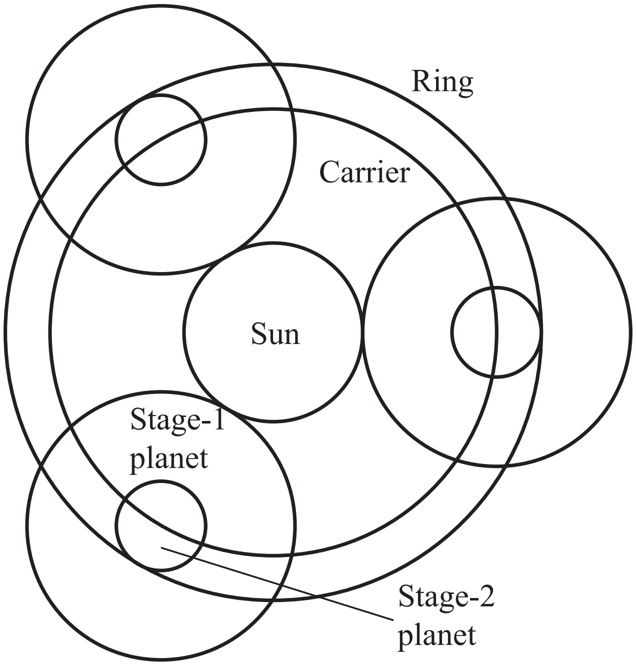

Figure 6.2: Schematic of a compound planetary gear with two stages of planets.

The current analytical model can be extended to include parametric excitations and tooth separation nonlinearity of sun-planet and ring-planet meshes with different mesh frequencies for compound planetary gears. Nonlinear dynamic responses can be simulated with numerical integration of the analytical model. Analytical solutions for dynamic responses near resonances can be derived with the method of multiple scales. How the two stages of mesh excitations interact with each other under resonant conditions needs investigation. The ratio of the two mesh frequencies may significantly influence the two stage mesh interactions. When this ratio is not an integer or its reciprocal, only one stage of mesh excitations is expected to drive a resonance. In contrast, the two stages of mesh excitations may jointly drive a resonance for the case where this ratio is an integer or its reciprocal. How planet mesh phasing influences the dynamic responses is unknown.

Bibliography

[1] P. D. McFadden, J. D. Smith, An explanation for the asymmetry of the modulation sidebands about the tooth meshing frequency in epicyclic gear vibration, Proceedings of the Institution of Mechanical Engineers, Part C: Journal of Mechanical Engineering Science 199 (1985) 65–70.

[2] J. McNames, Fourier series analysis of epicyclic gearbox vibration, Journal of Vibration and Acoustics 124 (2001) 150–153.

[3] M. Inalpolat, A. Kahraman, A theoretical and experimental investigation of modulation sidebands of planetary gear sets, Journal of Sound and Vibration 323 (2009) 677–696.

[4] F. Cunliffe, J. D. Smith, D. B. Welbourn, Dynamic tooth loads in epicyclic gears, Journal of Engineering for Industry 96 (1974) 578–584.

[5] M. Botman, Epicyclic gear vibrations, Journal of Engineering for Industry 98 (1976) 811–815.

[6] A. Kahraman, Planetary gear train dynamics, Journal of Mechanical Design 116 (1994) 713–720.

[7] A. Kahraman, Natural modes of planetary gear trains, Journal of Sound Vibration 173 (1994) 125–130.

[8] X. Gu, P. Velex, A lumped parameter model to analyse the dynamic load sharing in planetary gears with planet errors, Applied Mechanics and Materials 86 (2011) 374–379.

[9] J. Lin, R. G. Parker, Analytical characterization of the unique properties of planetary gear free vibration, Journal of Vibration and Acoustics 121 (1999) 316–321.

[10] C. G. Cooley, R. G. Parker, Vibration properties of high-speed planetary gears with gyroscopic effects, Journal of Vibration and Acoustics 134 (2012) 061014–061014.

[11] A. Masoumi, F. Pellicano, F. S. Samani, M. Barbieri, Symmetry breaking and chaos-induced imbalance in planetary gears, Nonlinear Dynamics 80 (2015) 561–582.

[12] S. M. Vijayakar, Calyx users manual (2005). http://ansol.us.

[13] A. Kahraman, S. Vijayakar, Effect of internal gear flexibility on the quasi-static behavior of a planetary gear set, Journal of Mechanical Design 123 (2001) 408.

[14] R. G. Parker, V. Agashe, S. M. Vijayakar, Dynamic response of a planetary gear system using a finite element/contact mechanics model, Journal of Mechanical Design 122 (1999) 304–310.

[15] A. Kahraman, A. Kharazi, M. Umrani, A deformable body dynamic analysis of planetary gears with thin rims, Journal of Sound and Vibration 262 (2003) 752–768.

[16] V. K. Ambarisha, R. G. Parker, Nonlinear dynamics of planetary gears using analytical and finite element models, Journal of Sound and Vibration 302 (2007) 577–595.

[17] A. Bodas, A. Kahraman, Influence of carrier and gear manufacturing errors on the static load sharing behavior of planetary gear sets, JSME International Journal Series C Mechanical Systems, Machine Elements and Manufacturing 47 (2004) 908–915.

[18] A. Singh, Application of a system level model to study the planetary load sharing behavior, Journal of Mechanical Design 127 (2004) 469–476.

[19] V. Abousleiman, P. Velex, A hybrid 3d finite element/lumped parameter model for quasi-static and dynamic analyses of planetary/epicyclic gear sets, Mechanism and Machine Theory 41 (2006) 725–748.

[20] V. Abousleiman, P. Velex, S. Becquerelle, Modeling of spur and helical gear planetary drives with flexible ring gears and planet carriers, Journal of Mechanical Design 129 (2007) 95.

[21] X. Wu, R. G. Parker, Modal properties of planetary gears with an elastic continuum ring gear, Journal of Applied Mechanics 75 (2008) 031014–031014.

[22] Z. Chen, Y. Shao, D. Su, Dynamic simulation of planetary gear set with flexible spur ring gear, Journal of Sound and Vibration 332 (2013) 7191–7204.

[23] A. Kahraman, Static load sharing characteristics of transmission planetary gear sets: model and experiment, in: SAE Technical Paper Series, 1999, pp. 1999–01–1050.

[24] G.-J. Cheon, R. G. Parker, Influence of bearing stiffness on the static properties of a planetary gear system with manufacturing errors, KSME international journal 18 (2004) 1978–1988.

[25] A. Singh, Influence of planetary needle bearings on the performance of single and double pinion planetary systems, ASME Journal of Mechanical Design 129 (2007) 85–94.

[26] H. Ligata, A. Kahraman, A. Singh, An experimental study of the influence of manufacturing errors on the planetary gear stresses and planet load sharing, ASME Journal of Mechanical Design 130 (2008) 041701.

[27] H. Ligata, A. Kahraman, A. Singh, A closed-form planet load sharing formulation for planetary gear sets using a translational analogy, ASME Journal of Mechanical Design 131 (2009) 021007.

[28] A. Singh, Load sharing behavior in epicyclic gears: physical explanation and generalized formulation, Mechanism and Machine Theory 45 (2010) 511–530.

[29] A. Singh, Epicyclic load sharing map: development and validation, Mechanism and Machine Theory 46 (2011) 632–646.

[30] B. Zghal, O. Graja, K. Dziedziech, F. Chaari, A. Jablonski, T. Barszcz, M. Haddar, A new modeling of planetary gear set to predict modulation phenomenon, Mechanical Systems and Signal Processing 127 (2019) 234–261.

[31] T. M. Ericson, R. G. Parker, Planetary gear modal vibration experiments and correlation against lumped-parameter and finite element models, Journal of Sound and Vibration 332 (2013) 2350–2375.

[32] T. Eritenel, R. G. Parker, Modal properties of three-dimensional helical planetary gears, Journal of Sound and Vibration 325 (2009) 397–420.

[33] A. Kahraman, Free torsional vibration characteristics of compound planetary gear sets, Mechanism and Machine Theory 36 (2001) 953–971.

[34] D. R. Kiracofe, R. G. Parker, Structured vibration modes of general compound planetary gear systems, Journal of Vibration and Acoustics 129 (2006) 1–16.

[35] Y. Guo, R. G. Parker, Purely rotational model and vibration modes of compound planetary gears, Mechanism and Machine Theory 45 (2010) 365–377.

[36] R. J. Harker, J. G. Bollinger, Instability potential of high speed gearing, Journal of Industrial Mathematics 17 (1967) 39–55.

[37] M. Amabili, A. Rivola, Dynamic analysis of spur gear pairs: steady-stage response and stability of the sdof model with time-varying meshing damping, Mechanical Systems and Signal Processing 11 (1997) 375–390.

[38] M. Benton, A. Seireg, Factors influencing instability and resonances in geared systems, ASME Journal of Mechanical Design 103 (1981) 372–378.

[39] G. V. Tordion, R. Gauvin, Dynamic stability of a two-stage gear train under the influence of variable meshing stiffnesses, Journal of Engineering for Industry 99 (1977) 785–791.

[40] M. Benton, A. Seireg, Normal mode uncoupling of systems with time varying stiffness, Journal of Mechanical Design 102 (1980) 379.

[41] J. Lin, R. G. Parker, Mesh stiffness variation instabilities in two-stage gear systems, Journal of Vibration and Acoustics 124 (2001) 68–76.

[42] P. Velex, L. Flamand, Dynamic response of planetary trains to mesh parametric excitations, ASME Journal of Mechanical Design 118 (1996) 7–14.

[43] J. Lin, R. Parker, Planetary gear parametric instability caused by mesh stiffness variation, Journal of Sound and Vibration 249 (2002) 129–145.

[44] R. G. Parker, X. Wu, Parametric instability of planetary gears having elastic continuum ring gears, Journal of Vibration and Acoustics 134 (2012) 041011–041011.

[45] X. Qiu, Q. Han, F. Chu, Investigation of parametric instability of the planetary gear under speed fluctuations, Shock and Vibration 2017 (2017) 1–14.

[46] R. W. Gregory, S. L. Harris, R. G. Munro, Dynamic behaviour of spur gears, Proceedings of the Institution of Mechanical Engineers 178 (1963) 207–226.

[47] G. W. Blankenship, A. Kahraman, Gear dynamics experiments part I: characterization of forced response, in: ASME Design Engineering Technical Conferences, San Diego, CA, 1996.

[48] M. Botman, Vibration measurements on planetary gears of aircraft turbine engines, Journal of Aircraft 17 (1980) 351–357.

[49] S. Li, Q. Wu, Z. Zhang, Bifurcation and chaos analysis of multistage planetary gear train, Nonlinear Dynamics 75 (2014) 217–233.

[50] T. Sun, H. Y. Hu, Nonlinear dynamics of a planetary gear system with multiple clearances, Mechanism and Machine Theory 38 (2003) 1371–1390.

[51] A. Al-Shyyab, A. Kahraman, A non-linear dynamic model for planetary gear sets, Proceedings of the Institution of Mechanical Engineers, Part K: Journal of Multi-body Dynamics 221 (2007) 567–576.

[52] A. Al-Shyyab, K. Alwidyan, A. Jawarneh, H. Tlilan, Non-linear dynamic behaviour of compound planetary gear trains: model formulation and semi-analytical solution, Proceedings of the Institution of Mechanical Engineers, Part K: Journal of Multi-body Dynamics 223 (2009) 199–210.

[53] Y. Guo, R. G. Parker, Dynamic analysis of planetary gears with bearing clearance, Journal of Computational and Nonlinear Dynamics 7 (2012) 041002–041002.

[54] Y. Guo, J. Keller, R. G. Parker, Nonlinear dynamics and stability of wind turbine planetary gear sets under gravity effects, European Journal of Mechanics - A/Solids 47 (2014) 45–57.

[55] W. Zhu, S. Wu, X. Wang, Z. Peng, Harmonic balance method implementation of nonlinear dynamic characteristics for compound planetary gear sets, Nonlinear Dynamics 81 (2015) 1511–1522.

[56] C.-J. Bahk, R. G. Parker, Analytical solution for the nonlinear dynamics of planetary gears, Journal of Computational and Nonlinear Dynamics 6 (2010) 021007–021007.

[57] C.-J. Bahk, R. G. Parker, Analytical investigation of tooth profile modification effects on planetary gear dynamics, Mechanism and Machine Theory 70 (2013) 298–319.

[58] P. Ma, M. Botman, Load sharing in a planetary gear stage in the presence of gear errors and misalignment, ASME Journal of Mechanisms, Transmissions and Automation in Design 107 (1985).

[59] A. Kahraman, Load sharing characteristics of planetary transmissions, Mechanism and Machine Theory 29 (1994) 1151–1165.

[60] G.-J. Cheon, R. G. Parker, Influence of manufacturing errors on the dynamic characteristics of planetary gear systems, KSME International Journal 18 (2004) 606–621.

[61] F. Chaari, T. Fakhfakh, R. Hbaieb, J. Louati, M. Haddar, Influence of manufacturing errors on the dynamic behavior of planetary gears, The International Journal of Advanced Manufacturing Technology 27 (2006) 738–746.

[62] M. Inalpolat, A. Kahraman, A dynamic model to predict modulation sidebands of a planetary gear set having manufacturing errors, Journal of Sound and Vibration 329 (2010) 371–393.

[63] X. Gu, P. Velex, A dynamic model to study the influence of planet position errors in planetary gears, Journal of Sound and Vibration 331 (2012) 4554–4574.

[64] X. Gu, P. Velex, On the dynamic simulation of eccentricity errors in planetary gears, Mechanism and Machine Theory 61 (2013) 14–29.

[65] F. Ren, D. Qin, T. C. Lim, S. Lyu, Study on dynamic characteristics and load sharing of a herringbone planetary gear with manufacturing errors, International Journal of Precision Engineering and Manufacturing 15 (2014) 1925–1934.

[66] W. Kim, J. Y. Lee, J. Chung, Dynamic analysis for a planetary gear with time-varying pressure angles and contact ratios, Journal of Sound and Vibration 331 (2012) 883–901.

[67] J. Yang, P. Yang, Random vibration and dynamic analysis of a planetary gear train in a wind turbine, Shock and Vibration (2016).

[68] Y. Shao, Z. Chen, Dynamic features of planetary gear set with tooth plastic inclination deformation due to tooth root crack, Nonlinear Dynamics 74 (2013) 1253–1266.

[69] Z. Chen, Y. Shao, Dynamic features of a planetary gear system with tooth crack under different sizes and inclination angles, ASME Journal of Vibration and Acoustics 135 (2013) 031004.

[70] Z. Chen, Y. Shao, Dynamic simulation of planetary gear with tooth root crack in ring gear, Engineering Failure Analysis 31 (2013) 8–18.

[71] X. Qiu, Q. Han, F. Chu, Load-sharing characteristics of planetary gear transmission in horizontal axis wind turbines, Mechanism and Machine Theory 92 (2015) 391–406.

[72] S. M. Vijayakar, H. R. Busby, D. R. Houser, Linearization of multibody frictional contact problems, Computers and Structures 29 (1988) 569–576.

[73] S. Vijayakar, A combined surface integral and finite element solution for a three-dimensional contact problem, International Journal for Numerical Methods in Engineering 31 (1991) 525–545.

[74] J. L. Lin, W. Soedel, On general in-plane vibrations of rotating thick and thin rings, Journal of Sound and Vibration 122 (1988) 547–570.

[75] J. Kirkhope, In-plane vibration of a thick circular ring, Journal of Sound and Vibration 50 (1977) 219–227.

[76] W. B. Bickford, E. S. Reddy, On the in-plane vibrations of rotating rings, Journal of Sound and Vibration 101 (1985) 13–22.

[77] C. G. Cooley, R. G. Parker, Vibration of high-speed rotating rings coupled to space-fixed stiffnesses, Journal of Sound and Vibration 333 (2014) 2631–2648.

[78] F. Gruttmann, W. Wagner, Shear correction factors in Timoshenko's beam theory for arbitrary shaped cross-sections, Computational Mechanics 27 (2001) 199–207.

[79] S. V. Canchi, R. G. Parker, Parametric instability of a circular ring subjected to moving springs, Journal of Sound and Vibration 293 (2006) 360–379.

[80] G. F. Carrier, On the vibrations of the rotating ring, Quarterly of Applied Mathematics 3 (1945) 235–245.

[81] C. W. Bert, T. L. C. Chen, On vibration of a thick flexible ring rotating at high speed, Journal of Sound and Vibration 61 (1978) 517–530.

[82] S. C. Huang, W. Soedel, Effects of Coriolis acceleration on the free and forced in-plane vibrations of rotating rings on elastic foundation, Journal of Sound and Vibration 115 (1987) 253–274.

[83] D. Zhang, S. Wang, J. Liu, Analytical prediction for free response of rotationally ring-shaped periodic structures, Journal of Vibration and Acoustics 136 (2014) 041016–041016.

[84] W. Kim, J. Chung, Free non-linear vibration of a rotating thin ring with the in-plane and out-of-plane motions, Journal of Sound and Vibration 258 (2002) 167–178.

[85] U. Nackenhorst, M. Brinkmeier, On the dynamics of rotating and rolling structures, Archive of Applied Mechanics 78 (2008) 477–488.

[86] C. G. Cooley, C. Liu, X. Dai, R. G. Parker, Gear tooth mesh stiffness: a comparison of calculation approaches, Mechanism and Machine Theory 105 (2016) 540–553.

[87] R. G. Parker, J. Lin, Mesh phasing relationships in planetary and epicyclic gears, Journal of Mechanical Design 126 (2004) 365–370.

[88] T. Hidaka, Y. Terauchi, K. Ishioka, Dynamic behavior of planetary gear (2nd report, displacement of sun gear and ring gear), Bulletin of JSME 19 (1976) 1563–1570.

[89] T. Hidaka, Y. Terauchi, M. Nohara, J. Oshita, Dynamic behavior of planetary gear (3rd report, displacement of ring gear in direction of line of action), Bulletin of JSME 20 (1977) 1663–1672.

[90] T. Hidaka, Y. Terauchi, K. Nagamura, Dynamic behavior of planetary gear (7th report, influence of the thickness of the ring gear), Bulletin of JSME 22 (1979) 1142–1149.

[91] P. Velex, V. Pichon, L. Randrianarivo, R. Wittman, Dynamic behavior of epicyclic trains: experimental and numerical analyses, in: Proceedings of the International Gearing Conference, Newcastle, UK, 1994, pp. 265–269.

[92] C. Shi, R. G. Parker, Vibration mode structure and simplified modelling of cyclically symmetric or rotationally periodic systems, Proceedings of the Royal Society A: Mathematical, Physical and Engineering Sciences 471 (2014) 20140672–20140672.

[93] B. Dong, R. G. Parker, Modal properties of cyclically symmetric systems with central components vibrating as three-dimensional rigid bodies, Journal of Sound and Vibration 435 (2018) 350–371.

[94] M. Endo, K. Hatamura, M. Sakata, O. Taniguchi, Flexural vibration of a thin rotating ring, Journal of Sound and Vibration 92 (1984) 261–272.

[95] X. Wu, R. G. Parker, Vibration of rings on a general elastic foundation, Journal of Sound and Vibration 295 (2006) 194–213.

[96] S. V. Canchi, R. G. Parker, Parametric instability of a rotating circular ring with moving, time-varying springs, Journal of Vibration and Acoustics 128 (2005) 231–243.

[97] C. G. Cooley, R. G. Parker, Limitations of an inextensible model for the vibration of high-speed rotating elastic rings with attached space-fixed discrete stiffnesses, European Journal of Mechanics - A/Solids 54 (2015) 187–197.

[98] W. Liu, Z. Shuai, Y. Guo, D. Wang, Modal properties of a two-stage planetary gear system with sliding friction and elastic continuum ring gear, Mechanism and Machine Theory 135 (2019) 251–270.

[99] The LMS Test.Lab modal analysis manual, 2012.

[100] L. Meirovitch, A new method of solution of the eigenvalue problem for gyroscopic systems, AIAA Journal 12 (1974) 1337–1342.

[101] R. Courant, D. Hilbert, Methods of mathematical physics, volume 1, six ed., Interscience Publishers, 1966.

[102] C. G. Cooley, R. G. Parker, Eigenvalue sensitivity and veering in gyroscopic systems with application to high-speed planetary gears, European Journal of Mechanics - A/Solids 67 (2018) 123–136.

[103] C. Liu, C. G. Cooley, R. G. Parker, Parametric instability of spinning elastic rings excited by fluctuating space-fixed stiffnesses, Journal of Sound and Vibration 400 (2017) 533–549.

[104] C. G. Cooley, R. G. Parker, Mechanical stability of high-speed planetary gears, International Journal of Mechanical Sciences 69 (2013) 59–71.

[105] R. G. Schlegel, K. C. Mard, Transmission noise control approaches in helicopter design, in: ASME Design Engineering Conference, New York, NY, 1967, pp. 67–DE–58.

[106] D. L. Seager, Conditions for the neutralization of excitation by the teeth in epicyclic gearing, Proceedings of the Institution of Mechanical Engineers 17 (1975) 293–298.

[107] W. Palmer, R. Fuehrer, Noise control in planetary transmissions, in: SAE Technical Paper, 1977.

[108] A. Kahraman, G. W. Blankenship, Planet mesh phasing in epicyclic gear sets, in: Proceedings of the International Gearing Conference, Newcastle, UK, 1994, pp. 99–104.

[109] R. L. Platt, R. D. Leopold, A study on helical gear planetary phasing effects on transmission noise, VDI Berichte 1230 (1996) 793–807.

[110] R. Parker, A physical explanation for the effectiveness of planet phasing to suppress planetary gear vibration, Journal of Sound and Vibration 236 (2000) 561–573.

[111] V. K. Ambarisha, R. G. Parker, Suppression of planet mode response in planetary gear dynamics through mesh phasing, Journal of Vibration and Acoustics 128 (2005) 133–142.

[112] G. Liu, R. G. Parker, Nonlinear dynamics of idler gear systems, Nonlinear Dynamics 53 (2008) 345–367.

[113] S. Theodossiades, S. Natsiavas, Non-linear dynamics of gear-pair systems with periodic stiffness and backlash, Journal of Sound and Vibration 229 (2000) 287–310.

[114] R. Parker, S. Vijayakar, T. Imajo, Non-linear dynamic response of a spur gear pair: modelling and experimental comparisons, Journal of Sound and Vibration 237 (2000) 435–455.